Universidade de Aveiro Departamento de Física
2014

Carlos Alexandre Fernandes dos Santos

Microestruturas para MPGDs: Estudos Experimentais e de Simulação

Thick-Microstructures for MPGDs: Simulations and Experimental Studies

Universidade de Aveiro Departamento de Física
2014

Carlos Alexandre Fernandes dos Santos

Microestruturas para MPGDs: Estudos Experimentais e de Simulação

Thick-Microstructures for MPGDs: Simulations and Experimental Studies

Tese apresentada à Universidade de Aveiro para cumprimento dos requisitos necessários à obtenção do grau de Doutor em Física, realizada sob a orientação científica do Doutor João Filipe Calapez de Albuquerque Veloso, Professor Auxiliar do Departamento de Física da Universidade de Aveiro e co-orientação do Doutor António Luís Campos de Sousa Ferreira, Professor Associado do Departamento de Física da Universidade de Aveiro, e da Doutora Silvia Dalla Torre, Diretora da secção de Trieste do Istituto Nazionale di Fisica Nucleare em Itália.

Apoio financeiro da FCT (Bolsas de Doutoramento com as referências SFRH/BD/60455/2009 e SFRH/BD/80985/2011) e do FSE/FEDER no âmbito do QREN através dos programas COMPETE e Adl. Projecto CERN/FP/123597/2011 e PTDC/FIS/110925/2009

o júri / the jury

presidente / president

Prof. Doutor Amadeu Mortágua Velho da Maia Soares
Professor Catedrático do Departamento de Biologia da Universidade de Aveiro

vogais / examiners committee

Prof. Doutor Joaquim Marques Ferreira dos Santos
Professor Catedrático do Departamento de Física da Universidade de Coimbra

Prof. Doutor Francisco Amaral Fortes Fraga
Professor Associado do Departamento de Física da Universidade de Coimbra

Prof. Doutor João Filipe Calapez de Albuquerque Veloso
Professor Auxiliar do Departamento de Física da Universidade de Aveiro

Doutor Nuno Filipe da Silva Fernandes de Castro
Investigador do LIP – Laboratório de Instrumentação e Física Experimental de Partículas do Minho

Doutor Carlos Davide da Rocha Azevedo
Bolseiro de Pós-Doutoramento do i3N da Universidade de Aveiro

Agradecimentos / acknowledgements

In the context of work performed in my PhD, along a period of 4 years, I would like to acknowledge all those who contributed with their support, either directly or indirectly. In particular I thank:

To my advisor Professor Doctor João Veloso, for granting me the opportunity to perform this work, along with providing me with all the necessary conditions to succeed in my tasks. Additionally, I thank him for his friendship, sympathy and constant readiness to help.

To my co-advisor Professor Doctor António Luís Ferreira, for his constant total support.

To my colleagues, and above all, friends, from the DRIM laboratory, namely Ana Luísa, Lara, Fábio, Pedro, Filipe, Luís, Carlos Azevedo and Carlos Oliveira, for their total support and friendship.

To my co-advisor Doctor Silvia Dalla Torre, for granting me with the opportunity to work in INFN – Trieste, providing all the necessary means for my fast integration and my success.

To my colleagues and friends in Trieste, Fulvio Tessarotto, Stefano Levorato, Shuddha Dasgupta, Giorgio Menon, Mauro Gregori, Maxim Alexeev, Renato Birsa, Federica Sozzi, Lukas and Katerina Steiger, for all their help and support, and for making me feel at home.

To Rob Veenhof, for his help in issues regarding Garfield.

To all my friends for their tireless support.

And at last, but not least, to my family, and in particular to my siblings, Rui and Sérgio, for everything.

palavras-chave Foto-deteção, detetores gasosos, MPGD, THGEM, IBF, COMPASS, RICH-1

resumo

Os detetores de RICH (do inglês Ring Imaging Cherenkov) requerem grandes áreas fotossensíveis, capazes de operar em regime de fotão único, de modo estável e com ganhos elevados, em ambientes radioativos, ao mesmo tempo que são submetidos a elevadas taxas de irradiação, proporcionando uma resposta rápida e boa resolução temporal, e sendo insensíveis a campos magnéticos.

O desenvolvimento de foto-detetores baseados em detetores gasosos micro-estruturados (Micro Pattern Gaseous Detectors – MPGDs) representa uma nova geração de foto-detetores gasosos. Em particular, detetores gasosos baseados em múltiplas camadas de THGEMs (THick Gaseous Electron Multipliers), ou de estruturas baseadas em THGEMs, acoplados com uma camada foto-conversora de CsI, parecem reunir os requisitos impostos para aplicação em detetores de RICH.

Este trabalho incide no estudo da resposta de detetores gasosos baseados em THGEMs, em função dos seus parâmetros geométricos, e dos potenciais e campos elétricos aplicados, com vista à futura atualização do detetor RICH-1 da experiência COMPASS, no acelerador SPS no CERN. São realizados estudos adicionais para reduzir o refluxo de iões para o fotocátodo para minimizar o seu envelhecimento, e maximizar a eficiência de extração de fotoeletrões. Os estudos experimentais são complementados com resultados de simulações, realizadas também no âmbito deste trabalho.

keywords Photon detection, Gaseous Detectors, MPGD, THGEM, IBF, COMPASS, RICH-1

abstract Cherenkov Imaging counters require large photosensitive areas, capable of single photon detection, operating at stable high gains under radioactive backgrounds while standing high rates, providing a fast response and a good time resolution, and being insensitive to magnetic fields.
The development of photon detectors based in Micro Pattern Gaseous detectors (MPGDs), represent a new generation of gaseous photon detectors. In particular, gaseous detectors based on stacked Thick-Gaseous Electron Multipliers (THGEMs), or THGEM based structures, coupled to a CsI photoconverter coating, seem to fulfil the requirements imposed by Cherenkov imaging counters. This work focus on the study of the THGEM-based detectors response as function of its geometrical parameters and applied voltages and electric fields, aiming a future upgrade of the Cherenkov Imaging counter RICH-1 of the COMPASS experiment at CERN SPS. Further studies to decrease the fraction of ions that reach the photocathode (Ion Back Flow – IBF) to minimize the ageing and maximize the photoelectron extraction are performed. Experimental studies are complemented with simulation results, also perfomed in this work.

Contents

List of Abbreviations And Symbols

COMPASS	COmmon Muon Proton Apparatus for Structure and Spectroscopy
CsI	Caesium Iodide
ECE	Electron Collection Efficiency
ETE	Electron Transfer Efficiency
ER	Energy Resolution
FWHM	Full Width at Half Maximum
GEM	Gaseous Electron Multiplier
GPD	Gaseous Photon Detector
HEP	High Energy Physics
HV	High Voltage
IBF	Ion Back Flow
MAPMT	Multi Anode Photomultiplier
MHSP	Micro Hole and Strip Plate
Micromegas	Micro-Mesh Gaseous Structure
MIP	Minimum Ionizing Particle
MPGD	Micro Pattern Gaseous Detectors
MSGC	Microstrip Gas Chambers

MSP	Micro Strip Plate
MWPC	Multiwire Proportional Chamber
PCB	Printed Circuit Board
PID	Particle Identification
PMT	Photomultiplier
QE	Quantum Efficiency
RICH	Ring Imaging Cherenkov
ROI	Region of Interest
THCOBRA	Thick-COBRA
THGEM	Thick Gaseous Electron Multiplier
VUV	Vacuum Ultraviolet

List of Figures

List of Tables

Introduction

The discovery of Cherenkov radiation [1], along with its potential for particle identification, allowed the development of concepts for Cherenkov radiation detection. In this sense, Jacques Séguinot and Tom Ypsilantis proposed, in 1977, the Ring Imaging detection technique [2]. Together with this technique appeared the first generation of gaseous photon detectors (GPDs) using photoconverting vapours as photosensors [3]. This led to the construction and implementation of the first large scale Ring Imaging Cherenkov (RICH) detectors at OMEGA [4,5] and DELPHI experiments, both at CERN [6].

The limitations imposed by the first generation of gaseous photon detectors, mainly due to the use of photoconverting vapours led to a second generation of gaseous photon detectors, where the essential upgrade was the introduction of a solid state photosensitive layer of CsI as photoconverter [7]. The photon detector combining CsI photocathode and MWPCs [8] achieved good performance and was used as RICH detectors, among which is included RICH-1 from COMPASS, which is a high energy physics experiment at the Super Proton Synchrotron (SPS) at CERN, Geneva.

Although the second generation of gaseous photon detectors was functional as RICH detectors, with time, experiments became more demanding, imposing higher requisites. The limitations of MWPCs, such as its susceptibility to photon feedback and a high fraction of ions reaching its photocathode, limited their operation at high gain and high rates, presenting also slow response due to signals created by ions [9,10]. The planned (and recently approved) enlargement of the physics programme of the COMPASS experiment foresees operation under increased rates, which requires the maintenance of the performance of RICH-1 over future years at the present level, in more challenging conditions [11].

Based on the development of the third generation of gaseous photon detectors (which comprise Micro Pattern Gaseous Detectors [12] and CsI photocathode), integrated in the framework of the RD51 collaboration, the possibility of the mentioned RICH-1 upgrade serves as motivation for the development of a particular group of these third generation GPD, that can suit their application in RICH-1. This application represents the motivation of this work, which leads to the study and development of Thick Gaseous Electron Multipliers (THGEMs) [13] based photon detectors that are capable of: single UV photon detection; close to full photoelectron extraction; stand stable high gain under radioactive backgrounds; stand high rate; fast response; good time resolution; and low sensitivity to magnetic fields.

Accordingly to this motivation, the following goals are proposed:

- The study and development of THGEM-based structures. Small ($30 \times 30\ mm^2$) and big ($300 \times 300\ mm^2$) are considered for these studies and developments.

- The study and optimization of the performance of THGEM-based detectors, when irradiated by soft X-ray sources, VUV photons or Cherenkov light (from test-beams). These studies are performed both in laboratorial conditions, and in experimental beam conditions (which resemble the environment under which the detector is expected to be operated).
- The evaluation, by simulation and experimental studies, of the intrinsic potential of THGEM-based detectors (comprising mainly THGEMs and THCOBRAs) as ion traps in electron cascade multipliers, in order to reduce the ion back flow.

The work to achieve the proposed goals was performed under strict collaboration of two institutions member of both RD51 collaboration and COMPASS experiment [14]: University of Aveiro, Aveiro, Portugal, and INFN, sezione di Trieste, Italy. While the THCOBRA studies were performed in the University of Aveiro, by the author, the majority of the THGEM studies were performed under the collaboration in INFN-Trieste, together with other team members. Simulation studies correspond to work done solely by the author.

Hereupon, this thesis is divided in 7 chapters. Chapter 1 to 3, all together correspond to a detector state-of-the-art and their fundaments. Chapter 4 to 6 correspond to the results achieved to accomplish the proposed goals. Chapter 7 are the conclusions.

In particular, chapter 1 is intended to present a generic view over gaseous detectors. It aims to provide the reader with the fundaments of gaseous detectors and introduce the gaseous detectors that are historically relevant, or relevant in the context of this work. Such introduction is done for generic radiation, and not with photon detection in mind.

Chapter 2 focuses on the application of the detectors introduced in chapter 1 for photon detection. With the goal in mind of detecting Cherenkov radiation, and in the present case, more specifically vacuum ultraviolet photons, this chapter gives a historical review of the several generations of gaseous photon detectors, from the use of photoconverting vapours with open-geometry gaseous detectors to solid state photocathodes coupled with MPGDs. The last section of this chapter introduces a group of tools that allow electrostatic calculations, and Monte-Carlo simulations regarding the drift of ions and electrons in gaseous detectors, to complement with the experimental studies.

As, in the perspective of this thesis, the main application of gaseous photon detectors is the detection of Cherenkov radiation, chapter 3 intents to give an overview of Cherenkov radiation, the COMPASS experiment and its RICH detector – RICH-1. This chapter ends with the planned RICH-1 upgrade, presenting its requirements, which justify the need of the studies performed under this thesis.

Chapter 4 presents the results of the performance characterization of THGEM based detectors. Mainly, experimental results, achieved in laboratorial conditions, of gain variation and breakdown

voltages are presented. These results include the characterization of small THGEM prototypes ($30 \times 30\, mm^2$) in single, double and triple layer configurations, of big prototypes ($300 \times 300\, mm^2$) in single layer, and of a hybrid approach that merges together Micromegas and THGEMs.

In order to study the efficiency of THGEM-based structures in the reduction of the fraction of ions that reach the surface of the photocathode, many studies were performed. Chapter 5 summarises these results, which were achieved with small area prototypes, with THGEMs alone, or with addition of THGEM-like structures with dedicated electrodes for ion collection. Such studies include experimental studies in laboratorial conditions, and simulation studies based on Garfield, which is a widely used program for detailed simulation of electron and ion drift in gaseous based detectors.

Chapter 6 intents to present the THGEM-based photon detector performance in test-beams. These experimental conditions allow the operation of the detectors with Cherenkov light, while being subject of simultaneous interaction with minimum ionizing particles. These studies are done both for small and big triple THGEM-based photon detectors.

Chapter 7 corresponds to the conclusions, where the main results achieved in this work are pointed out. Additionally, ongoing and future work in the sequence of this thesis, are also discussed.

1. Introduction to Gaseous Detectors

Gaseous Detectors are widely used in physics related fields when it comes to radiation detection, and their usage seems likely to increase in the future. Their relatively simple architecture allows construction over large areas at relatively low cost when compared with competitor technology, such as semiconductor detectors, without compromising its performance. These kind of detectors are commonly used in high energy physics, in applications such as particle tracking, calorimetry or particle identification, among others [15,16].

A Gaseous detector consists mainly on a chamber comprising a gas that works as an active medium (radiation interacts directly with it), charge amplification structures (that may be optional) and charge collection electrodes that allow, through an applied electric field, the collection of the charge created in the gas. **Figure 1.1** schematically illustrates the fundamental components of a gaseous detector.

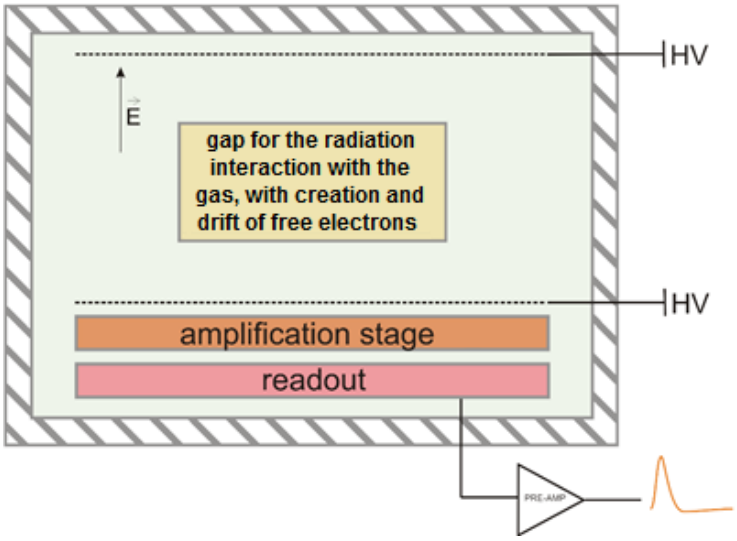

Figure 1.1 – Scheme of a gaseous detector, with particular emphasis to the chamber, the amplification stage, and the readout element.

The operation of any radiation detector basically depends on the way the radiation, to be detected, interacts with the material of the detector itself. An understanding of the response of a specific type of detector must, therefore, be based on the familiarity with the fundamental mechanisms by which radiations interact and lose their energy in the matter, and all the further interactions that happen afterwards.

1.1. Radiation Interaction

For the general purposes of gaseous radiation detectors, the detectable radiation can be divided mainly into “charged particulate radiation” comprising fast electrons and heavy charged particles, and “uncharged radiation” containing electromagnetic radiation and neutrons [17]:

Charged particulate radiation:

- Fast electrons
- Heavy charged particles

Uncharged radiation:

- Electromagnetic radiation
- Neutrons

As the names of the two main groups suggest, the fundaments for such a division are related to the presence or absence of charge, which is related to their emission process [17]:

- Fast electrons include beta particles (positive or negative) emitted in nuclear decays, as well as energetic electrons produced by any other process.
- Heavy charged particles denote a category that encompasses all energetic ions with mass of one atomic unit or greater, such as alpha particles, protons, fission products, or the products of many nuclear reactions.
- Electromagnetic radiation, emitted in the rearrangement of electron shells of atoms (such as X-rays) or emitted from transitions within the nucleus itself (gamma rays)
- Neutrons generated in various nuclear processes.

These four categories of radiation cover a wide range of energies, ranging from just few eV up to 20 MeV.

The detection of such radiation is only possible as a result of its interaction with matter. This means that the lower energy bound of a detector is set by the minimum energy required to produce a desirable interaction.

When radiation interacts with matter, in all cases of practical interest, there is a full or partial transfer of energy from the incident radiation to the constituents of the atoms that make part of the active medium. The way this energy transfer takes place defines the type of interaction, which is mainly dependent on the nature of the radiation. Taking as reference the classification stated above, charged particulate radiation is characterised by continuously interacting with the electrons of the medium through its path, by Coulomb force, while the non-charged radiation is characterised by interactions that radically change the properties of the incident radiation in a single encounter [17].

Regarding charged particulate radiation, Coulomb force is primarily responsible for the interaction of the electrically charged incident particle with the orbital electrons of the atoms of the medium with which the radiation is interacting. Interactions between these charged particles and the nuclei of the atoms is possible too, but less likely to happen, and therefore, radiation

detectors rely on the interaction with electrons for the detectors response. The interactions occur simultaneously with many electrons in the vicinity of the particle, and depending on the proximity of the encounter, the electron might be raised to a higher-lying shell of the atom – excitation – or might be completely removed – ionization. Due to energy loss upon these interactions, the particle's velocity will decrease.

Although these physical principles are valid either for heavy charged particles or for fast electrons, still the response to the interaction for these two types of particles may vary. Fast electrons, mainly due to their lower mass, lose their energy at a lower rate than heavy charged particles. Additionally, because their mass is equal to the orbital electrons of the atoms, they follow a much more tortuous path, which might lead to large deviations in its trajectory.

Regarding uncharged radiation, because there are no electrical charges involved, Coulomb force has no role in the interactions. Electromagnetic radiation, while interacting with the medium, can transfer all or part of its energy to the orbital electrons of the medium atoms. The incident radiation might interact with the active medium mainly through photoelectric absorption, Compton scattering, pair production or coherent scattering (Rayleigh). The predominance of each interaction is a function of the radiation's energy, and the medium's properties. After any of these interactions, the photon either disappears entirely, or is scattered through a significant angle.

In the context of the detectors presented in this work, it is of major interest that the interactions with electromagnetic radiation result in ejected electrons from the medium. These ejected electrons present a very close similarity to the fast electrons radiation.

Neutrons, due to their absence of charge, do not undergo interactions through Coulomb force. Instead, they interact with the nucleus of the absorbing medium. As a result of this interaction, the neutron might either disappear while being replaced by secondary radiations (mainly heavy charged particles), or its energy or direction might change significantly. As interactions of radiation with atoms nucleus are less probable, neutrons can travel through several centimetres of matter without undergoing any kind of interaction, being therefore invisible for common size detectors [17].

Generically, the radiation might interact with all matter and not only the active gaseous medium. Therefore, all the components of the detector must be thought in order to maximize their performance for their specific functionality, e.g., the windows thickness and material must be such to minimize the probability of interaction with the incident radiation, while a detector shield must maximize its absorption to radiation.

1.2. Charge Interactions

The interaction of radiation with a gaseous medium results primarily in ionization and excitation of the gas molecules. Although appropriate signals can be extracted from excited gas molecules (as

in gas scintillators), the majority of gaseous detectors – as the ones described along this work – rely on the capability of detecting the ionization created by passage of photons or particles. When a neutral molecule is ionized, an ion pair, which corresponds to a free electron and a positive ion, is created. Although this ion pair will be the basis of the electric signal developed by the detector, before they become of any use being collected in readout electrodes, they suffer several physical interactions with the medium. Some of these interactions can be desirable, such as the charge drift along the detector due to an applied external electric field, or they can be undesirable, such as diffusion, attachment, charge transfer, or recombination, as they limit the gaseous detector performance [17].

Charge mobility

Free electrons and positive ions are the main product of the interaction of radiation with the gas. In the absence of an applied external electric field, these species (electrons and ions) are subject to thermal energy ε_T, which induces thermal motion. This energy is function of the gas temperature T, and is defined by equation 1.1 [18]:

$$\varepsilon_T = \frac{3}{2}kT \tag{1.1}$$

Where k is Boltzmann's constant.

This component of energy imposes different behaviour in electrons and in ions, mainly due to their significant mass difference. Because of their low mass, electrons lose energy at a low rate, having a random scattering of the electrons along no preferred direction. Ions, on the other hand, due to their high mass, lose energy at a higher rate, not changing significantly their velocity and position between collisions.

Because thermal energy is incapable of imposing the particle's motion along a defined direction for the charge collection, an external electric field E, is applied in gaseous detectors. The electric force induced by this applied electric field forces the charge migration and collection, forcing the separation of free electrons and positive ions, as opposite charges drift along opposite directions under an electric field.

The energy ε, of these electrons or ions, is now given by

$$\varepsilon = \varepsilon_E + \varepsilon_T \tag{1.2}$$

Where ε_E is the energy due to an externally applied electric field. This means that the particles motion inside the gas is now a superposition of the random thermal motion with the drift motion in a given direction.

In the range of electric fields that are often applied in gaseous detectors, the condition $\varepsilon_E \gg \varepsilon_T$ is verified, which means that the thermal component can be often neglected. The motion of free electrons and ions in a gas become then function of the applied electric field, the gas pressure

(which defines the mean free path), and the mobility coefficient of each particle for each gas. Overall, these variables lead to different behaviour of electrons and ions [19,20].

Ion Drift

Ions are characterized by small mobility coefficients when compared with electrons, which along with their high mass, contribute to an insignificant change of direction between collisions, and are therefore scattered along a preferential direction imposed by the applied electric field. Thus, ion trajectories in a gaseous medium, are fairly accurately represented by the ion drift lines, which are represented by the electric field lines. Additionally, ion transit can be in the order of milliseconds per centimetre, which is considered a very long time in particle detection standards, if considered for the detector signal development [18,20].

Electron Drift

Electrons, in opposition to ions, present a significantly higher mobility coefficient. As consequence, their transit time becomes in the order of microseconds per centimetre. Nonetheless, although to first approximation their trajectory follow the electric field lines, we can no longer say that this path prediction is fairly accurate. Macroscopically, electrons tend to follow the direction imposed by the electric field and therefore follow the predicted behaviour; microscopically, their behaviour is fairly unpredictable. As electrons are randomly scattered between collisions, each electron follows a slightly different path, introducing deviations to the average trajectory and that increase with the transit distance of the particle leading to a diffusion phenomenon [18,19].

Diffusion

As mentioned previously, due to their thermal energy, ions and electrons present random thermal motion (**Figure 1.2**), and tend to diffuse away from regions of high density. This phenomena is mostly visible for electrons, as ions have a mass comparable to neutral atoms/molecules of the gas, and therefore don't present a much different behaviour compared to these. Therefore, in the absence of an applied electric field, electrons, between collisions, tend to spread about the original point into a Gaussian spatial distribution, and whose projection over an arbitrary orthogonal axis, allows to define the standard deviation σ, as [17]

$$\sigma = \sqrt{2Dt} \tag{1.3}$$

Being t the elapsed time and D a gas diffusion coefficient.

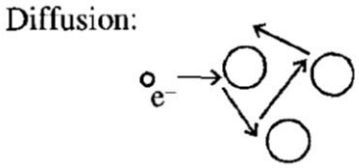

Figure 1.2 – Scheme of the electron diffusion between collisions with neutral atoms or molecules (represented as simple circles) [17].

In the presence of an external electric field, the diffusion coefficient D, becomes function of the applied field. In this situation, literature suggests [18] that the projection of the standard deviation of the electron distribution, orthogonal to the electrons longitudinal trajectory, can be shown as

$$\sigma_x = \sqrt{\frac{2kTL}{eE}} \tag{1.4}$$

Where E is the electric field strength, e the electron charge and L the distance over with the electron is expected to transit. Equation 1.4 indicates that diffusion is higher for larger transit distances, although it can be decreased for higher electric fields. High electron diffusion may limit the position resolution in "position-sensitive" gaseous detectors, or increase the detector's time response as electrons tend to cover longer distances.

Charge transfer

Charge transfer (**Figure 1.3**), is an interaction that can happen between positive ions and neutral gas atoms/molecules. During a collision between these two elements, the transfer of an electron between the neutral specie and the ion is possible, reversing the role of each. Such interaction tends to be more significant in gas mixtures that contain different molecular species.

Figure 1.3 – Scheme of charge transfer [17].

Electron attachment

While the interaction between position ions and neutral species may lead to charge transfer phenomena, free electrons can undergo interaction with these neutral species too. Because charge cannot be transferred from the electron, such interaction leads to the possibility of the electron being attached to the neutral gas atom/molecule, forming a negative ion – electron attachment (**Figure 1.4**). As this interaction results in the loss of free electrons, which represent the essence of the detector signal, it is highly desirable that it is minimized. Because the electron attachment

coefficients are proportional to the electronegativity of the neutral specie involved, the fill gas must be chosen accordingly. In this regard, noble gases, nitrogen or hydrocarbon gases are characterized for low electron attachment coefficients, while oxygen, for instance, highly electronegative, must be avoided [17].

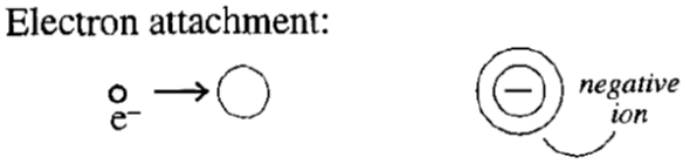

Figure 1.4 – Scheme of electron attachment, leading to the creation of a negative ion [17].

Recombination

If on one side, electron attachment and charge transfer translate the interactions between charged species and neutral atoms/molecules, on the other side, recombination describes the interaction between electrons and ions (**Figure 1.5**) [17]. The simplest type of recombination happens as the capture of a free electron by a positive ion, after a collision, resulting in the return of the ion to its charge neutrality state. Because a free electron is lost in this recombination, it cannot further contribute to the output detector signal. Alternatively, recombination might happen between negative and positive ions, where the extra electron from the negative ion is captured by the positive one, resulting in the return to the neutral charge state of both species.

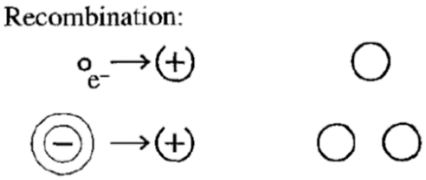

Figure 1.5 – Scheme of the recombination interaction, both between electron and positive ions, and negative and positive ions. The resulting neutral species are represented as simple circles [17].

Because the collision frequency is proportional to the product of the concentrations of the two species involved, the recombination rate can be written by equation 1.5 [17]:

$$\frac{dn^+}{dt} = \frac{dn^-}{dt} = -\alpha n^+ n^- \qquad (1.5)$$

Where n^+ is the concentration of positive species, n^- is the concentration of negative species, and α is the recombination coefficient.

The recombination between ions is usually significantly higher when compared to recombination between positive ions and free electrons.

1.3. Charge Amplification

In an applied electrical field, if free electrons and ions do not suffer electron attachment or recombination, they will drift towards their respective electrodes (anodes). Because ions don't have enough energy to trigger ionizations, they play no role in charge multiplication. Electrons, on the contrary, behave differently. Although for low applied fields electrons are mainly characterized by the previously described interactions, above a certain threshold electric field, they can gain enough kinetic energy, between collisions, to excite (photon emission is not considered in the context of this work) and ionize the neutral gas atom or molecule. Because the "ejected" electrons are subjected to the same field as their predecessors, they end up ionizing further gas atoms/molecules, promoting charge multiplication. This multiplication takes the form of a cascade and it is known as *Townsend* avalanche [17]. The threshold electric field that allows this charge multiplication is a function of the gas, as well as its pressure and temperature.

The fractional increase in the number of electrons n, in a *Townsend* avalanche, per unit path length z, is governed by the *Townsend* equation [17]:

$$\frac{dn}{n} = \alpha dz \tag{1.6}$$

Where α is the first *Townsend* coefficient for the gas, and is a function of the applied electric field. Its value is zero for electric field values below the multiplication threshold and increases with increasing field values above the threshold.

Considering a spatially constant field above the threshold, α is constant, and therefore a solution for equation 1.6 is given by [17]

$$n(z) = n(0)e^{\alpha z} \tag{1.7}$$

Predicting that the number of electrons grows exponentially with distance as the avalanche progresses. Analytically, the multiplication factor M, of this avalanche can be given by [17]

$$M(z) = \frac{n(z)}{n(0)}e^{\alpha z} \tag{1.8}$$

And it corresponds to the average number of produced electrons per primary electron, along all its path, and it corresponds, at some extent, to the detectors gain.

Considering that the electric field is rarely constant inside a gaseous detector along the electrons path, then an approximation for the multiplication factor can be given by the following equation: [17]

$$M(z) = e^{\int_{z1}^{z2} \alpha(z)dz} \tag{1.9}$$

Because the electric field applied for drift purposes is, in the majority of the cases, insufficient to trigger a *Townsend* avalanche, amplification structures can be introduced. Such structures, some

of which concern the main study of this work, are built to allow intense fields, above the ionization threshold. Some of these structures, showing different geometries and introduced over time, will be presented further ahead.

The processes of inducing charge multiplication is quite important in gaseous detectors, as most of the times, and in what concerns this work, the charge created in the primary interaction is not enough to be measured. Charge multiplication tries to guarantee an output signal that is significantly higher than the electronic noise level, and therefore capable of being measured. Despite charge multiplication capability, other type of detectors, here neglected, rely in light amplification capability – electroluminescence – as consequence of the excited atomic or molecular states that may be formed with the radiation interaction and electron drift. Further information about these type of detectors can be found, for instance, in references [21,22].

1.4. Operation Regions of a Gaseous Detector

When an external electric field is created in a gaseous detector through an applied voltage, the probability of happening any of the previously described interactions becomes function of the applied voltage. This leads to different possible detector outputs, which will define several types of gaseous detectors, each of which operates in a well-defined mode that depends on the amplitude of the applied potentials [17]. The functioning region of each one is illustrated in **Figure 1.6**. The amplitude of the detectors output signal is presented schematically in the plot as a function of the applied voltages.

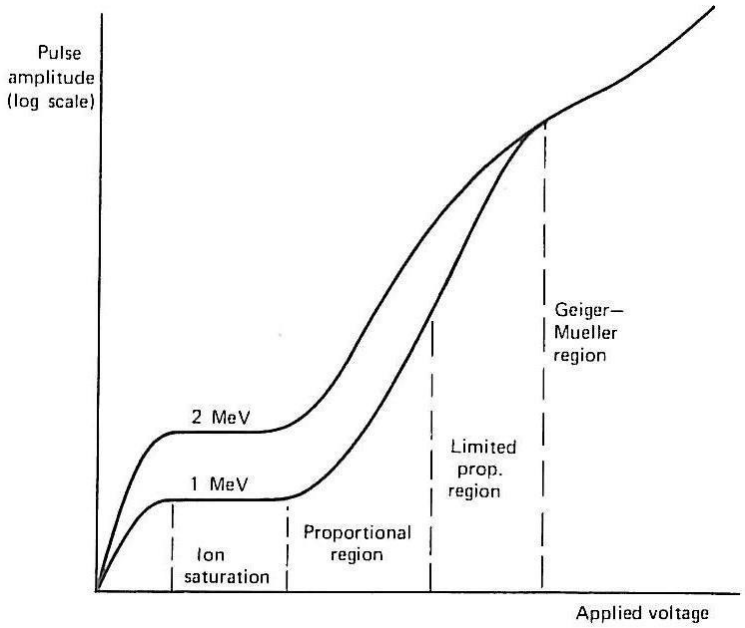

Figure 1.6 – Gaseous detector operating regions [17].

For very low voltages, the field is insufficient to prevent the recombination of the ion-electron pairs created by a primary interaction and, therefore, the collected charge is lower than the initial charge.

Increasing the applied potential, we go to a region where ion saturation prevails: the field is enough to avoid the pair recombination, but still insufficient to lead to new ionizations of the medium atoms/molecules. In this way, the measured signal remains approximately constant between this range of voltages, before the ionization threshold of the gas is achieved. This corresponds to the ionization chamber operation regime.

Increasing the potential beyond this threshold, we go to the proportional region. This region is, in fact, the most important in the context of the detectors here described. Here, the charge collected is directly proportional to the number of primary electrons, once the collected electrons suffer a multiplication process, producing each one, on average, equal number of new ionizations. This region corresponds to the operation regime of the proportional counters, described in section 1.6.

If the field becomes too high, non-linear effects start to appear. The most important of these effects is related with the positive ions that are produced in the avalanche process. With the increasing of the field, the concentration of these ions increases. Once they move in the opposite way of electrons, and with a much lower velocity, due to their mass, they start to accumulate in the gaseous medium, creating an opposite field, and limiting the avalanche process.

Increasing the field even more, avalanche multiplication proceeds, until the number of positive ions becomes sufficiently high to create a space charge that decreases the electric field to a value below the ionization threshold. Because this charge saturation is consequence of the applied field, and not of the number of ion pairs that are created by the radiation interaction with the gas, then the detectors' pulse amplitude is constant, and does not reflect any property of the incident radiation. Additionally, in between the period when the electric field drops due to the positive space charge, and the time that all the ions are collected, restoring the original applied field, the detector cannot detect new events. This corresponds to the Geiger-Mueller region.

1.5. Filling Gases

The key element of a gaseous radiation detector is, as suggested by its name, the gaseous medium that fills the detector. As the use of specific gases delivers specific particularities to the detector, it is of the major importance to guarantee the uniqueness of the gas that is enclosed in the detector by avoiding undesirable gas mixtures or contaminations (such as oxygen, which due to its high electronegativity tends to capture free electrons by attachment). This constrains the construction of the vessel to be used as a chamber for gaseous detectors. Because keeping the boundaries closed between the chamber inner and outer volume is a must, two approaches are

presented to provide the filling-gas to the detector: the gas can be permanently sealed within the detector; or it can be circulated through the detector in a continuous flow design [17].

Permanently sealed detectors are more convenient as they require no connection to gas systems. Additionally, they easily allow the detector to be operated over a wide range of pressures. Nonetheless, it's barely impossible to avoid microscopic leaks over time, which lead to gradual contaminations of the gas, imposing limited gas lifetimes. At the same time, replacing the filling gas consists in a more laborious task.

On the other hand, detectors with a filling-gas supplied by continuous flow systems require more complex systems, but they bypass potential problems due to gas purity, as the level of gas impurities in the flow line can be measured and/or controlled. This kind of system also allows the possibility of changing the fill gas when desired, without the need to change the layout of the system. These systems can be of the "once through" type, where the output gas is exhausted into the atmosphere, or of the closed circuit type where the output gas is recycled.

The type of system to be used shall depend mainly on the environmental factors of the gas, and its cost.

Despite the approach that is followed to provide the filling gas, the choice of such gas is proven to be of fundamental importance. Since ionization, and subsequently, avalanche multiplication occurs in all gases, virtually any gas or gas mixture could be used as filling gas. However, experimental requisites might restrict the choice to several families of compounds. The chosen gas must maximize the interaction probability with the incident radiation (or maximize the photon-extraction if and when photoconverters are applied); must match the desirable diffusion and drift characteristics of electrons and ions; and it might also need to allow low working voltage, high gain operation, good proportionality, high rate capabilities, long lifetime, fast recovery, etc., depending on the application.

As a result of these possible constrains, the most commonly used families of compounds are the noble gases, in particular argon due to good performance and cost factors, and organic hydrocarbon gases, such as methane or ethylene. These compounds can be used in a pure form, or in mixtures, such as the mixture of 90% of argon and 10% of methane, known as P-10 gas, and which is probably the most common general-purpose proportional gas. Additionally, when a radiation passes through a gaseous medium, photons are also created due to molecular excitation. In this regard, a small portion of some organic gases with large photon absorption coefficients, such as methane, may be added to the gas to avoid the propagations of the photons. Such gases with such purpose get the name of quench gases, and their use is fundamental to suppress the photon-induced effects, such as the loss of proportionality and/or spurious pulses [17].

1.6. Proportional Counter

The detectors that work in the proportional region emerged with the appearance of the so called proportional ionization counters [17]. These are in fact the simplest devices which operate in this region, and they can be used to a better understanding of more complex detectors working in the same region.

This device is formed by one conductive wire, which works as anode, surrounded by an also conductive cylindrical surface, equidistant to the central wire, in all its length, which works as cathode (**Figure 1.7**). Between these two conducting elements, a voltage V is applied within the proportional operation range, which results in an electrical field, that depends on the distance to the wire r, in the following way:

$$\varepsilon(r) = \frac{V}{r \cdot ln(b/a)} \tag{1.10}$$

Where a and b are the anode and cathode radius respectively.

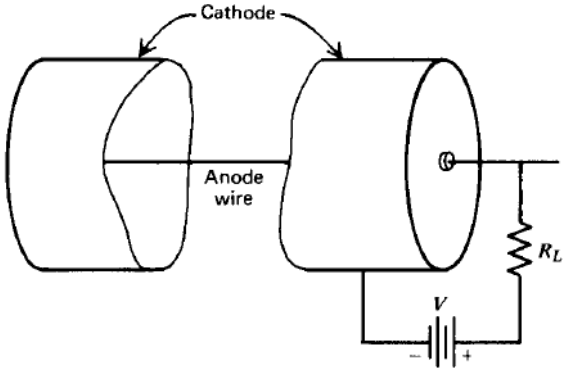

Figure 1.7 – Scheme of a proportional counter [17].

Between both conducting surfaces there is a gas, in which the charge amplification occurs, through an avalanche process. The used gas must be chosen as a function of the detectors components, and the specific application for the detector.

When a photon interacts with the detector through photoelectric effect, gas atoms are ionized, with the number of primary electrons produced, dependent on the energy of the incident photon. The released electrons in the ionization process are accelerated towards the anode, due to the electric field. As the electric field increases in the same direction that the electrons that are moving, then, these will acquire increased energy between collisions. When the field reaches a certain value, the electron acquires enough energy to ionize new atoms. This process leads to an avalanche process near the wire (where the field is more intense), where the number of electrons collected in the anode is proportional to the number of primary electrons.

From the process described above, it's possible to define two distinct regions in the detector that, in spite of having no physical delimitation, present different physical behaviour (**Figure 1.8**).

One first region, quite distant from the anode, where the electron's energy acquired between collisions is small, and therefore, there are no new ionizations, only electron's drift towards the wire. Near the anode, we have another region, where the electron's kinetic energy, acquired between collisions, is already enough to ionize more atoms, and therefore, the avalanche process is possible.

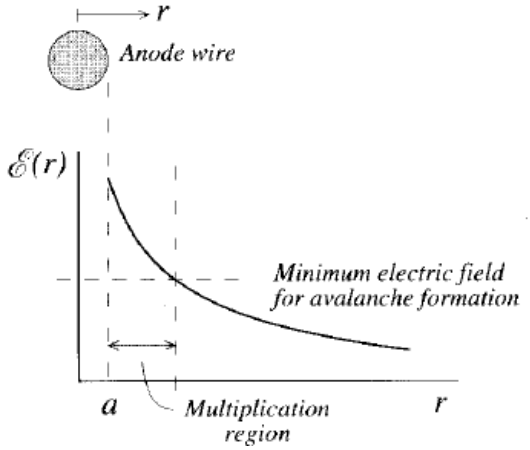

Figure 1.8 – Electrical field in function of the wire distance, in a proportional counter [17].

More complex detectors appeared after the proportional counter, but despite their complexity, they are based in the same working principle.

1.7. Multiwire Proportional Chamber

In order to solve the limitation existent on the proportional counter, where the space localization capability is limited to the determination where a particle has or has not traversed the counter's volume, Georges Charpak and collaborators introduced in 1968 the MultiWire Proportional Chamber (MWPC) [23], which comprises, in its simplest form, a set of anode wires closely spaced along the same plane, typically distanced between 1 and 2 mm, all at the same potential, each wire acting as an independent counter, as schematically shown in **Figure 1.9** (left).

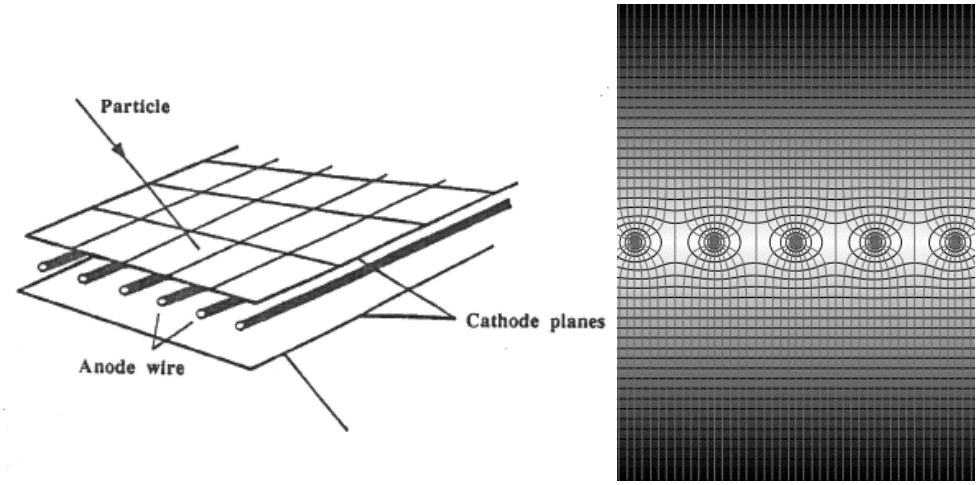

Figure 1.9 – MWPC scheme (left) [24]; field lines configuration in a MWPC (right).

This set of wires is sandwiched between two cathode planes, whose distance to the anode wires is usually three to four times the wire spacing. Such configuration, as shown in **Figure 1.9** (right) which schematically illustrates the MWPC cross-section, allows an uniform drift field away from the wire plane, which increases intensity in the proximity of each wire.

Electrons that are created in primary interactions with the gas, drift along the constant field towards the anode wires. As electrons approach the wire plane, the field increases in the direction of each wire, focusing electrons to a particular wire where they undergo avalanche multiplication. Because the signal induced by the created charge is bigger in the wire where the charge is collected, and smaller in the neighbouring wires, it is possible to track the wire where multiplication occurred, and therefore infer where the radiation interaction happened. Configurations are possible to allow simultaneous 2D spatial discrimination of the primary interaction, using for instance an orthogonal segmented bottom cathode. The weighing of the signal created in each pad by the arriving ions, created in the multiplication process in the wires, will allow the position determination.

Multiwire Proportional chambers represented the first gaseous detector with economic and robust construction that was suitable for covering large areas for particle identification and tracking in high energy physics, leading to a huge advance in particle physics.

1.8. Micro Pattern Gaseous Detectors

Although the invention of the MWPC was a breakthrough development in gaseous detectors, it still offered several limitations undesirable for several applications [12]:

- As ions have to travel a significant longer distance to their collection electrodes at a significant lower velocity, compared to electrons, a space-charge effect is frequent as a consequence of the ions being drained at a lower rate than desirable, causing a distortion of the electric field, limiting the rate at which the detector can perform.

- Because such detectors are based on an open geometry, they cannot prevent photon feedback, this is, that photons which are emitted from excited molecules/atoms interact with the electrodes and/or the detector walls, inducing undesirable avalanches;
- Although the construction concept is quite simple, it is difficult for large areas to guarantee the parallelism between the wires.

With the development of the semiconductor industry, production techniques such as photolithography, etching and laser machining were developed. Such techniques, allowed the construction of new amplification structures architectures that helped to overpass the limitations stated above. Micro Pattern Gaseous Detectors – MPGDs – [12] appeared as a result of such process. These are globally characterized by good spatial resolution, fair energy resolution, operation stability under high rates and high radiation hardness.

Although MPGDs comprise a wide variety of detectors, only the ones with practical or historical interest are presented below.

1.8.1. Microstrip Gas Chamber

Microstrip Gas Chambers – MSGC – were the first type of gaseous detectors based on MPGDs. It comprises a Micro Strip Plate – MSP – which was developed by A. Oed in 1988 [25], and consists in several metallic strips (anodes and cathodes alternated in the same plane), supported by an isolating substrate. When polarized, electrons are driven to the anodes, suffering charge amplification through an avalanche process, near the anode. The anode's width, in this structure, is usually smaller than the cathode width (typically $10\ \mu m$ and $100\ \mu m$ respectively). This way, it's possible the increase of the field lines' convergence in the anode, leading to a maximized amplification.

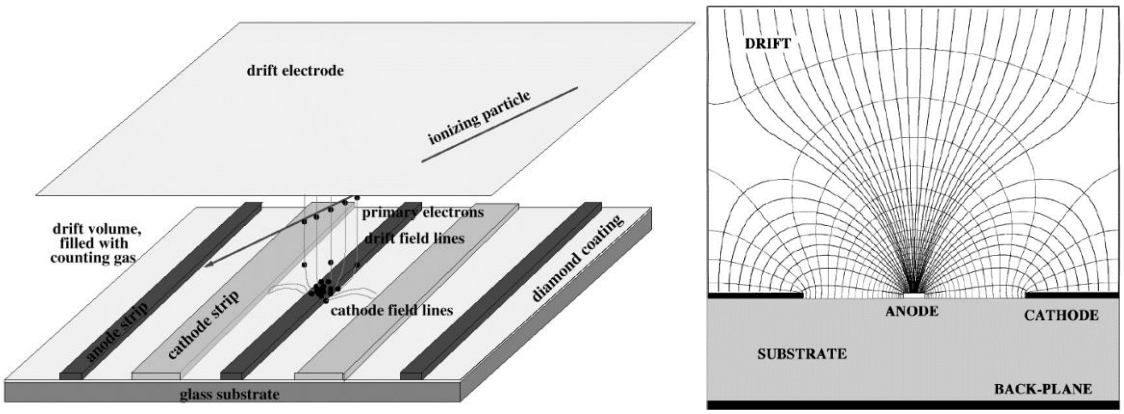

Figure 1.10 – MSGC scheme, with emphasis to the strips layout (left) [26]; MSGC field lines configuration (right) [12].

This structure shares similarities with the MWPC concept, and although it remains an open geometry configuration, the alternation of anode and cathode separated by very small distances (typically $100\ \mu m$) supress the long distances that ions had to travel in the MWPC, increasing its capability to operate under high rates. Additionally, these small spacing distances allow an improved spatial resolution, and allow energy resolutions of 15% (FWHM) in pure xenon for $5.9\ keV$ X-rays [27].

1.8.2. Micromegas

Although MSGC appeared to suppress limitations of the MWPC, they introduced some limitations themselves too. One of these limitations is the fact that avalanche multiplication does not exceed 10^4. This limitation is imposed first by voltage breakdowns between electrodes, and second, by the positive ions that are created during the avalanche process and that are accumulated on the insulator, which locally modify the electric field and cause a drop of the gain in the irradiated area of the detector [28].

To go over these new limitations, in 1996, a two-stage parallel plate avalanche chamber was introduced, known as Micromegas (MICRO-MEsh GAseous Structure) [29]. The Micromegas (**Figure 1.11**) consists of a gas-filled region with two volumes that are asymmetrically divided by a porous metallic micromesh structure. This micromesh is placed in between the electrodes, making the two volumes parallel, resembling a two-stage parallel plate avalanche chamber [30,31].

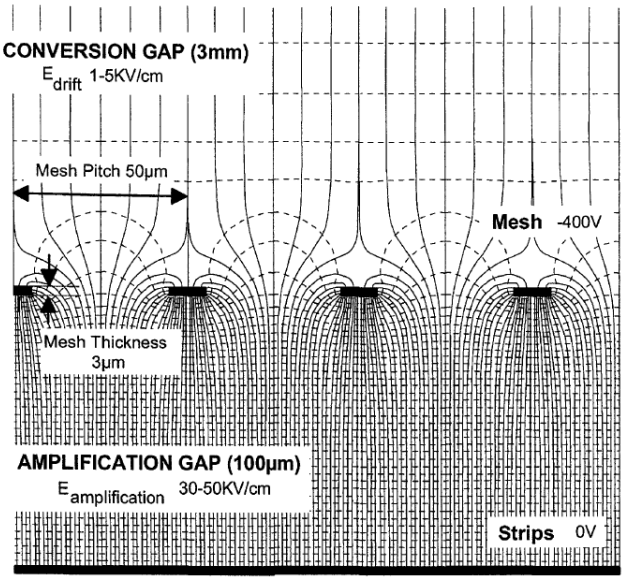

Figure 1.11 – Micromegas scheme along with the electric field lines [32].

The upper volume, comprised between a drift electrode – cathode – and the micromesh, corresponds to the conversion gap and its depth is typically of a few millimetres ($3\ mm$ is often a typical value). The incident radiation/particle interacts with the filling gas, and creates electron-ion

pairs, and the ionization electrons are drifted towards the micromesh through the presence of a low electric field, that is intended to be below the threshold for the gas multiplication. The thickness of the gas in the order of few millimetres is typically enough to maximize the probability of the creation of electron-ion pairs, maximizing the detection efficiency of the detector.

The lower volume is defined between the micromesh and the anode and corresponds to the amplification gap. This gap can be as small as $100\ \mu m$, but defining its optimal value is not trivial, as it will be described later. This small spacing allows, through the application of reasonable voltages, a very intense electrical field, as high as $100\ kV/cm$, which leads to charge amplification under an avalanche process, resulting in typical gains of between 10^3 and 10^4 [29]. Because each avalanche is approximately equal in gain, the total gain of the detector will be a function of the number of created electron-ion pairs. The small gap also favours the formation of fast (nanosecond scale) pulses.

The parallelism between the mesh and the anode is accomplished by the use of insulating pillars uniformly distributed, between the micromesh and the anode. These pillars are usually spaced by $2\ mm$, having diameters of around $150\ \mu m$, and are printed on a thin epoxy substrate by conventional lithography. The height of these pillars define the amplification gap.

As mentioned above, the optimal gap thickness is not trivial to determine. From one side, the production techniques limit the choices, while from the other side, physical phenomena impose other limitations for optimal performance. Theory [32] shows that the electron multiplication "M" in the uniform electric field between two parallel plates, which is a valid approximation for the anode and the micromesh, in a gas at a pressure p, is described by [32]

$$M = e^{\alpha d} \tag{1.11}$$

Where d is the distance between the two parallel electrodes and α is the *Townsend* coefficient. A good approximation of this coefficient is given by Rose and Korff formula [32]

$$\alpha = pAe^{-\frac{Bp}{E}} \tag{1.12}$$

Where E is the electric field and A and B are parameters depending on the gas mixture. At high electric field values the *Townsend* coefficient saturates because its value approaches the mean free path given by the inelastic collision cross section, which is constant. The electric field E is given by

$$E = \frac{V}{d} \tag{1.13}$$

Where V is the applied voltage. By substituting equations 1.12 and 1.13 into equation 1.11 we find that [32]:

$$M = e^{Apde^{-\frac{Bpd}{V}}} \tag{1.14}$$

This substitution shows that the multiplication factor M is a function of the quantity pd, thus a function of the gas pressure and the distance between the parallel electrodes. As the experimental

verification of the distance dependence is difficult, due to experimental constrains, then, such verification can be done from the analytical calculation of equation 1.14. A study regarding these calculations is presented in literature [32] and shows the multiplication/gain as function of the gap d, for a mixture of Ar + 5% DME, for three sets of voltages ($V = 300\,V$, $V = 350\,V$ and $V = 400\,V$) and a constant pressure $p = 1\,bar$. **Figure 1.12** shows the results of these calculations.

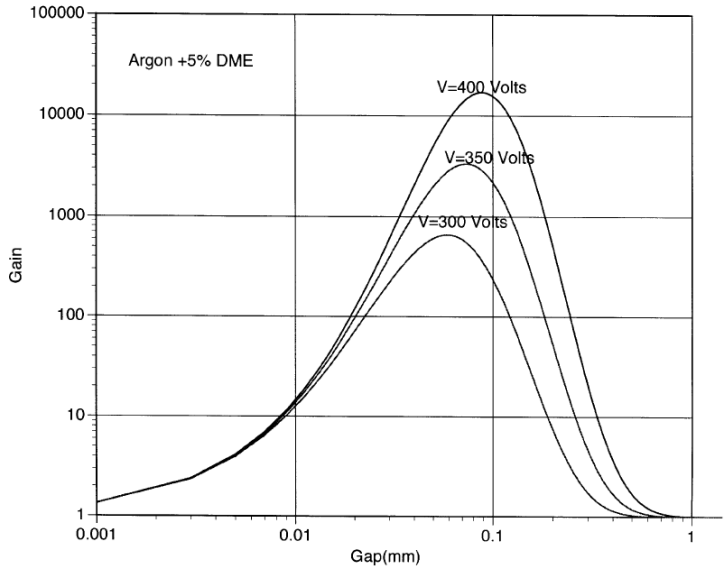

Figure 1.12 – Gain calculation for a Micromegas detector, as function of the amplification gap, for three sets of voltages [32].

As the results show, the multiplication rises with the increase of the gap distance until a global maximum, after which the increase of distance leads to a decrease of gain. The results also show that despite the effect that the applied voltage has in gain, it has just little effect over the position of the distance at which the gain is maximum, which is between 60 and $100\ \mu m$. These results set the gap to be produced with $100\ \mu m$ in most of the Micromegas, as it is convenient for production issues, and it fits most if the applied voltages with optimal gain. Additionally, because the maximum gain peaks for the majority of the applied voltages are achieved for distances a little below $100\ \mu m$, it means that small variations of the amplification gap, due to mechanical defects, are compensated by an inverse variation of the amplification factor, which is a major advantage for the use of such structures. As the referred article also suggests [32], the gas mixture tends to have a small effect in the choice of the optimal gap distance.

The key element of this detector – the micromesh – introduces another potentially interesting feature. This grid, with a thickness of just few μm, has high transparency for the ionization electrons, which makes it an easy process for these created electrons to pass through the micromesh and continue on towards the anode after suffering a multiplication process in the

amplification gap. Nonetheless, the opposite movement of the ions, that are created in the amplification gap and drift toward the conversion gap, can be minimized by proper choice of the applied voltages, which force part of these ions to be collected by the mesh.

Calculations presented in literature [29] regarding this subject, show the effectiveness of the micromesh as an ion blocker. These calculations are presented as function of the ratio between the electric fields in the amplification and in the conversion regions - ξ.

$$\xi = \frac{E_{amplification}}{E_{conversion}} \tag{1.15}$$

Figure 1.13 shows the electron and ion transmission through the micromesh. The larger the values of ξ, the higher the electron transparency, reaching values of 100% for ξ larger than 20. On the opposite side, ion transmission is extremely low and becomes lower with the increasing of the ratio ξ. These results show the importance of the correlation of the fields above and below the micromesh, which can simultaneously allow a full electron transparency with a significant ion blocking. An efficient ion blocking by the micromesh is important because it minimizes the distance over which the ions must drift, promoting a faster recovery from space charge effects, which allows operation at higher rates.

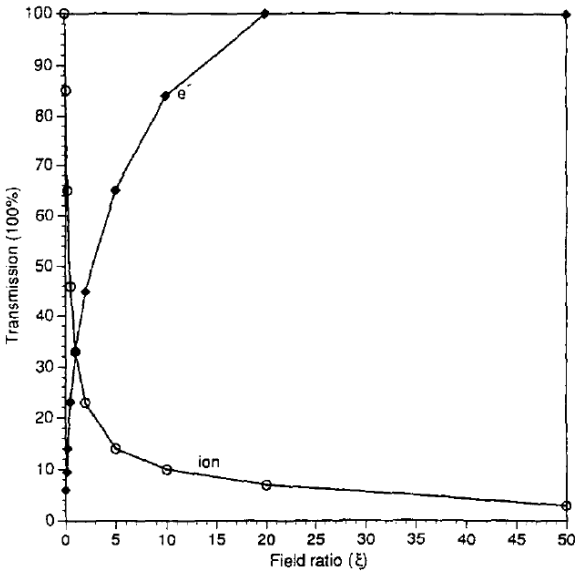

Figure 1.13 – Calculated ion and electron transparency, for a Micromegas detector, as function of the electric field ratio, ξ [29].

Using a segmented anode configuration (such as strips or pixels), it's possible to localize spatial position of the formed avalanche centroid, allowing imaging applications, such as high energy particle tracking. Under favourable circumstances, spatial resolution can be as good as 10 to 15 μm. The possibility of bulk production confers Micromegas the advantage of covering large areas [33].

Additionally, energy resolution is about 14% (FWHM) in a Ar:CH_4 (90:10) gas mixture [29], when measured with $5.9\ keV$ soft X-rays. Also, Micromegas find application, for instance, in Altas MAMMA project [34] at CERN, or as readout for the Time Projection Chambers (TPCs) of the T2K experiment [35].

1.8.3. Gaseous Electron Multiplier (GEM)

Gaseous Electron Mulitpliers – GEMs - were developed by Fabio Sauli in 1996 [36], and they are produced from a thin film of an isolating polymer (Kapton™), typically $50\ \mu m$ thick, in which a metallic layer (usually copper), of typically $5\ \mu m$ is deposited in both sides. After that, submilimetric biconical circular holes are created in the structure, crossing the entire thickness, and are periodically distributed on the surface in a hexagon pattern, with a pitch of typically $140\ \mu m$ (**Figure 1.14**).

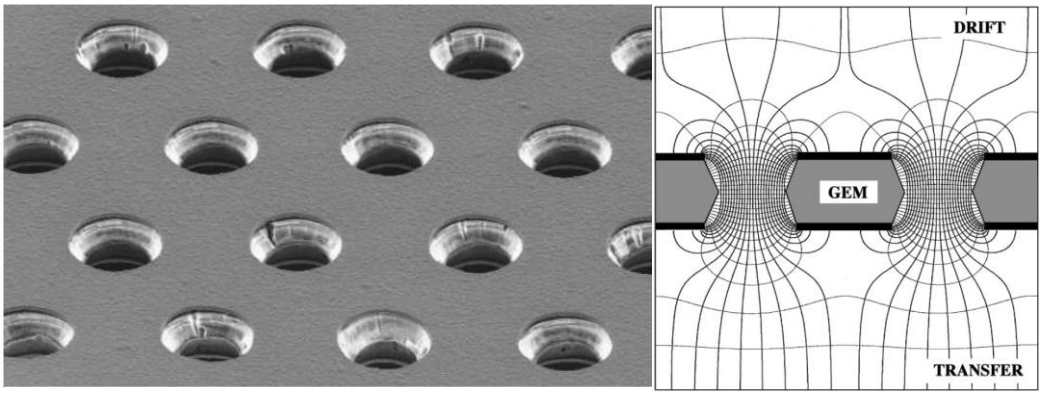

Figure 1.14 – GEM hole pattern (left) [37]; GEM scheme with the related field lines (right) [12].

If each metallic layer is properly polarized, and if electrons are led towards the structure by the influence of a drift electric field, then these electrons will be focused into the existing holes, due to the strong field inside them (due to the high concentration of field lines, because of the isolator influence), which is high enough to produce an avalanche, resulting in charge amplification. The intensification of the field due to the concentration of the field lines is schematically shown in **Figure 1.14** (right).

Since the majority of the ionizations that lead to the avalanche multiplication happen inside the hole, it implies that the optical transparency is significantly decreased, reducing secondary photon-feedback effects, enabling higher gains. GEMs consist then, by definition, to a closed geometry configuration.

An additional characteristic is the possibility to cascade several GEMs (**Figure 1.15**) to reach higher gains, up to $10^5 - 10^6$ [38]. Such configuration contemplates the existence of electric fields between the cascaded GEMs – transfer fields – to allow the transfer of the amplified charge in each stage, along the detector.

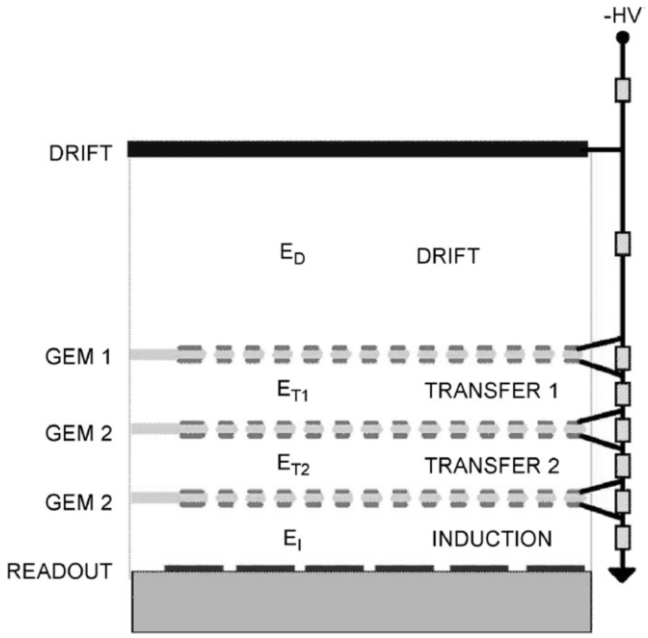

Figure 1.15 – Exemplification of the use of GEM structures in a multi-layer configuration.

As the total produced charge is expected to be collected in the readout anode, using a pad or strip segmented anode allows a two dimensional position discrimination [37].

The energy resolution of GEM detectors is around 20% (FWHM) in Ar:DME (80:20) gas mixtures for $5.9\ keV$ [39], and GEM-based detectors can be found as trackers in COMPASS experiment [40], or in TOTEM experiment at CERN.

1.8.4. Micro Hole and Strip Plate (MHSP)

Micro Hole and Strip Plate – MHSP – [41] is a hybrid structure that combines the microstructures MSP and GEM. It consists in a thin Kapton™ substrate, with a thin layer of copper in each side of this substrate. Biconical holes are made in this set, crossing the whole structure, with a hexagonal distribution on the surface (this distribution is the one that increases the compression factor, increasing the sensor efficiency). In one of the substrate surfaces, using the deposited copper layer, anode and cathode strips are produced, through lithographic processes, alternatively. This surface corresponds to a MSP type.

From the radiation interaction with the chamber gas, through photoelectric absorption, results an electron cloud that by action of a week electric field, converge in the direction of the MHSP. **Figure 1.16** illustrates, schematically, the detector components, and the electron average path. A voltage difference is applied between the top surface ("top") and the cathodes. Since there is convergence of the field lines inside the holes, the electric field is high and, therefore, electrons suffer charge amplification in that region.

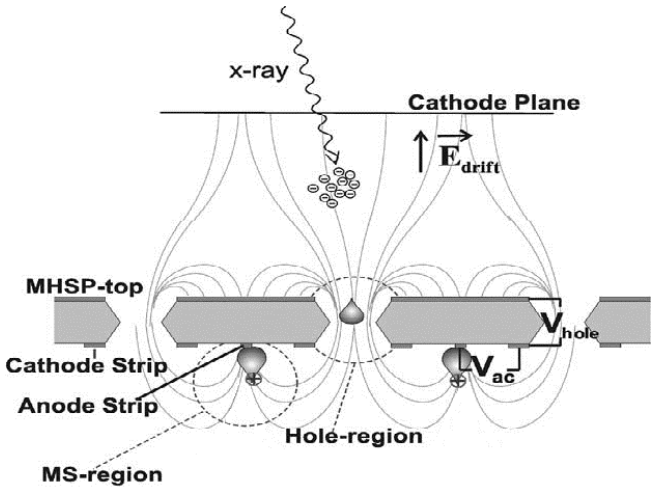

Figure 1.16 – Scheme of a MHSP, emphasising the field lines. Adapted from [42].

A voltage difference is also applied between the cathodes and the anodes, in the MSP type side, whose field leads to a new amplification through an avalanche process. This new avalanche is due to the fact that the anodes width are very small. Once the field lines are gathered in the anode, and their width is very small, the field lines density is very high, which means that the field is very intense. The charge produced in the process is then collected in the anode.

As a MHSP in its normal operation mode contemplates two stages of multiplication, it is able to achieve gains higher than GEMs. Additionally it is also able to provide a better energy resolution of 14% (FWHM) in pure xenon, for $5.9\ keV$ soft X-rays [43].

Due to its geometric similarities to GEMs, it is possible to assemble multi-layer detectors with GEMs and MHSPs, simultaneously, as illustrated in **Figure 1.17**.

This possibility allows a better customisation of the detector as function of its application. MHSPs, when used in multi-layer configurations, have also the possibility to entrap ions that move towards the top of the cascade (a process later described as Ion Back Flow), by reversing the polarisation of its anode and cathode. Such option will be introduced in chapter 2.

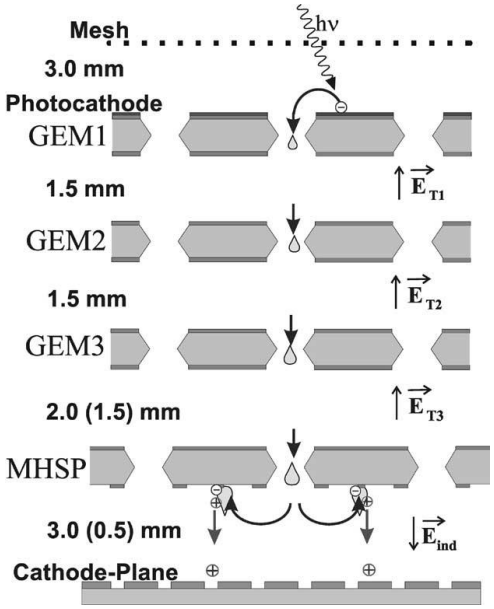

Figure 1.17 – Exemplification of the use of a MHSP structure in a GEM multi-layer configuration [42].

1.8.5. Thick Microstructures

The charge multiplication through avalanche processes using small holes (GEM and MHSP) is attractive, as the avalanche's high confinement inside the holes reduces considerable secondary effects. Nevertheless, due to the reduced dimensions of these structures, it is hard to produce large area detectors at an effective cost, that are capable of achieving a desirable gain, while at the same time it is difficult to guarantee the structure uniformity. As the main limitations of these structures seem to be imposed by their dimensions, naturally appeared a new set of structures, with improved dimensions, to overcome the limitations of the older structures: Thick Microstructures, which comprise Thick Gaseous Electron Multipliers (THGEMs) and Thick-Cobras (THCOBRAs).

Thick Microstructures define themselves for presenting dimensions that are scaled up by approximately one order of magnitude when compared with the former structures. Such scaling happens for the characterizing parameters: Pitch (defining the distance between consecutive holes), thickness and holes diameter. Because the production technique is also changed, it implies that the previously used Kapton™ is now replaced by printed circuit board (PCB). Due to the newly introduced production techniques, the biconical holes, are now replaced by straight holes, with a clearance ring, surrounding the hole at the copper level, and achieved by the copper etching: rim.

These characteristics confer to thick microstructures: mechanical robustness to allow its self-support; electrical robustness against electric discharges; the capability of sustaining higher dipole voltages; higher gains due to longer multiplication paths; and the capability of large size industrial production at low cost.

Despite the pointed advantages of these structures, the enlargement of the holes lead to a bigger charge dispersion, compromising the space resolution of the device. Nonetheless, this might not impose a limitation for some of the aimed applications, such as Cherenkov Imaging counter.

1.8.5.1. Thick Gaseous Electron Multiplier (THGEM)

Thick Gaseous Multipliers (THGEMs) [13,44,45] were introduced in parallel by several groups, as an evolution of GEMs. THGEM structures consist of a drilled set of insulating material (PCB) with copper layers, which allow the application of a dipole field to induce charge multiplication, by analogy with GEMs. The set of parameters, comprising pitch, hole diameter, thickness and rim, characterize the THGEM at a geometrical level. The combination of all these parameters allows many varieties of THGEMs with different properties. The study and optimization of some of these parameters will be mentioned later along this work. Typical dimensions for these parameters are: pitch: $0.5 - 1.2\,mm$; hole diameter: $0.3 - 1\,mm$; thickness: $0.4 - 1\,mm$; rim: $0 - 0.1\,mm$. Although the utility of the rim is not consensual, its desirable dimensions might change the production technique of THGEMs.

Generically, the production of THGEM structures comprise photolithographic process, mechanical drilling and chemical etching. The different combination of these three process allow several type of overall procedures, from which the two mainly adopted ones, for tiny and big rims, are schematically illustrated in **Figure 1.18**.

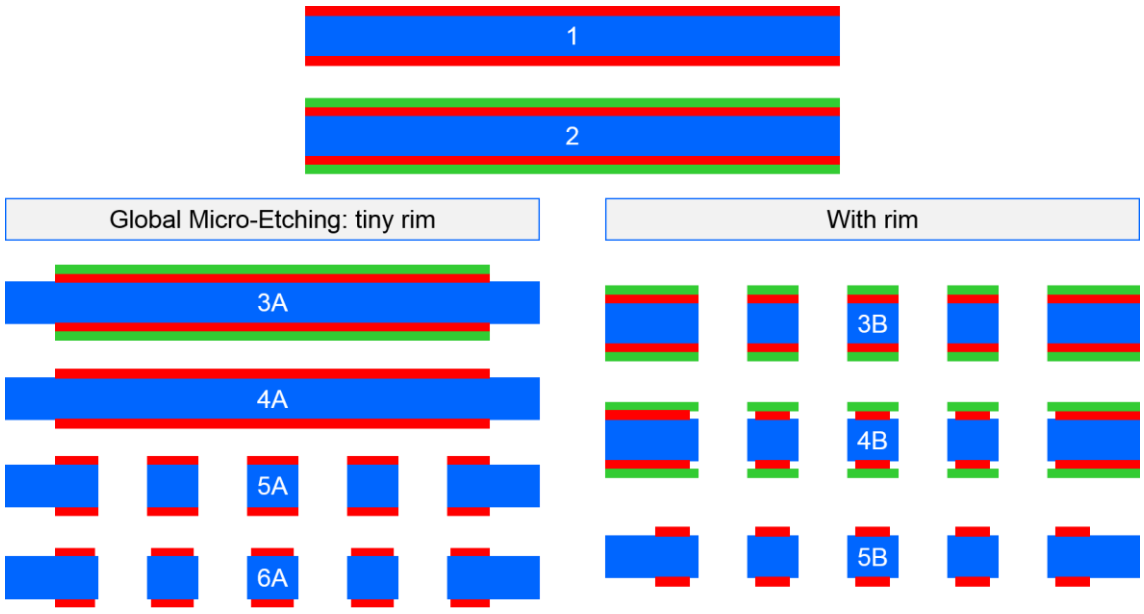

Figure 1.18 – Schematic representation of THGEM production techniques, for small and big rim.

The description of both these procedures, based on the scheme of **Figure 1.18**, is the following:

1 – The process starts with a printed circuit board with a copper layer in each side of each surface.
2 – The PCB is covered with a photoresist.

Global Micro-Etching: tiny rim	**With rim**
3A – Electrodes are etched.	3B – The holes are drilled.
4A – The photoresist is removed.	4B – The structure is object of an etching process to create the rim. Because the copper upper surface is still covered with the photoresist, only the lateral surface is etched, resulting in the rim creation.
5A – The holes are drilled.	5B – Electrodes are etched and the photoresist is removed.
6A – Micro etching: the structure is subject to a mild etching to remove drill remnants. This process leads to a slight etching of the copper surface, resulting in a minor rim (< 10 µm).	

The presented procedures include more exhaustive steps, which aim to guarantee the quality of the final THGEM. A bad quality check or choosing a wrong production procedure might lead to production defects, such a decentred rims, scratched surfaces, or copper remnants inside the holes, as exemplified in **Figure 1.19** (left).

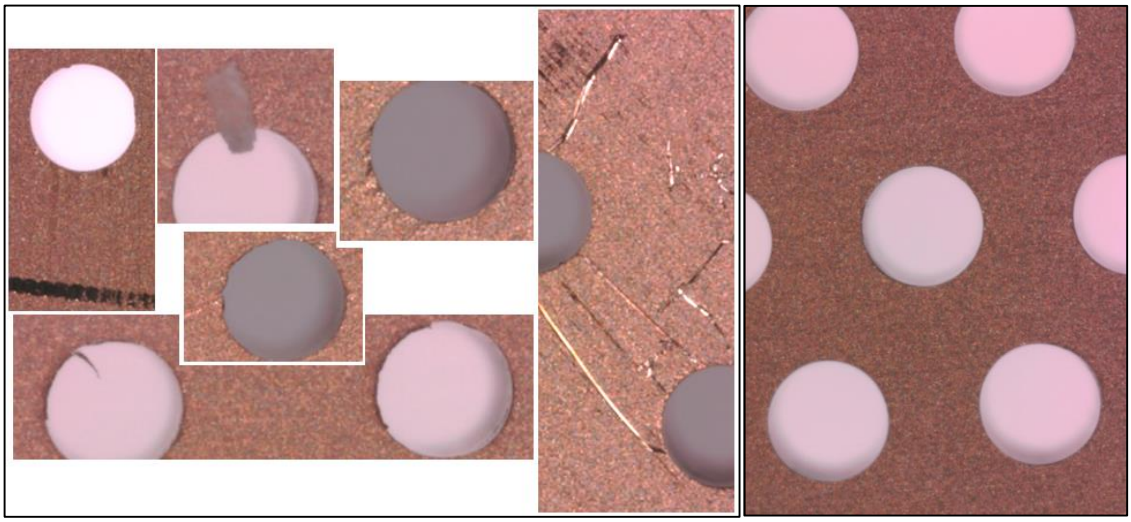

Figure 1.19 – THGEM defects due to faulty production (left); physical aspect of a desirable THGEM (right).

An inspection of the produced THGEMs is thus recommended, and a possible post production treatment (including for instance the surface polishing, simple cleaning or further micro-etching), might be required, in order to achieve the high standard quality, as shown in **Figure 1.19** (right).

So far, the production and operation of THGEM prototypes of $30 \times 30\ mm^2$, $100 \times 100\ mm^2$ and $300 \times 300\ mm^2$, single layer or cascaded, has been achieved. A Prototype with $600 \times 600\ mm^2$, with approximately $650\,000$ holes has been produced, although not characterized yet.

1.8.5.2. THCOBRA

Following the success of the MHSP in some applications, the THCOBRA was introduced [46]. With the MHSP as comparison, THCOBRA consist of a PCB, with a continuous copper layer over one surface, and independent electrodes over the remaining surface. Contrarily to the MHSP, which uses straight electrodes, this new structure used curved electrodes, whose shape is represented in **Figure 1.20**. Such shape aims to create a uniform electric field around the holes, which could not be achieved with straight electrodes.

With dimensions and production techniques similar to THGEMs, these structures permit to operate in single layer, or in multi-layer with other THCOBRAs or THGEMs. By analogy with THGEMs, since their introduction that the production procedures have been developed in order to provide an improved design quality, as exemplified in **Figure 1.20**.

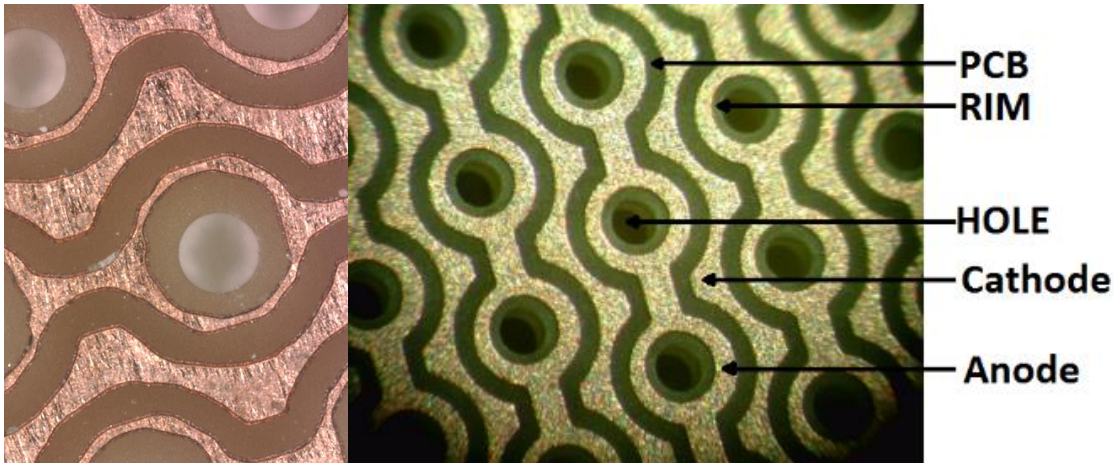

Figure 1.20 – THCOBRA electrodes pattern. The evolution of the production technique allowed to move from poorly shaped electrodes (left) to a good quality design (right).

The operation mode of THCOBRAs resembles the one from MHSP, where two stages of multiplication can coexist: the first stage is inside the hole, due to the dipole field between the two opposite surfaces of the structure, and the second amplification stage that can happen between the THCOBRA electrodes. This later stage of multiplication can be replaced by the capability of entrapping ions, by reversing the polarization of the related electrodes. This capability is of major importance in the interest of this work, and shall be discussed later.

THCOBRA prototypes with an active area of $15 \times 15\, mm^2$ have been produced and characterized in single layer, achieving gains of about 10^4, with energy resolution (FWHM) of 12.2% at $22.1\ keV$ [46]. Additionally, THCOBRA structures with an active area of $100 \times 100\, mm^2$ are currently produced and applied [47].

Due to their promising properties, Thick Microstructures, and THGEMs in particular, will correspond to the main subject in study, in particular in chapters 4 to 6.

2. Gaseous Detectors with Single Photon Detection Capability

The development of high energy and nuclear physics, along with astrophysics and medical imaging, require the development of large area photon detectors. Ring Imaging Cherenkov Counters (RICH) [48,49], in particular, require detection areas of several square metres and the capability of single photon detection (later described in chapter 3). Semiconductor based detectors, despite their eventually good performance for such applications, do not represent a cost effective solution. Vacuum photon detectors, and photomultipliers (PMTs) in particular, are reliable detectors, with fast response, high sensitivity to photons and high gains. Nonetheless, their vacuum construction limits their maximum size, they might not be reliable under magnetic fields, as they present a high cost solution. Additionally, their position resolution is restricted to approximately $1\ mm$, even when Multi-Anode PMTs (MAPMTs) are used (although this restriction does not impose a limitation for RICH detectors).

Gaseous photon detectors appear as an obvious option for such applications. Their cost effectiveness for large areas, their compatibility with magnetic fields and their capability to offer minimum material budget (important when photon detectors have to fit in the experimental acceptance), explains why the research and development of gaseous photon detectors is still ongoing, despite of some objective and intrinsic difficulties (as it will be pointed out along this chapter).

Although gaseous detectors were already introduced in chapter 1, their presentation was generic, and as stated, the minimum radiation energy that they are capable of detecting is defined by the incident radiation's minimum energy to create ion pairs, by interaction with the gaseous medium, that allow the creation of a signal distinguishable from the electronic noise background. Generically, such process of direct ionization of the gas atoms is valid for heavy charged particles, fast electrons or high energy electromagnetic radiation, such as X-rays or Gamma-rays. But not all gaseous detectors are meant for high energy radiation. Some are conceived for the detection of low energy quanta, such as VUV photons from Cherenkov light, or noble gases electroluminescence. Nonetheless, these photons no longer fulfil the energy requirements to create free electrons and positive ions through direct interaction with the gas. The implemented solution to overpass such limitation defines the concept of gaseous photon detectors, and it is defined by the coupling of gaseous detectors to photoconverters.

Photoconverters (or photocathodes when applied in solid state), when matched to the range of energies of the incident radiation, have the capability of producing photoelectrons (free electrons) upon the interaction of low energy photons..

As VUV photons cross the detector gaseous medium (generically all low energy quanta, but from now on only VUV photons are considered, in the interest of this work), they do not suffer energy loss. When they encounter the photoconverter, they can interact with it through photoelectric effect, with a probability of ejecting a photoelectron. Such photoelectron, once it exists, behaves as the previously described primary free electrons, and is capable of triggering the normal

functioning of the gaseous detector, as presented in chapter 1. The photoconverter is, therefore, an intermediate stage, to match the energy of VUV radiation to a standard gaseous detector.

As we are interested in photon detectors with single-photon detection capability, this is, detectors that are capable of producing a response to a single photon, it would be of our interest that each photon would eject a photoelectron. Unfortunately, the photoconverter response to a light stimulus is not simple. It depends obviously on the chosen material of photoconversion, but also on the electric field to which it is subject, the wavelength of the incident radiation, or even the status of its surface, and the geometry or the deposition technique, in the situation where a solid state photoconverter is used. The quantity that allows to qualify the suitability of a photoconverter, is the quantum efficiency – QE:

$$QE = \frac{N_e}{N_{photons}} \tag{2.1}$$

Which correlates the number of ejected photon electrons N_e, with the number of incident photons $N_{photons}$. Thus, such material must be chosen accordingly to the desirable application.

The association of different types of photon converters with different types of gaseous detectors leads to the identification of three generations of gaseous photon detectors [50]:

- Photon detectors making use of photon converting vapours;
- Open geometry detectors equipped with solid state CsI photocathodes;
- Closed geometry detectors equipped with solid state CsI photocathodes.

As previously stated, these photon detectors are meant to be effective in the VUV range.

2.1. The First Generation of GPD: Detectors using Photoconverting Vapours

This first generation of photon gaseous detectors appeared in the early 1980s with the development of RICH detectors [48]. They consisted of large-area coordinate gaseous photon detectors coupled with photoconverting vapours of organic substances with low ionization potential, sensitive in the vacuum ultraviolet range, such as TMAE (tetrakis-dimethylamino-ethylene) and TEA (triethylamine) [3]. TMAE is for instance used in OMEGA RICH [4], DELPHI RICHs [6] and SLD SCRID [51], while TEA is employed in E605 RICH [52] and in CLEO-III RICH [53].

TMAE has non-negligible quantum efficiency only below $220\ nm$ [3], presenting a peak of 58% at $146\ nm$ and rising towards shorter wavelengths (**Figure 2.1** (top)).

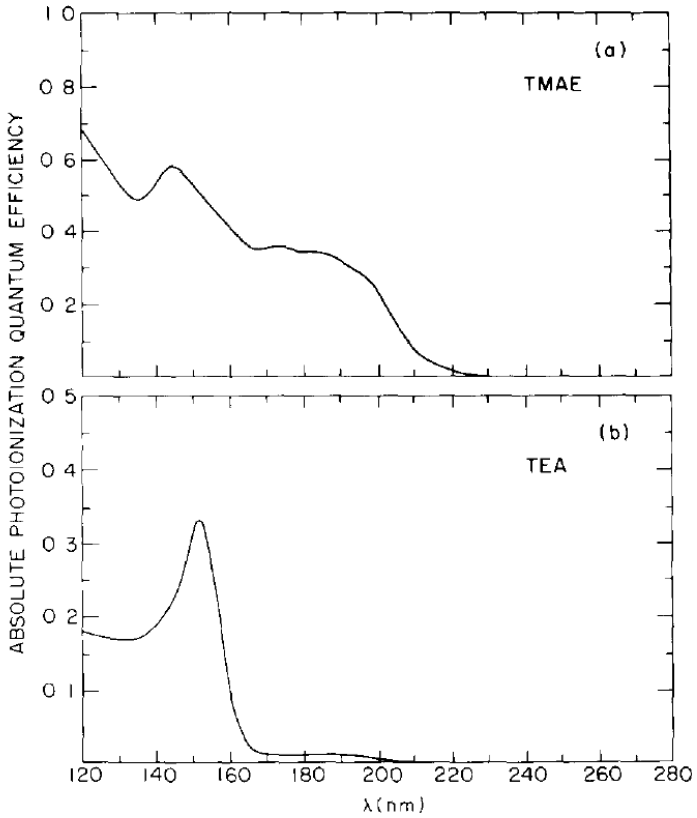

Figure 2.1 – Absolute photoionization quantum efficiency versus wavelength (average of three pressures): TMAE (top); TEA (bottom) [3].

When coupling TMAE with good quality fused silica windows, which guarantee good transmission in the UV range above roughly $160\ nm$, the wavelength range for effective photon detection is between 160 and $220\ nm$. However, TMAE presents some practical disadvantages: at $300\ K$ its vapour pressure is $0.55\ Torr$. As a consequence, at atmospheric pressure, the amount of vapour that can be introduced in the detector is low. Two different strategies can be applied, alone or combined, in order to surpass this previous limitation and assure good photon conversion probability: increase the gap by which the photons must cross, in order to increase the interaction probability; or to operate the photon detector at a higher temperature than the room temperature, where the vapour pressure becomes higher, and therefore the amount of TMAE that can be introduced is higher. Nonetheless, these possible solutions impose limitations to the overall detector too. Increasing the gap means an increase on the detector volume, which might not be an option in some applications. As the created photoelectrons have to travel a longer distance, the detectors response to light becomes slower, and parallax errors can be introduced in the position discrimination of the photon. On the other hand, a possible increase of temperature of the detector might not be possible in some applications and it can harmful for electronic read-out systems. Along with the implementation of such approaches, some obvious limitations such as the incapability of operation at cryogenic temperatures, or the impossibility of using sealed chambers. Additionally,

the use of TMAE imposes restrictions in the choice of the detector material as well controlled purity of the gases, as TMAE is chemically extremely reactive.

TEA, on the contrary to TMAE, has high vapour pressure, thus, does not present all the limitations that are intrinsically associated to low vapour pressures, and that were previously described. Additionally, it is not as chemically reactive as its competitor, which does not impose tight requirements in the gas or detector material. Nonetheless, its effective wavelength range is more limited than TMAE, having a non-negligible quantum efficiency only below $165\ nm$ [3] as shown in **Figure 2.1** (bottom). It presents a peak of 33% of QE at $153\ nm$, and below $135\ nm$, its quantum efficiency decreases to plateau of about only 17%, leading to an effective range between $135\ nm$ and $165\ nm$. As fused silica allows high transparency only above $160\ nm$, other window materials must be chosen in order to fully take advantage of such narrow wavelength range. Lithium fluoride (LiF) is often used as window when TEA is used as photoconverter.

Transversal to which photoconverting vapour is used, photons emitted during excitation processes of gas molecules easily interact with the photoconverter – photon feedback - creating spurious signals, which represent a drawback in such devices.

2.2. The Second Generation of GPD: MWPCs with Solid State Photocathodes

The second generation of gaseous photon detector appears as a consequence of the limitations imposed by the photoconverting vapours of the first generation of GPD. It is defined by a new concept of photoconverter: a solid state photocathode, to be coupled with multiwire proportional chambers [54], and such research was performed in the framework of RD26 collaboration.

Generically, solid state photocathodes have strong potential to be applied for operation in a wide range of temperatures and pressures, have compatibility with sealed detectors, and allow a variety of methods on which they can be coupled to the amplification structures inside the gaseous detector. The fact that they can be coupled together, or close to, the amplification structure, simultaneously helps to provide better time resolution and a parallax free location compared to when TMAE or TEA are used. To find the most suitable of these photocathodes, envisaging VUV detection, research was done among several compounds that could fulfil some of the requirements. **Figure 2.2** shows the quantum efficiency as function of the incident wavelength for several compounds that could be considered as solid state photocathodes.

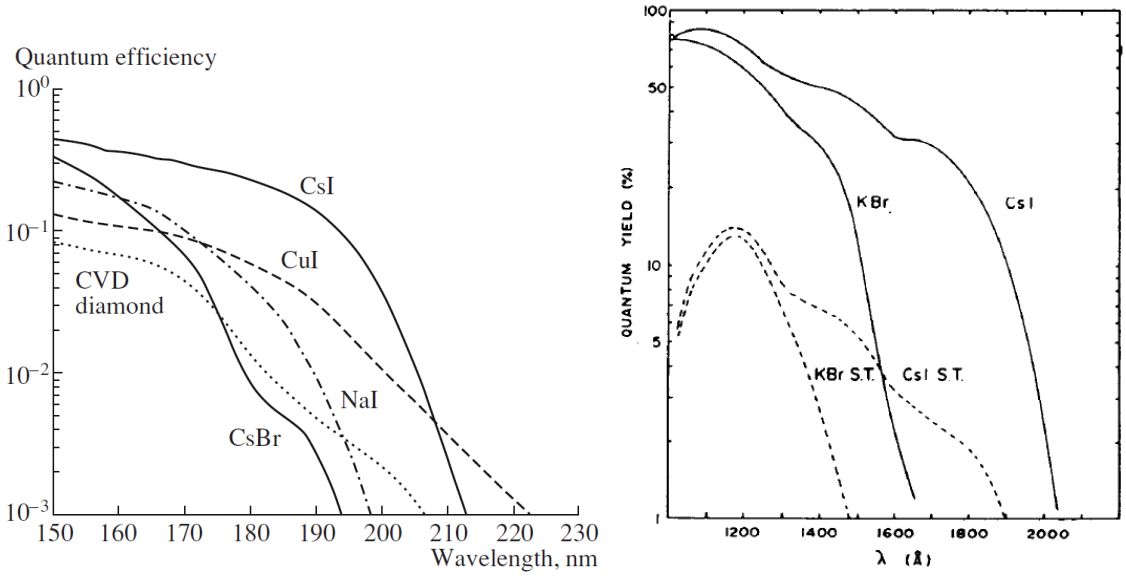

Figure 2.2 – Comparison of the quantum efficiencies of diamond, CuI, CsBr, NaI and CsI (left) [8]; comparison of the quantum yields of typical reflective and semi-transparent photocathodes of CsI and KBr (right) [55], in vacuum.

As the optimal solution theoretically would be the one that could deliver the maximum quantum efficiency possible over the widest range of wavelengths, in the range of interest, research pointed that caesium iodide (CsI) meets the suggested requirements, among diamond, CsBr, Kbr, CuI and NaI [8,55]. CsI is indeed, without any doubt, the most commonly used and suitable photocathode for the VUV range. Due to intrinsic properties that contrast with other compounds, CsI has continuously been subject of research, from where the following main characteristics are known:

- Its quantum efficiency is high (up to approximately 30%) below $210\ nm$;
- When coupled with good quality fused silica window, it results in an effective photon detection range of $160\ nm - 210\ nm$;
- Simple preparation by standard thermal evaporation;
- Suitable to be applied over several different subtracts;
- Possible to be applied over large areas;
- Radiation-hardness, which allows operation under high flux radiation environments.
- Hygroscopic, which means that contact with moisture must be avoided in order to avoid degradation. Nonetheless, it's not sensible to oxygen.

Additionally to the presented characteristics, CsI (and generically all solid state photocathodes) quantum efficiency is function of the electric field at the photocathodes surface, as well as the gas. When a photoelectron is ejected from the CsI, it will interact with the gas molecules. If such interaction is elastic, there's the possibility that some of the photoelectrons are backscattered

towards the photocathode [56] where they are absorbed, not leading to an effective signal. To avoid such process, which leads to the loss of performance of the detector, it's important to guarantee that the component of the electric field orthogonal to the photocathode, immediately above this, is high enough to accelerate the created photoelectrons away from the photocathode, decreasing this way, the probability of backscattering. In this regard, studies of effective quantum efficiency, as a measure of the created photocurrent, as a function of the applied electric field above the photocathode, and as function of different gas mixtures, have been performed. **Figure 2.3** illustrates such measurements, for CsI, at atmospheric pressure.

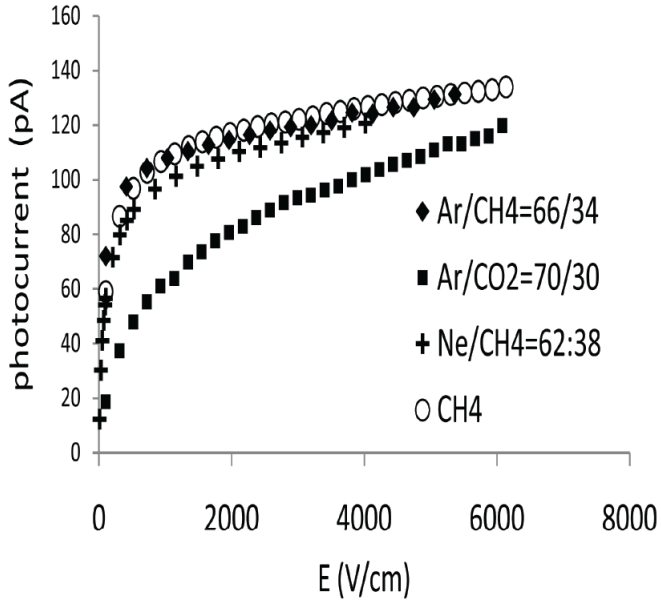

Figure 2.3 – CsI photocurrent as function of the applied field in various gas and gas mixtures at atmospheric pressure [57].

For the presented gas mixtures in **Figure 2.3**, at atmospheric pressure, the effective quantum efficiency increases significantly up to electric field values of $1\ kV/cm$. Above that field value, the incremental trend remains, but not as significantly as before. Such behaviour is shared among the several gases, and empirically allows to define the value of $1\ kV/cm$ as minimum electric field acceptable to maximize the photo-extraction. Amongst the plotted gases, methane (or gas mixtures containing a significant fraction of methane) presents the best performance. The majority of the photon detectors developed under the RD26 using CsI use pure methane. Although it is not plotted, due to experimental constrains, the quantum efficiency is optimal in vacuum. Under a gaseous atmosphere, for high electric fields, QE tends to match the vacuum values. This optimization of QE in vacuum explains the slightly better sensitivity to photons of vacuum photon detectors when compared to GPDs.

These RD26-like detectors share very similar architectures, and **Figure 2.4** illustrates the MWPC based photon detector, used in COMPASS RICH-1 [14], meant to be used coupled to a CsI photocathode.

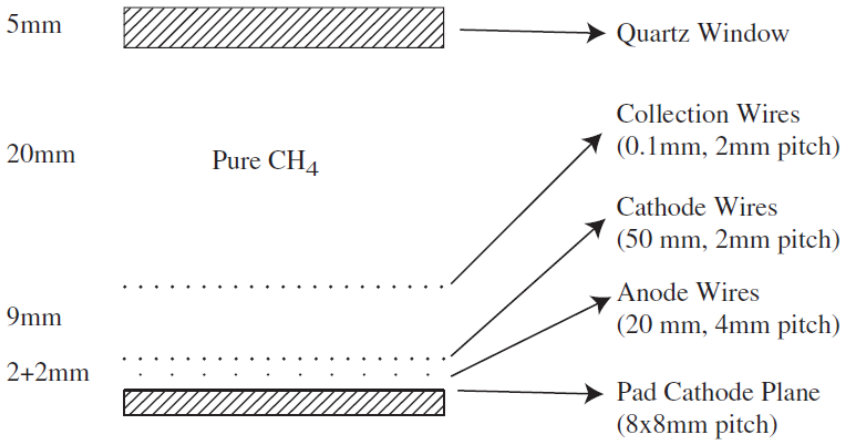

Figure 2.4 – Schematic cross-section of the COMPASS RICH-1 gaseous photon detector comprising a MWPC.

Briefly, such detector consists of two cathodes and the anodic wires, which together define the MWPC, a quartz window meant to be transparent to VUV photons, and a set of collection wires, which when polarized, is meant to collect minimum ionizing particles that cross the detector, and are undesirable to the MWPC. The bottom cathode plane is segmented into $8 \times 8\ mm^2$ pads, which grant an imaging capability to the detector, by weighting the different signals induced in different pads by the ions that result from the charge multiplication near the anodic wires.

Although CsI photocathodes are chosen to be coupled to such detectors, their application can be done in two different ways, as it is shown in **Figure 2.2**: semi-transparent or reflective [58]. Despite the fact that the plotted quantum efficiency is significantly better for reflective CsI, there are many other factors suggesting the advantages of this option instead of the semi-transparent CsI:

Reflective CsI:

- Is applied over or close the amplification structures;
- Higher quantum efficiency, in a wider range of wavelengths;
- Thickness uniformity is not a critical issue for photon-extraction.

Semi-transparent:

- Are applied under the detector window;
- Require the application, onto the detector window, of a thin metallic film to keep the photocathode at a fix potential, but such film absorbs photons;
- Photon-extraction critically depends on the thickness of the photocathode. Guaranteeing the thickness uniformity is not trivial, imposing limitations in the construction of large area detectors;

Considering these characteristics, reflective CsI photocathodes are preferred, in the majority of the applications. In the MWPC, the coupling of the reflective CsI (from now on referred only as CsI, unless specified otherwise), is done over the segmented pad cathode plane. Photons travel across the whole detector volume, insensible to the applied electric fields, until they reach the CsI and eject a photoelectron. If the photoelectron succeeds to avoid backscattering, due to the applied field, it will move towards the anodic wires, where it will undergo multiplication, leading to a production of a signal induced by the approximately 50% of the ions that move back from the anode to the segmented cathode.

Although CsI photocathodes stand moderate photon fluxes, high fluxes ($\geq 10^{12}\ cm^{-2}s^{-1}$ [10]) tend to damage the photocathode. As the intended applications, Cherenkov light detection, do not achieve such photon intensity, this limitation is not a threat to the CsI lifetime. Nonetheless, the photocathode can be damaged by exposure to ionizing radiation. While minimum ionizing particles (MIPs) can be kept away (or at least their number minimized) by the set of collection wires of the MWPC, ions cannot be avoided, as the detector's signal is dependent of their movement towards the cathode/CsI. Such intense CsI bombardment by ions, can cause the ageing of the photocathode, mainly due to the degradation of its quantum efficiency [10,59]. This flow of ions toward the photocathode gets the name of Ion Back Flow (IBF), and it's a variable that will be transversal along this whole work.

In order to evaluate the performance of CsI photocathodes for the MWPCs of the ALICE's High Momentum Particle Identification Detector (HMPID), with regard to the ageing effect, a 2D mapping of the photocurrent of a CsI photocathode was performed [60], after 250 days of irradiation with ^{90}Sr sources of different activities in different points, under a methane atmosphere [61]. **Figure 2.5** shows this 2D mapping. The places marked with a cross represent the irradiation points. Reportedly, the positions with an integrated irradiation of $0.2\ mC/cm^2$ did not show a measurable degradation of the quantum efficiency after 250 days. In the position that had an integrated irradiation of $1\ mC/cm^2$, a strong drop of about 55% was verified, showing the ageing effect.

As a large CsI photocathode bombardment by ions leads to the degeneration of its quantum efficiency, it imposes a limitation in the detectors gain, as the total number of ions is function of such variable. Additionally, such bombardment might lead to the ejection of further electrons, creating undesired spurious signals.

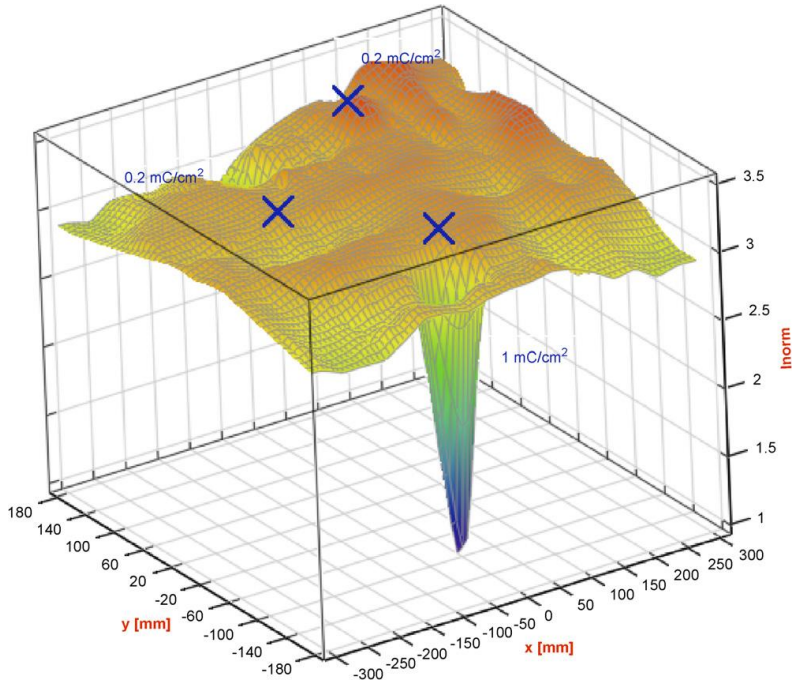

Figure 2.5 – 2D mapping of the CsI photocurrent, after a 250 days integrated irradiation, from a ^{90}Sr source, of $0.2\,mC/cm^2$ and $1\,mC/cm^2$, over the marked crosses [61].

Considering the properties of MWPCs and CsI reflective photocathode, all together, they permit to cover large area photon detectors, but:

- They present moderate effective gain (in the order of 10^4).
- Their efficiency is challenged by aging (above integrated irradiations of about $1\,mC/cm^2$).
- Their signal is slow, as it is originated by ion drift (in the range of $100\,ns$).
- Their stability is limited in presence of radioactive backgrounds.
- Their recovery time is long after electrical discharges (in the range of 1 day).
- Gain limitations due to photon feedback.

Despite these limitations, such generation of gaseous photon detectors has been successfully applied in several experiments: NA44 [62], HADES [63], COMPASS [64] (with a total active surface of $5.3\,m^2$), STAR [65], JLab-HallA [66], and ALICE (with active surface larger than $10\,m^2$). Nonetheless, the performance of gaseous photon detectors, in terms of rate capability and noise rejection cannot be increased without a change of the concept of gaseous detector.

2.3. The Third Generations of GPD: MPGDs with Solid State Photocathodes

In the second generation, the use of open-geometry detectors did not help suppressing the photon feedback, its impossibility to decrease the ion back flow induced a quick photocathode ageing, unless used under low gain, and obtaining signals from ions led to a slow detector's response to photons. This limited their use in applications where high gains and high rate environments are required.

The third generation of gaseous photon detectors appears with the development of some micro pattern gaseous detectors, and as a consequence of the limitations imposed by the preceding generation. The introduction of GEMs and THGEMs were two milestones that changed the course of gaseous photon multipliers, splitting the research into two major groups of detectors: the ones using GEMs, or GEM-based structures; and the ones using THGEMs or THGEM-based structures. Despite such splitting, these two groups share the same research background, as both share similarities in architecture and in operating principles, as described in chapter 1.

Because of their hole-type design with capability of application in multi-layer configuration [67] for multi-stage charge multiplication, these two subsets of third generation of gaseous photon detectors, permit high gains, and due to their closed-geometry, have the capability of reducing or even supressing the photon-feedback [68]. The same geometrical constrains, might allow some ion blocking, leading to smaller ion back flow when compared to MWPCs. Although this IBF reduction is just mild, the detector architecture allows several different approaches to achieve a significant IBF reduction, as it will be later described. Additionally, as charge multiplication happens inside the holes, it is easier to achieve a better longitudinal migration of the charge along the detector with smaller deviations from the interaction point, leading to smaller position parallax errors, and allow better 2D position determination. As electrons are responsible for the signal generation, this third generation of GPD is characterized by its intrinsically fast response to photons.

Although research is extensive regarding GEM based photon detectors, their description in this work is brief, and limited to the information necessary to understand its fundaments, or to the information/research that is important to transfer to THGEM-based photon detectors, where relies the main goal of this work.

2.3.1. GEM-Based photon detectors

GEM-based photon detectors, consists on the coupling of a multi-layer GEM detector with a CsI photocathode [69]. **Figure 2.6** illustrates the possibilities of coupling the CsI photocathode into a triple layer GEM detector.

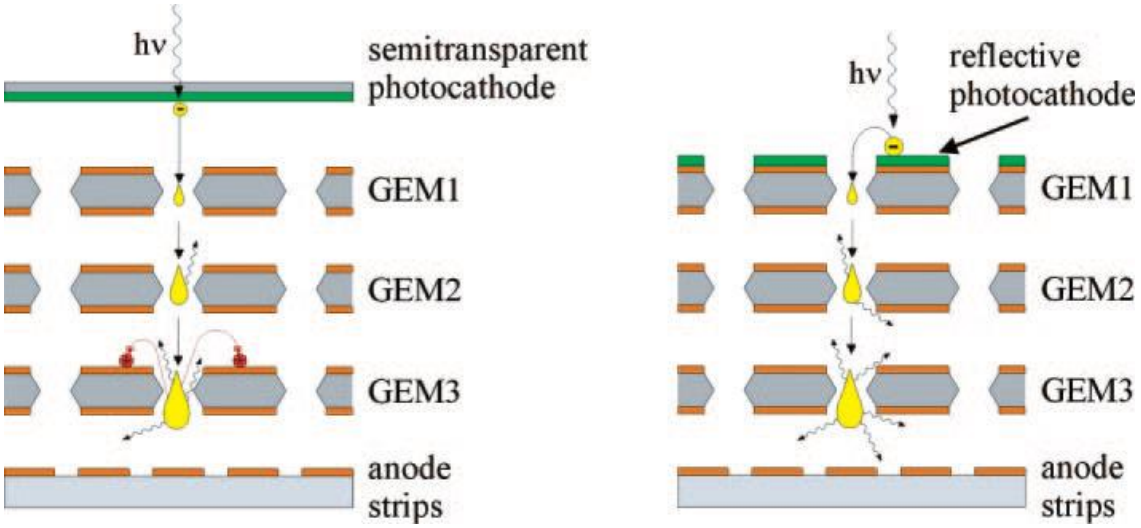

Figure 2.6 – Schematic of the use of GEM structures in a triple layer configuration for photon detection, coupled with: semi-transparent photocathode (left); reflective photocathode (right) [70].

The previously introduced option of application of CsI photocathodes in MWPCs, reflective or semi-transparent, are reintroduced again in GEM-based detectors. Considering the exemplified triple layer GEM detector (which is the most common multi-layer configuration used), one can define, just for geographical orientation, that the top of the detector corresponds to the irradiated region. With this consideration in mind, it is possible to couple a semi-transparent CsI photocathode below the detector window (**Figure 2.6** (left)), or a reflective CsI layer [71] immediately above the top of the top GEM (**Figure 2.6** (right)). In either situations, the photocathode is applied before any of the multiplication stages.

In spite of the limitations suggested before for the semi-transparent CsI photocathode, and also that the reflective photocathode option is still the most commonly adopted in the third generation of GPD, the later introduces now some limitations/difficulties that need to be weighted upon use:

- A GEMs surface is typically a thin film of copper, and CsI chemically reacts with copper. A direct deposition of a CsI layer over a Cu film, leads to a very strong non-homogeneity of the photocathodes surface, resulting in a very poor photon yield. In order to guarantee the good condition of the photocathode, an intermediate layer, between the Cu and CsI, of Ni and Au is necessary to avoid the mentioned chemical reaction.
- Because a GEM surface is not continuous due to their hole pattern, a deposition of a photocathode over its surface means an automatic loss of active photoconverting area.
- In a semi-transparent photocathode condition, an applied electric field between the window and top GEM is required in order to drift photoelectrons into the multiplication region – drift field. In reflective conditions this field is prejudicial as it will drift electrons away from the multiplication region, or increase the photoelectron backscattering, depending on the direction of the field. A null (or approximately null) electric field is thus

desirable. This means that the only field that will be felt by photoelectrons upon emission, is the applied dipole field in the GEM itself. This defines regions on the CsI, far from the holes, where the dipole field might not be strong enough to avoid the backscattering effect, leading to a "dead" photoconverting area.

The latter two points oblige a balanced choice of the GEMs parameters: pitch, thickness and holes diameter. A bigger pitch and smaller holes lead to a bigger active area, but will impose a bigger "dead" area too, as the dipole field will be significantly smaller in most of the GEMs surface. A compromise between these variables is then a must, in order to maximize the sensitivity of the detector to the desirable photons.

Despite this limitation, triple GEM based photon detectors coupled with reflective CsI [72] has successfully been put into use in the threshold Cherenkov counter Hadron Blind Detector (HBD) [73] of the Phenix experiment, covering a total area of about $1.5\,m^2$ under a CF_4 gaseous atmosphere. Such detector manages to operate at low total gain (of about 5000) [74], while the noise level is at about 1000 electrons equivalent. The operation at low gain is possible because several photoelectrons are detected by a single read-out pad (covering $6.2\ cm^2$). Imaging counters cannot operate at such low gains, as they require single photon detection, and therefore larger gains are compulsory.

To repel MIPs, the GEM based photon detector in use in HBD, applied a mild reverse drift-field [70,72,74], as illustrated in **Figure 2.7** (left).

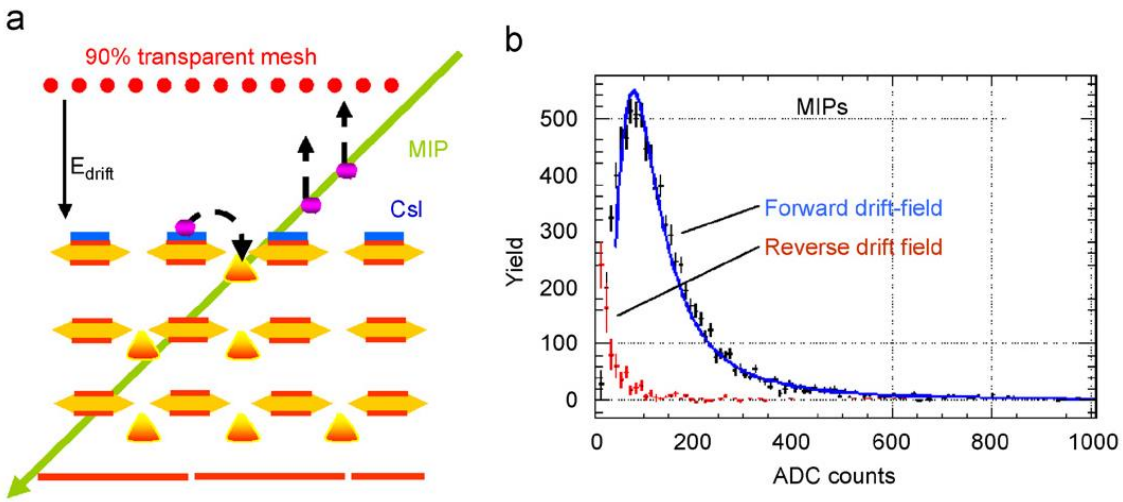

Figure 2.7 – Scheme of a windowless triple GEM gaseous photon detector coupled with reflective CsI, emphasising the applied reverse drift field (left); Comparison of the MIPs yield, between forward and reverse drift field, pointing to significant reduction for reverse drift field [70].

Although a reverse drift field (in the direction of the incident particles) can drift away the extracted photoelectrons, it can simultaneously keep minimum ionizing particles away from the reflective photocathode. Is a mild reversed drift field is chosen, it can minimize the first effect, maintaining good photoelectron extraction, while still decreasing the MIPs effect in the detector. **Figure 2.7** (right) shows the efficiency of such process in the referred detector, where a relativistic particle rejection of approximately 85% was achieved. Such property is of prime importance in Cherenkov detectors operating under intense particle background.

Another characteristic of GEM-based photon detectors, is their capability to allow an IBF reduction. Although a simple optimization of the electric fields between consecutive GEMs [75] might achieve a reduction of few percent on IBF, a more significant reduction is mandatory. Such significant reduction can be achieved by the introduction of more complex GEM-based structures with extra electrodes, such as MHSPs. Such structures have been implemented in GEM based GPD, with successful results regarding IBF reduction.

MHSPs can be applied in two different ways for IBF reduction. When MHSP was introduced, its extra electrode away from the hole (anode), was meant for a secondary stage of amplification within the same structure, and for electron collection. Nonetheless, inverting their polarization with the neighbouring cathodes, MHSPs can be used as ion traps, collecting them in the middle electrode, away from the holes. For such application, if the MHSP's MSP-like electrodes (comprising anodes and cathodes) face the bottom of the detector (considered as the MHPS's standard orientation), the structure is operated in a reversed-mode (R-MHSP), and it is illustrated in **Figure 2.8** (left). If the MHSP is flipped, it operates in a flipped-reversed-mode (F-R-MHSP): **Figure 2.8** (right).

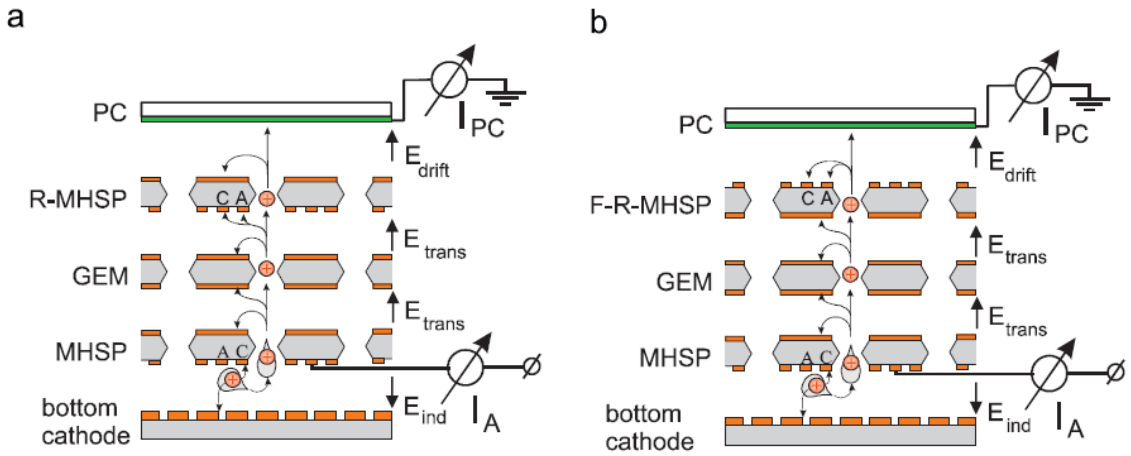

Figure 2.8 – Exemplification of the use of a MHSP in GEM based photon detectors, for IBF reduction, operated in reversed mode (left), and in flipped-reversed mode (right) [70].

As the ion's trajectories are from the bottom of the detector towards its top, it is of the best interest to place the R-MHSP or the F-R-MHSP as the first layer of the cascade, replacing the first GEM. Operating in R-MHSP mode allows the collections of ions produced below the MHSP, while

operating in F-R-MHSP mode allows the collection of all the ions production below the MHSP, plus the ions produced in the holes of the MHSP itself. Nonetheless, the first allows the coupling of a reflective photocathode, while the second obliges the use of a semi-transparent one.

Experimental results, in **Figure 2.9**, show the effectiveness of the MHSP for ion blocking, for the two referred operating modes illustrated in **Figure 2.8**.

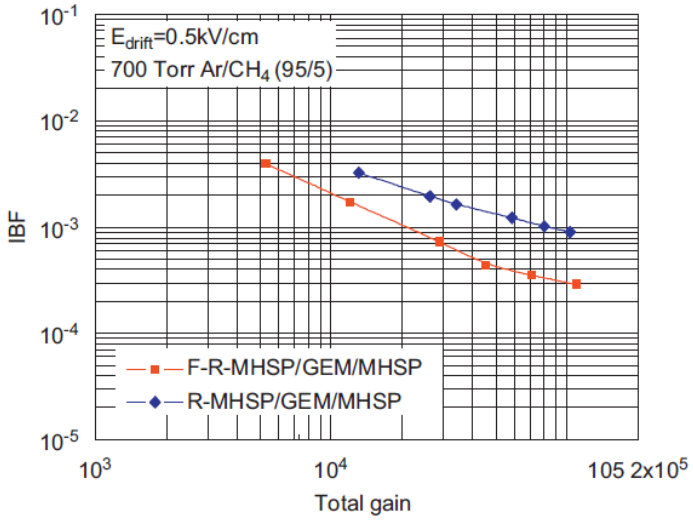

Figure 2.9 – IBF reduction as a function of the gain, for the detector configurations illustrated in **Figure 2.8**, under a Ar/CH_4 (95/5) atmosphere at 700 Torr [70].

In a Argon-Methane gas mixture, with the ratio of $95{:}\,5$, at a pressure of $700\ Torr$, and using a semi-transparent CsI photocathode, a IBF reduction up to about 10^{-3} is possible in a R-MHSP mode, while a reduction of up to about 10^{-4} is achievable with a F-R-MHSP [76–78].

Because the Ion Back Flow ratio is a variable that will be mentioned several times along this work, it is important to mention that its definition is not entirely consensual among the scientific community. Although everyone agree that it is a measure of the total number of ions that reach the photocathode, not all agree to what it should be normalized. One definition normalizes it to the total gain (given by the total amount of created electrons/ions), while the other definition normalizes the value to the effective gain (given by the total number of electrons that are collected in the readout element, neglecting all others that are collected by any other structure along its path). From now on, unless specified otherwise, the prevailing definition is the one that relates the number of ions in the photocathode with the total gain.

The ratio between the effective gain and the total gain defines the electron transfer efficiency (ETE), and it's a measure of the transparency of the structures holes to electrons.

2.3.2. THGEM-Based photon detectors

GEM-based photon detectors were a remarkable step forward towards the implementation of micro pattern gaseous detectors in Cherenkov imaging counters. Despite all their appealing characteristics, they fail partially in two particular points: high gain and robustness to sparks. Although in laboratory studies, gains of around 10^6 were achievable, their application in HBD achieve gains of only around 5000, and in trackers in other experiments, gains at most of 10^4. This proved the incapability of GEM based photon detectors standing high gains in the presence of intense radioactive background, mainly due to permanent damage of the GEM structures, after strong electrical discharges.

Even though THGEM-based photon detectors rely essentially on the GEM-based ones, the intrinsic mechanical properties of THGEMs, mainly due to their bigger dimensions, allow to bring these type of photon detectors a step forward towards the desirable application: RICH detectors. Thus, in addition to the enumerated advantages that are shared among the third generation photon detectors, THGEMs deliver mechanical robustness that permit an easy application over large areas, and deliver electrical robustness, allowing stable gains up to 10^6 [79] when cascaded in triple layer detectors. Additionally, they can stand rates up to $10\ MHz/mm^2$, although, due to the production technology, their material budget is not as low as GEM based detectors, and they do not offer a space resolution as good as GEMs.

Their typical application as GPD resembles the one based on GEMs: Multiple THGEM layers, usually 3, sensitive to the incident VUV photons due to a reflective CsI photocathode that is coupled to the top THGEM (Au/Ni coated), as schematically illustrated in **Figure 2.10**. A set of wires is mounted above the top THGEM to allow to define the electric field at the CsI surface.

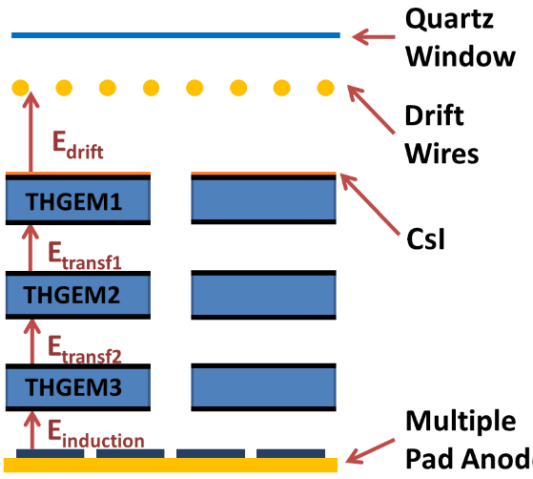

Figure 2.10 – Scheme of a triple layer THGEM detector, coupled with CsI photocathode, for photon detection.

As a matter of convention to be followed henceforth on this work, and in accordance with **Figure 2.10**, THGEMs are numbered from 1 to 3, from the top (closet to the quartz window) to the bottom

(closer the readout anode). The dipole field applied in each THGEM is generated by an applied voltage difference between the two copper electrodes (commonly named as top and bottom) of each structures, generating a ΔV_1, ΔV_2 and ΔV_3 voltage drop in THGEM 1, 2 and 3 respectively. Both the photoelectron collection and the charge transfer along the detector is possible due to the drift field (in the drift gap - E_{drift}), the transfer field 1 (between THGEM 1 and 2 – $E_{transf1}$), the transfer field 2 (between THGEM 2 and 3 – $E_{transf2}$) and the induction field (in the induction gap – $E_{induction}$).

Although this present work aims to develop THGEM-based detectors, which will be object of study along some of the chapters ahead, it's not its purpose to start from scratch, as many research has been performed before, mainly in the characterization of $30 \times 30\ mm^2$ THGEM structures. As the study of the photocathode does not represent a major study at this point, some of the characterization of THGEM structures or THGEM-based detectors can be done independently of the photocathode, allowing the use, for instance of soft X-ray sources and electron emission from the top of THGEM 1's copper electrode. In the point of view of laboratorial work, the absence of CsI in the study of the referred structures, is convenient in the sense that it allows the use of gases more suitable for such conditions (non-flammable, for instance), and allows an easy access to the detector's interior (without the risk of exposing the photocathode to air).

Below, a brief description of previous results, mainly in the optimization of the THGEM's parameters, is presented [57]. The study of gaseous photon detectors based in THGEM structures presented in this work, relies in these studies to assemble more complex detectors.

As the results presented below were performed for single layer THGEMs, Figure 2.11 illustrates the configuration that made such studies possible.

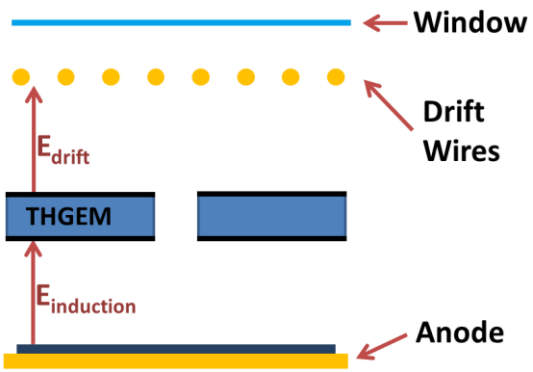

Figure 2.11 – Scheme of the configuration used for the characterization of single THGEM structures.

Studies have been performed to evaluate the role of the rim. Two THGEMs, diverging only in the rim dimensions, were characterized and compared:

- $THGEM_A$: Pitch: $0.8\ mm$; thickness: $0.4\ mm$; hole diameter: $0.4\ mm$; rim: $0.1\ mm$.
- $THGEM_B$: Pitch: $0.8\ mm$; thickness: $0.4\ mm$; hole diameter: $0.4\ mm$; rim: $0\ mm$.

The characterization for both pieces is performed under an Ar/CO_2 $(70:30)$ gaseous atmosphere, at atmospheric pressure, with soft X-ray sources (producing approximately 300 primary electrons).

Despite the fact the test is done applying different voltages, $\Delta V_{THGEM_A} = 1750\,V$ and $\Delta V_{THGEM_B} = 1330\,V$, the difference of the results goes beyond a difference in gain due to different dipole fields. The gain variation as a function of the elapsed time under continuous irradiation, for both THGEMs, is presented in **Figure 2.12**.

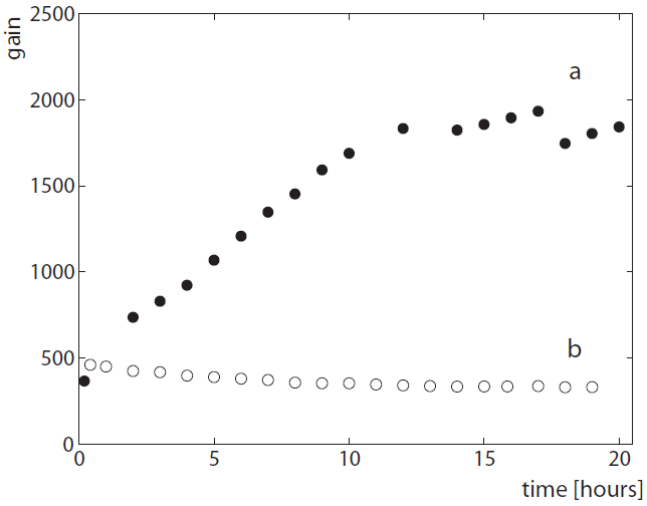

Figure 2.12 – Gain behaviour in function of time, for two THGEMs with the following geometrical parameters: thickness $0.4\,mm$, pitch $0.8\,mm$ and hole diameter $0.4\,mm$ (common parameters); different parameter: rim of $0.1\,mm$ for (a), and no rim for (b). Continuous irradiation; ΔV for $1750\,V$ for (a) and $1330\,V$ for (b) [57].

Although both THGEMs have different applied ΔVs, for the initial instant when the irradiation starts, surprisingly the gain is approximately the same. In a time range of 20 hours, $THGEM_B$, with no rim, tends to present a reasonably constant gain, with gain variations smaller than 20%. $THGEM_B$ on the other hand, shows a significant increase in gain over time.

These gain variations are verified not only for a continuous irradiation of the detector, but also for situations where the irradiation, or the powering of the detector, are interrupted. The plots of **Figure 2.13** represent this situation.

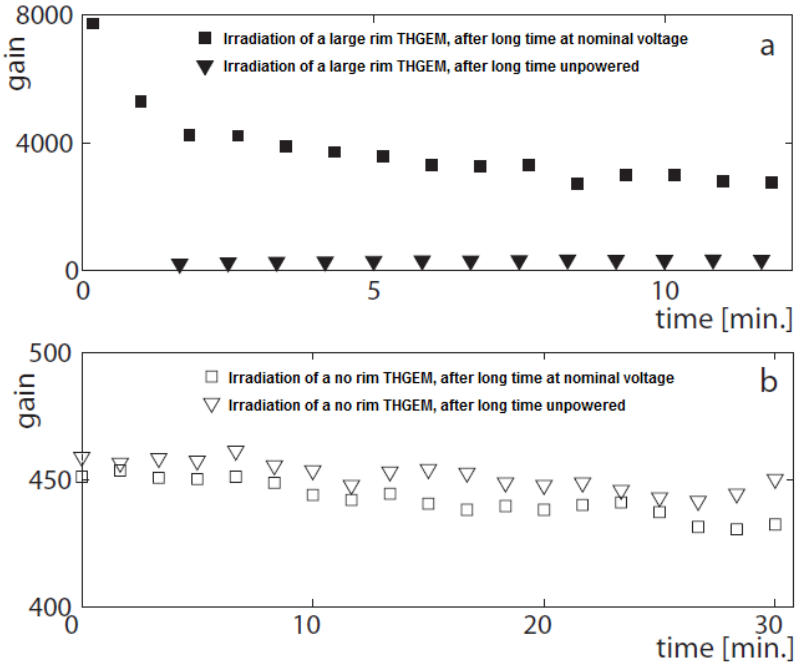

Figure 2.13 – Gain in function of time for the THGEMS (a) and (b) described in **Figure 2.12**). Full (empty) square points represent the gain measured irradiating the THGEM with large (no) rim after it has been for 10 hours at nominal voltage without irradiation. Full (empty) triangles points represent the gain measured irradiating the THGEM with large (no) rim immediately after switching on the high voltage, after it has been switched off for 1 day [57].

Considering the situation where the irradiation of the THGEM detector is interrupted for a period of 10 hours, but the detector is kept at nominal voltage, after that time, and while being irradiated again for some minutes, the THGEM with large rim denotes, again, a significant gain variation over time (**Figure 2.13**(a)). In the situation where the detector is unpowered for a period of one day, when returning to the characterization condition, the gain drops again to a low value (**Figure 2.13** (a)). These two studies applied to the THGEM with no rim lead to an insignificant variation in gain (**Figure 2.13** (b)), showing that this structure with no rim has almost no dependency on previous ΔV and irradiation history.

Although THGEMs with large rims certainly allow a bigger ΔV to be applied, leading to higher gains, at the same time they present a larger PCB area that is exposed to charges. Over time, the deposition of charge over these areas, tend to locally change the field configurations, leading to bigger field distortions that lead to gain variation. This phenomena of the dielectric charging up (when irradiated) and of loss of charge (when no irradiation is applied), is slow (in the range of hours or days). In situations of high rate or high gain, the charge displacement is higher, leading to bigger variations in gain, over time.

Figure 2.14 correlates the gain as function of the maximum ΔV applied (defined by the maximum allows voltage difference before the voltage breakdown), for THGEM samples with different rim sizes and thicknesses.

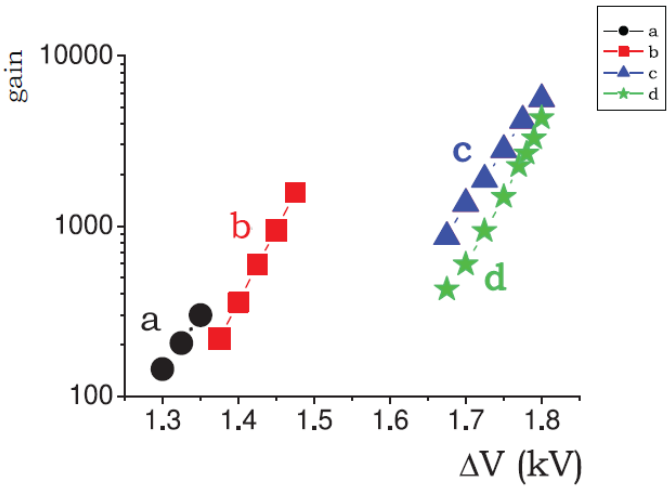

THGEM	Diameter (mm)	Thickness (mm)
a	0.0	0.4
b	0.01	0.4
c	0.1	0.4
d	0.0	0.6

Figure 2.14 – Effective gain as a function of the applied ΔV for THGEMs with holes diameter of $0.3\ mm$ and pitch of $0.7\ mm$, having different rim sizes and thicknesses [57].

As it could be extrapolated from the previous plots, gain increases for THGEMs with increasing rim. Nonetheless, gain increases too for thicker THGEMs.

As in this work, both high gain and high stability are aimed, the later variable is usually preferred, as it allows us to rely on the detectors behaviour. Therefore, THGEMs with no rim are theoretically the best option, although pieces with very small rim ($< 10\ \mu m$) are usually chosen, due to the production procedure presented in chapter 1.8. Because negligible rims are chosen, high gain, when desired, can be achieved by increasing the thickness of the THGEM.

The remaining parameters that define the THGEM, pitch and hole diameter, also influence its gain. **Figure 2.15** shows the gain variation as function of the applied ΔV, for a set of pieces with $0.6\ mm$ thickness, no rim, and with different hole diameter and pitch.

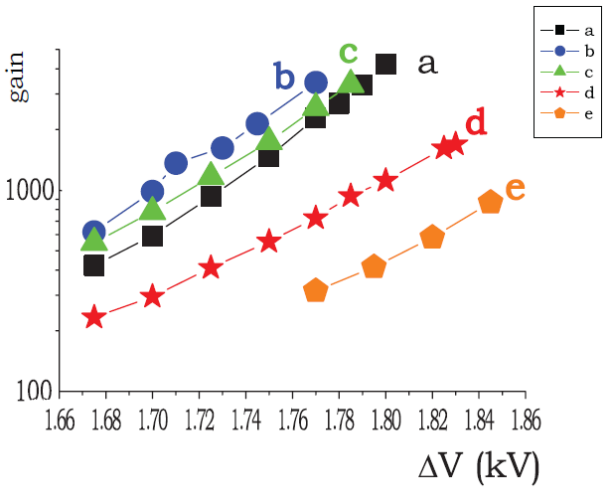

THGEM	Diameter (mm)	Pitch (mm)
a	0.3	0.7
b	0.3	0.6
c	0.3	0.5
d	0.4	0.7
e	0.5	0.7

Figure 2.15 – Effective gain as a function of the applied ΔV for THGEMs with $0.6\,mm$ thickness and no rim, having different hole diameters and pitches [57].

Results point that the pitch does not seem to have an important role in the maximum gain achievable, while smaller hole diameter leads to bigger gains. These results could lead to the conclusion that the choice of the pitch parameter is irrelevant, which is not true when the THGEM is meant to be coupled with a CsI photocathode. Surely the increasing of the pitch results in a bigger active area for the photocathode deposition, but as mentioned previously, the CsI photoelectron extraction is maximized only above a certain threshold of the electrical field at the CsI surface (approximately $1\ kV/cm$).

The electric field at the CsI surface, is the combination of the applied drift field, with the dipole field on the THGEM, which means that each of these factors needs to be understood independently.

Figure 2.16 shows the variation of the anodic current of a single THGEM coupled with a reflective CsI layer, while irradiated with UV light, as function of the drift electric field. In such condition, the anodic current is proportional to the photocurrent.

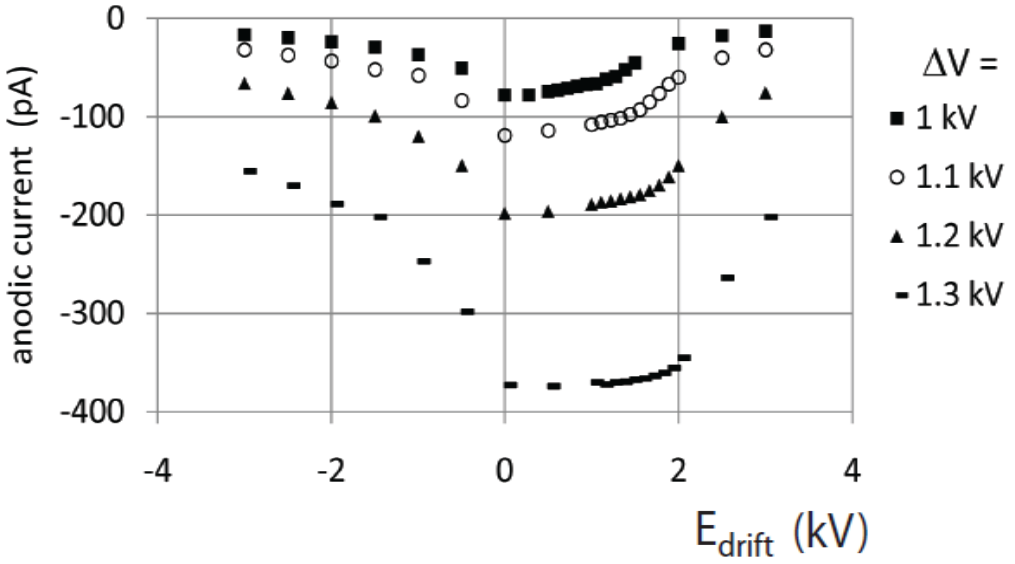

Figure 2.16 – Anodic current measured in a single THGEM detector with CsI reflective photocathode, as a function of the drift electric field, for different applied ΔVs, under UV light irradiation [57].

Results indicate that the optimal drift field for an optimized photoelectron extraction is $0\ V/cm$. Negative fields push the electrons away from the multiplication region, while positive fields increase the probability of backscattering.

The field at the surface of the CsI photocathode will then depend entirely on the vertical component of the dipole field at the surface. This can be guaranteed by increasing the dipole voltage (up to certain limit due to the breakdown voltage), or by decreasing the pitch.

Therefore, following calculations, the way to correlate the hole diameter and the pitch, in order to maximize gain, active area, and photoelectron extraction, is guaranteeing a ratio between diameter and pitch of $1{:}\ 2$, resulting in an active area of 77% of the surface. The choice of this ratio is explained further, in section 4.2.1, supported by electrostatic calculation studies.

The studies presented in chapters 4 to 6, take these previous results as background for further characterizations. Studies are performed for single, double and triple layer configurations, using ionizing particles generated from soft x-ray sources, and single photoelectrons from the conversions of UV light both from sources and Cherenkov effect in test beam exercises.

Further testing is performed for IBF reduction, by several approaches, like electric field optimizations, or introduction of THCOBRA in flipped-reversed mode, by analogy with similar experiments done with GEM/MHSP, to entrap ions (**Figure 2.17** (left)).

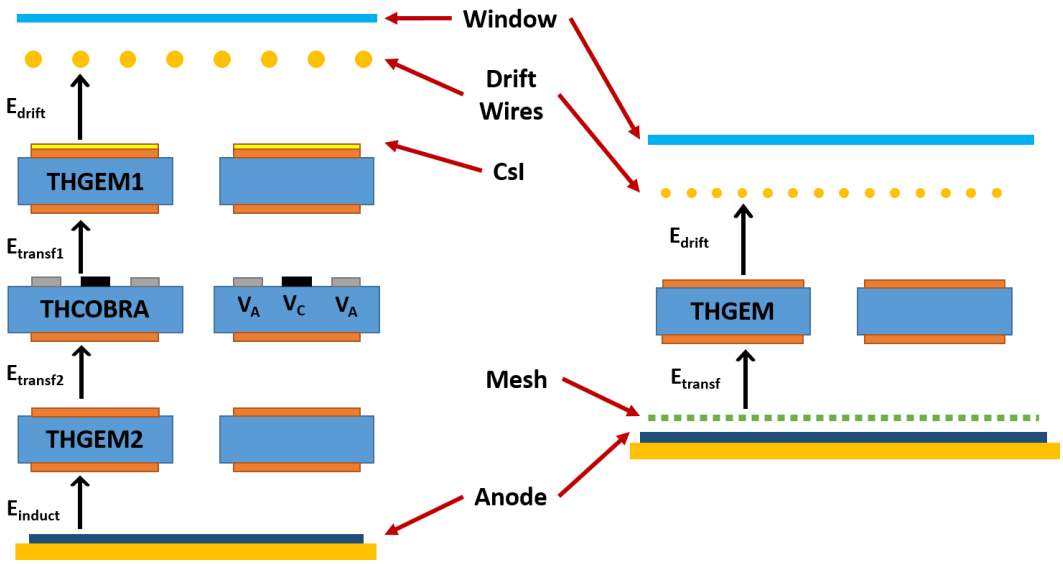

Figure 2.17 – Schemes of exemplified configurations to be studied. THGEM-based detector with THCOBRA operated in flipped-reversed mode for IBF reduction (left); Micromegas with THGEM pre-amplification (right).

Additionally, and inspired in a similar detector proposed with GEMs, a Micromegas with THGEM pre-amplification will be introduced, taking advantage of the properties of both Micromegas (low IBF, fast signal, high gains) and THGEMs (good QE on the reflective photocathode over the THGEM, fast signal, photon feedback suppression; high gains), and exemplified in **Figure 2.17** (right).

2.4. Simulation tools for Gaseous Detectors with single photon detection capability

The study and characterization of gaseous photon detectors is achieved mainly due to experimental studies. Nonetheless, electrostatic calculations and charge drift simulations can provide useful help in such work, by complementing or predicting results, or just by allowing further understanding regarding operation behaviours.

2.4.1. Electric Field Calculations

As the operation principle of gaseous detectors rely on the capability to apply high electric fields to induce ionizations, the study of such fields in the detector can be of major interest in the study and optimization of the structures parameters. These electric fields can be calculated using finite element method [80] software's, such as Ansys[1]. Additionally, the calculations permit to create a field map of the detector, or of a region in study, to be used by other simulation methods.

[1] Ansys, Inc., Canonsburg, PA, USA. http://www.ansys.com/

2.4.2. Monte-Carlo Simulations

Detailed simulations of the drift of electrons and ions in the gas of a gaseous detector can also be achieved using Garfield[2], which is a widely used software extensively used in the field of research that concerns this work. Garfield, among its various applications, allows the Monte-Carlo "microscopic technique" [81] to track electrons and ions, at a molecular level, using procedures and cross-sections available from Magboltz[3] (which is a program that solves the Boltzmann transport equations for electrons in gas mixtures under the influence of electric and magnetic fields), and using as input the field maps created by finite element method software's.

It's important to mention that this simulation method does not simulate the interaction between photons and gas molecules and/or with the photocathode. In the context of this work, and in what concerns simulations, the software relies on the assumption that a photoelectron was extracted.

The mentioned simulation method is presented in the diagram of **Figure 2.18**.

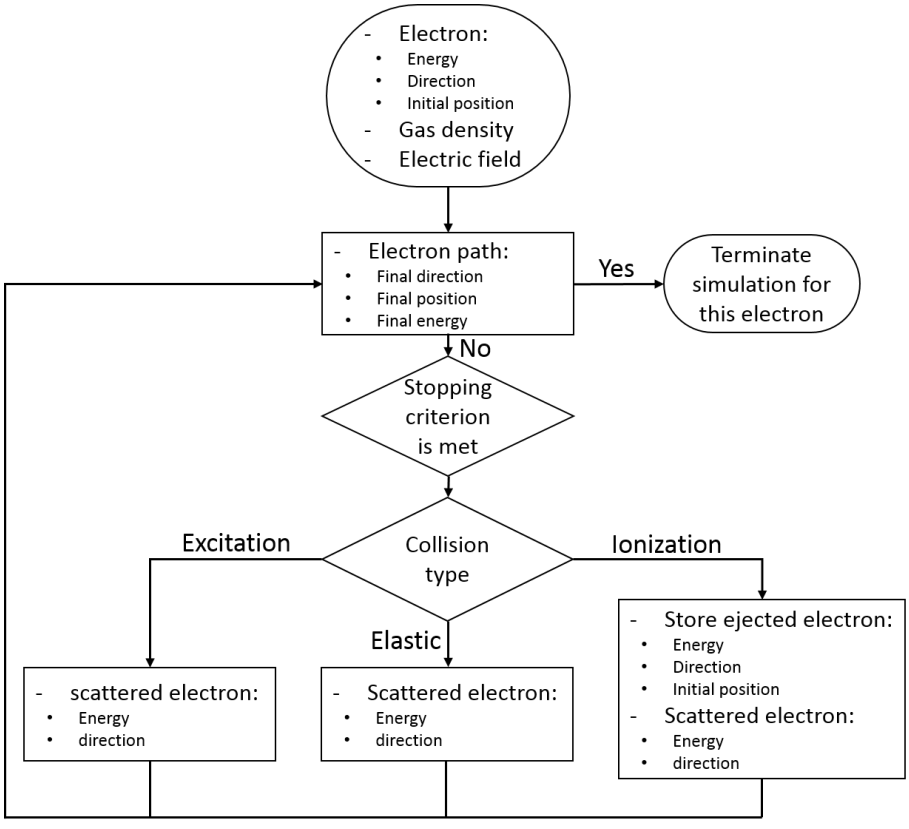

Figure 2.18 – Simulation diagram for the Monte-Carlo microscopic method. Adapted from [81].

[2] Garfield - Simulation of gaseous detectors, CERN. http://garfield.web.cern.ch/garfield/
[3] Magboltz - transport of electrons in gas mixtures, CERN. http://consult.cern.ch/writeup/magboltz/

The process starts with an initial electron, with known initial energy, position and direction, inserted in a known gas, under the effect of a known electric field.

Assuming that the velocity between collisions is constant, the program iterates the particle's position over a time step (defined by the user, or calculated as an estimate of the time of flight). Along the path of the electron, the interactions due to collisions with the gas molecules are considered.

Each collision with the gas molecule is categorised in the following way:

- Elastic: energy conservation;
- Inelastic: the electron excites a gas molecule e losses energy in the process;
- Super-elastic: interactions where the electron gains energy;
- Attachment: loss of the electron through attachment;
- Ionization: production of an additional electron;

The choice is probabilistically done in accordance with the cross-sections of each process for the electron's energy immediately before the collision. These cross-sections for each type of interaction are provided by Magboltz.

In the situation where the electron interacts by excitation or elastic collision, the information regarding energy, direction and position of the electron, is stored after the iteration step, and will serve as the input information for the reset of the cycle. In case an ionization happens, two electrons will coexist for an instant. Immediately after that instant, they will be treated as independent from each other. For the previously existent electron, the updated position, energy and direction is stored, and the cycle will restart with this new information. For the ejected electron, the same type of information is collected, and it will start its own iteration cycle. It is important to point out that elastic collisions are always possible, while excitations and ionizations require that the electrons energy is above the excitation or ionization threshold, respectively.

The simulation process continues until a stop criteria is verified. For each independent electron, the stop criteria are the following:

- The electron reach an electrode;
- The electron is lost through an attachment process;
- The electron "leaves" the simulated volume, due to the diffusion process.

The overall simulation gets to an end once the stop criteria are verified for all the existent electron.

From this simulation process, it is possible to extract all the stored parameters, such as energies, spatial position of ionizations and attachments, or even the final position of each electron.

Although these simulations are rich in information, as electrons are simulated as independent from all the others, the process can be very time consuming, in particular when high gains are simulated.

In a similar way, tracking of ions is also possible.

2.4.3. Field Lines

On the contrary to the microscopic method, which relies in the interactions at a microscopic level, field lines intent to provide a macroscopic view of the trajectory of particles in the gas, providing the user with the average drift lines of both ions and electrons. Due to the fact that it is a macroscopic quantity, and because it represents only the average trend of the particles, it is independent from the used gas, and therefore does not take possible interactions, like diffusion or multiplication, into account.

In order to provide these average drift lines, this method, also integrated in Garfield, calculates, numerically, the differential motion equation of each particle, which is function of the electric field (given by the field map). The numerical method applied for these calculations is the Runge-Kutta-Fehlberg method [82].

The iteration process stops when one of the following conditions is verified:

- The particle reaches an electrode;
- The particle's velocity becomes zero or less;
- The particle moves in the opposite way towards which it was expected to move;
- When stop criteria of the numerical method are verified;

Overall, these referred tools will be used for non-experimental studies, in chapter 4 and 5, allowing a deeper understanding of properties and operation of the detectors under study, complementing, in some cases, the data obtained experimentally.

3. Ring Imaging Cherenkov Detectors

The previous chapters, and in particular chapter 2, recurrently refer to the application of gaseous photon detectors in Ring Imaging Cherenkov (RICH) detectors for particle identification (PID) in high energy physics (HEP).

Although the subjects regarding RICH and PID techniques are extensive, and out of the context of this thesis, still this chapter aims to provide the reader with the minimum necessary information about such topics, in order to allow a bridge between them and the development of gaseous photon detectors, and to understand the requisites that these must match. A further and comprehensive reading about Cherenkov radiation and RICH detectors can be found in reference [49].

Particle identification represents a fundamental aspect in high energy physics experiments. In the past, this identification relied on visual techniques, such as bubble chambers, nuclear emulsions or streamer chambers, providing a direct imaging of the particles. Although of invaluable interest at that time, such techniques presented various limitations, such as limited rate capability and triggerability, and their methods to reconstruct events were highly time consuming. With the development of high energy physics experiments, and their operation in more demanding environments, the applications of the referred outdated techniques became of no value. The development of alternative techniques was therefore mandatory to encompass all the features for achieving an efficient particle identification in modern experiments.

The advent of particle identification techniques is then driven by their physical performance as a function of the experiment environment (such as event rates, triggering considerations, ...), and the experimental setup (namely material budget, size and space requirements, area coverage, compatibility with of detectors,…).

Apart from the techniques that can be applied for identifying particles, a particle is identified univocally on the basis of its mass and electrical charge. The different PID techniques rely then in the determination of these factors to identity the particle. The charge sign, and the momentum p of a charged particle can be obtained by the measurement of the curvature of its trajectory. Nonetheless, there are no direct ways of determining the particles mass m, and can only be inferred by the correlation of its momentum and its velocity, by the following relation [49]:

$$m = \frac{p}{c\beta\gamma} \tag{3.1}$$

where β is the particle's velocity, normalized to the speed of light in vacuum c, and γ is the Lorentz factor that relates the particle's energy E with its mass:

$$\gamma = \frac{E}{mc^2} \tag{3.2}$$

Techniques for PID rely then on the capability of measuring the particles' velocities, which can be achieved by several methods such as: the measurement of the ionization energy loss; time of flight, detection of transition radiation, and detection of Cherenkov radiation.

Depending on the aimed range of momentum of the particles to be identified, and the desirable velocity resolution, different methods for the velocity determination can be chosen. In particular, in momentum ranges from few GeV/c up to several tens of GeV/c, with velocity resolutions of just few percent, the detection of Cherenkov radiation appears as an optimal solution.

3.1. Cherenkov Radiation

Cherenkov radiation is a possible outcome from the traversing of high energy charged particles through a dielectric medium with refractive index n [17,49]. When these particles cross such medium, they can interact with it, inducing atom excitation, leading to light emission. If the particle has a velocity βc higher than the local phase velocity of light, thus verifying the condition $\beta > 1/n$, then the light resulting from the excitation process is emitted in the form of a coherent wavefront, at a fixed angle with respect to the trajectory of the particle.

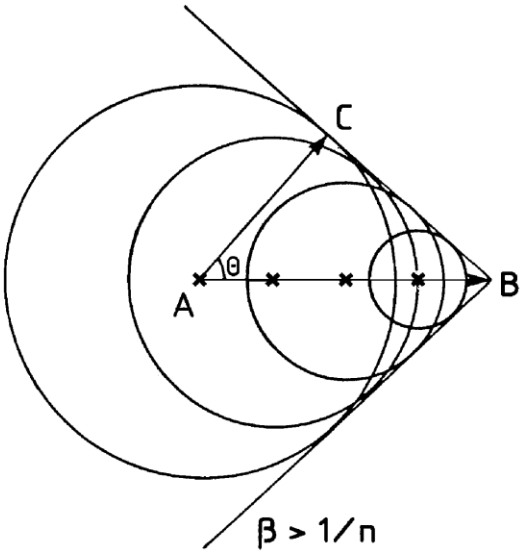

Figure 3.1 – Huygens reconstruction for $\beta > 1/n$. The cone, built up from all the combined wavefronts, has an opening angle which depends on the ratio of particle's speed to the light speed [49].

From the Huygens reconstruction, under the referred condition, represented in **Figure 3.1**, it is possible to conclude that, the combined wavefronts form a conic surface around the axis of the particle's trajectory (therefore with a will defined direction), which has an opening angle θ_c, called Cherenkov angle, given by [17]:

$$\cos(\theta_c) = \frac{1}{\beta n} \tag{3.3}$$

The emission of Cherenkov radiation results in a continuous spectrum with particular incidence for the blue and ultraviolet bands of wavelengths.

Additionally, because the condition $|\cos\theta_c| \leq 1$ must be verified, there must be a threshold velocity, which is expressed by the threshold Lorentz factor γ_t, below which the emission of Cherenkov radiation does not take place [49]:

$$\gamma_t = \left(1 - \frac{1}{n^2}\right)^{-\left(\frac{1}{2}\right)} \tag{3.4}$$

As the particle's energy loss process is fast, it results in the emission of Cherenkov light for a very short time. Also, the number of produced Cherenkov photons is very low.

3.2. Cherenkov Imaging Detectors

The Cherenkov light emitted at a certain θ_c appears as a footprint of a particle, and depends on its momentum. Some detectors, like the Cherenkov counters or the Differential Cherenkov counter, limit their operation to the detection of the light intensity as function of the particle's energy, but such methods are highly dependent on statistical fluctuations. Ring Imaging Cherenkov counters/detectors, however, base their operation principle on the detection and imaging of the ring resulting from the projection of the Cherenkov cone light over a planar surface [49]. As such ring is geometrically a function of the Cherenkov angle, the interpretation and analysis of such ring allows the determination of the particles velocity, based on equation 3.3. Thus, detectors must be built to permit the imaging of such Cherenkov light rings. These detectors generically comprise a dielectric medium (radiator) to allow the Cherenkov emission, optical elements, to allow the focusing, or just transmission of the light, and photon detectors with imaging capability.

Because the emission of Cherenkov light is feeble and short-timed, the photon detectors must be chosen accordingly to such impositions. They must provide single photon sensitivity, fast response and low noise and high gain to allow single electron detection. Additionally they must allow large area covering (in the order of m^2), moderate spatial resolution to permit the ring imaging, and be sensitive in the short wavelength range of Cherenkov light emission [49].

Two classes of detectors fulfil the referred impositions: vacuum and gaseous photon detectors. Because both classes of detectors are coupled with photocathodes for photon detection, and since the majority of the photocathode, in the referred wavelength range, are not sensible to the visible range, then these detectors only rely on the UV component of the Cherenkov light for its detection.

As vacuum photon detectors present some limitations cheaply covering large areas, and are sensible to operation in magnetic fields, the choice for large area RICH photon detectors, in the past years, has been in the direction of the gaseous class, in particular second generation gaseous photon detectors [48,83,84]. Their limitations, described in chapter two, and their difficulties in operating in more demanding environments, lead to the present research of the third generation of GPD based in THGEMs [13,85–87].

Regarding the radiator (which might be gaseous, liquid or solid), and the configuration of the optical elements, their choice too must obey several requirements imposed by experimental constrains, such as momentum range, particle separation power, space availability, counting rate, etc [49].

The arrangement of these elements leads to mainly three types of possible configurations, whose design is taken into account to minimize the loss of Cherenkov photons: Mirror Focused RICH Counter; Proximity Focused RICH Counters; and Detection of Internally Reflected Cherenkov light (DIRC) [49].

3.2.1. Mirror Focused RICH Counters

Mirror Focused RICH counters, schematically represented in **Figure 3.2**, are considered for low refractive index radiators (mainly gases), presenting a long depth, along with spherical converging UV mirrors, or set of mirrors, that focus the produced Cherenkov photons into the photon detectors. The long length vessel, typically in the order of metres, is a consequence of the small number of photons emitted in low refractive index radiators, and therefore its length is required to provide a satisfactory number of detected photoelectrons per ring.

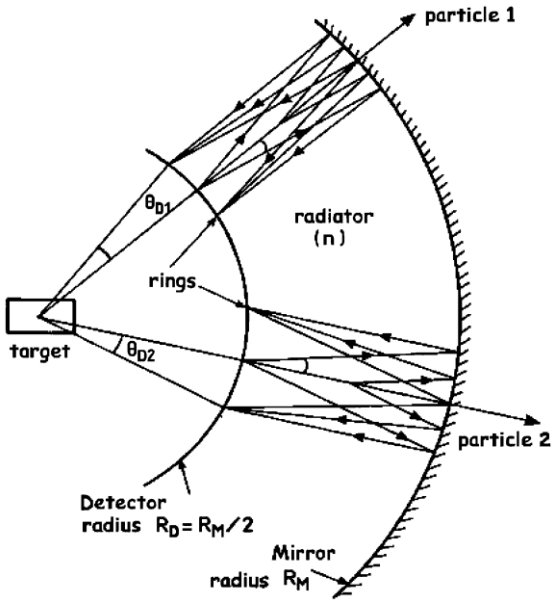

Figure 3.2 – Scheme of the working principle of a Mirror Focused RICH counter [49].

In this configuration, the charged particle emitted from the target crosses the radiator, emitting Cherenkov light at a certain θ_c, which is then reflected and focused by the mirrors, into a ring image, detected by the photon detectors.

Due to the optical properties of the spherical converging mirror, mirror focused RICH counter have the capability of producing identical rings for incident parallel particles that travel at the same

speed, despite possible optical aberrations. Additionally, as the photon detectors are not placed in the path of the charged particles, their operation is not limited by the possible interactions with these (although the photon detectors still need to take into account incident MIPs that are scattered).

Such detectors have applications for instance in the DELPHI detector at CERN [6].

3.2.2. Proximity focused RICH Counters

Proximity focused RICH counters, illustrated in **Figure 3.3**, represent a different configuration of RICH detectors, allowed by the use of liquid or solid radiators (with higher refractive indexes when compared to the gaseous ones). Typically these type of radiators allow, for a charged particle and over just a thin radiator, a large Cherenkov light intensity.

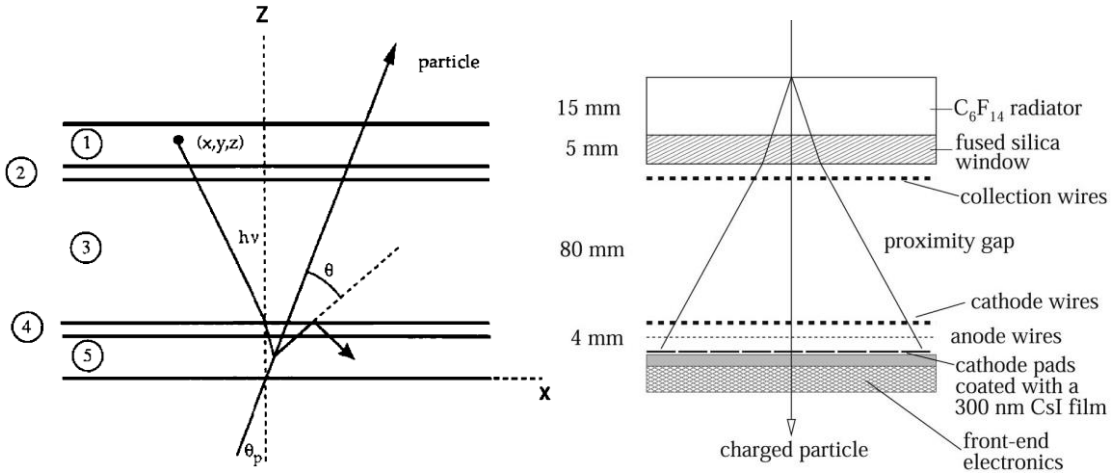

Figure 3.3 - Scheme of the working principle of a Proximity Focused RICH counter: (1) photon detection volume, (2) UV window, (3) proximity gap, (4) UV window, (5) radiator volume (left) [49]; Schematic layout of the ALICE RICH, coupled with a CsI-MWPC (right).

In this situation, the detector allows the direct projection of the emitted cone light from the radiator, into the surface of the photon detector, placed at a close distance from the radiator. This distance, separating the radiator from the photon detector is considerably smaller than in mirror focused configurations, and is typically in the range of centimetres.

This configurations presents the drawback of placing the photon detector in the trajectory of the incident particles, limiting their performance under such irradiation.

Proximity focused RICH counters are applied for instance in ALICE experiment at CERN [88,89].

3.2.3. Detection of Internally Reflected Cherenkov light

Another possible configuration, conceptually different from the two presented above, is the DIRC (Detection of Internally Reflected Cherenkov light) detector [90,91].

The conceptual scheme of this configuration is presented in **Figure 3.4**. It is based in a thin solid radiator, typically quartz, perpendicularly coupled to a photon detector, as evidenced in the scheme. While proximity focused RICH counters uses the solid radiator exclusively for Cherenkov light emission, DIRC additionally uses it as a light guide.

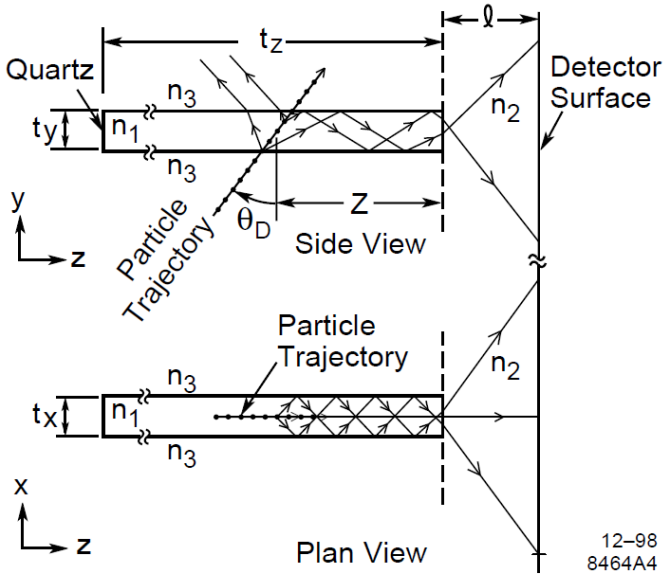

Figure 3.4 – Scheme of the working principle of a DIRC detector, emphasising the light internal reflection over the radiator/light guide (represented horizontally), until its detection by a photon detector (represented vertically). Side view (top); plan view (bottom) [91].

When a charged particle crosses the radiator, shaped as a long thin bar with a rectangular cross section, it emits a Cherenkov cone of light. Because of the refractive index differences between the radiator medium and the outside medium, instead of the light being refracted as in a common RICH detector, the light is subjected of total internal reflection over the flat surface of the radiator, allowing its propagation along this guide. As the cone of light results in different reflection angles, the projection ring can be created on the photon detectors.

The overall detection process, allows very good angular resolution due to the transmission of the photons over a light guide, but on the other hand they demand the use of solid radiators, and they present limited time resolution, due to the fact that photons, from a same event, might have to travel significant different distances.

The first large scale application of a DIRC detector is on the BABAR detector at the PEP-II accelerator in SLAC [91].

3.2.4. Radiators

As mentioned along this chapter, the choice of a dielectric medium as radiator for Cherenkov light emission must match both the range of particles momenta, and the RICH detector geometrical configurations.

Cherenkov light, coherent and emitted along a defined direction, can easily be distinguished from the scintillation photons, emitted isotropically. Despite this fact, as the number of photons emitted from scintillation process can be orders of magnitude above Cherenkov photons, it is of major interest to minimize this undesirable component. Therefore, the choice of a radiator must rely in materials that ideally have no scintillation component. Additionally, the material must have good optical transmission properties, this is, must not have absorption bands in the wavelength range to be used.

Overall, a radiator is characterized by [49]:

- The Lorentz factor at the threshold (defined by equation 3.4);
- The optical transparency;
- The chromatic dispersion.

Additionally, based on the refractive index, radiators can be divided into four major groups, each of which corresponds, roughly, to a defined physics application range [49]:

i) $1 < n < 1.12$ $(\gamma_t > 2.147)$
In this interval the radiator are:
- Gaseous (below the critical point);
- Cryogenic liquids, such as He, Ne, Ar or H_2;
- Solid as the silica aerogel.

ii) $1.12 < n < 1.35$ $(1.49 < \gamma_t < 1.35)$
In this interval the radiator are liquid, mostly fluorocarbons:
- At low temperature (CF_4; C_2F_6; C_4F_{10}):
- At room temperature (C_5F_{12}; C_6F_{14}).

iii) $1.33 < n < 1.47$ $(1.37 < \gamma_t < 1.52)$
This interval concerns essentially liquid radiators, transparent to the visible light and the near UV (water, alcohol, glycerine, …).

iv) $n > 1.46$ $(\gamma_t < 1.37)$
All the radiators characterized by these high refractive indexes are solid, either transparent to the visible light (glass, or plastics, …) or to the UV light (quartz, crystals of CaF_2, NaF or LiF, …).

3.2.5. Particle Identification using RICH detectors

Ring Imaging Cherenkov detectors aim to image a ring, capable of being used to determine a particle's speed. Still, the fact that the photon detectors require the capability of singe photon detection, it means that each photon is detected independently from the other photons that originate the ring. As a result of such process, *offline* algorithms are built in order to correlate photon events with triggered particles in a certain time range. This helps distinguishing rings originated by different events, or different particles with different momenta, and allows to discriminate from undesired events. This process leads to the ring reconstruction, as exemplified in **Figure 3.5** based in a real RICH-1 event, at the compass experiment [92].

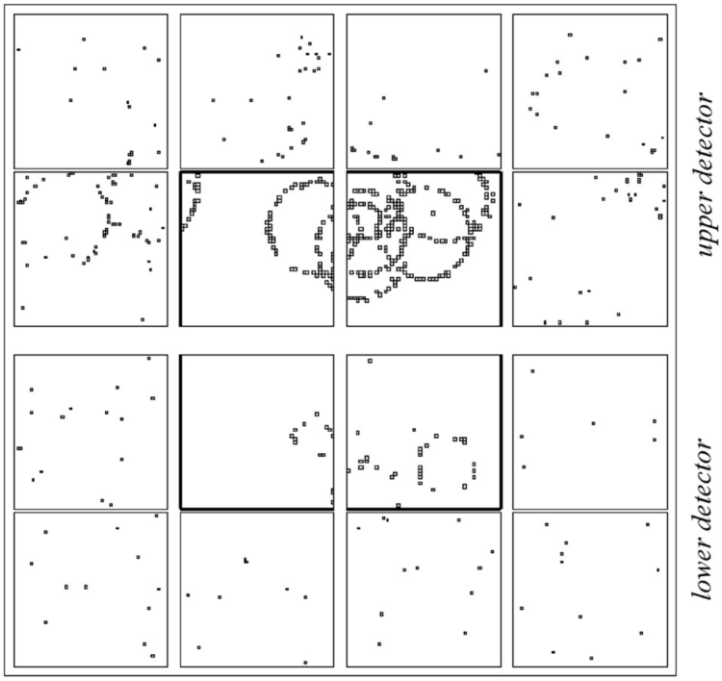

Figure 3.5– Example of a typical event display where many Cherenkov rings are visible, extracted from COMPASS RICH-1. For this specific RICH detector, the photons in the peripheral area are detected by CsI-MWPCs, while the photons from the inner region are detected by MAPMTs (the squares corresponding to this inner region with MAPMTs are highlighted) [92].

Analysing the displayed rings, and based in the geometrical parameters from the RICH detector, it's possible to trace back the Cherenkov angle from the light cone. Thus, with the knowledge of θ_c and the refractive index of the medium, the particle's velocity can be determined through equation 3.3. This information, with addition to the previously known momentum, permit to infer the particles mass, allowing its identification. As an example, **Figure 3.6** shows the $\pi/K/p$ separation performance of the COMPASS RICH-1 detector, based on the particles' mass separation.

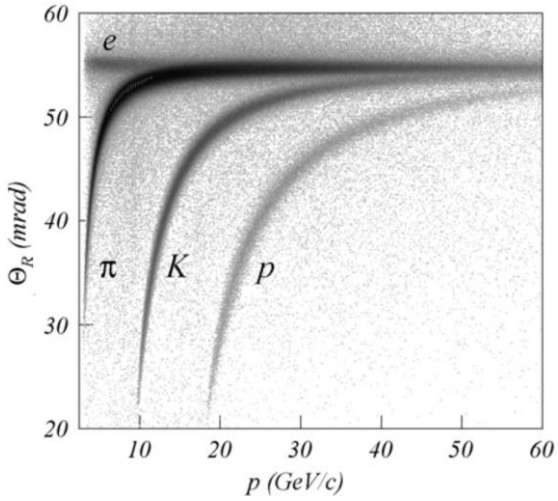

Figure 3.6 – Example of the measured Cherenkov angle (θ_C) as a function of the particle's momentum, showing the $\pi/K/p$ separation, extracted from COMPASS RICH-1 [92].

3.3. COMPASS Experiment

The use of RICH detectors became, in the last decades, of indispensable valuable in high energy physics experiments. In particular, the RICH detector from the COMPASS experiment, from which part of the work mentioned in this thesis is aimed. Although a brief description of this RICH detector will be introduced later, in order to contextualize it under the whole experiment, a brief description of COMPASS and its apparatus is presented below. Further and comprehensive reading about such experiment can be found in reference [14].

The COMPASS experiment lies on the M2 Beam Line of the Super Proton Synchrotron (SPS) at CERN in Geneva, Switzerland. It consists on a high energy experiment, and its purpose is the study of the nucleon spin structure and the spectroscopy of hadrons, with high intensity muon and hadron beams. The experiment was approved in 1997, commissioned in 2001, and data taking started in 2002. COMPASS relies on a collaboration of nearly 220 physicists enrolled in 24 institutions from 13 countries.

The broad physics programme of the COMPASS experiment imposes specific requirements to the experimental setup, which is illustrated in **Figure 3.7**. The need to collect particles in a large range of momentum and polar angle, demand an experimental apparatus with large acceptance, track reconstruction and identification capabilities in very different regions of the phase space. Additionally, due to operation under high luminosity conditions, the detectors requires the capability of standing high rates while operating with high time resolution, an efficient trigger system, and a good data acquisition system capable of handling high flux data.

To meet the referred requirements, the experimental apparatus mainly comprises two different spectrometers, which cover a total length of over 50 metres. These are the Large Angle

Spectrometer (LAS) and the Small Angle Spectrometer (SAS), and together they complement each other in order to allow the wide range of momentum and angular acceptance. LAS is the first spectrometer in the beam direction, and it has an angular acceptance of $\pm 180\, mrad$, and its purpose is to measure and identify particles that are emitted at larger angles. SAS is second in the beam direction, and it aims to provide the same information for more energetic particles emitted at smaller angles from the beam axis.

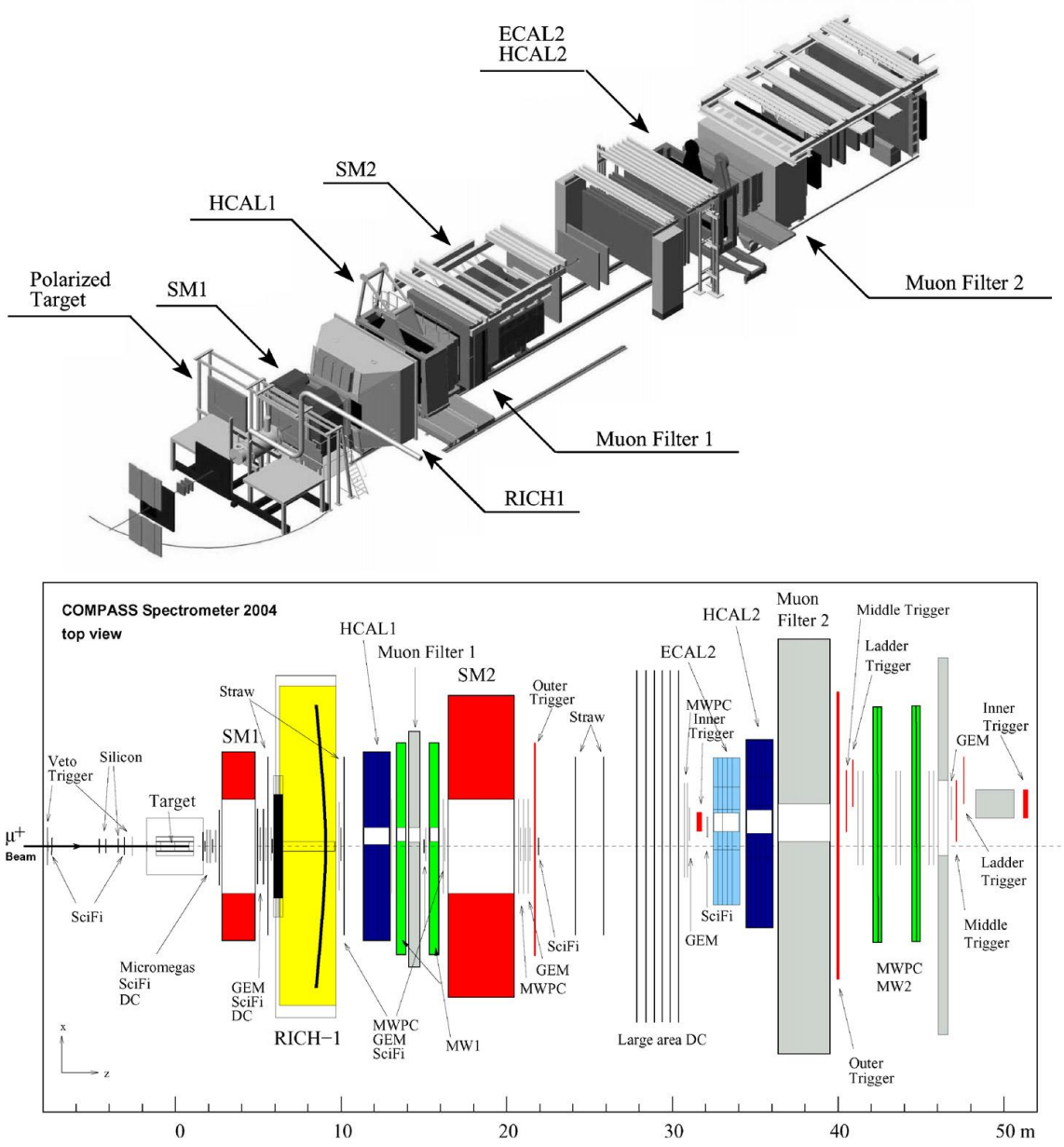

Figure 3.7 - Compass 2004 apparatus artistic view (top), and schematic top view of the experimental setup (bottom) [14].

Briefly, the COMPASS experimental apparatus comprises the following elements:

Beam line

The CERN SPS beam line M2 can be tuned for either high-intensity positive muon beams up to $190\ GeV/c$ or high intensity hadron (mainly proton or mainly pion, positive or negative) beams up to $280\ GeV/c$.

Polarized target

Allows spin asymmetry measurements using muon beam.

Large Angle Spectrometer (LAS)

This spectrometer has been designed to ensure $\pm\ 180\ mrad$ polar acceptance, and it is built around a dipole magnet (SM1). It includes a RICH detector (RICH-1, where relies our interest, and which is explained in section 3.4), with large transverse dimensions to match the LAS acceptance requirement, which is used to identify charged hadrons with momenta ranging from a few Gev/c up to approximately $60\ GeV/c$. Additionally, it contains a large hadron calorimeter (HCAL1), used to detect outgoing hadrons, and for trigger formation. The spectrometer is completed by a muon filter.

Small Angle Spectrometer (SAS)

The SAS is built to detect particles at small angles ($\pm\ 30\ mrad$) and momenta of $5\ GeV/c$ or higher. In analogy with the LAS, it is too built around a dipole magnet (SM2), and it includes an electromagnetic calorimeter (ECAL2), used to detect photons and neutral pions, a hadron calorimeter (HCAL2), used for hadron detection and trigger formation, and is completed by a muon filter.

Tracking Detectors

These detectors aim to track crossing particles. Because the particle flux varies transversely with the distance to the beam axis, under the overall spectrometer acceptance, it is important to provide detectors that match with the requirements at different distances from the beam axis. Far from the beam, the resolution constraint can be relaxed, but larger areas are required. The near-beam and beam regions, cover smaller areas, but are more demanding in rate and time/spatial resolution capabilities. This results in the sub-division into 3 groups of trackers:

- Very Small Area Trackers (VSAT)

Small size detectors, covering the area in and around the beam, which must combine high flux capabilities and excellent space and time resolutions. Scintillation fibres and silicon microstrip detectors are used to provide the imposed requirements.

- Small Area Trackers (SAT)

Medium size detectors, featuring high space resolution and minimum material budget, applied for distances larger than $2.5\ cm$ from the beam. The SAT comprises gaseous detectors for such purpose, namely triple-GEM detectors, and Micromegas.

- Large Area Trackers (LAT)

LAT consist of large area detectors, placed at large angles, capable of good spatial resolution. They include drift chambers, straw drift tubes and MWPCs.

Muon Filters

Muon filters (MW1 and MW2) consist of detectors to identify scattered muons. They comprise an absorber layer, which is preceded and followed by tracker stations. The role of the absorber is to stop incoming hadrons, while letting muons go through. Muons are positively identified when a track can be reconstructed in both set of trackers.

Trigger System

The trigger system consists of several dedicated components all along the experiment, in addition to the triggers from the hadronic calorimeter. The main purpose of this system is to distinguish a good event candidate in a highly crowded environment, within a very small time ($< 500\ ns$ [14]), and low dead time. It provides also the signal for the detectors front-end electronics to start the data acquisition.

3.4. RICH-1

RICH-1 is a Ring Imaging Cherenkov detector [14,64,93,94], which is a key element of COMPASS Large Angle Spectrometer, and the main responsible for hadron identification in the experiment.

The detector, in operation since COMPASS' commissioning in 2001, is based in a mirror focused RICH configuration, with minimum material budget over the spectrometer's acceptance, and its scheme is illustrated in **Figure 3.8**.

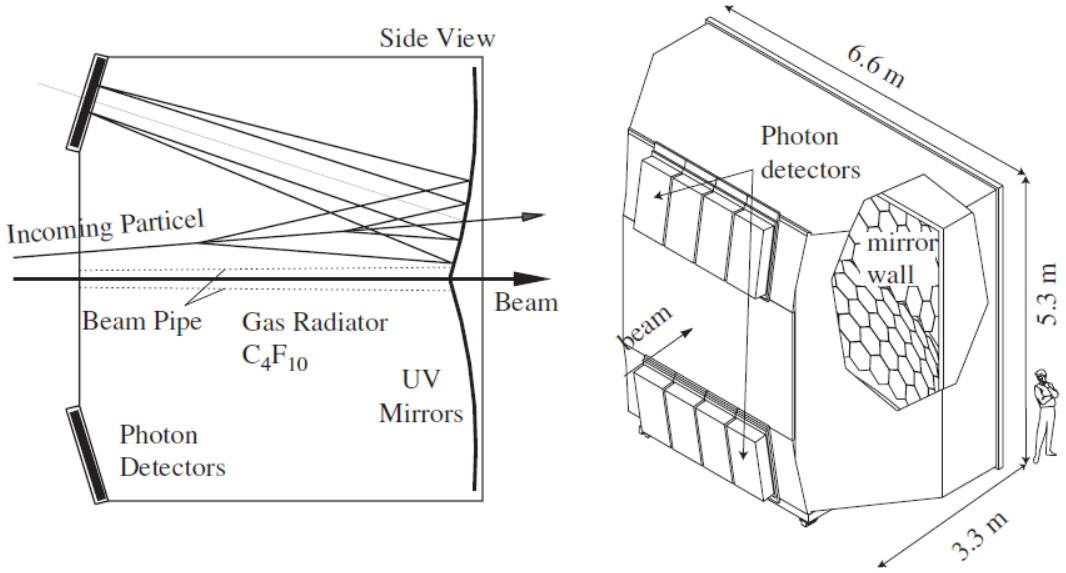

Figure 3.8 – COMPASS RICH-1: Operation principle (left); Artistic view (right) [14].

It covers wide momentum range for particle identification, from a few GeV/c up to $60\ GeV/c$, along 3 meters long, in order to maximize the emission of Cherenkov photons from the particles crossing the detector. The vessel dimensions match also with the overall spectrometer's acceptance ($\pm 250\ mrad$ horizontally $\pm\ 180\ mrad$ vertically). Accordingly to this specific RICH configuration, charged particles crossing the gaseous radiator, emit Cherenkov light that is then reflected on the spherical converging mirrors, into the set of photon detectors which are located outside the spectrometer acceptance.

Gas and Gas System.

The RICH-1 comprises a radiator vessel with a length of approximately $3\ m$ and a volume of about $80\ m^3$, filled with C_4F_{10} in a gas phase as radiator. The choice of this radiator is related with its very low chromaticity and its refractive index ($n\ =\ 1.0015$ for $7\ eV$ photons) allowing hadron identification from few GeV/c up to $60\ GeV/c$ [14].

The radiator transparency in the range of wavelengths comprehended between 160 and $200\ nm$ is essential for RICH-1 operation, as the photon detectors, coupled with CsI, are highly sensitive only in this range. These limitations impose a very low level of contamination of impurities such as water and O_2. These impurities, can be kept as low as $1\ ppm$ and $3\ ppm$ respectively, and it is achieved by a cleaning and filtering procedure applied by the gas system before the insertion of the gas into the vessel. This gas system consists of a closed circuit system, that additionally to circulating the gas between the vessel and the storage tank, allows to avoid the gas stratification inside the vessel and controls the radiator pressure in order to avoid mechanical stress to the thin vessel surfaces in the acceptance region and to the photon detector windows.

In order to minimize the number of photons emitted by excitation processes of the gas molecules, induced by the beam muons, a $10\ cm$ diameter pipe filled with Helium is positioned inside the vessel, around the beam axis, to absorb such photons.

Mirror System

The optical system of RICH-1 [93] that defines its mirror focused configuration is defined by two large spherical converging mirrors, with a radius curvature of $6.6\ m$. In order to avoid the photon image of being focused inside the spectrometers acceptance, the curvature centres of the two mirrors are vertically placed at $\pm\ 1.6\ m$ from the beam axis.

The two mirror surfaces form a mosaic type composition, comprising 116 pentagonal or hexagonal mirrors, covering an area of approximately $21\ m^2$. These mirrors are very thin in order to limit the multiple scattering of particles crossing the detector, and are made of $7\ mm$ of borosilicate glass covered with a layer of UV reflecting material (approximately $80\ nm$ of Al). Additionally, they include another layer of $30\ nm$ of MgF_2 to protect the Al surface material from water vapour and O_2 contamination. The total material is about 5.5% of radiation length, and its reflectance is above 80% in the wavelength range of 160 to $200\ nm$.

The mirrors are supported in the nodal points of a minimalist net-like mechanical structure, which aims to minimize the amount of material in the spectrometer acceptance. **Figure 3.9** shows the reflecting surfaces of the spherical mirrors, and their mechanical supports.

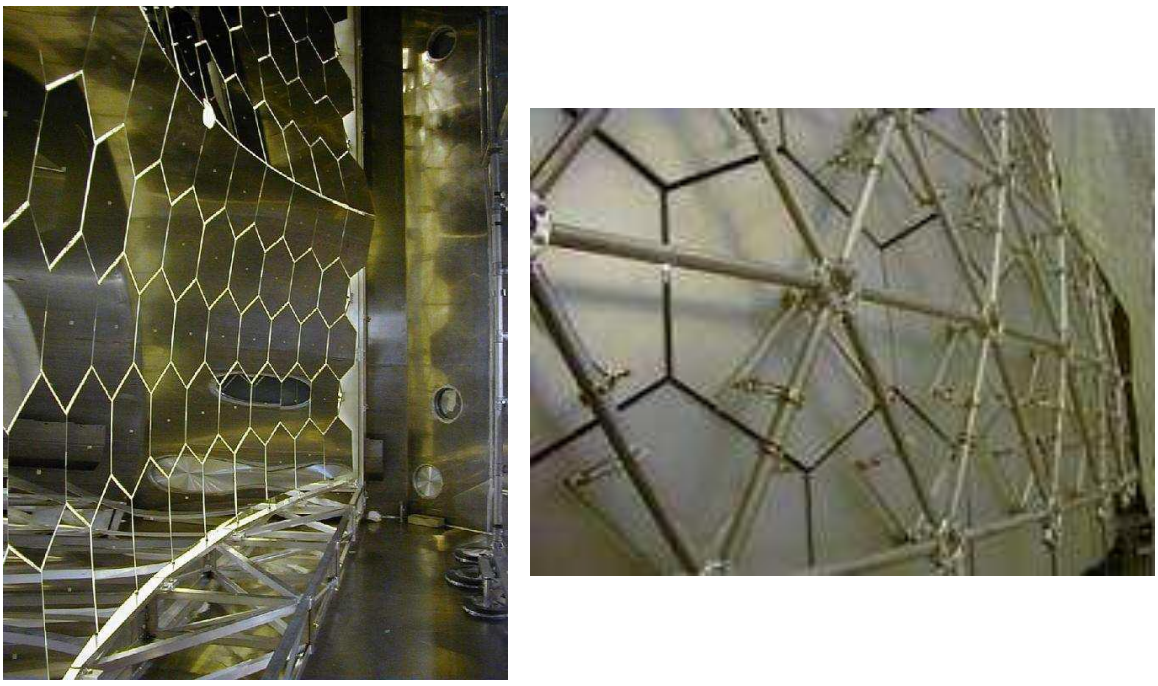

Figure 3.9 – Picture of the reflecting surfaces of the spherical mirrors (left); Mechanical support structure of the mirrors (right).

Photon Detectors

Originally, the RICH-1 photon detection system consisted of a second generation gaseous photon detector, comprising 8 large size MWPCs ($567 \times 1152\ mm^2$), operated with CH_4 gas at atmospheric pressure, transparent to the VUV photons, and separated by the radiator gas by a fused silica window. Each MWPC was coupled to a $500\ nm$ thick CsI photocathode, covering a total area of around $5.2\ m^2$, and its surface (of each chamber) was segmented in 72×72 pads of $8 \times 8\ mm^2$, determining the spatial resolution of the photon detector. This detector configuration is shown in **Figure 3.10**.

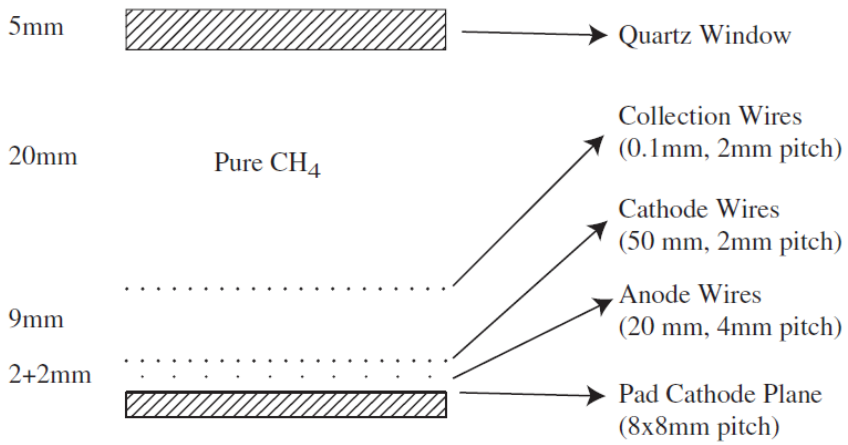

Figure 3.10 – Scheme of the CsI-MWPC RICH-1 photon detector [14].

This photon detector configuration was under operation up to autumn 2004. Nonetheless, large uncorrelated background present in the RICH-1 environment was limiting the global resolution on the measured Cherenkov angle, and a foreseen increase, at the time, of the beam intensity and trigger rates on COMPASS, led to an upgrade of the RICH-1 photon detector, between autumn 2004 and spring 2006. Such upgrade, consisted on substituting the central region of the photon detectors (totalizing 25% of the total photon detector surface) with a new fast detection system [95–97]. The new central photon detection system was based in 576 Multi Anode Photon Multipliers (MAPMTs) Hamamatsu[4] R7600-03M16, with 16 channels and UV extended glass window. This system was coupled with a fused silica lens telescope (comprising a field lens and a condenser lens), which was required to provide a large demagnification factor (to enlarge the effective active area of the photon detectors) and to have a wide angular acceptance. This telescope coupled with the MAPMT is schematized in **Figure 3.11** (left), while **Figure 3.11** (right) shows the distribution of 144 field lenses over a $600 \times 600\ mm^2$ frame.

[4] Hamamatsu Photonics K.K., Japan. http://www.hamamatsu.com

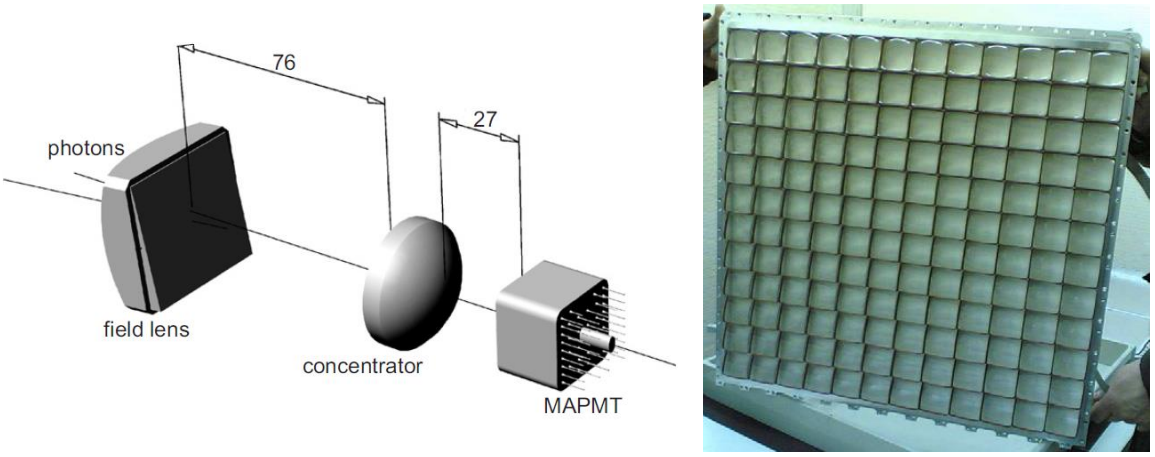

Figure 3.11 - Scheme of the two-lens telescope system coupled to the MAPMT (distances in mm) (left) [98]; Frame holding a set of 144 field lenses that make part of the telescope systems, coupled to the MAPMTs (right) [97];

A visual representation of the area that was upgraded, can be found in **Figure 3.5**, where it's exemplified the ring reconstruction from RICH-1, and where the upgraded area is emphasised.

During the referred update, the remaining 75% of the photon detector area were kept untouched, having just their readout system upgraded to as faster system.

Thus, the MWPCs are connected to APV25-S1 chips, which are a 128 analogue channel preamplifiers/shapers, and whose peaking time is adjustable in a wide range from 50 to $300\ ns$, opening the possibility to use to read ''slow'' detectors such as MWPCs. They are coupled with ADCs to provide digital signals [99].

Regarding the MAPMT's readout, they are connected to a fast digital electronics system based on the MAD4 preamplifier/discriminator, which is characterized by small noise level ($5 - 7\ fC$), and can operate up to approximately $1\ MHz$ per channel. The MAD4s are connected to a digital card called DREISAM, which fully exploits the good time resolution of the MAPMTs by presenting a time resolution of approximately $110\ ps$, and is capable of operating with higher rates compared to MAD4. **Figure 3.12** shows the assembly of the whole readout system to the photon detectors, in a $600 \times 600\ mm^2$ frame [98].

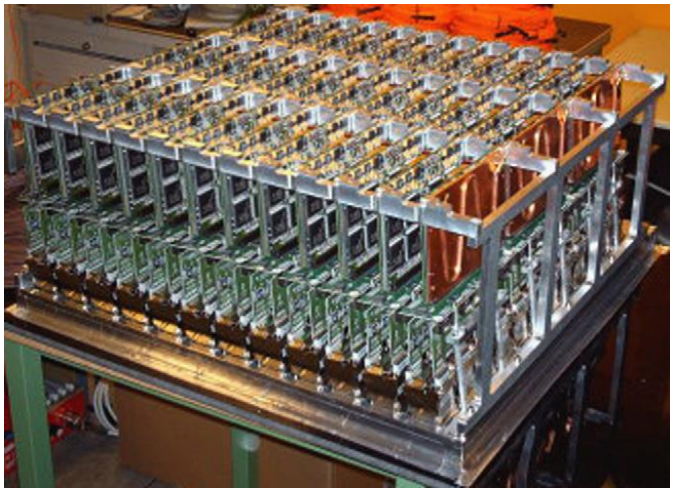

Figure 3.12 – Complete assembly of the digital readout system, coupled to the photon detectors, comprising the two-lenses telescope systems and the MAPMTs [98].

All the electronic components of the readout system are mounted directly on the detector, in order to increase the compactness of the setup. Additionally, the readout is coupled with a copper plate for electromagnetic shielding and cooling.

3.5. COMPASS RICH-1 Upgrade

The majority of the topics of the COMPASS physics programme that were performed so far, required hadron identification, which was provided by RICH-1 detector. Its performance, since its upgrade in 2006, under demanding conditions, was favourable, mainly due to the capabilities of the MAPMTs, located in the most populated light region, standing high light intensities and high rates.

Despite this good performance, in 2010, an extension of the COMPASS programme has been approved by the CERN Research Board [11], and in January 2013 a new Memorandum of Understanding was signed, in order to fulfil this programme.

Such enlargement of the physics programme of the COMPASS experiment, requires the maintenance of the RICH-1 counter at the present performance level over the future years, and in significantly more challenging and demanding operating conditions related to increased rates.

Although the central area photon detectors, comprised by the MAPMTs, can deliver such level of performance over the years and under higher rates, the MWPCs suffer significant ageing under higher photon fluxes, as well as their performance is limited by high rates, like it was evoked in section 2.2. A RICH-1 upgrade, to operate under the referred condition, signifies then an upgrade of the MWPCs installed in the peripheral area. This upgradable area, that currently comprises the MWPCs, is schematically illustrated in **Figure 3.13**, empathising also the MAPMT detectors in the central area.

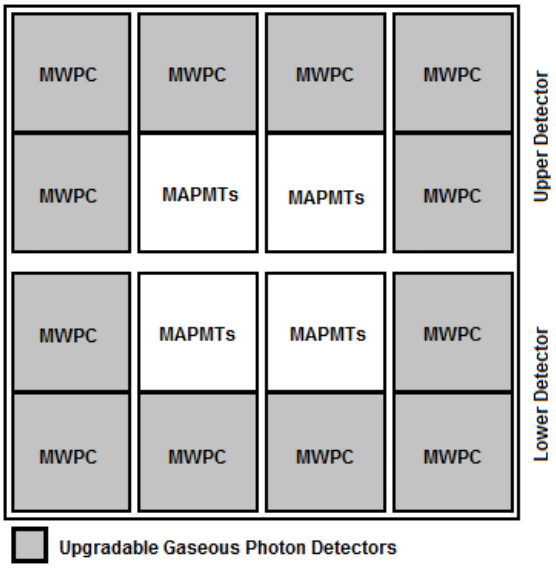

Figure 3.13 – Scheme of the disposition of MWPCs and MAPMTs as RICH-1 photon detectors. The shaded area, corresponding to 75% of the total photon detection area, illustrates the GPD upgradable area, divided in 12 $600 \times 600\ mm^2$ photon detectors.

This upgrade corresponds to the motivation to perform the studies described along this work, and allows to connect chapter 2 (and in particular section 2.3) to a real and well defined application. As described in section 2.3, THGEM based detectors seem capable of meeting the requirements to provide a solution for the RICH update, which are:

- Simple, robust and cheap basic elements, compared with MAPMTs, to allow a large area covering;
- Signals generated by drifting electrons, to provide a good time resolution ($\sim 10\ ns$);
- Closed geometry to avoid photon feedback;
- Large gain ($\sim 10^5$) to guarantee good single photon detection;
- Reduced IBF to the CsI photocathode ($< 5\%$) to increase stability and avoid aging problems (such reduction is needed to compensate the increase in the number of ions, compared to the MWPC, consequence of the increase in gain);
- Good stability of the response both in time and under different irradiation conditions.

Therefore, studies are performed envisaging the replacement of the MWPCs in RICH-1 by THGEM-based photon detectors, coupled with CsI photocathodes, with a sensitive area of $600 \times 600\ mm^2$, and with readout pad sizes equal to ones used in MWPC ($8 \times 8\ mm^2$).

4. THGEM-based Detectors

The development of third generation gaseous photon detectors based in THGEM structures for RICH applications, relies essentiality in two different aspects: the study and optimization of the THGEMs geometrical parameters, and the assembly of these structures in multi-layer arrangements, with optimized drift, transfer and induction fields.

In the regard of the mentioned development, this chapter aims to understand THGEM structures and detectors, not seeking their fully optimized performances, but searching instead to study how the multiple variables influence the behaviour of such devices, based on the overall assumption that high gains up to 10^6 [79,87] are possible in triple-layer THGEM configurations.

4.1. Experimental Considerations

All the studies presented along this chapter were performed under laboratorial conditions. The characterization of THGEM-based detectors was achieved with ionizing particles or single photoelectrons. The ionizing particles were generated using a $5.9\ keV$ ^{55}Fe soft X-ray source, generating approximately 300 primary electrons. Single photoelectrons were obtained from the conversion of UV light. Two UV light sources were used for such purpose: a UV LED type LED-255 by Seoul Optodevice[5] which provides a light spectrum peak around 255 nm and a spectral line width better than $20\ nm$ FWHM; and a PLS 265-10 pulsed LED with spectral response centred at $265\ nm$ and controlled by the PDL 800-D by Picoquant[6], capable of delivering pulses as short as $600\ ps$ and with pulse repetition rate up to $40\ MHz$.

Although the referred wavelengths are outside the range of wavelengths where CsI shows a good quantum efficiency, the photoelectron extraction can still happen by increasing the light intensity. Even though this solution is not an option under Cherenkov light, were the number of photons cannot be increased, it is a feasible solution in laboratorial conditions using UV LEDs were an increase of the intensity leads to an increase of photon flux. If the intensity is high enough, photoelectron extraction can happen directly on the copper surface of the THGEM, allowing the operation in single photoelectron mode, without the coupling of the CsI photocathode. This approach is of particular interest in laboratorial context, as it allows an easier handling of the THGEMs, with no constrains of their exposure to air.

Because tests are performed without the use of the CsI photocathode, for the majority of the applications, methane based mixtures, previously used to maximize the photoelectron extraction efficiency, can be replaced by non-inflammable gas mixtures, allowing an easier operation in laboratorial conditions. In this regard, and although specified along each experiment, the standard gas mixture for laboratorial tests is Ar/CO_2, typically at a ratio of $70:30$. The provision of the gas mixture, whatever it is, is done through a “once-through” gas circuit type, at atmospheric pressure.

[5] Seoul Optodevice Co., Ltd, Seoul, South Korea. http://www.seoulviosys.com/
[6] PicoQuant GmbH, Berlin, Germany. http://www.picoquant.com/

The gas mixture can be achieved directly by mixing the desired ratio of each independent gas (argon, methane or carbon dioxide) through a Bronkhorst[7] gas flow meter, or in the specific case of Ar/CO_2 $(70:30)$, a premixed mixture can be used.

The electric drift field is defined by a planar set of parallel wires placed above the upper THGEM. The wires typically have a diameter of $100\ \mu m$, with a pitch of $2\ mm$. Such parameters permit a uniform drift field, while at the same time they allow an optimized transparency to radiation.

In what regards the detector's signal collection, a single-channel electronic readout chain is used to collect the amplitude spectra of the signal. For this purpose, a Cremat[8] CR-110 charge sensitive preamplifier is connected to the set of anode pads, connected in parallel. The preamplifier is then connected to an Ortec[9] 672 (or Ortec 590A) shaping amplifier, which is further digitised by an Amptek[10] MCA8000A multichannel analyser. Due to the connection of the anode pads in parallel, the imaging capabilities of the detector are disabled, allowing only its characterization.

Additionally, a good signal to noise ratio is mandatory, so that the threshold setting does not result in critical measurement issues. In this regard, reasonable high gains, and a good grounding of the detector are essential in order that the good ratio between signal and noise is verified.

4.2. THGEM Detectors

4.2.1. THGEM: The Key Element

The response of THGEM-based detectors depends, in a first stage, on the response of its elementary blocks individually. This is the reason why, typically, each THGEM is characterized independently from each other, in single layer configurations. Although such experimental characterization is essential, it does not allow to understand the intrinsic operation of the structure. Electrostatic calculations and simple simulations applied to small sections of a single THGEM help in further understanding of the chosen parameters and operation modes.

The choice of parameters such as rim, thickness and hole diameter can easily be understood by the results presented in section 2.3.2, knowing that gain increases with an increasing thickness of the structure, with the decrease of the holes diameter, and with the presence of big rims. Depending on the application, the optimized parameters can, therefore, be easily predictable. Nonetheless, one point remains unanswered: which is the optimized ratio between the holes diameter and the pitch? This ratio has even more interest for THGEMs suitable for coupling with a

[7] Bronkhorst High-Tech B.V., Ruurlo, The Netherlands. http://www.bronkhorst.com/
[8] Cremat, Inc., Watertown, MA, USA. http://www.cremat.com/
[9] ORTEC - Advanced Measurement Technology, Inc., Oak Ridge, TN, USA. http://www.ortec-online.com/
[10] Amptek, Inc., Bedford, MA, USA. http://www.amptek.com/

photocathode layer, where in one hand, a small ratio (smaller holes compared to the pitch) is preferable to allow a bigger active area for the photocathode deposition, and on the other hand, a big ratio (holes size in the order of the dimension of the pitch) is recommended in order to maximize the field at the CsI surface to allow a maximized photoelectron extraction. Although typically the used ratio is of $1{:}\,2$, the following calculations are meant to prove why.

The values of the calculated relative active area, for different ratios between hole diameter and the pitch are presented in **Table 4.1**

Table 4.1 – Relative active area of a THGEM surface as function of the ratio between hole diameter and pitch.

Ratio Hole diameter : Pitch	Relative Active Area	Ratio Hole diameter : Pitch	Relative Active Area
0:10	100%	5:10	77.33%
1:10	99.09%	6:10	67.35%
2:10	96.37%	7:10	55.56%
3:10	91.84%	8:10	41.96%
4:10	85.49%	9:10	26.54%

These calculations point out, as it would have been expected, that in this regard, smaller holes compared to the pitch are preferable, as it allows a larger active area. With the increasing of this ratio, a fast decrease in the relative active area is observed.

Additionally, as it was mentioned in chapter 2, the photoelectron extraction on a CsI photocathode applied in reflective mode, is maximized when the magnitude of the electric field component, orthogonal to the photocathode, is higher than approximately $1\ kV/cm$, and points in the direction of the THGEM (defined as a negative field according to the referential adopted all along this work). In this regard, the z component of the electric field, $10\ \mu m$ above a $0.4\ mm$ thick THGEM, with $0.8\ mm$ pitch and no rim, and with a dipole voltage of $1500\ V$, was calculated using Ansys, a finite element method software. The calculations were performed for a set of 4 holes diameter 0.24 0.32 0.40 and $0.48\ mm$, corresponding to a ratio of $3{:}\,10$, $4{:}\,10$, $5{:}\,10$ and $6{:}\,10$ respectively. The results for each unit cell (the minimum geometrical unit necessary to reproduce the whole THGEM), showing the area at which the z component of the electric field is above the defined threshold of $1\ kV/cm$ (in magnitude), are presented in **Figure 4.1**, for a drift field of $0\ V/cm$ and an induction field of $3\ kV/cm$.

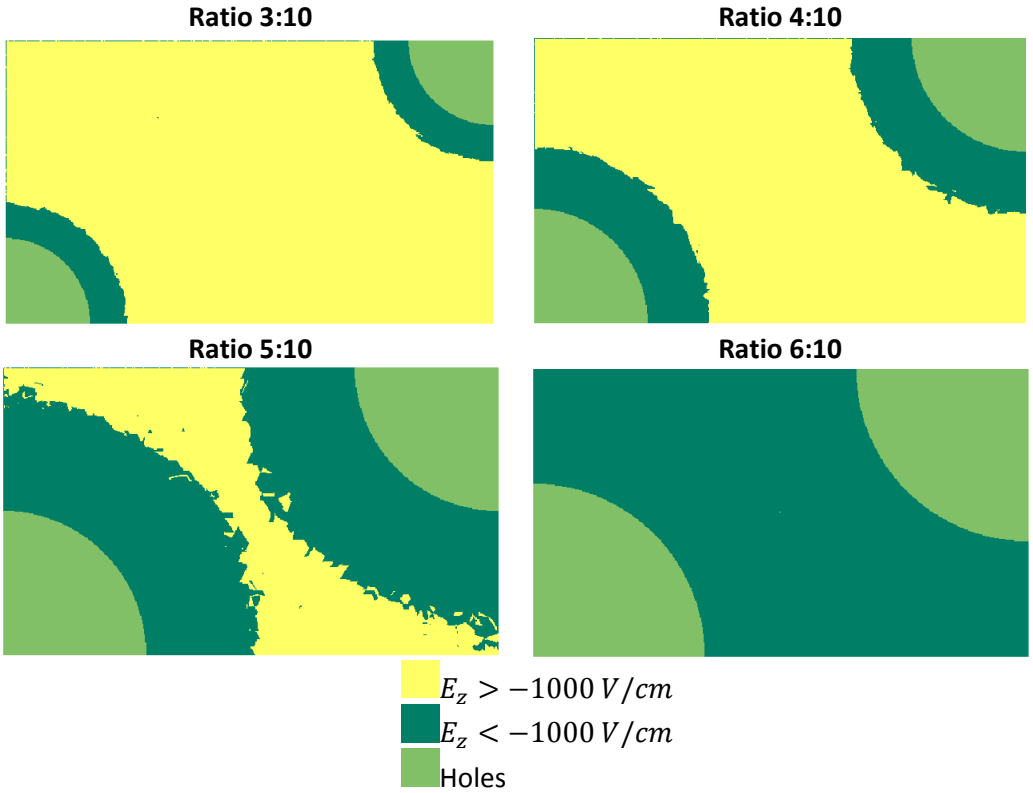

Figure 4.1 – Dependency of the ratio "hole diameter: pitch", in the relative area of the upper surface of the THGEM with $E_z < -1000\ V/cm$. The results correspond to electrostatic calculations, $10\ \mu m$ above the surface of a THGEM, with thickness of $0.4\ mm$, pitch of $0.8\ mm$, no rim, and variable hole diameter, with $\Delta V = 1500\ V$, $E_{drift} = 0\ V/cm$ and $E_{induction} = 3\ kV/cm$.

The results show that ratios up to $4:10$ lead to an insufficient electric field strength in the majority of the THGEM surface to allow a good photoelectron extraction efficiency. In the same conditions, a ratio of $5:10$ shows a significant increase of the area with a desirable electric field, but still shows a "dead" area in distances far from the holes. In ratios bigger than $6:10$, for the referred thickness and ΔV, the "dead" area is insignificant or inexistent.

It is important to point out, that for the same thickness, the field is function of the applied ΔV. Although the presented calculations refer to a $\Delta V = 1500\ V$, realistic results of the operation of $0.4\ mm$ thick THGEMs in methane mixtures, allow an applied ΔV of at least $1600\ V$, leading to a minor or inexistent "dead" area in the ratio $5:10$. This fact, associated to a relative active area of 77% represent the reason why this ratio is the chosen for THGEM structures to be coupled with a CsI photocathode.

Although these issues represent no constrains for the choice of the parameters of the THGEMs to be used in second and third stages of multiplication, the ratio is often kept unchanged. For instance, small ratios can lead to a big charge dispersion due to electron diffusion, which can affect the spatial resolution, and big ratios, can create regions of high density of charge, which can lead to electrical discharges.

The results shown in **Figure 4.1** were achieved under the assumption of a $0\ V/cm$ drift field. This means that the field at the surface of the THGEM is consequence only of the applied dipole field. When a drift field different from zero is applied, the electric field at the surface of the THGEM becomes a function of the superposition of the drift field and the dipole field. **Figure 4.2** shows the simulated electron drift lines, starting from the upper surface of a THGEM with no rim, $0.4\ mm$ of hole diameter, $0.4\ mm$ thickness, and $0.8\ mm$ pitch, with an applied induction field of $3\ kV/cm$ and a $\Delta V = 1500\ V$. The results in the figure aim to show the dependence of the photoelectrons, represented by the electron drift lines, under the influence of different drift fields, in an Ar/CO_2 (70: 30) mixture.

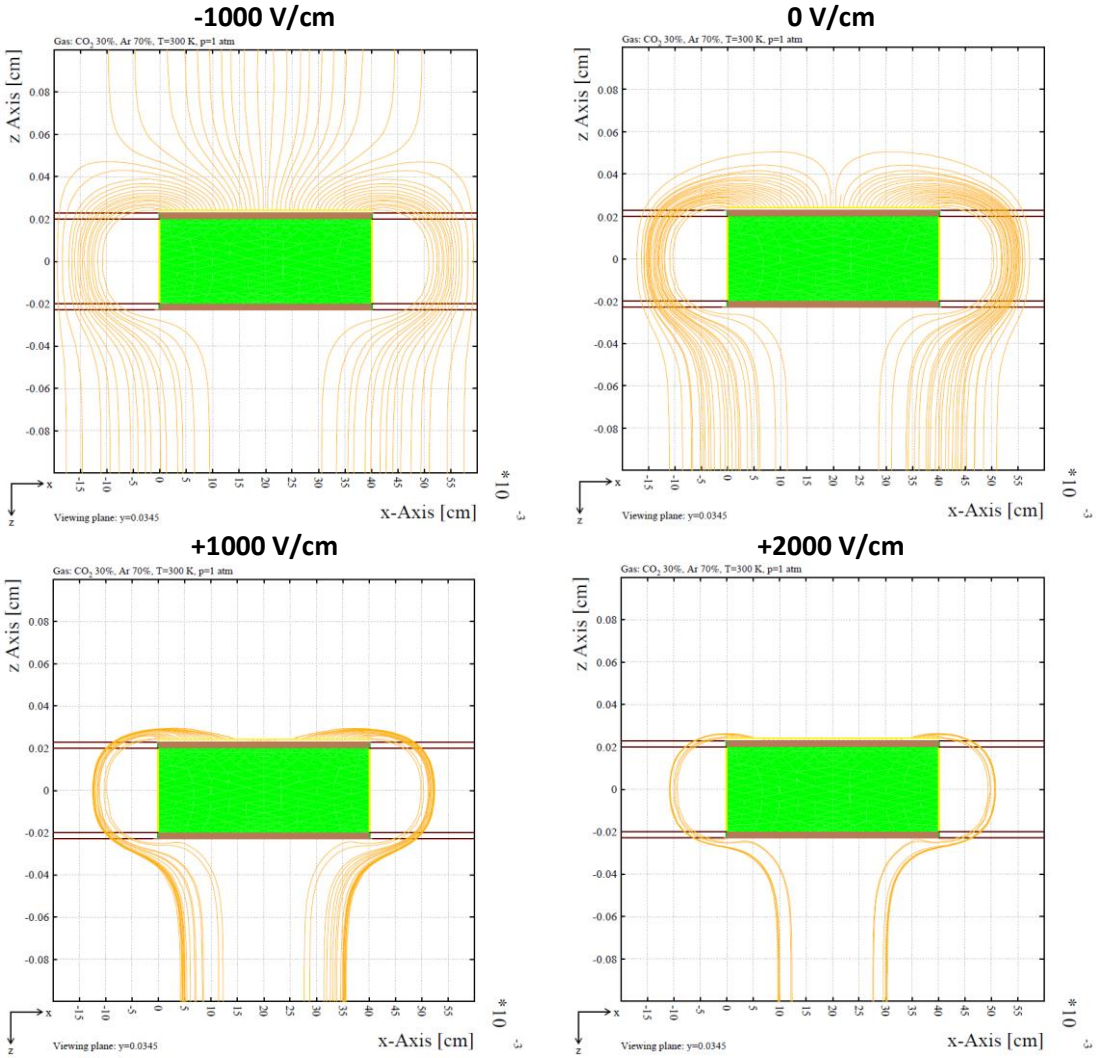

Figure 4.2 – Electron drift lines, connecting two consecutive holes, at the upper surface of a THGEM with no rim, $0.4\ mm$ of hole diameter, $0.4\ mm$ thickness, and $0.8\ mm$ pitch, with a dipole voltage of $1500\ V$, for a set of 4 drift fields ($-1\ kV/cm$, $0\ V/cm$, $+1\ kV/cm$ and $+2\ kV/cm$), illustrating the effect of the drift field in the photoelectrons created at the photocathode.

The simulated electron drift lines represent the expected average trajectory of electrons, released $10\ \mu m$ above the copper surface, along a straight line connecting two consecutive holes.

Following the suggested orientation of the detectors, it is considered as positive electric field when the direction of the field points towards the top of the detector.

In the situation of an applied negative drift field, the photoelectrons at the surface of the THGEM, mainly the ones far from the influence of the dipole field, tend to be driven away from the THGEM. When a positive drift field is applied, photoelectrons tend to be backscattered. This phenomena is more visible for areas with lower influence of the dipole field, but such influence tends to decrease as the magnitude of the drift field increases. When an $E_{drift} = 0\,V/cm$ is applied, the effect of this field is lost, and electrons are once again just dependent on the dipole field, which represents the optimal solution, strictly from the point of view of photoelectron extraction. This corresponds to the reason why along this work, studies performed with UV light are done under a $0\,V/cm$ drift field.

As the dipole field represents then, in this situation, to the most important variable under a $E_{drift} = 0\,V/cm$, **Figure 4.3** (left) shows the z component of the electric field for the same structure under the same conditions, also $10\,\mu m$ above the copper surface.

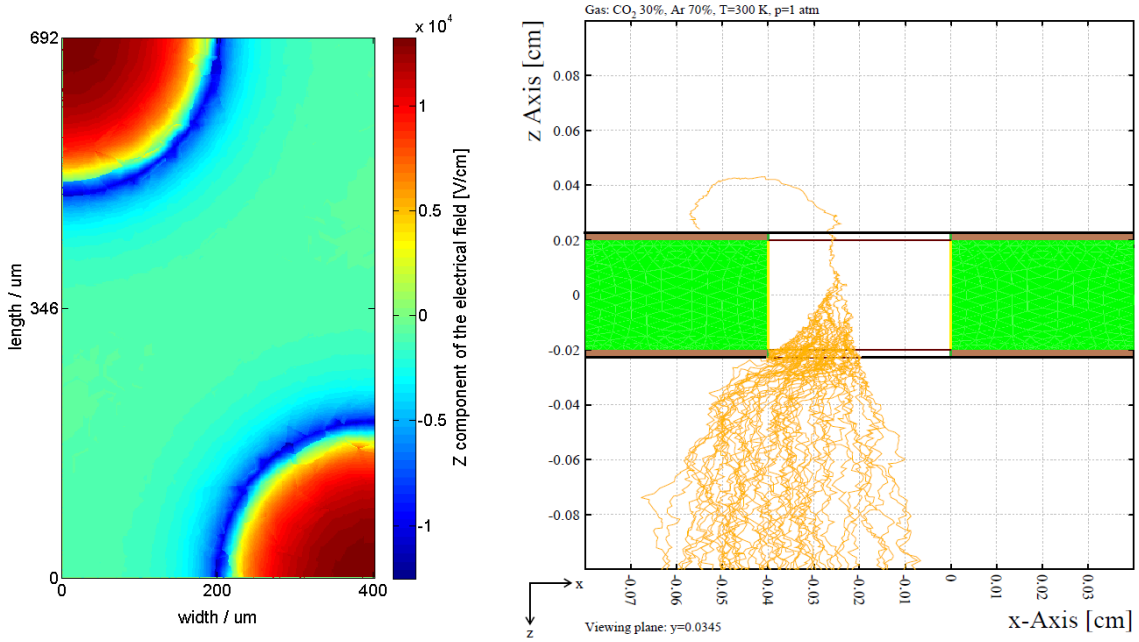

Figure 4.3 – z component of the electric field, for the mentioned THGEM structure, for a $E_{drift} = 0\,V/cm$ and $\Delta V = 1500\,V$, $10\,\mu m$ above the upper metallic surface of the THGEM (left); representation of a simulated photoelectron at the surface of the THGEM, illustrating the avalanche multiplication process (right).

Such field shape has an important role in the focusing of electrons towards the holes. A negative component of the field near the hole border is responsible for moving electrons slightly away from the edges of the copper, avoiding their collection by the metallic surface. Electrons are then focused into the strong positive electric field inside the holes, where the field is strong enough to induce ionizations. An example of such process is represented in **Figure 4.3** (right), where a simulated

photoelectron is released from the THGEM surface, and focused towards the hole, exemplifying the avalanche charge multiplication process.

Figure 4.4 allows a better understanding of the development of a charge multiplication avalanche inside a hole, which is illustrated in **Figure 4.3**, by representing the projection of ionizations along two different planes.

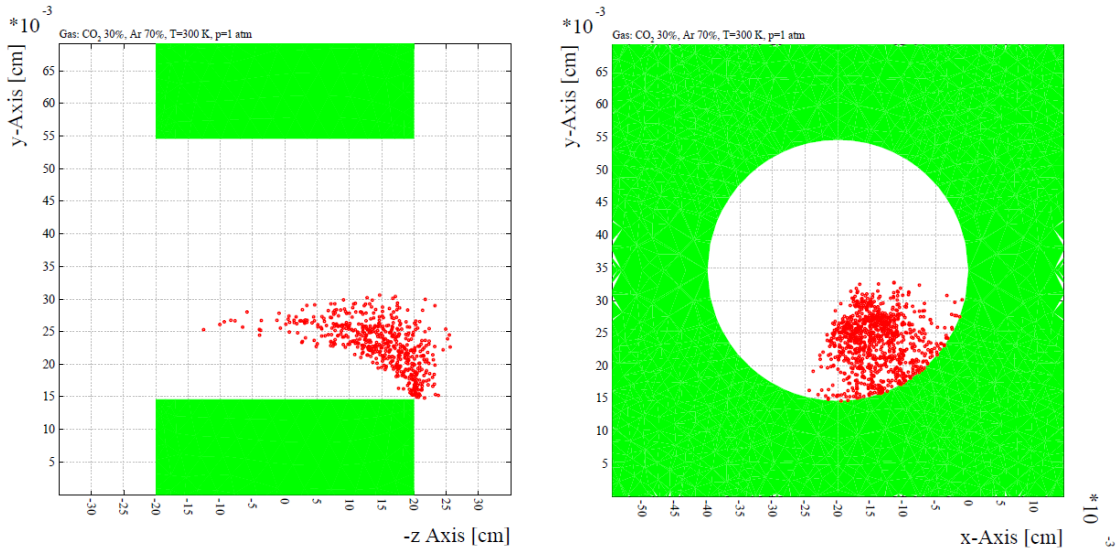

Figure 4.4 – Distribution of the simulated ionizations of the avalanche process inside the THGEM hole, due to a single event: Projection in the plane longitudinal to the hole (left); Projection in the place transverse to the hole (right). The red dots correspond to the spatial coordinates of the ionizations, while the green area corresponds to the dielectric.

The projection of the ionizations in the plane longitudinal to the hole allows to understand that the avalanche is comprehend mostly in the second half of the dielectric, with ionizations barely happening outside the confinement of the hole. This shows the importance of the holes in such concept of multiplication structure, along with the importance of the thickness of the THGEM in what regards gain, as thicker pieces allow a longer length over which ionizations are possible.

Additionally, the projection of the ionizations into the transverse plane of the hole, shows the radial distribution of such interactions within the hole. The interpretation of this simulation shows that tendentiously, the majority of the ionization happen in a mid-distance between the hole centre and the dielectric edges.

4.2.2. THGEM Characterization

As a consequence of the importance of each individual THGEM in the overall THGEM-based detector, the characterization of each individual piece is advised. This characterization can be done with two specific purposes. First, to study the role of all the possible variables in the performance of the structure. Secondly, after knowing the expected behaviour of a piece, based on its

parameters, a THGEM can be characterized in order to evaluate the quality of the piece, by checking its capability of responding in the expected way. Although this chapter focus essentially in the first point, the second one is of fundamental importance, and it is required while performing the assembly of a THGEM-based detector. In this regard, over 50 pieces have been tested, starting with visual inspection in search of mechanical problems, passing through eventual post-production treatment, and ending in their characterization. This characterization presupposes initially the determination of the breakdown voltage, followed typically by the attainment of the gain variation curve as a function of the dipole voltage.

Following the intention of this chapter of studying mostly the effect of different variables, such as dipole voltages, and electric fields, in the performance of the devices, similar gain variation curves as a function of each of the nominated variables can be obtained.

Although the characterization of the effect of the THGEM parameters in the structure's performance was already introduced along section 2.3.2, additional studies regarding the dependence of thickness in gain, for different gas mixtures, were performed.

Such studies were performed in a single layer configuration, as schematically represented in **Figure 4.5**. These studies relied on THGEMs with an active area of $30 \times 30\ mm^2$, as illustrated in the same figure.

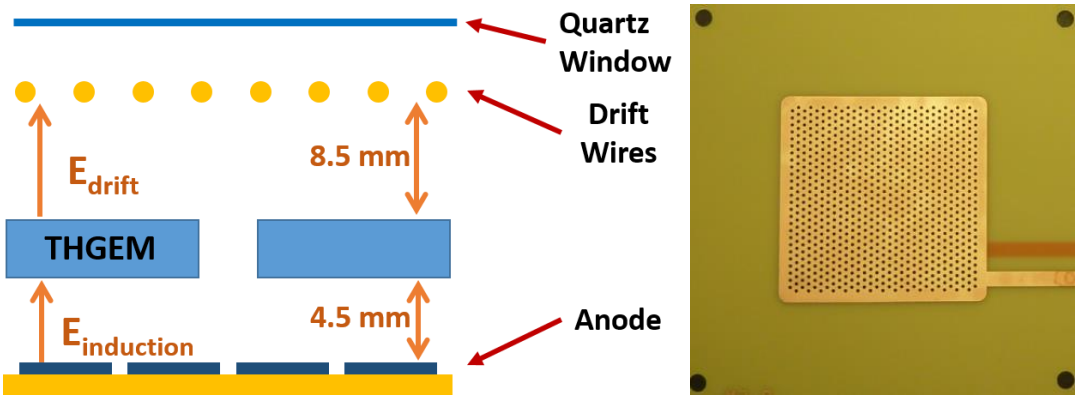

Figure 4.5 – Scheme of the configuration used to characterize the THGEM structures, emphasising the positioning of the THGEM comprehended between the anodic pads and the drift wires, along with the detector window. The field directions are represented by the direction of the arrows (left); $30 \times 30\ mm^2$ THGEM prototype (right).

The measurement of gain was achieved while irradiating the detector with pulsed UV light in a single photoelectron condition, with a $E_{drift} = 0\ V/cm$ and $E_{induction} = 1.67\ kV/cm$.

The detector's response to light, under the referred conditions, is an exponential distribution, as exemplified in **Figure 4.6**, for a THGEM with $0.6\ mm$ thickness, $0.4\ mm$ holes and $0.8\ mm$ pitch, with an applied $\Delta V = 1840\ V$, in a Ar/CO_2 $(70{:}\ 30)$ atmosphere.

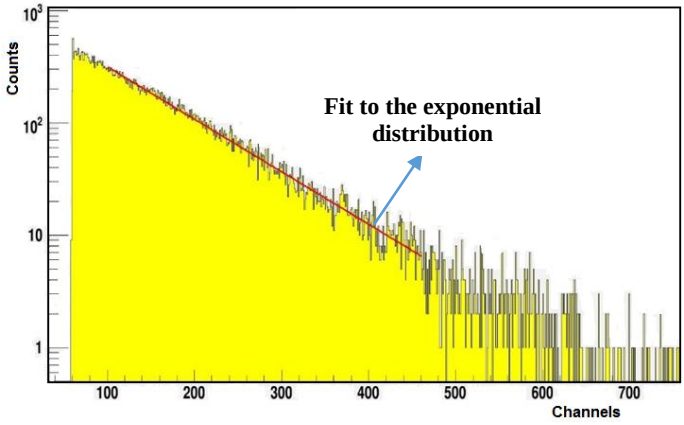

Figure 4.6 – Example of the exponential distribution for single photoelectrons signals, and its fit, obtained from a single THGEM $0.6\,mm$ thick, with holes diameter of $0.4\,mm$ and pitch of $0.8\,mm$, with a $E_{induction} = 3\,kV/cm$ and $E_{drift} = 0\,V/cm$, corresponding to a gain of 5800 at $\Delta V = 1840\,V$.

Although the amplitude spectra of single photoelectrons signals are Polya functions, at low gains (up to 10^5), the amplitude spectra can be approximated by an exponential curve [100]. In a charge calibrated amplitude spectra, the fit of the exponential distribution, allows the determination of the detector's gain.

Following these procedures, the following 3 THGEMs with different thicknesses were tested, for Ar/CO_2 $(75:25)$ and Ar/CH_4 (with different ratios) mixtures.

Table 4.2 - Geometrical parameters of THGEM A,B and C

THGEM	Rim /µm	Thickness /mm	Hole Diameter /mm	Pitch /mm
A	25	0.4	0.4	0.8
B	< 5	0.6	0.4	0.8
C	< 5	0.8	0.4	0.8

The result of the mentioned tests, performed under $E_{drift} = 0\,V/cm$ and $E_{induction} = 1.67\,kV/cm$, are presented in **Figure 4.7**, **Figure 4.8** and **Figure 4.9**, for THGEM A, B and C, respectively. The different gas mixtures are introduced along with the plots.

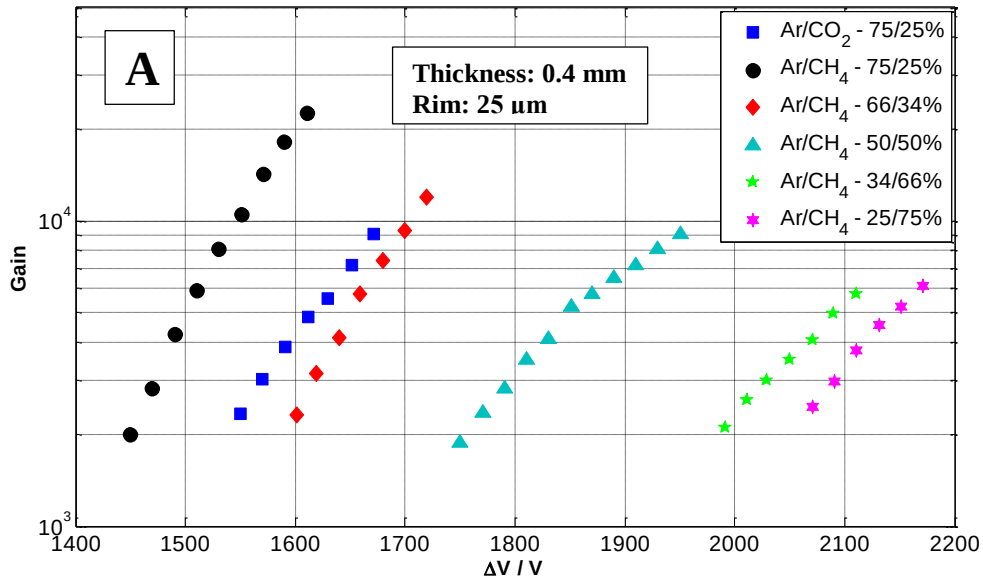

Figure 4.7 – Experimental gain achieved as function of the dipole voltage, for different gas mixtures, obtained for THGEM A, in single layer arrangement, based on the configuration of **Figure 4.5** [101].

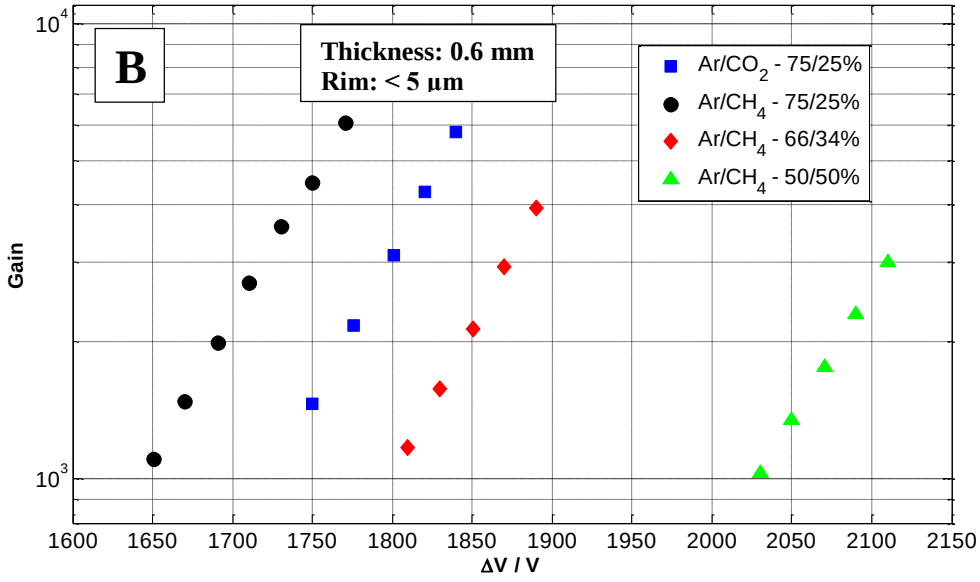

Figure 4.8 – Experimental gain achieved as function of the dipole voltage, for different gas mixtures, obtained for THGEM B, in single layer arrangement, based on the configuration of **Figure 4.5** [101].

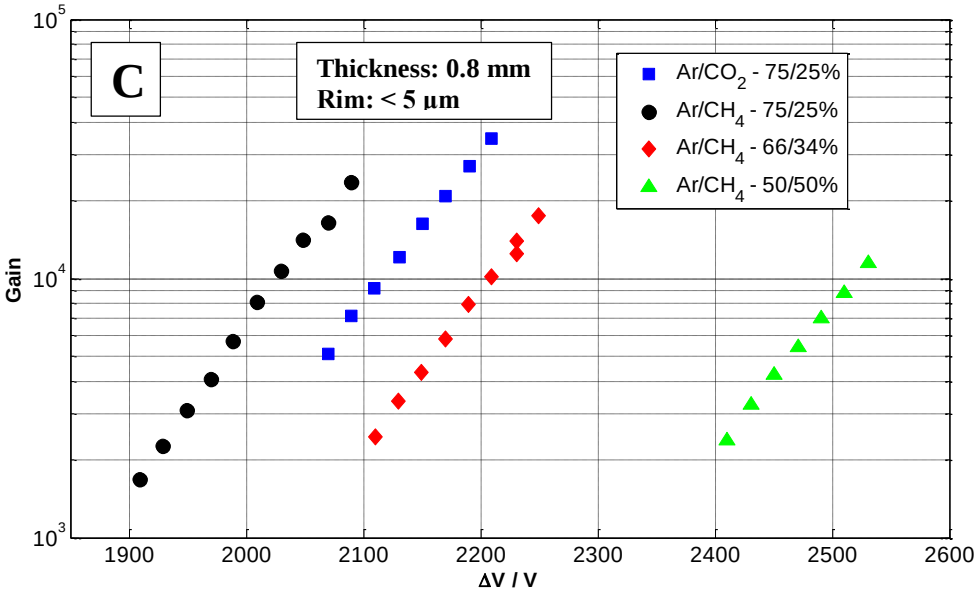

Figure 4.9 – Experimental gain achieved as function of the dipole voltage, for different gas mixtures, obtained for THGEM C, in single layer arrangement, based on the configuration of **Figure 4.5** [101].

The analysis of these results, in a first stage, point to previously known (and mentioned) results: increasing the thickness of a THGEM permits higher applied dipole voltages, which lead to higher gain, that can go up to 10^4 in $0.8\ mm$ thick THGEM. Although THGEM A presents similar values of gains for considerable lower voltages, it is important to mention that, despite its smaller thickness, it is the only THGEM (among the 3 tested) that has rim, which, as mentioned in chapter 2, results in higher gains, despite all the mentioned limitations.

The evaluation of the gain curves as function of the gas mixtures show, as expected, that Ar/CO_2 mixture, although preferable for laboratorial use, is the one that allows lower applied ΔVs, while being capable of achieving high gains. When moving to Ar/CH_4 based mixtures, the trend shows that bigger fractions of methane allow a significant increase of ΔV before the breakdown voltage of the THGEM. Despite this fact, the results also show that increasing fractions of methane, lead to small decreases in gain. These results are important for the operation of these detectors in beam conditions. Because stability is an essential element, operating with Ar/CH_4 mixtures, allows a relaxation of the applied voltages, increasing the breakdown voltage, allowing a more stable operation. At the same time, methane mixtures maximize the photoelectron extraction efficiency in CsI. Therefore, in beam conditions, Ar/CH_4 based mixtures are used, with a fraction of methane not small than 30%, nor bigger than 50%.

4.2.2.1. Response of Identical Structures

Another important aspect in the characterization of THGEMs is related on how THGEMs theoretically equal (with the same parameters), respond under the same conditions. In order to evaluate such response, 8 THGEMs with $0.8\,mm$ thickness, $0.4\,mm$ holes diameter and $0.8\,mm$ pitch, were tested in the configuration represented in **Figure 4.10** (left), with soft X-rays, under an Ar/CO_2 $(70:30)$ atmosphere. Drift field was set to $1.9\,kV/cm$ and induction field to $2\,kV/cm$.

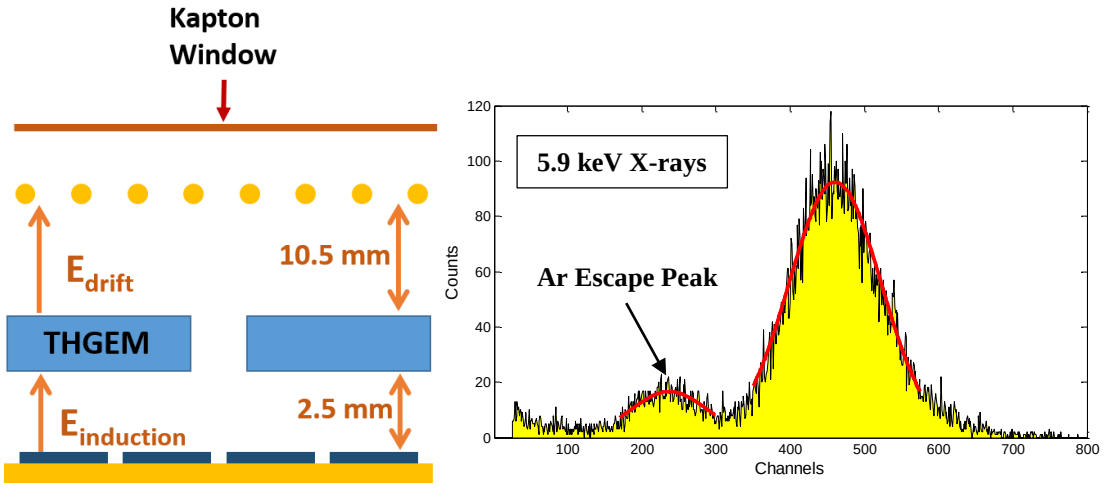

Figure 4.10 – Scheme of the configuration used for the testing of 8 identical THGEMs with ^{55}Fe source, emphasising the spacing distances and the Kapton™ window (left); an example of the amplitude spectrum obtained with the ^{55}Fe source, being visible the Gaussian peak corresponding to the energy of the X-rays, and the Ar escape peak (right).

The irradiation of the detector with soft X-ray sources, contrarily to single photoelectrons, results in pulse amplitude spectrum with a Gaussian peak, corresponding to the energy of the X-rays, and depending on the energy resolution of the detector. A second Gaussian peak can be visible corresponding to the argon escape peak. This type of pulse amplitude spectrum is exemplified in **Figure 4.10** (right). The gain of the detector can be calculated through the determination of the peak centroid in a charge calibrated spectrum.

Regarding the comparison of behaviour of the 8 identical THGEM's, **Figure 4.11** shows the variation of gain as a function of ΔV, for each of the pieces, up to the maximum ΔV allowed in each one, in a stable condition.

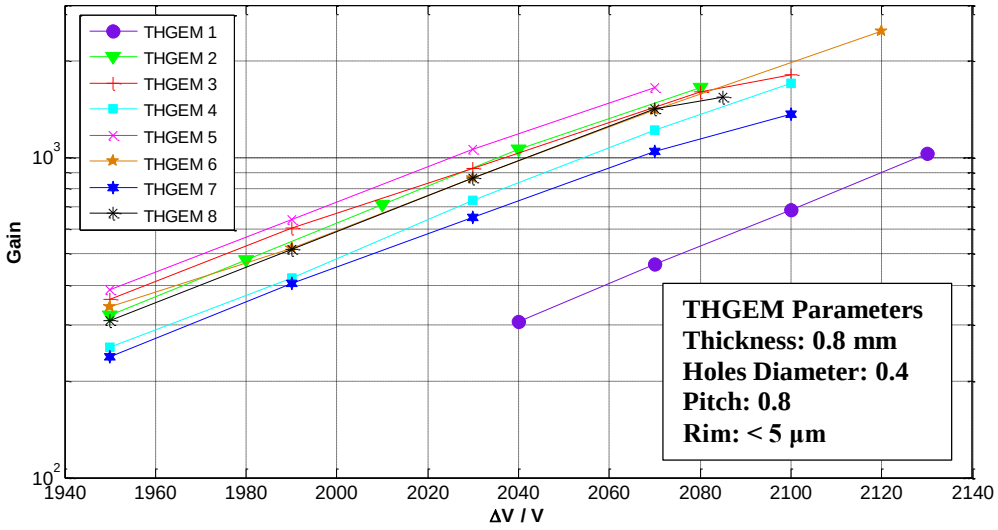

Figure 4.11 – Gain characterization of 8 identical THGEMs as function of the applied dipole voltage, for an Ar/CO_2 (70:30) mixture. The characterization was achieved based in the configuration presented in **Figure 4.10**, using the ^{55}Fe source, and with THGEMs with the following parameters: thickness: $0.8\,mm$; holes diameter: $0.4\,mm$; pitch: $0.8\,mm$.

The analysis of the presented results show that identical pieces do not necessarily present identical responses, with the maximum applied ΔVs ranging between $2070\,V$ and $2130\,V$, and maximum gains ranging between 1000 and 2500. Although the majority of the pieces share an approximate gain curve, they differentiate each other by different maximum ΔVs. Even if the production procedure is equal for all pieces, mechanical procedures like drilling or polishing can result in unique characteristics, such as different surface scratching, metal remnants inside the holes, etc., which conceive different operating properties to the THGEMs. Additional treating like polishing, micro-etching or "baking" (to remove humidity) may be necessary to standardize the piece's performance.

Altogether, the characterization of each individual piece is mandatory, prior to its application.

4.2.2.2. Drift and Induction Field Dependence.

The characterization of THGEMs is a fundamental procedure, as THGEMs are the fundamental elements of THGEM-based detectors. Nonetheless, other aspects have influence in the detector's performance as well. Namely the drift field (for ionizing sources) and the induction field, play an important role in the gain performance of the detector.

Although the fields' dependence is correlated with the THGEM's properties, still its effect in the detector can be studied. Following the configuration schematized in **Figure 4.12**, studies of the gain variation as function of the drift field and the induction field were performed.

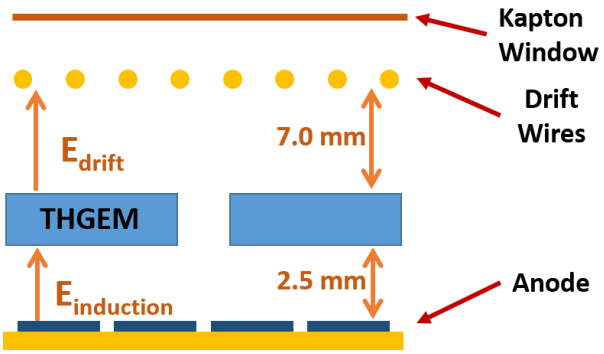

Figure 4.12 – Scheme of the configuration used for the study of the influence of the drift and induction fields in the gain variation of a single THGEM, under ^{55}Fe irradiation.

The referred studies were performed for a THGEM with $0.8\,mm$ thickness, $0.4\,mm$ holes diameter and $0.8\,mm\,pitch$, in an Ar/CO_2 $(75:25)$ atmosphere, while irradiating with ^{55}Fe soft X-ray source. The dependence of the drift field, shown in **Figure 4.13**, was achieved by setting the induction field at $3\,kV/cm$ and $\Delta V\ at\ 1800\,V$, while the dependence of the induction field, shown in **Figure 4.14**, was achieved for the same ΔV, and by setting the drift field at $0.5\,kV/cm$. The direction of the applied fields is in accordance with the direction represented in **Figure 4.12**.

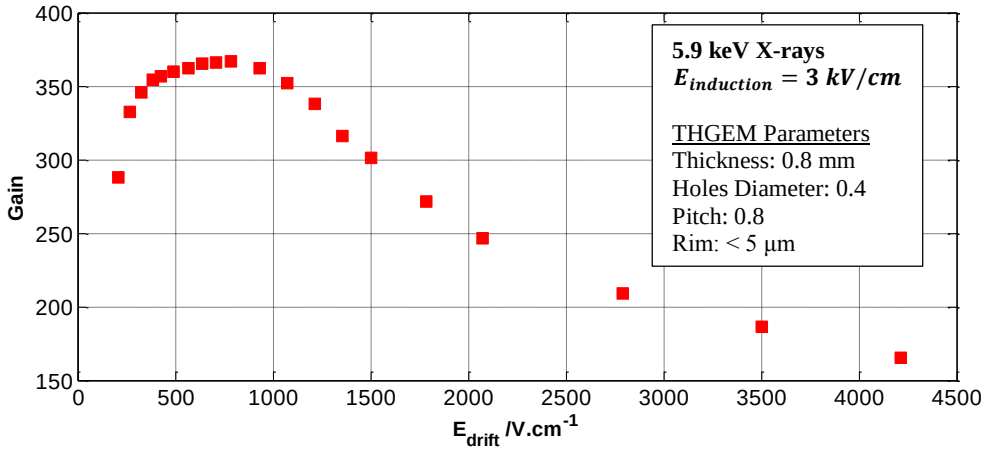

Figure 4.13 – Gain variation as a function of the drift field, for a single THGEM, based on the configuration presented in **Figure 4.12**, in a Ar:CO_2 $(75:25)$ atmosphere, with $E_{induction} = 3\,kV/cm$ and $\Delta V = 1800\,V$. The tested THGEM had the following parameters: thickness: $0.8\,mm$; holes diameter: $0.4\,mm$; pitch: $0.8\,mm$.

The study of the variation of gain as function of the drift field (**Figure 4.13**), is essentially a qualitative analysis rather than a quantitative one. The independent effect of the drift field is complicated to evaluate, as it would need to be detangled from the effect of the dipole field of the THGEM. Because the primary electrons are created far from the multiplication stage, a very small drift field might not be enough to drift electrons towards the THGEM, and some of the electrons

can be lost, resulting in a lower gain. If the drift field is increased, the gain will increase too up to a value of drift field between 0.5 and $1\ kV/cm$. In this range of fields, the field strength is already enough to minimize the diffusion phenomena, leading electrons towards the THGEM, but near the THGEM the dipole field is still dominant, focusing electrons into the structure's holes. Above these drift fields, the gain decreases with the increase of the field. In this stage, the drift field becomes continuously more dominant than the dipole field, above the THGEM structure, which leads to the loss of primary electrons, due to their collection on the metallic surface of the THGEM.

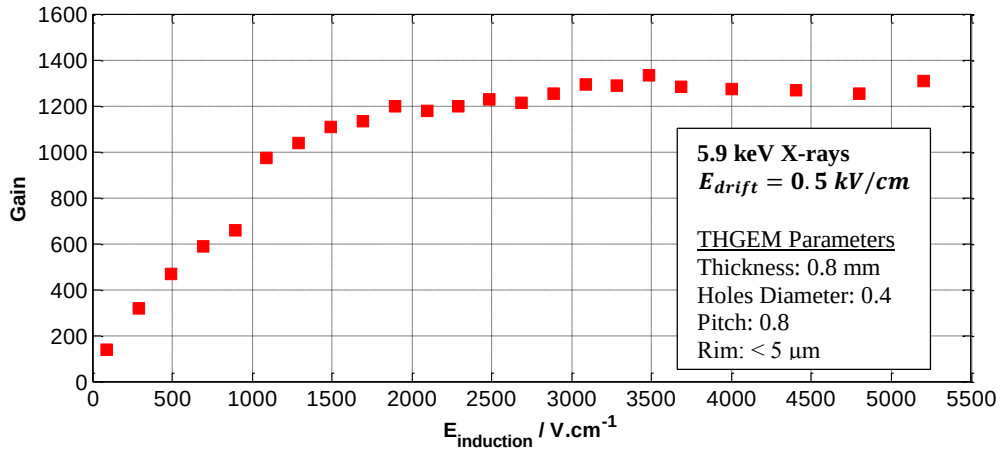

Figure 4.14 - Gain variation as a function of the induction field, for a single THGEM, based on the configuration presented in **Figure 4.12**, in a Ar:CO_2 (75: 25) atmosphere, with $E_{drift} = 0.5\ kV/cm$ and $\Delta V = 1800\ V$. The tested THGEM had the following parameters: thickness: $0.8\ mm$; holes diameter: $0.4\ mm$ and pitch: $0.8\ mm$.

The dependence of the induction field (**Figure 4.14**) in the gain variation, also depends, slightly, on the dipole field. For very low induction fields, the dipole field is still dominant, and a large fraction of electrons is collected in the bottom surface of the THGEM. Additionally, for these low values of field strength, diffusion also plays an important role, leading to the charge dispersion, or even its loss. With the increasing of the induction field, this field gains dominance over the dipole field and diffusion, which leads to an increase in the measured gain, as a larger fraction of electrons is collected by the anode. Around $3\ kV/cm$, the induction field becomes dominant, and therefore, a gain plateau is achieved.

4.2.3. Multilayer THGEM based detectors

So far THGEMs have been applied in single mode, allowing the characterization of the structures, and the optimization of the electric fields in the detector. Nonetheless, one of the advantages of THGEMs is their capability to operate in multilayer configurations. Although triple-layer THGEM-based detectors are aimed, the study of double-layer detectors allows an easier understanding of the role of the field between two consecutive THGEMs – transfer field.

4.2.3.1. Double-layer THGEM detectors

The presented study in a double layer configuration is intended, above all, to evaluate the gain dependence of the detector, on the transfer field. The study is performed under a Ar/CO_2 $(75:25)$ atmosphere, with the pulsed UV LED, using two identical THGEMs with the following parameters: $0.8\ mm$ thickness, $0.4\ mm$ hole diameter, and $0.8\ mm$ pitch. The configuration is schematically represented in **Figure 4.15**, with drift field set to $0\ V/cm$, induction field set to $3\ kV/cm$, and ΔV_1 and ΔV_2 set to $1650\ V$.

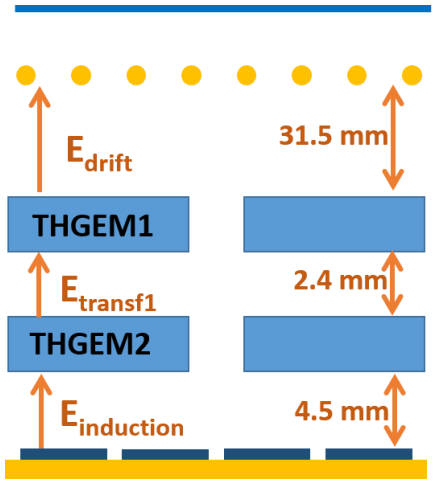

Figure 4.15 – Scheme of the configuration used to study the effect of the transfer field in a double-layer THGEM configuration, under UV irradiation.

Based on this experimental configuration, the evaluation of the variation of gain as a function of the transfer field is presented in **Figure 4.16** (top). The direction of the applied field corresponds to the direction represented in **Figure 4.15**.

It is important to note that in this study the optimized performance of the THGEM-based detector is not aimed. Instead, just a qualitative analysis of the influence of the transfer field is meant.

The transfer field between the two THGEMs is strongly coupled with the dipole fields of both structures. For very low values of the transfer field, the dipole field of THGEM 1 is dominant, and therefore, electrons exiting the holes of this first structure are mainly collected by it. Therefore, in this situation, the number of electrons that is transferred from the first to the second THGEM is reduced, leading to smaller gains. This behaviour leads not only to small gains, but also to low electron transfer efficiency. Although the transfer efficiency cannot be easily measurable, as all other variables remain constant, its variance can be qualitatively extracted from the variation of the rate of measured events, represented in **Figure 4.16** (bottom).

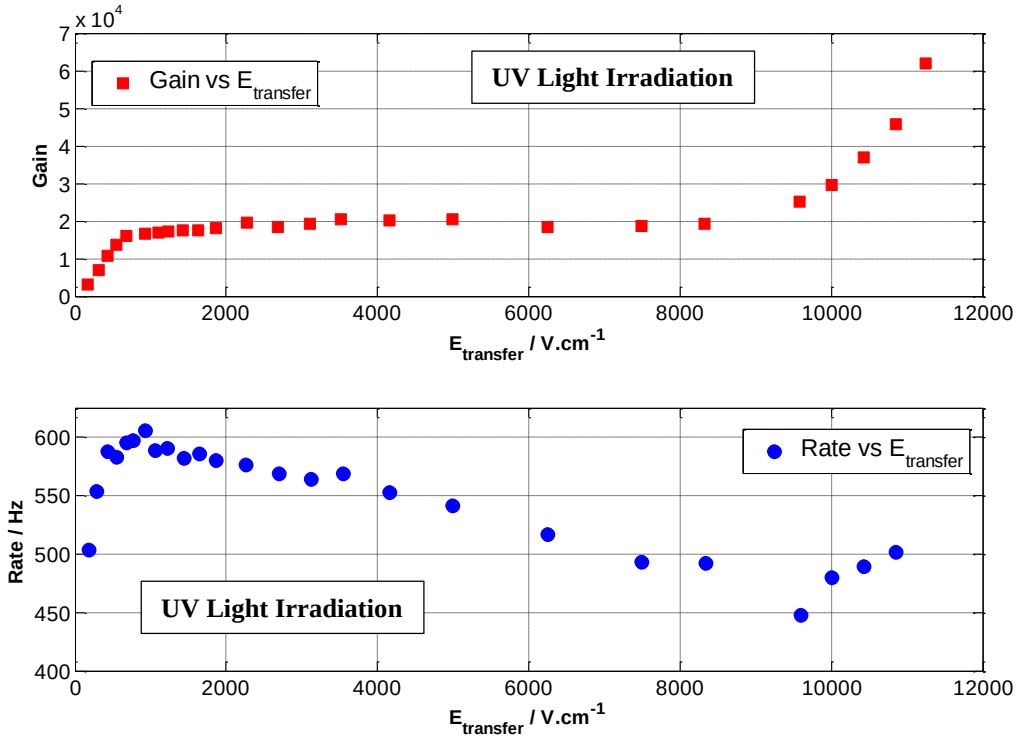

Figure 4.16 – Gain (top) and rate (bottom) variation as a function of the transfer field, for a double-layer THGEM detector, based on the configuration presented in **Figure 4.15**, in a Ar:CO_2 (75:25) atmosphere, with $E_{induction} = 3\,kV/cm$, $E_{drift} = 0\,V/cm$ and $\Delta V1 = \Delta V2 = 1650\,V$. Both THGEMs had the following parameters: thickness: $0.8\,mm$; holes diameter: $0.4\,mm$; pitch: $0.8\,mm$.

With the increase of the transfer field, this field starts to be dominant over the dipole field of THGEM 1, leading to the transfer of the multiplied electrons in the first stage of multiplication towards THGEM 2. This points to a continuous increase in gain and in the electron transfer efficiency up to approximately $1\,kV/cm$. After this value of the transfer field, a gain plateau is achieved, but the rate of measured events decreases. This implies that although each event can generate a stable gain, due to the strong transfer field, some events can be lost, as the electrons by them generated can be collected on the top surface of THGEM 2. The probability of such process increases with the field strength, which explains the continuous decrease of rate after $1\,kV/cm$. At extremely high transfer fields, an increase of gain if verified, as such high transfer fields allow charge multiplication directly in the transfer gap. The gain increase leads again to an increase of the measured rate, translating into an increase of the electron transfer efficiency.

Therefore, optimized values of transfer field are found between $750\,V/cm$ and $2000\,V/cm$.

4.2.3.2. Triple-layer THGEM detectors

The assembly of a triple-layer THGEM-based detector corresponds to the ultimate stage of optimization of the detector. **Figure 4.17** (left) schematically represents the assembly of such configuration. A simple test was performed to evaluate the variation of gain in function of the total applied ΔV. Such study was done under an Ar/CH_4 $(65:35)$ atmosphere, with pulsed UV LED, using the following THGEMs:

- THGEM 1: $10\ \mu m$ rim; $0.4\ mm$ thickness; $0.4\ mm$ holes diameter; $0.8\ mm$ pitch.
- THGEM 2 & 3: $0.8\ mm$ thickness; $0.4\ mm$ holes diameter; $0.6\ mm$ pitch; $<\ 5\ \mu m$ rim.

The drift field was set to $0\ V/cm$, the induction field to $3\ kV/cm$, and both transfer fields were set to $1.5\ kV/cm$.

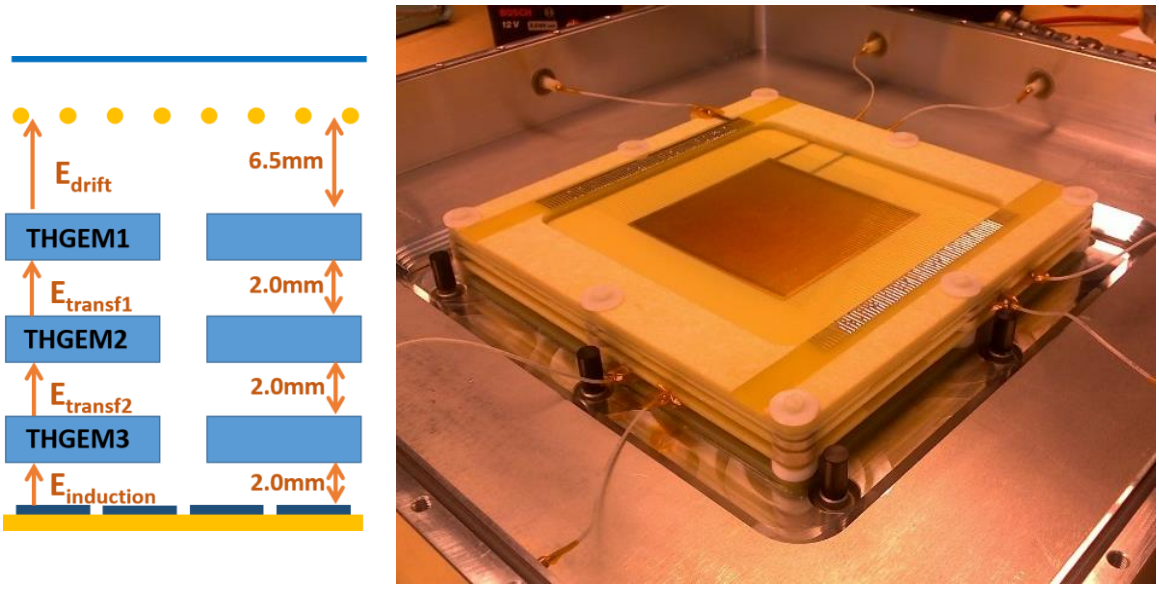

Figure 4.17 – Scheme of the configuration used to study a triple-layer THGEM configuration, under UV irradiation (left); experimental assembly of a triple-layer THGEM detector (right).

The results of this study are presented in **Figure 4.18**.

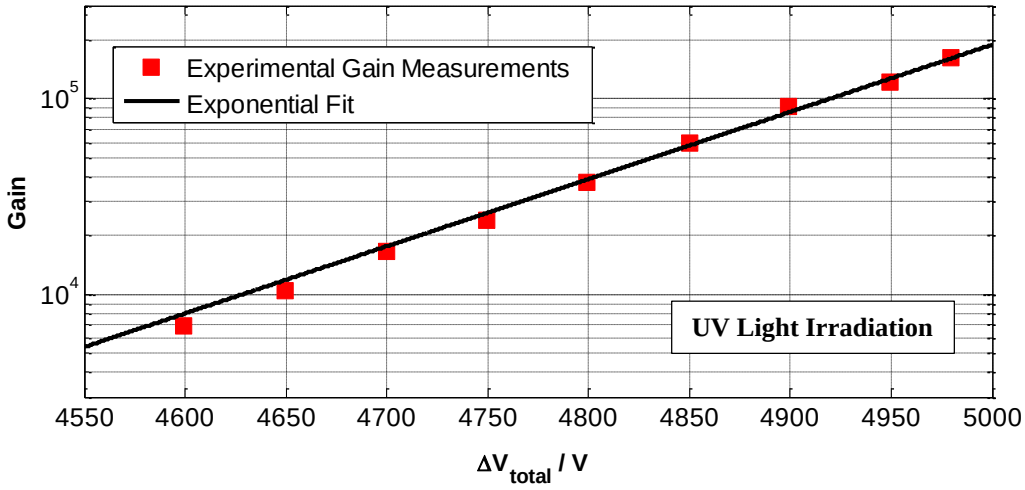

Figure 4.18 – Gain variation as a function of the total applied dipole voltages, for a triple-layer THGEM detector, based on the configuration presented in **Figure 4.17**, in a Ar:CH_4 (66:34) atmosphere, with $E_{induction} = 3\ kV/cm$, $E_{drift} = 0\ V/cm$ and $E_{transf1} = E_{transf2} = 1.5\ kV/cm$. The point at $\Delta V = 4980\ V$ corresponds to the maximum voltage allowed by the configuration.

Such study does not aim to optimize the maximum achievable gain with such configuration, as gains up to approximately 10^6 are reported with identical configurations. These results show essentially that the gain exponential dependence with ΔV verified in single layer THGEMs is kept for triple layer THGEM detectors where the gain exponential variation as a function of the total applied voltage, this is, $\Delta V_1 + \Delta V_2 + \Delta V_3$. It is also visible that gains up to 10^5 are easily achievable with triple-layer THGEM detectors, without observing any electrical discharges.

The choice of thicknesses of $0.4\ mm$, $0.8\ mm$ and $0.8\ mm$ for THGEM 1, 2 and 3 respectively are not random. In fact, this set of thicknesses is often kept for the triple-layer THGEM detectors presented along this work. A thinner THGEM applied as the upper layer, due to its lower gain, leads to a lower value of ions, created in its own multiplication stage, reaching the structure's surface, where a CsI shall be placed. This first structure has also the function of maximizing the photoelectron extraction, and the transparency to photoelectrons. Thicker THGEMs for the second and third stages of amplification allow an optimized charge multiplication.

4.2.4. Towards Larger Prototypes

The development of THGEM-based detectors, in the context of this work, as recurrently mentioned, aims the implementation in RICH-1 detector. Such application requires the development of optimized THGEM structures with an active area of $600 \times 600\ mm^2$. Although the production procedure allows the direct production of pieces with such area, it is not granted that the scaling of the area from $30 \times 30\ mm^2$ to $600 \times 600\ mm^2$ will allow similar performances.

Thus, a gradual increase in area, with its respective characterization, is advised. In this regard, prototypes of an intermediate size, with an active area of $300 \times 300\ mm^2$, were produced and tested.

Although the production of THGEMs with larger areas follow the production techniques and the optimized parameters achieved for small area prototypes, still they demand an optimization of engineering aspects. A significant increase in area, leads also to a significant increase in the THGEM capacitance. Such aspect can be harmful, both for the structure itself and for the electronic readout, in case of electrical discharges. Additionally, the overall operation performance of the THGEM is limited to the best performance of its weakest point. To overcome these two limitations, a segmentation in six contiguous sectors, of the $300 \times 300\ mm^2$ area THGEM, was implemented. This solution allows primarily a lower capacitance in each sector, and limits eventual discharges to the sector where they happen, and secondarily, they permit the operation of each sector with independent performance from the neighbouring sectors, which leads to an overall optimized operation of the whole structure. **Figure 4.19** illustrates, schematically, the pattern of the THGEM segmentation and the way each sector is numbered, and it shows simultaneously a produced and tested prototype.

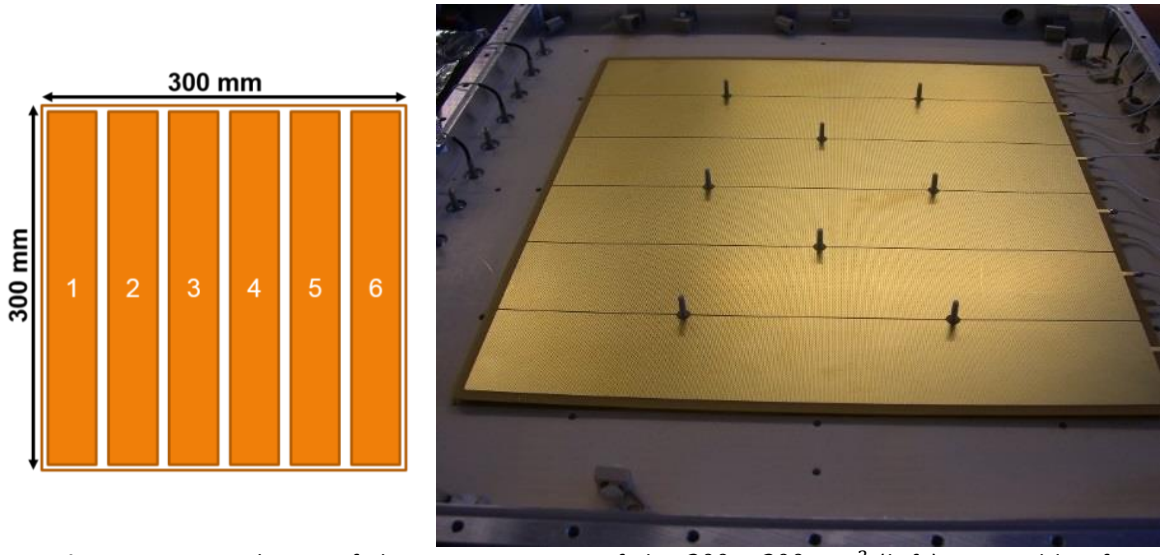

Figure 4.19 – Scheme of the segmentation of the $300 \times 300\ mm^2$ (left). Assembly of a real prototype in a single layer configuration, with emphasis to the pillars mounted to allow the uniform spacing of the whole structure (right).

The scaling of the area of the THGEM obliged a similar scaling of the anodic structure. Although the layout and the pad size remains unchangeable compared to the smaller previous detectors, an increase in the total number of pads is verified (**Figure 4.20** (left)). Because the response of each sector of the $300 \times 300\ mm^2$ THGEM is intended to be obtained individually, the segmentation of the anode, as shown in **Figure 4.20** (right), is possible and mandatory.

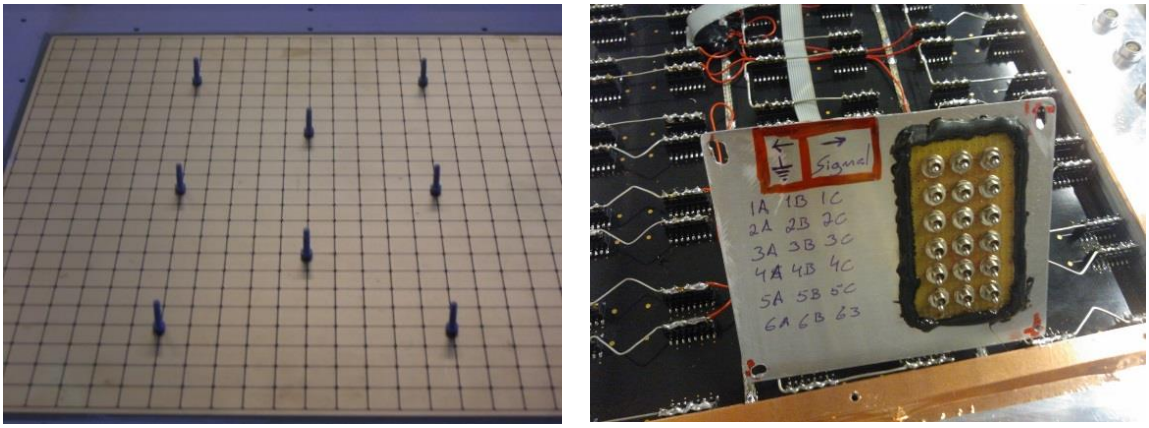

Figure 4.20 – Anodic pads of the chamber used to characterize the $300 \times 300\ mm^2$ prototype, with emphasis of the support pillars mounted over the anode (left). Segmentation of the anode, controlled by a binary switch, allowing the operation of each of the 18 segments individually.

Even though each THGEM is segmented in only 6 sectors, the disposition of the anode allows a more refined segmentation. Because the anode consists in a set of 24×24 pads, the association in smaller sets of 4×8 pads, for readout purposes, allows the segmentation of the anode in 18 sectors, which mean 3 virtual sectors for each THGEM segment. Although all the virtual sectors along a physical THGEM sector are subject to the same voltage conditions, this additional segmentation allows a deeper characterization of the THGEM. **Figure 4.21** (left) schematically represents the segmentation of the THGEM due to the anode splitting, while **Figure 4.22** (right), shows the segmentation of the Kapton™ window, necessary for the testing of each individual sector.

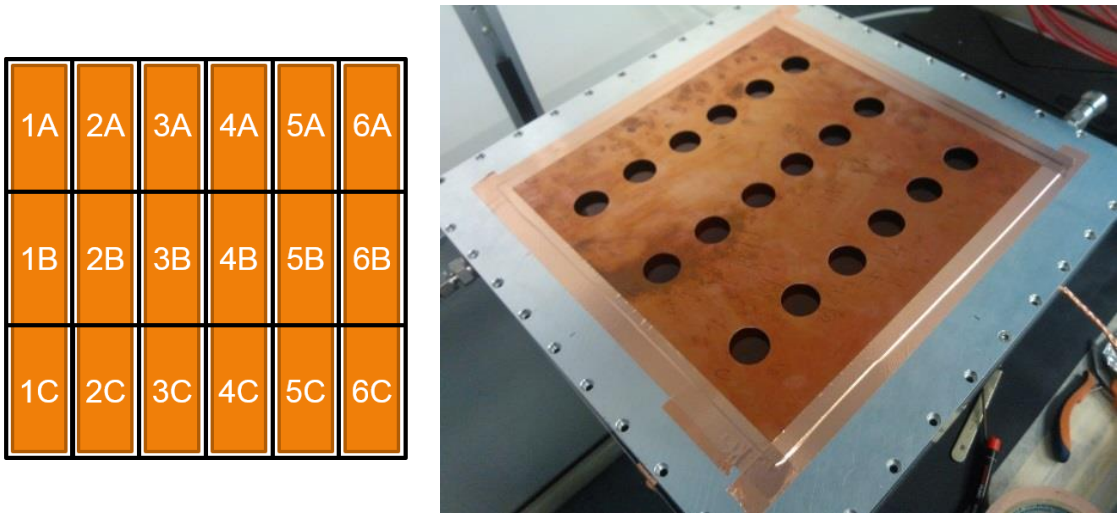

Figure 4.21 – Scheme of the "virtual" division of each of the segments, allowing the segmentation of the anode (left); Segmentation of the Kapton™ window, to allow the characterization of different pieces in the exact same locations.

In order to perform the mentioned test for the characterization of each sector of the THGEM, the configuration schematically represented in **Figure 4.22** was set. The configuration comprises

the segmented Kapton™ window shown in **Figure 4.21** (right), and the segmentation of the anode, shown in **Figure 4.20** (right), controlled via a binary switch system.

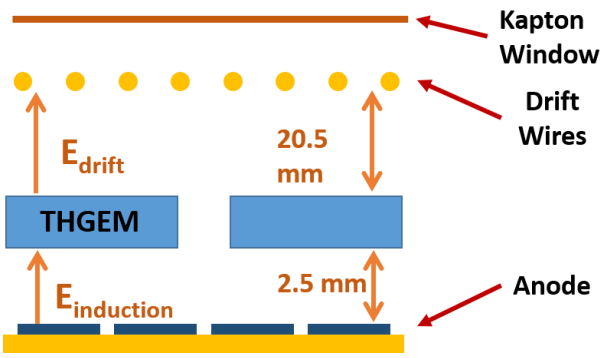

Figure 4.22 – Scheme of the configuration used to characterize the $300 \times 300\ mm^2$ prototypes, under ^{55}Fe irradiation.

In what matters the choice of the parameters for the production of the large area THGEMs, the knowledge obtained with the small THGEM prototypes is transferred to these $300 \times 300\ mm^2$ structures. This includes the maintenance of the ratio between hole diameter and pitch of $1{:}\,2$, with the choice of 0.4 and $0.8\ mm$ respectively, and negligible rims (smaller than $5\ \mu m$). The choice of thicknesses follows the intention to produce triple-layer THGEM detectors with a first layer $0.4\ mm$ thick and the second and third with $0.8\ mm$ thick. Altogether, this set of parameters correspond to what is for us considered the standard THGEM parameters.

Therefore, few prototypes with 0.4 and $0.8\ mm$ thicknesses were produced. The testing of one produced THGEM of $0.4\ mm$ thick, relied essentially on the test of the maximum voltage allowed, in air, before the breakdown voltage. The breakdown voltage is expected to be function of the thickness and to follow the Paschen curve [102], which for such thickness, in air at atmospheric pressure, indicates an approximate value of $2250\ V$, before electrical discharges are expected, even though such value is very susceptible to small gap and pressure variances. The appliance of this test, in a $0.4\ mm$ thick THGEM, cleaned and dried, led to breakdown voltages in the order of $1.5\ kV$ for all sectors. The realization of this fact, under no apparent reasons, led to the coating of the piece with polyurethane with its subsequent polishing. The goal of such technique is to smoothen the edges of the structures, aiming to improve its performance. Such procedure, indeed seemed to improve the response of the piece to high voltage, allowing breakdown voltages, in air, in all sectors around $2.2\ kV$. The apparent success of this procedure led to its application in the remaining $0.8\ mm$ thick THGEMs, where more detailed tests were performed.

Therefore, under the configuration presented in **Figure 4.22**, with a drift field of $150\ V/cm$, an induction field of $2\ kV/cm$, and in an Ar/CO_2 $(70{:}\,30)$ atmosphere, a $0.8\ mm$ thick THGEM was tested, whose amplitude spectra for each sector, while irradiated with ^{55}Fe, is presented in **Figure 4.23**.

The referred test was done for a ΔV of $2200\ V$, which corresponds to the maximum balanced voltage allowed by the THGEM in the referred gas mixture. This aims to set all the THGEM sectors at the same conditions. Although the gain is not optimized, a direct comparison of the response of each sector is permitted.

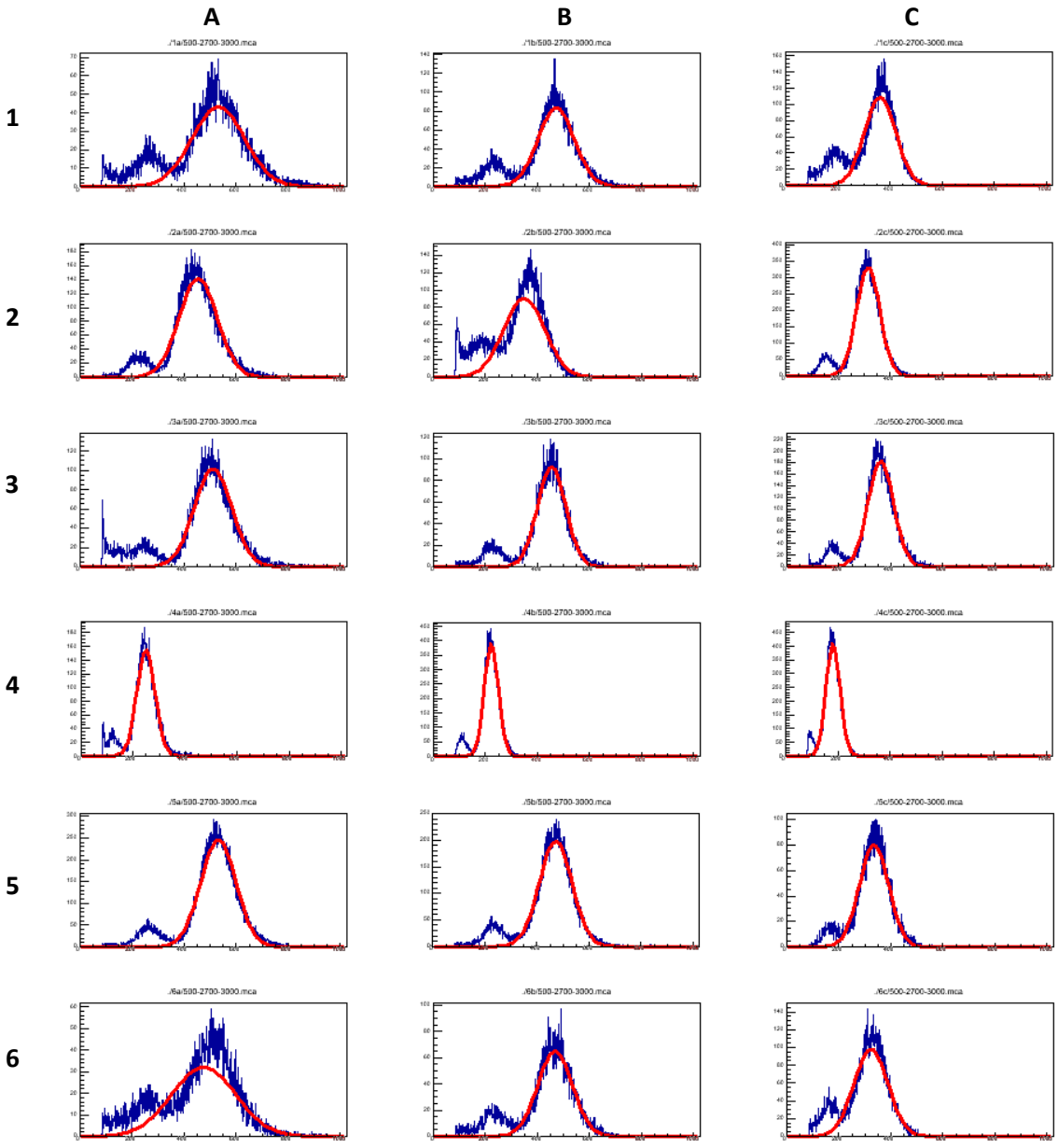

Figure 4.23 – Amplitude spectra, and the Gaussian fit, at each of the 18 segments (6 physical segments, numerated from 1 to 6, each of each characterized in 3 different places, label from A to C) of a $300 \times 300\ mm^2$ THGEM, tested in the configuration represented in **Figure 4.22**. The results correspond to an operation in an Ar/CO_2 mixture, with $E_{drift} = 150\ V/cm$, $E_{induction} = 2\ kV/cm$ and $\Delta V_{All\ sectors} = 2200\ V$. The THGEM parameters are: thickness: $0.8\ mm$; holes diameter: $0.4\ mm$; pitch: $0.8\ mm$.

Prior to the interpretation of the spectra of **Figure 4.23**, it's important to point out that all the spectra share the same channel scale.

A visual interpretation of these spectra point to surprising results. A THGEM that is expected to be homogeneous, with all sectors operated in the exact same conditions, lead to quite significantly different amplitude spectra. Not only each sector demonstrates different behaviour compared to its neighbouring sectors, with sector 4 in particular showing poor performance, but also the loss in gain inside each sector, from subsector A to C, translated by the shift of the peak towards lower channels. The quantitative evaluation of the gain, extracted from the charge calibrated spectra, is shown in **Figure 4.24**.

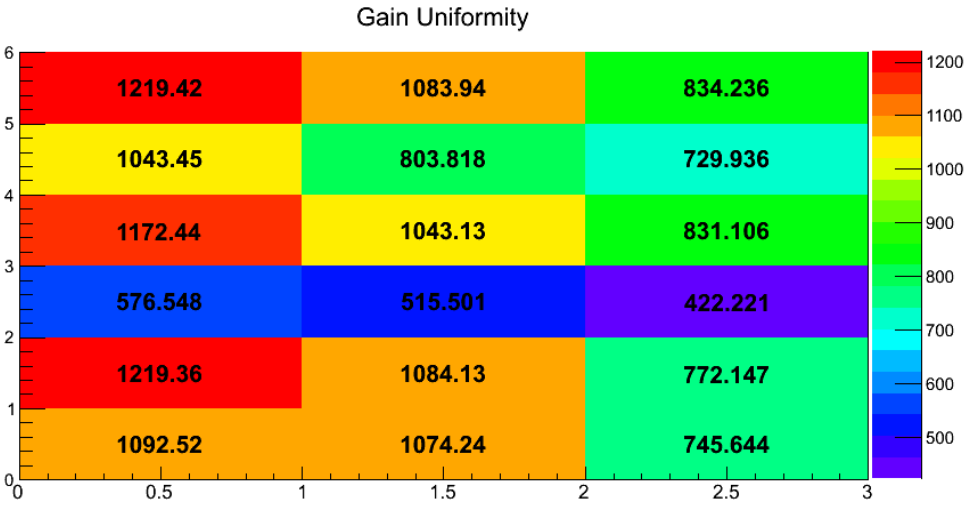

Figure 4.24 – Gain values extracted from the amplitude spectra of **Figure 4.23**.

A careful look to the gain variation shows that the peak displacement, visible in the spectra, results in an effective gain variation up to a factor of 3 between the segment with the lowest gain and the one with the highest. Despite this significant gain variation, the order of magnitude of the gain values match the values achieved in small prototypes, under non-optimized conditions.

The testing of additional THGEMs with the same area provided equal behaviour, showing that the phenomena was not isolated. In order to understand such behaviour in all THGEMs, the thicknesses of several pieces of raw PCB (comprising the dielectric and the copper layers) were measured. Such raw PCB used for the THGEM production presents an area of approximately $500 \times 500\, mm^2$, and the thicknesses were measured in points equally distributed along the surface of the material. **Figure 4.25** shows two examples of such measurements performed in a $0.8\, mm$ thick raw PCB. Although only two sets of thickness measurements are presented, over 75 pieces with theoretical thickness of 0.4, 0.6 and $0.8\, mm$ were measured, indicating similar behaviour to the ones now exemplified.

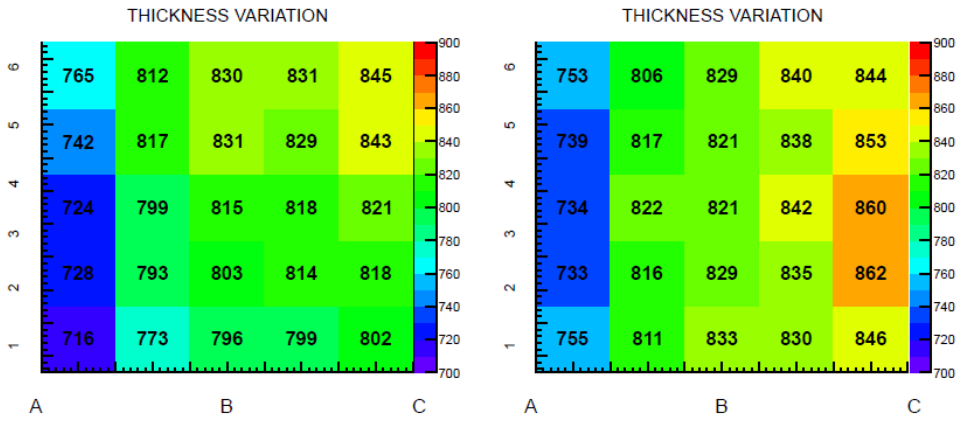

Figure 4.25 – Thickness of two different pieces of raw PCB (theoretically comprising a 0.8 mm thick dielectric plus 2 copper layers, 35 μm thick) with an area of $500 \times 500\ mm^2$. The measurements are performed along the surface of the raw PCB at points equally distributed, with the corresponding thickness values in μm.

The parameter "thickness" is by definition the thickness of the dielectric. Considering that the copper layers, prior to any chemical or mechanical procedure, have a thickness of $35\ \mu m$ each, it would be expected that the measured thickness of the raw PCB all along its surface, would be of $870\ \mu m$. However, results proven to be significantly different. Not only is the expected thickness never measured, but most importantly, thickness' variations of more than $100\ \mu m$ are found. These thickness variation are not random. On the contrary, they exhibit a specific tendency towards one side of the material. Such geometrical arrangement of the thickness' variances finds an equivalent geometrical arrangement regarding the gain variations. Because for the same voltages, thinner thicknesses correspond to higher gains, its logic to conclude that the PCB anomalies might correspond to the reason why $300 \times 300\ mm^2$ THGEM prototypes demonstrate an anomalous behaviour in what regards its gain characterization.

Despite these issues, $300 \times 300\ mm^2$ THGEMs have been able to operate in triple layer configurations, in beam environment, as it will be introduced in chapter 6.

For future productions, the thickness measurements of the raw PCB is of particular interest, in order to allow the choice of pieces that demonstrate the smallest variation.

4.3. Hybrid Detectors

Micromegas detectors, introduced in section 1.8.2, present several intrinsic properties of undeniable interest: their capability of blocking ions while being transparent to electrons, their fast response, and their high gain. Additionally, its geometry is compatible with its coupling with other amplification structures. Therefore, and based in concepts where GEMs were coupled to Micromegas as pre-amplification stages [103,104], the development of a hybrid detector comprising a Micromegas with THGEM structures, was considered. The implementation of such

concept aims to combine the advantages of both structures into a single gaseous photon detector, with a THGEM as pre-amplification stage with photon detection capability, and the Micromegas as second stage of amplification with intrinsic ion blocking capability. Although this approach corresponds to a completely novel detector, preliminary tests have been performed, in order to evaluate the reliability of such concept.

4.3.1. Micromegas Detector

In order to perform such preliminary tests, there were several attempts to produce a "homemade" Micromegas. The lack of knowhow in this particular field, and the limitation of the production technique available under such conditions, led to the failure of the structure, due to the impossibility of guaranteeing the planarity of the micromesh. To surpass these limitations, a bulk Micromegas, courtesy of CEA Saclay, was used instead. This Micromegas consisted on a micromesh with an active surface of $60 \times 100\ mm^2$, placed at a distance of $128\ \mu m$ from a stripped anode, which was connected to the standard analogue readout chain. This device is shown in **Figure 4.26** (left).

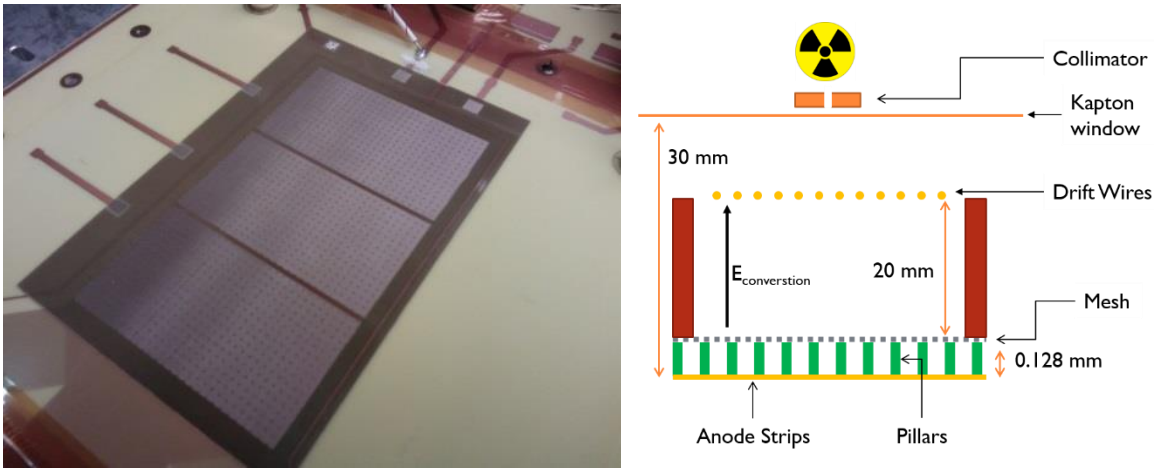

Figure 4.26 – Micromegas detector with an active surface of $60 \times 100\ mm^2$, and stripped anode (left); Scheme of the configuration used to test the Micromegas in standalone mode, under ^{55}Fe irradiation (right).

To study the effect of the addition of a THGEM in a Micromegas detector, the later was initially tested in a standalone configuration, in order to allow a future comparison with a Micromegas plus THGEM configuration. This initial study, based on the configuration schematically represented in **Figure 4.26** (right), was performed under a Ar/CO_2 $(70:30)$ atmosphere, while irradiated with a collimated ^{55}Fe source.

The applied voltage on the micromesh was set at $620\ V$, which for the mentioned amplification gap, corresponds to an amplification field of approximately $48\ kV/cm$. The variation of the conversion field was varied between 340 and $2000\ V/cm$, in order to study the variation of gain,

energy resolution and the rate of measured events, as function of ξ ($\xi = E_{amplification}/E_{conversion}$). These results are presented in **Figure 4.27**.

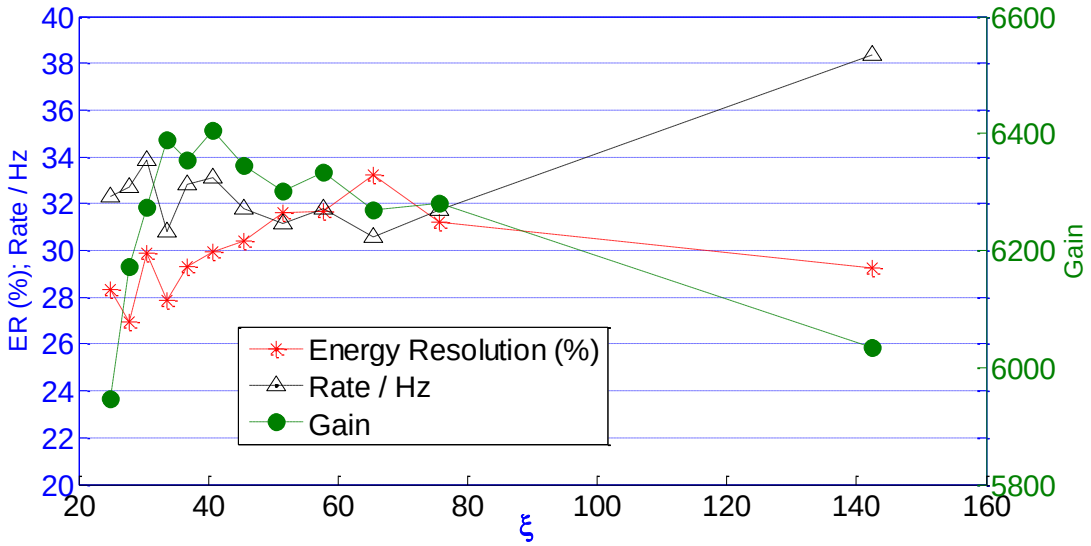

Figure 4.27 – Gain, energy resolution (ER) and rate variation as function of ξ, based in the configuration of **Figure 4.26**, under a Ar/CO_2 (70:30) atmosphere, with the voltage of the micromesh set at $620\,V$.

Considering that these consist on preliminary tests, an optimized performance was not envisaged, just the understanding of the detector's operation when compared to the information available in literature.

In order to evaluate the variation of gain as function of ξ, it is important to note that the gain is defined essentially by the strength of the amplification field. As the micromesh is set to a fixed voltage, a significant gain variation, as function of the field above the micromesh, is not expected. The interpretation of **Figure 4.27**, in what gain is regarded, points towards the same conclusion. Despite a maximum global gain around $\xi = 40$, after which the gain tendentiously decreases, the overall variation is not significant, as gain remains comprehended between 6000 and 6400. An insignificant variance is visible too for the study of the energy resolution as function of ξ, where an approximately constant value of 30% is verified. This value is far from the values reported in literature [29], but then again it's important to point that such studies were performed under non-optimized conditions.

The rate, for these range of ξ values, is approximately constant. This helps to evaluate, in a qualitative way, the transparency of the micromesh to electrons, which accordingly to the calculations presented in **Figure 1.13**, suggest that it should be maximum, and constant, for these range of field ratios. The same results pointed to a significantly reduced ion transparency, whose study in this particular device was not yet implemented.

4.3.2. Micromegas coupled with THGEMs

Given the brief knowledge acquired previously with the Micromegas detector, its coupling with a THGEM structure was considered for the very first time. The intention was mainly to evaluate the general behaviour of the simultaneous operation of two devices with distinct properties. In this regard, the configuration illustrated in **Figure 4.26** (right) was adapted in order to accommodate a $30 \times 30\ mm^2$ active area THGEM, $0.6\ mm$ thick, $0.4\ mm$ hole diameter and $0.8\ mm$ pitch, $5\ mm$ away from the micromesh, as schematically represented in **Figure 4.28** (left). No study was performed in order to optimize distance of the different components. **Figure 4.28** (right) shows the physical implementation of the THGEM and the drift wires above the Micromegas.

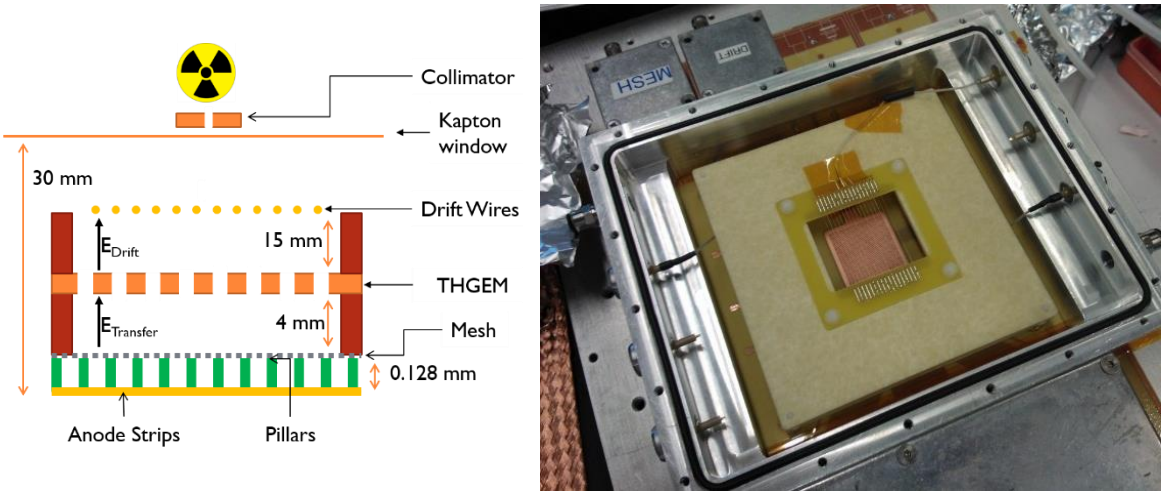

Figure 4.28 – Scheme of the configuration used to test the Micromegas coupled with a single THGEM layer, under ^{55}Fe irradiation (left); assembly of the THGEM structure and the drift wires over the micromesh (right).

In this situation, the micromesh was set to $590\ V$, corresponding to an amplification field of approximately $46\ kV/cm$, while the THGEM dipole voltage was set to $1400\ V$. A drift field of $700\ V/cm$ allows the operation of the detector with the ^{55}Fe source. As in the previous exercise, the independent variable under test remains ξ, which in the context of this configuration gains a slightly different interpretation. Although it remains the ratio between the field below and above the micromesh, the previous conversion field above the structure is now replaced by the transfer field from the THGEM above, whose variance might also introduce implications for the THGEM's performance. **Figure 4.29** shows the variation of gain, event rate and energy resolution, of the mentioned hybrid detector, as function of ξ.

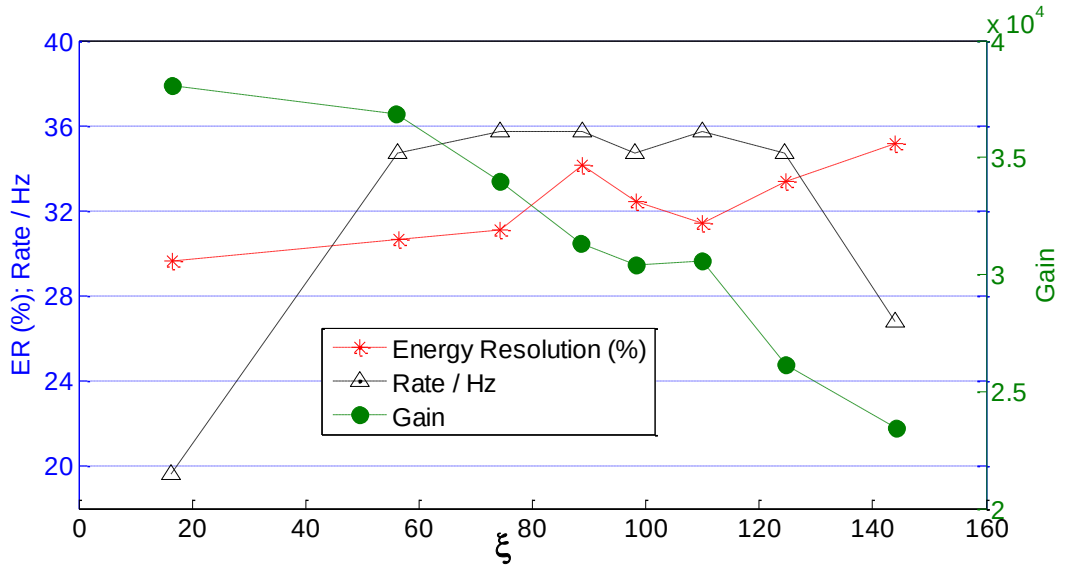

Figure 4.29 – Gain, energy resolution (ER) and rate variation as function of ξ, based in the configuration of **Figure 4.28**, under a Ar/CO_2 $(70:30)$ atmosphere, with the voltage of the micromesh set at $590\,V$. The THGEM (thickness: $0.6\,mm$; hole diameter: $0.4\,mm$; pitch: $0.8\,mm$) was operated with a $E_{drift} = 700\,V/cm$ and $\Delta V = 1400\,V$.

The evaluation of the rate variation, as previously, remains just as a qualitative measure of the electron transparency. In this regard, in the range of ξs presented, the introduction of the THGEM does not seem to introduce any significant perturbation on the Micromegas detector, with exception of very small ξs (out of range in **Figure 4.27**), where the high transfer field leads to a decrease in the rate, eventually due to the collection of electrons by the micromesh. A decrease in rate is also observed for very high ξs, where the strong THGEM dipole field becomes dominant over the transfer field, corresponding to a possible loss of electrons multiplied inside the THGEM holes, to the bottom holes.

The variation of gain, however, shows a significant variation as a function of ξ, pointing to a decrease in gain from approximately $38k$ down to approximately $25k$, in the range of presented ξ. The resemblance of this variation with the one shown in section 4.2.3.1, where the gain variation as function of the transfer field is presented, leads to conclude that such variation is indeed due to the presence of the THGEM (note that in the plot of **Figure 4.29**, small ξ correspond to high transfer fields, and vice-versa). Despite this decrease in gain for lower transfer fields, it is important to remark the capability of achieving higher gains, under non-optimized conditions, when compared to the operation of the Micromegas alone, showing the capability of the THGEM to work as a pre-amplification stage coupled to a Micromegas detector. Additionally, the evaluation of the energy resolution seems to suffer no effect from the THGEM, in the presented range of ξ, showing an approximately constant value between 30 and 35%.

Although this device lacked optimization of distances and voltages/fields, it aimed to prove the possibility of the operation of such hybrid detector, with its ion blocking capability yet to be tested.

Yet, this same detector, showed the capability of operating with significant higher gains, compared to the ones previously shown, by increasing the amplification field (**Figure 4.30** (left), performed with ^{55}Fe), or by increasing the THGEM dipole voltage (**Figure 4.30** (right), under UV light). The operating conditions of each measurement are indicated along with the figure, illustrating a gain of 10^5 achieved with the ^{55}Fe source, and a gain of approximately 10^6 achieved with the UV LED.

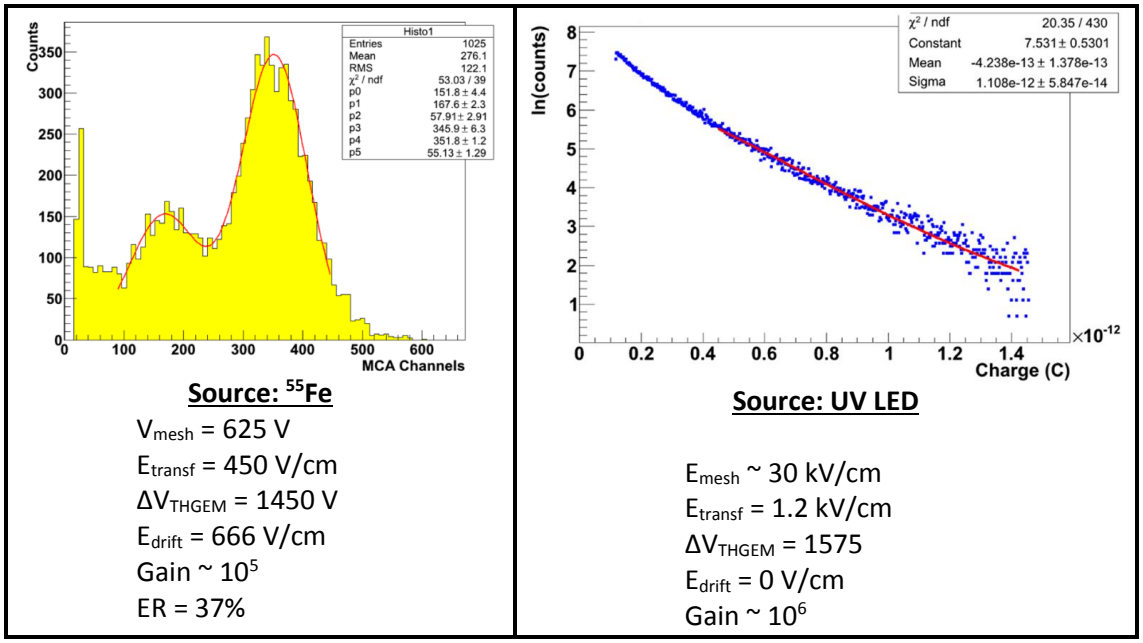

Figure 4.30 – Amplitude spectrum of the hybrid detector, operated in the conditions described in the figure, irradiated with ^{55}Fe (left), and UV light (right), illustrating that higher gains are possible.

4.4. Conclusions

The studies performed along this chapter, with $30 \times 30\ mm^2$ THGEM prototypes, aimed essentially a deeper understanding of the overall variables associated to THGEM based detectors.

In a first stage, these results, complemented by previously mentioned results, show that higher values of gain can be achieved with thicker THGEMs and with smaller holes, while a ratio of $1{:}\,2$ between the holes diameter and pitch correspond to the best geometrical configuration, in what regards the maximization of the THGEM's active area and the photoelectron extraction efficiency.

The study of the gain dependence on the gas mixture, for the mentioned structures, showed that Ar/CH_4 mixtures, with methane ratios up to 50% allowed higher applied dipole voltages, with no compromise in gain, when compared to the standard Ar/CO_2 gaseous mixture, although this later mixture is still preferable for laboratorial use, for safety reasons.

The referred structures also allowed the study of the effect of the applied electric fields in the detector. The drift field, although ideally null for photon detection, presents an optimized gain

operation for ionizing radiation for values around the interval between 500 and $1000\ V/cm$. On the other hand, the transfer field permits best detector performance's for high fields, above approximately $2.5\ kV/cm$, in order to allow an enhanced charge collection by the anode. In multi-layer THGEM detectors, the optimal transfer fields are around $1\ kV/cm$, in order to allow an optimized gain with optimized electron transfer efficiency.

Additionally, triple layer configurations have been proved possible, with the gain being proportional to the sum of the applied dipole voltages. The study of these configurations is complemented in the next chapters.

Regarding the $300 \times 300\ mm^2$ prototype, the non-homogeneity of the thickness along the whole surface of the THGEM represents a major issue in the THGEM performance. Nonetheless, its operation in stable conditions has been possible, with gains around 10^3, for a $0.8\ mm$ thick structure. Triple-THGEM detectors based in these larger prototypes have been later operated in beam conditions, as described in chapter 6. These large area prototypes represents a relevant step towards the final detector with an active area of $600 \times 600\ mm^2$, for RICH-1 upgrade, making use of all the studies earlier performed in the small area structures.

Finally, preliminary studies in the hybrid detector, combining together a Micromegas and a THGEM structure, showed no performance degradation when coupling the two detectors. This allows this hybrid configuration to be considered for further studies, aiming the development of a gaseous photon detector with the intrinsic capability of ion entrapment, with high gain and fast signal development.

5. Ion Back Flow Studies

The Ion Back Flow, as already introduced in section 2.2, introduced limitations to the operation of second generation of gaseous photon detectors, due to the ions bombarding the photocathode, leading to field distortion, feedback pulses and the ageing of the photocathode. The success of the third generation of GPD based in THGEMs envisaging RICH applications, relies in the capability of reducing the ion back flow in the photocathode region, without the loss of performance of the detector, and at the same time, provide a higher gain that lead to a higher photon detection efficiency.

In a standard triple-THGEM photon detector, the IBF, although dependent on several variables, is typically comprehended between 20 and 30% of the total produced ions in the multiplication processes, for the standard operating conditions. **Figure 5.1** illustrates, as an example, the spatial charge distribution on a typical triple-THGEM detector. Although such distribution is dependent on the strength of the transfer fields, as it will be further studied, this given example aims to emphasise the charge splitting and the large fraction of ions over the upper electrode of THGEM 1, where the photocathode is expected to be deposited.

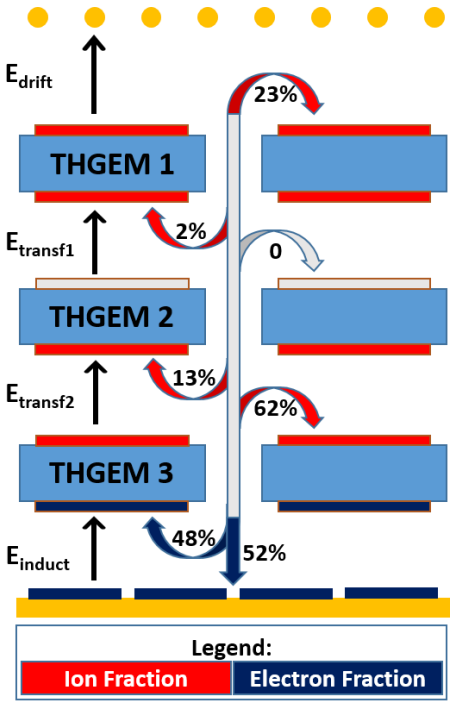

Figure 5.1 – Example of the typical spatial distribution of charges along the several electrodes of a triple THGEM detector, with special emphasis to the 23% of ions reaching the upper electrode of THGEM 1. This charge distribution was obtained by direct measurement of the currents in each layer, with $E_{drift} = 0\,V/cm$, $E_{transf1} = 2\,kV/cm$, $E_{transf2} = 1\,kV/cm$ and $E_{induction} = 3\,kV/cm$, in a Ar/CO_2 (70:30) atmosphere.

From this example, it's important to note that the majority of the electrons are collected in the induction gap, while ions are mostly collected in the transfer 2 gap, and undesirably in upper electrode of THGEM 1, where roughly one quarter of the total ions is collected (these values are specific to this example, whose details are described in the legend of the figure).

These typical values of IBF, for these type of configurations, correspond to a value far above of what is consider as acceptable. Because values of IBF in the order of just few percent ($< 5\%$) are aimed, the adaption and optimization of the THGEM-based photon detectors was considered, in order to achieve the proposed goal. In this regard, two different philosophies were followed: IBF reduction by staggered hole configurations; and IBF reduction by dedicated electrodes.

The first approach relies on the simplicity of the THGEM geometry and tries to take advantage of the vertical alignment of the holes of each THGEM [105], while the second is based on the replacement of a THGEM by a THCOBRA, envisaging the ion collection with its extra electrode.

For both approaches, experimental studies were performed in order to understand the capability of the configurations to entrap ions before they reach the photocathode, while understanding their effect in the electrons behaviour (gain and electron collection efficiency). Additionally, simulation studies compare and complement the experimental data.

5.1. Ion Back Flow Reduction by Staggered Hole Configurations

This first approach is based on the diffusion properties of electrons and ions, and aims to study the effect of the alignment of the holes of consecutive THGEMs in the trajectories of these species, aiming the blocking of ions. In this regard, 3 specific triple-THGEM configurations were considered and studied:

- Aligned configuration;
- Misaligned configuration;
- “Flower” configuration.

Each of these configuration is explained below, and their study is focused in the effect of both transfer fields in gain and IBF.

5.1.1. Experimental and Simulation Considerations

For the three presented configurations (aligned, misaligned and “flower”), distances were set to 2.5 mm between consecutive THGEMs, $2.0\ mm$ between the anode pads and the bottom THGEM (induction gap), and $7.6\ mm$ between the first THGEM and the drift wires (drift gap). All layers had an active area of $30 \times 30\ mm^2$. The photon detectors were operated under an Ar/CO_2 $(70{:}\,30)$ mixture, and measurements were performed with a $255\ nm$ peaked UV LED, whose light is attenuated in order to establish the single photoelectron mode, in the absence of a photocathode. The drift field was set to $0\ V/cm$ and the induction field to $3\ kV/cm$. Transfer fields 1 and 2 were scanned between 1 and $6\ kV/cm$ each. The tuning of the transfer fields allows to study the ion back flow process, and the gain variation.

The gain calculation is accomplished by the same analogue readout chain and method described in section 4.1.

The determination of the IBF is permitted by the measurement of the currents in each individual electrode of the THGEM-based detector. This current measurement is achieved by connecting each electrode to a custom, fully floating, battery powered picoammeter with resolution at the $1\ pA$ level. As the measurement of the currents, at a given instant, results in the reading of a set of 8 currents (drift wires + two electrodes per THGEM + anode), the simultaneous reading of the digital displays of the picoammeters is achieved by imaging acquisition (photograph).

For each set of measurements, in a given instant, the sum of all the negative currents I_- and the sum of all the positive charges I_+ is calculated. The total current I_{total} is therefore defined as the average of the absolute values of these currents, given by equation 5.1.

$$I_{total} = \frac{|\sum I_+| + |\sum I_-|}{2} \tag{5.1}$$

As the charge conservation, inside the detector, must be verified, the algebraic sum ΔI, of $|\sum I_+|$ and $|\sum I_-|$ is expected to be zero. The checking of the condition $\Delta I / I_{total} < 2\%$ guarantees the acceptance of the measured values.

The calculation of the IBF, for these configurations, is then defined as the ratio between the current in the upper layer of THGEM 1, and I_{total} (equation 5.2).

$$IBF = \frac{|I_{top1}|}{I_{total}} \tag{5.2}$$

The application of this IBF measuring method is based on two different assumptions. Firstly, that the electrons and ions are disentangled in each electrode, this is, that electrodes with negative currents are consequence of the collection of electrons only, while electrodes with positive currents are consequence of the collection of ions only. Although such assumption is not true, still, it is expected not to be very far from reality, and its adoption is a must, as the disentanglement of the two species is impossible. However, the consequence of such assumption is that I_{total} can be indeed higher than the determined value, leading to an optimized IBF. Secondly, and correlated with the first assumption, it is assumed that the photocurrent in the upper electrode of THGEM 1 is negligible compared to the charge in that electrode due to ion bombardment.

The determination of IBF, through the described method is, therefore, just an approximated estimation, but nonetheless, adequate for the purpose of the IBF study in this work.

The gain and IBF experimental determination are complemented by Monte-Carlo simulations and electron and ion drift lines. Such simulations are performed for the unit cell of each configuration, this is, the minimum area of each detector necessary to reproduce the whole detector, by symmetry operations. The used unit cells are presented together with each of the mentioned configurations. Furthermore, simulated gain is calculated as the total number of

production ionizations, normalized to the number of primary electrons. IBF is calculated as the number of total ions collected in the upper electrode, normalized to the total number of produced ionizations.

5.1.2. Aligned Configuration

The aligned configuration corresponds to the standard triple layer detector where the holes are vertically aligned (**Figure 5.2**). All the three THGEM layers were geometrically equal, with hole diameter of $0.4\ mm$, pitch of $0.8\ mm$ and thickness of $0.6\ mm$, presenting also a rim smaller than $5\ \mu m$.

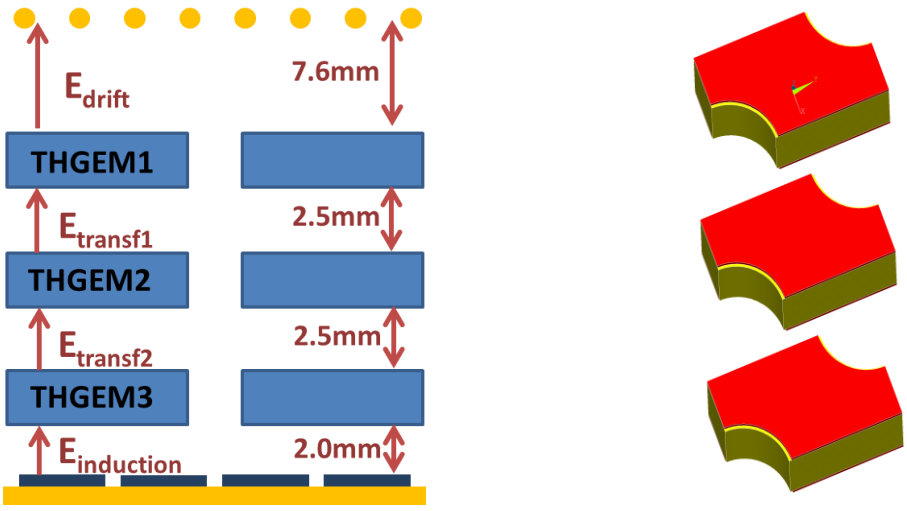

Figure 5.2 – Scheme of the standard aligned triple-THGEM photon detector (left); representation of the simulation unit cell of the aligned configuration (right).

For this configuration, the voltages were set so that $\Delta V_1 = 1450\ V$, $\Delta V_2 = 1500\ V$ and $\Delta V_3 = 1550\ V$, following the desirable operation mode where the gain is smaller in the first stage of amplification, subsequently leading to the creation of a smaller number of ions near the photocathode region. Transfer field 1 and transfer field 2 were scanned from 1 to $6\ kV/cm$, allowing the evaluation of the variation of IBF and gain, as function of these two electric fields. For the indicated ΔVs, **Figure 5.3** shows the experimental values of gain and ion back flow as function of $E_{transf1}$ and $E_{transf2}$.

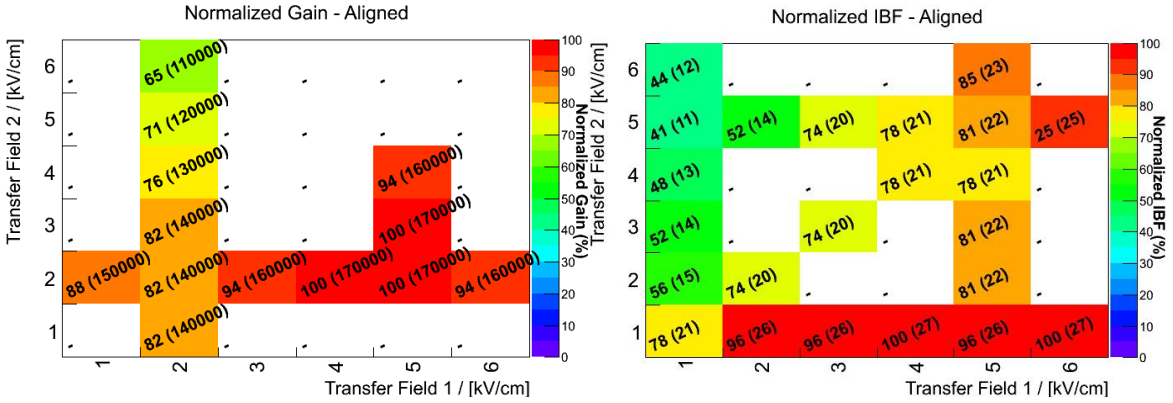

Figure 5.3 – Gain (left) and IBF (right) experimental results, as a function of $E_{transf1}$ and $E_{transf2}$, for the aligned configuration illustrated in **Figure 5.2**, in a Ar/CO_2 (70:30) atmosphere. The values are normalized to the maximum value achieved in each set of measurements, while the absolute value is presented inside brackets [105].

In this configuration, for the set of the measured fields, gain does not vary much with both transfer fields, presenting a roughly constant gain with a magnitude of 10^5, and having slightly higher values for higher $E_{transf1}$. Despite the negligible impact in gain variation, results show that it is possible to reduce the ion back flow by roughly a factor of 2.5, via tuning the transfer fields, from 27% with high transfer field 1, to 11% with low transfer field 1 and high transfer field 2.

To have a complete map of the gain and IBF behaviour, Monte-Carlo simulations were considered to understand the trend of the two parameters (gain and IBF). **Figure 5.4** shows the average simulated values of gain and IBF for 100 primary electrons, for simulations performed for the detector's unit cell represented in **Figure 5.2** (right).

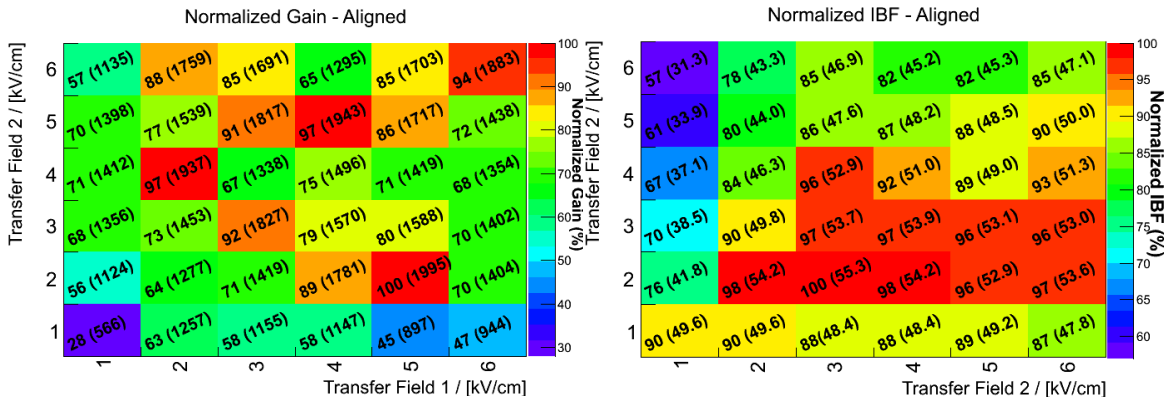

Figure 5.4 – Gain (left) and IBF (right) simulation results, as a function of $E_{transf1}$ and $E_{transf2}$, for the aligned configuration illustrated in **Figure 5.2**, in a Ar/CO_2 (70:30) atmosphere. The values are normalized to the maximum value achieved in each set of measurements, while the absolute value is presented inside brackets.

As a first comparison with experimental results, it's visible that simulated gain is considerably smaller (up to 2 orders of magnitude) than experimental values. Nonetheless, it's also clearly visible

that they share the same trend. We can, therefore, use the simulations values to extract qualitative information's regarding the missing experimental values. Gain is approximately constant in all the range of transfer fields, matching qualitatively with the information obtained experimentally, while IBF has its bigger reduction for lower $E_{transf1}$ and higher $E_{transf2}$. This situation can be schematically presented in **Figure 5.5**, where it shows the electron drift field lines (left) from the upper surface of the top THGEM, and the ion field lines (right) from the bottom of the detector until its top, for $E_{transf1} = 1\ kV/cm$ and $E_{transf2} = 4\ kV/cm$.

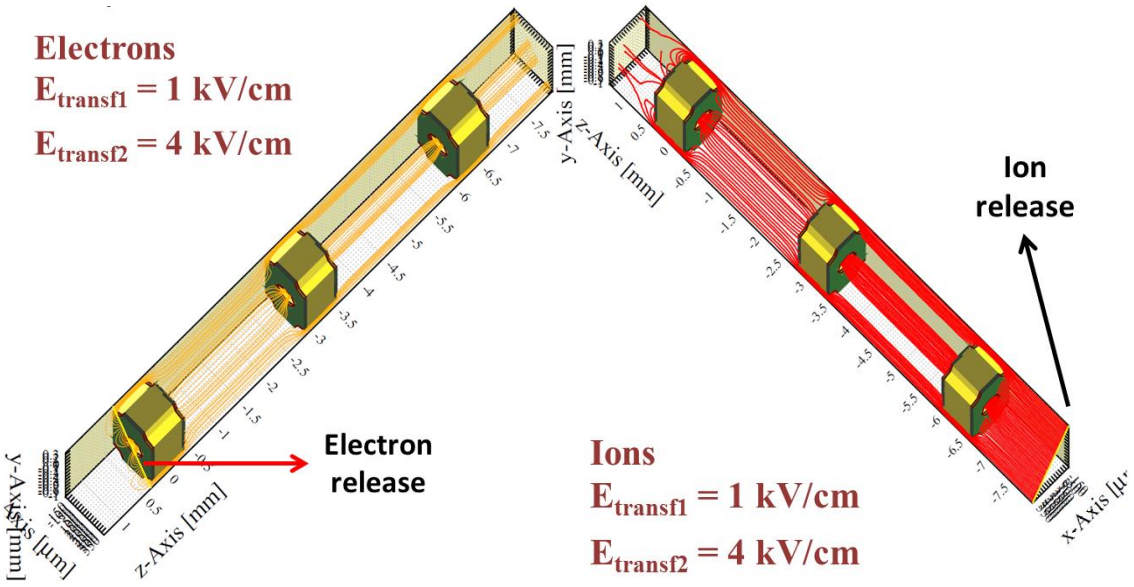

Figure 5.5 – Simulated electron (left) and ion (right) drift lines, for $E_{transf1} = 1\ kV/cm$ and $E_{transf2} = 4\ kV/cm$, for the aligned configuration.

The interpretation of these field lines, for the specific set of transfer fields, although not completely representative of all the complex behaviour of the detector, allows to understand that the vertical alignement of the holes permits on average (as diffusion of not taken into account in such representation), a fully transmission of the electrons along the cascade. This disposition of the holes, however, simultaneously allows the transmission of ions from the bottom of the detector (where the majority is produced) up to the top, leading to a poor performance of this configuration in IBF reduction. Nonetheless, the small decrease in IBF for lower $E_{transf1}$ can be explained by the dispersion of the ion drift lines in the transfer 1 gap, leading to the collection of some ions by the bottom surface of the top THGEM.

Note that the ion release in the bottom of the detector, for the ion drift lines, is just representative of their overall behaviour. Monte-Carlo simulations, on the contrary, study their trajectory from the point where they are created in the ionization.

5.1.3. Misaligned Configuration

As seen, the vertical alignment of the holes of the THGEMs, lead to a poor performance of the standard configuration in IBF reduction. The misaligned configuration aims to study the ion back flow reduction by guaranteeing the misalignment of the holes of consecutive THGEMs. Therefore, this configuration was based on the aligned one, and compared to it. It had the middle THGEM displaced in such a way that its holes were staggered compared to the ones above and below, avoiding any direct path between the first and the last THGEM (**Figure 5.6**). This configuration was inspired by pioneer studies to reduce the ion back flow using GEM multi-layer detectors with staggered hole alignment, performed by F. Sauli and collaborators [106].

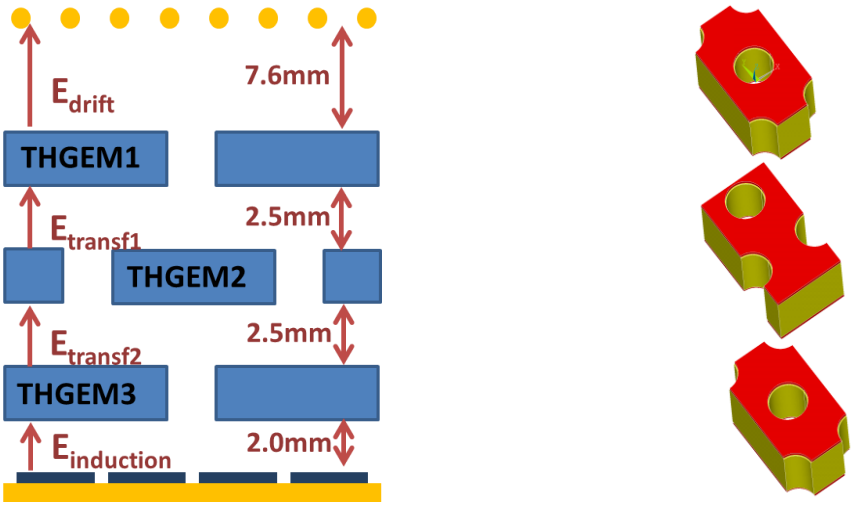

Figure 5.6 – Scheme of the misaligned triple-THGEM photon detector (left); representation of the simulation unit cell of the misaligned configuration (right).

The three THGEM layers were geometrically equal, with hole diameter of $0.4\ mm$, pitch of $0.8\ mm$ and thickness of $0.6\ mm$, presenting also a rim smaller than $5\ \mu m$. Additionally, the dipole voltages and drift and induction fields remain the same as in the previous configuration.

This configuration tries to take advantage of the diffusion properties of ions and electrons. Due to their different masses and once the related diffusion coefficient is extremely different, electrons will scatter over a bigger area compared to ions, due to diffusion processes. In presence of an applied external electric field it is then expected that ions most likely follow the electric field lines without departing from them, while electrons not.

Therefore, if in a cascade configuration, the THGEM holes of consecutive layers are not aligned, and the field configuration is chosen so that most of the field lines between two multiplication layers end up in a hole free region, ions from the multiplication processes will most likely get trapped in their way back towards the photocathode by the electrode, while electrons are not.

Figure 5.7 shows, for the misaligned configuration, the experimental values of gain and ion back flow, as function of $E_{transf1}$ and $E_{transf2}$.

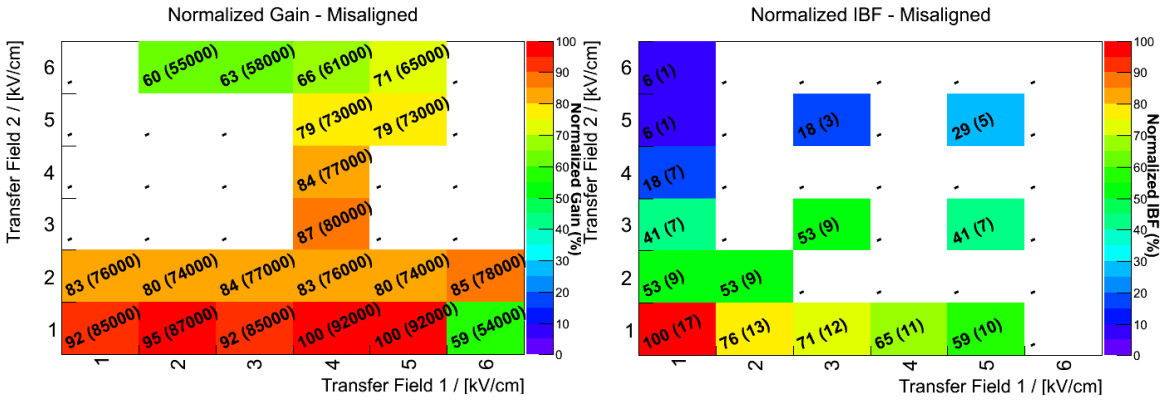

Figure 5.7 – Gain (left) and IBF (right) experimental results, as a function of $E_{transf1}$ and $E_{transf2}$, for the misaligned configuration illustrated in **Figure 5.6**, in a Ar/CO_2 (70:30) atmosphere. The values are normalized to the maximum value achieved in each set of measurements, while the absolute value is presented inside brackets [105].

For this set of measurements, although gain remains approximately constant, not far from 10^5, for transfer fields up to $5\ kV/cm$, its absolute values suffers a decrease of a factor of 2 when compared to the aligned configuration. For extremely high transfer fields ($6\ kV/cm$), a reduction in gain, up to a factor of 2, is observed. On the other hand, IBF results clearly show the effectiveness of the entrapment created by the misaligned structure, particularly for low transfer field 1 and high transfer field 2, where reductions up to only few percent of IBF are achieved.

Figure 5.8 shows the average simulated values of gain and IBF for 1000 primary electrons, for simulations performed under the unit cell represented in **Figure 5.6** (right).

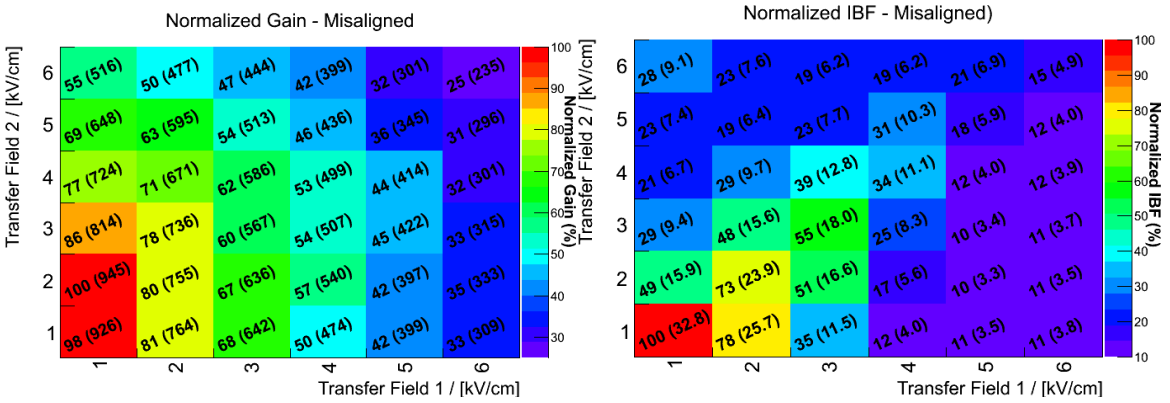

Figure 5.8 – Gain (left) and IBF (right) simulation results, as a function of $E_{transf1}$ and $E_{transf2}$, for the misaligned configuration illustrated in **Figure 5.6**, in a Ar/CO_2 (70:30) atmosphere. The values are normalized to the maximum value achieved in each set of measurements, while the absolute value is presented inside brackets.

These results, complementary to the experimental ones, lead to conclude that further IBF reduction could be possible for higher transfer values of transfer field 1, although such transfer field 1 values correspond to the domain where the decrease in gain starts to be observed.

The effectiveness of the ion entrapment of the displaced middle THGEM under the referred configuration can be understood by the simulated electron and ion drift lines, illustrated in **Figure 5.9**, for the same $E_{transf1} = 1\ kV/cm$ and $E_{transf2} = 4\ kV/cm$.

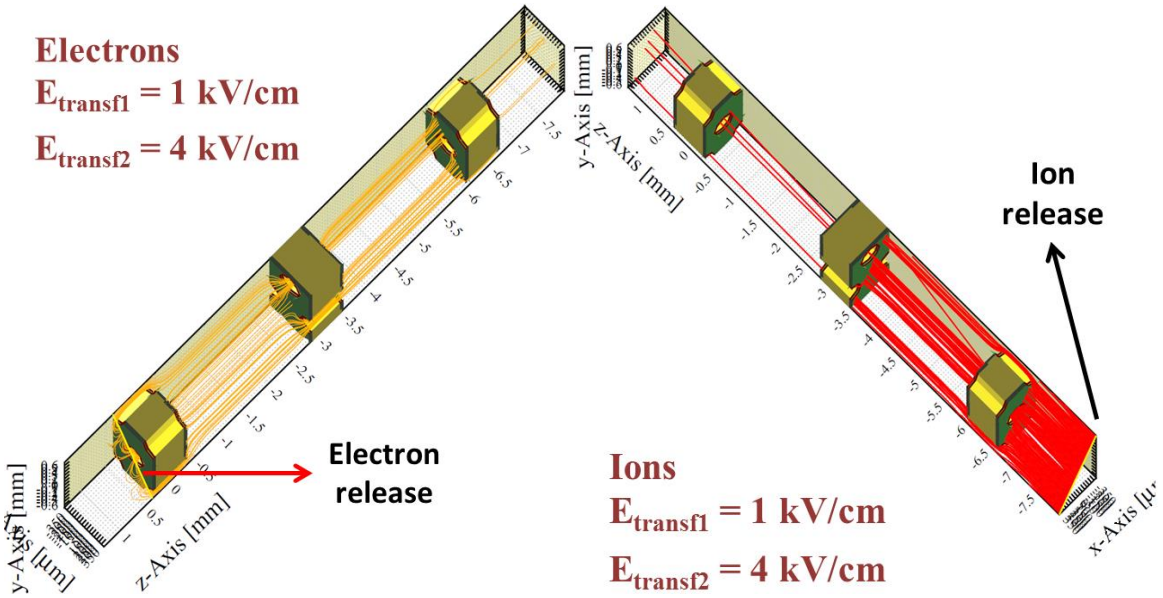

Figure 5.9 – Simulated electron (left) and ion (right) drift lines, for $E_{transf1} = 1\ kV/cm$ and $E_{transf2} = 4\ kV/cm$, for the misaligned configuration.

The evaluation of the ion drift lines (right) show that a high transfer field 2 allows the ion collection by the bottom electrode of the middle THGEM, by not allowing their deviation towards the holes. Accordingly to the simulated values, a similar high transfer field 1 could replicate the process and collect a significant part of the remaining ions in the bottom electrode of the top THGEM. Nonetheless, as the majority of the ionizations happen below the middle structure, a significant reduction in IBF can be achieved by a high transfer field 2 alone. High transfer fields also decrease the transparency to electrons. The electrons drift lines (**Figure 5.9** (left)), show that the transparency to these drift lines is high for transfer field 1, which is low, while it is significantly reduced for transfer field 2. Although such drift lines are not very representative for electrons, as diffusion is not taken into account, still, their loss in the upper surface of the bottom THGEM, for $E_{transf2} = 4\ kV/cm$, reflects the probability of losing transparency to electrons, and proves the reason why very high transfer fields must be avoided.

5.1.4. "Flower" Configuration

As the misaligned configuration proved to be effective in the IBF reduction, by collecting ions in the hole free area of bottom electrodes, a new configuration – "flower" configuration – was designed in order to maximize the hole misalignment, while simultaneously increasing the hole free area of the middle THGEM. Therefore, taking advantage of the mentioned operation principles, a

detector with a geometrical configuration was chosen so that the two consecutive THGEMS, THGEM 1 and THGEM 2 placed in a first and second multiplication stages respectively, had the following parameters:

- THGEM 1: pitch = p_1; holes diameter = d_1;
- THGEM 2: pitch = p_2; holes diameter = d_2;

So that $p_2 = p_1/2$ and $d_2 = d_1/2$. Additionally, a hole was eliminated from the centre of the hexagonal pattern distribution of the holes of THGEM 2. The pattern created with this hole removal, resulted in a sort of a flower shape (**Figure 5.10** (left)), which gave the name to this configuration. This resulted in a complete misalignment between the holes of the two first layers (**Figure 5.10**).

For the study of this configuration, THGEM 1 had a pitch of $1.2\ mm$, with a hole diameter of $0.6\ mm$ and thickness of $0.4\ mm$. THGEM 2 ("flower" structure) had a pitch of $0.6\ mm$, hole diameter of $0.3\ mm$ and thickness of $0.8\ mm$. Finally, THGEM 3 had a pitch of $0.8\ mm$, hole diameter of $0.4\ mm$ and thickness of $0.6\ mm$. All layers had rim small than $5\ \mu m$.

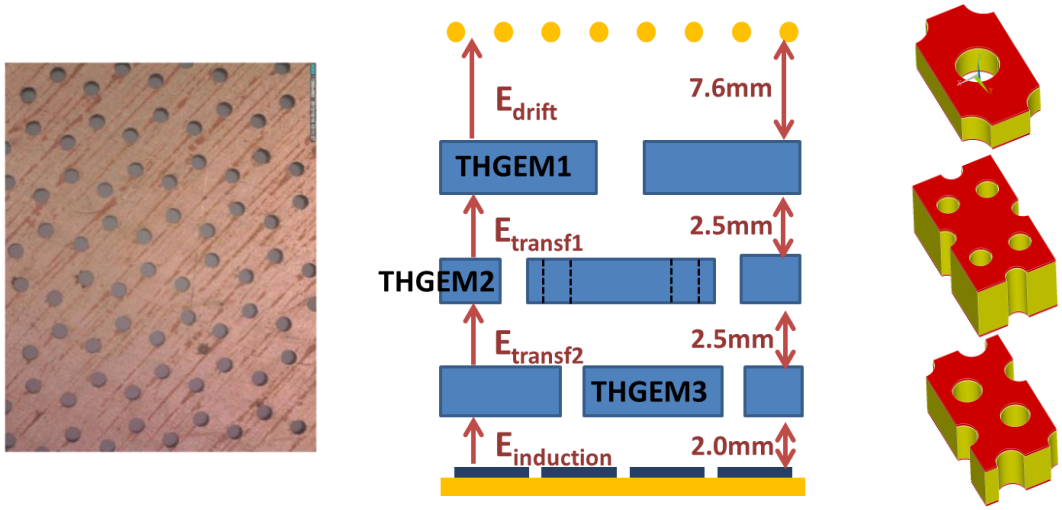

Figure 5.10 – "Flower" THGEM, with a pattern similar to a flower (left); scheme of the "flower" triple-THGEM photon detector (middle); representation of the simulation unit cell of the "flower" configuration (right).

For the "flower" configuration, voltages were set so that $\Delta V_1 = 950\ V$, $\Delta V_2 = 1900\ V$ and $\Delta V_3 = 1550\ V$ (totalizing $100\ V$ less than the previous configurations), while keeping everything else the same compared to the previous setups. **Figure 5.11** shows the experimental values of gain and ion back flow as function of $E_{transf1}$ and $E_{transf2}$.

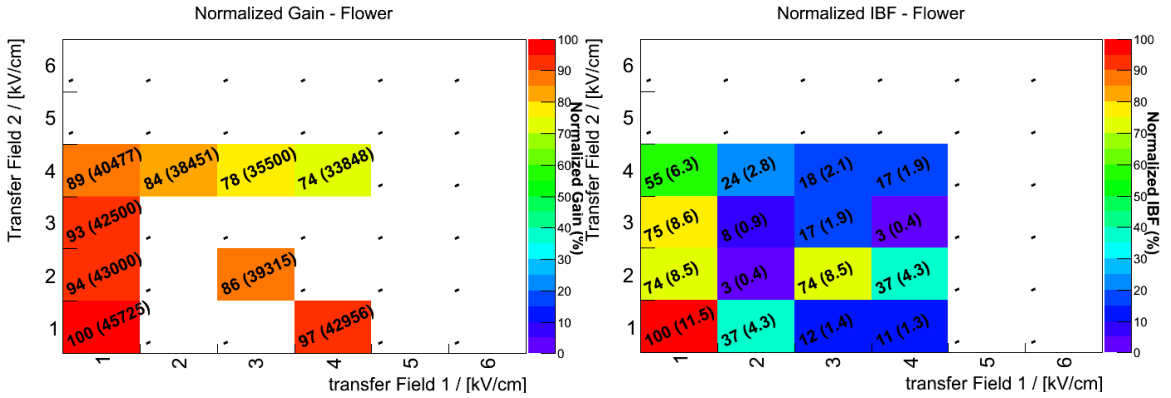

Figure 5.11 – Gain (left) and IBF (right) experimental results, as a function of $E_{transf1}$ and $E_{transf2}$, for the "flower" configuration illustrated in **Figure 5.10**, in a Ar/CO_2 (70:30) atmosphere. The values are normalized to the maximum value achieved in each set of measurements, while the absolute value is presented inside brackets.

As the few experimental results show, the gain in this configuration is reduced compared to the previous configurations, pointing to gains around 4×10^4. Nonetheless, it's important to point out that such reduction was expected, as the total applied voltage is smaller. Despite this foreseen reduction, the experimental values of gain remain approximately constant up to transfer fields of $4\ kV/cm$. In the same range of transfer fields, the IBF reductions presents a similar behaviour compared to the misaligned configuration, pointing to a slightly better effectiveness in ion entrapment, but leading overall to reductions of just few percent, in the same range of values as the misaligned configuration.

Figure 5.12 shows the average simulated values of gain and IBF for 1000 primary electrons, for simulations based on the unit cell illustrated in **Figure 5.10** (right).

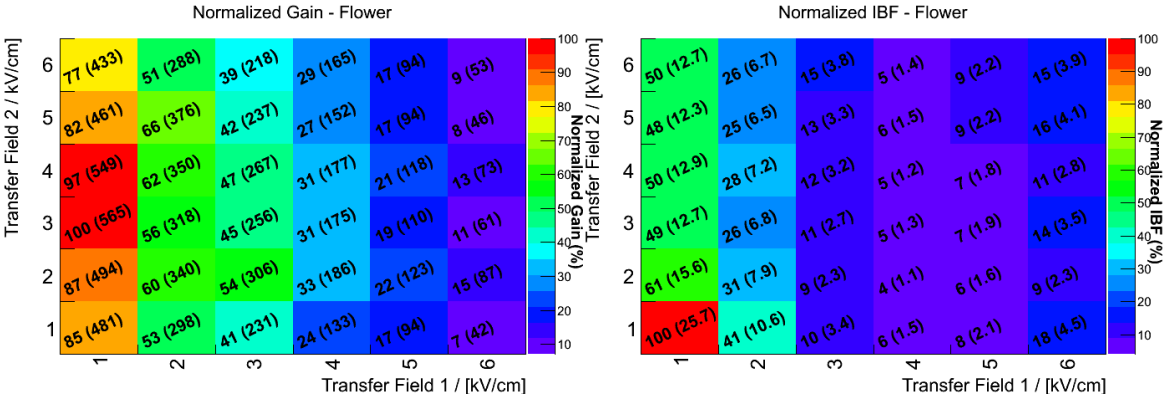

Figure 5.12 – Gain (left) and IBF (right) simulation results, as a function of $E_{transf1}$ and $E_{transf2}$, for the "flower" configuration illustrated in **Figure 5.10**, in a Ar/CO_2 (70:30) atmosphere. The values are normalized to the maximum value achieved in each set of measurements, while the absolute value is presented inside brackets.

The interpretation of such simulations allows to show that the qualitative gain variation (left) is similar to the variation observed in the misaligned configuration, while very low IBF, around few

percent, can be achieved at reasonable high transfer field 1 (~$E_{transf1} = 4\,kV/cm$), although transfer field 2 does not seem to have an important role in the IBF reduction. The irrelevance of transfer field 2 is mainly related to the fact that the hole misalignment, in this configuration, is enhanced between the first and second THGEMs, while the misalignment between the second and third structures is not necessarily guaranteed.

Figure 5.13 shows the simulated ion field lines for this configuration, for the same $E_{transf1} = 1\,kV/cm$ and $E_{transf2} = 4\,V/cm$.

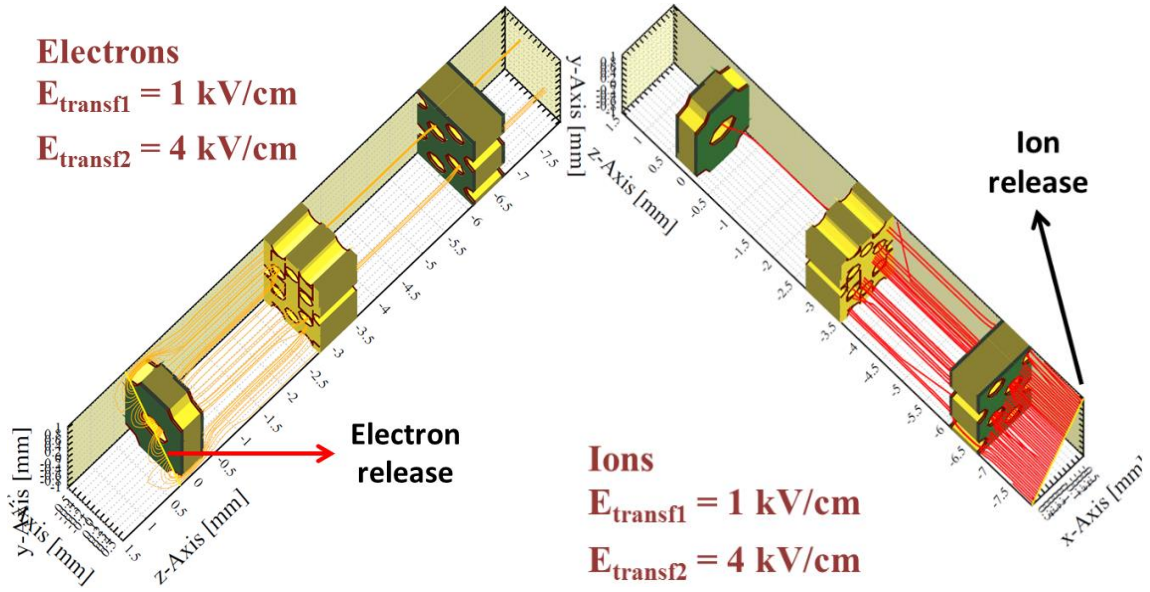

Figure 5.13 – Simulated electron (left) and ion (right) drift lines, for $E_{transf1} = 1\,kV/cm$ and $E_{transf2} = 4\,kV/cm$, for the "flower" configuration.

The transfer fields for these drift lines, although chosen to allow its comparison with the other structures, do not show the optimized performance of this configuration. Still, it shows the effectiveness of the blocking of ions in the middle structure, illustrating a quite similar behaviour when compared to the misaligned configuration.

In order to allow a direct comparison between the 3 suggested configurations to reduce ion back flow, **Figure 5.14** summarises the ionization spatial distribution and the ion collection spatial distribution, for the exemplified $E_{transf1} = 1\,kV/cm$ and $E_{transf2} = 4\,kV/cm$, based on the Monte-Carlo simulations performed. Just a qualitative analysis of the ionization and ion collection distribution are intended.

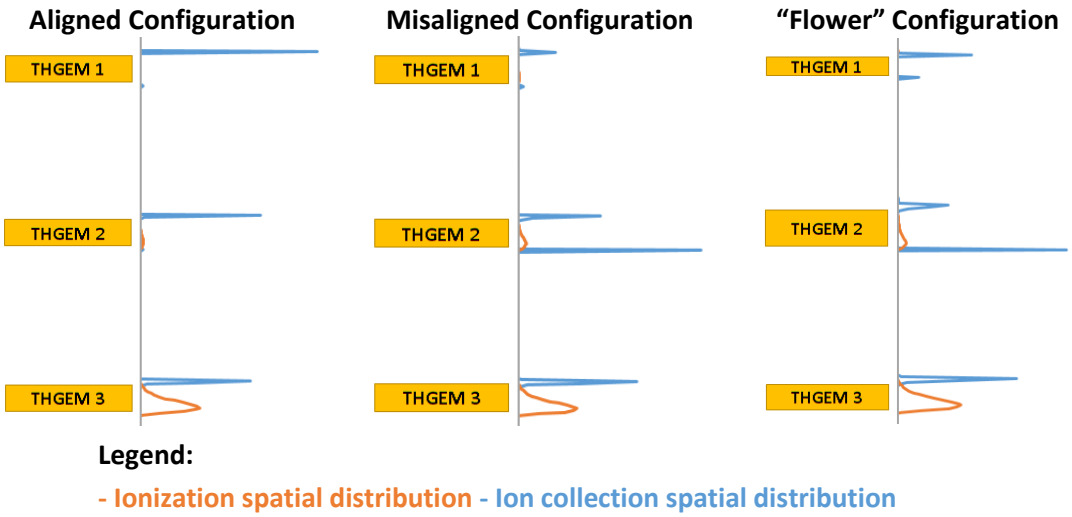

Figure 5.14 – Comparison of the simulated ionization spatial distribution, and ion collection distribution, between the aligned, misaligned and "flower" configuration, with $E_{transf1} = 1\ kV/cm$ and $E_{transf2} = 4\ kV/cm$. The height of the distributions is scaled for each configuration, but is not between configurations.

Common to the three configurations, the most significant amount of ionizations happen, as expected, in the last stage of amplification, which correspond to the creation of the majority of ions, at the opposite extreme of the electrode where the CsI photocathode is expected to be placed. In the aligned configuration, a significant part if the ions is collected by the upper electrode of THGEM 3, another significant part is collected by the upper electrode of THGEM 2, and the remaining are mainly collected by the top electrode of THGEM 1. As observed, the bottom electrodes of the 3 THGEMs play no significant role in the ion collection. Moving to the misaligned configuration, the growing role of the bottom electrodes is the main responsible of the effectiveness of the configuration for ion entrapment. While approximately the same ratio of ions, as in the previous configuration, is collected in the upper electrode of THGEM 3, a significantly large fraction is now collected by the bottom electrode of THGEM 2, consequence of the misalignment of the holes, resulting in a subsequent decrease of ions collected by the upper electrode of THGEM 1. The "flower" configuration presents a similar distribution of ion collection as the misaligned one, with a small share of ions being collected in the bottom electrode of THGEM 1, consequence of the optimised hole misalignment between THGEM 1 and THGEM 2.

5.2. Ion Back Flow Reduction by a THCOBRA-based Configuration

The approaches mentioned so far to provide a reduction of the ion back flow rely essentially on THGEM based configurations, or THGEM alike ("flower" configuration). An alternative to these approaches is the introduction of structures with additional electrodes dedicated to the ion collection. In this regard, the application of the THCOBRA was considered. Following the success of the MHSP operated in flipped-reverse mode, reaching IBF values of about 0.01%, the THCOBRA

was implemented in the same operation mode (flipped-reverse), replacing the second stage of multiplication of a THGEM based detector, aiming to collect ions from the second and third stages of multiplication.

For the study of the effectiveness of this configuration for IBF reduction, as well as its effect in gain and in photoelectron collection efficiency, the configuration CsI-THGEM/THCOBRA/THGEM was implemented (**Figure 5.15**).

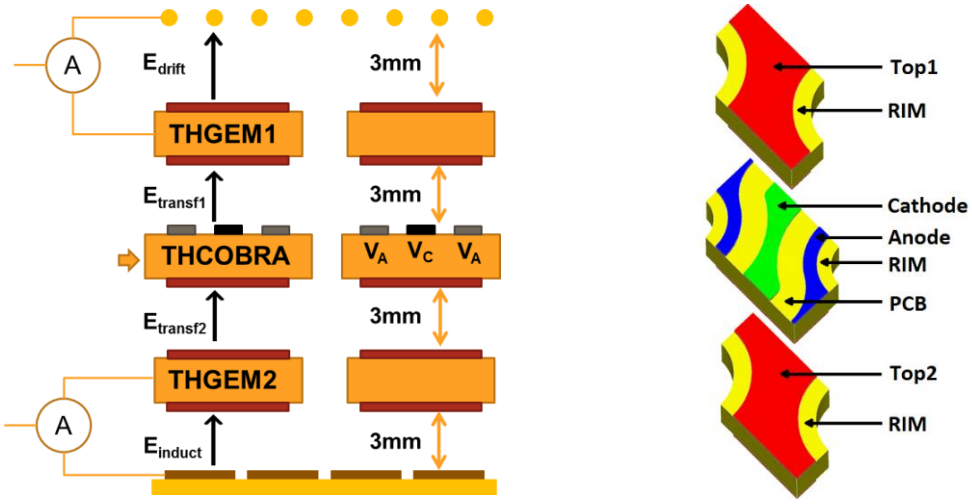

Figure 5.15 – Scheme of the THCOBRA configuration, with emphasis to the THCOBRA in flipped reversed mode as second stage of amplification, and to the interconnection of the induction gap and the drift gap (left); representation of the simulation unit cell of the THCOBRA configuration (right).

As this study was performed independently from the previous ones, in different institutions with different laboratorial conditions, the experimental setup varies, as well as the measurement techniques further explained.

A layer of approximately $500\ nm$ thick CsI photocathode was deposited by thermal evaporation on top of the first THGEM. A metallic grid is used to define the drift gap, and distances between consecutive elements (grid and first THGEM, first THGEM and THCOBRA, etc.) were set to $3\ mm$. The THCOBRA, as already referred, was used in a flipped configuration with reversed polarization, this is, the voltage of the additional electrode – cathode, is not higher than the other electrode – anode: $V_C \leq V_A$ (the naming of these electrodes is in accordance with its representation in **Figure 5.15**).

The first THGEM had a pitch of $1.0\ mm$, hole diameter of $0.5\ mm$ and rim of $0.1\ mm$; the THCOBRA had a pitch of $1.0\ mm$, hole diameter of $0.3\ mm$ and rim of $0.08\ mm$; the second THGEM had a pitch of $1.3\ mm$, hole diameter of $0.7\ mm$ and rim of $0.1\ mm$. The three structures had a thickness of $0.4\ mm$ and an effective area of $28 \times 28\ mm^2$.

For the set of performed measurements, the drift grid and the top of the first THGEM were interconnected ($\Delta V = 0\ V$), this is, their currents were measured together. In a similar way, the avalanche charge current was measured as the sum of the current in the readout pad and the current in the bottom of the last THGEM, being interconnected too (as schematically represented in **Figure 5.15**). The photon detector was operated in a Ne/CH_4 $(95\colon 5)$ mixture. A Hg(Ar) VUV lamp ($187\ nm$ peaked) was used for the measurements.

Figure 5.16 shows the internal and external appearance of the detector, complementary to its scheme previously presented in **Figure 5.15**.

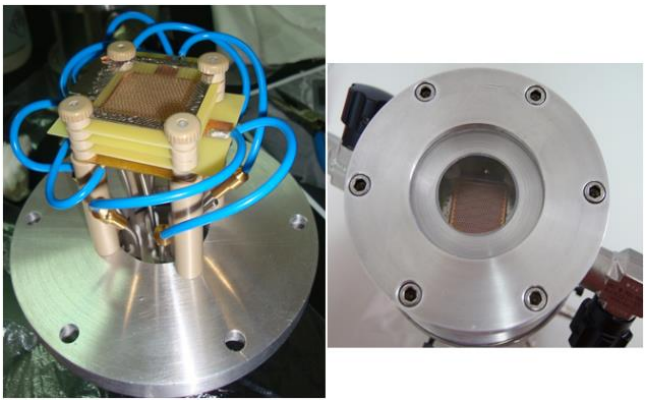

Figure 5.16 – THCOBRA detector layout: assembly of the THGEMs and THCOBRA (left); external view (right).

For this configuration, being ΔV_1, ΔV_2 and ΔV_3 the voltage difference between top and bottom of THGEM 1, THCOBRA and THGEM 2 respectively, ΔV_1 was set at $525\ V$, ΔV_2 at $580\ V$ and ΔV_3 at $600\ V$. E_{drift} was set to $0\ V/cm$ and $E_{transf2}$ to $666\ V/cm$, while varying V_{AC} ($V_{anode} - V_{cathode}$) for a set of 4 values of $E_{transf1}$ ($333\ V/cm$, $567\ V/cm$, $800\ V/cm$ and $1067\ V/cm$). Contrarily to previous configurations, the induction field was set to $0\ V/cm$, allowed as a consequence of the interconnection of the anode and the bottom electrode of THGEM 2.

The gain was estimated by exponential fits to the MCA amplitude spectra, as in the previous configurations. IBF was estimated through the ratio of the currents measured in the first interconnected stage (drift grid + top 1) and the second interconnected stage (bottom 3 + readout pad, which is roughly the total charge produced). The measurement of these currents was achieved by monitoring the voltage drop on a $10\ M\Omega$ resistor.

The determination of the photoelectron collection efficiency, however, corresponded to a rather more complex method. Such measurement was unable to be performed in current mode, as it is impossible to dissociate current variations from either gain or electron collection efficiency variations. These two components, however, can be dissociated in pulse mode, in a qualitative way. As equal gains, from two independent situations, can be evaluated from equal slopes from their single photon amplitude spectra, then, it's possible to comparatively evaluate the electron collection efficiency by comparing the number of events of each spectra, in an equal region of

interest (ROI). **Figure 5.17** exemplifies two single photoelectron amplitude spectra, with equal gain, and the region of interest, defined in the middle of the spectra, far from possible fluctuations due to electronic noise. In this regard, electron collection efficiency measurements for the THCOBRA-based configuration, were achieved under VUV irradiation. A set of spectra was acquired, over a constant time, for different values of V_{AC} at a fixed value of gain. The comparison of the number of the events, for a defined ROI, of each spectrum with the equivalent spectrum for $V_{AC} = 0\ V$ (where the THCOBRA is assumed to be equivalent to a THGEM, and therefore has a collection efficiency of 100%), allowed the evaluation of ECE.

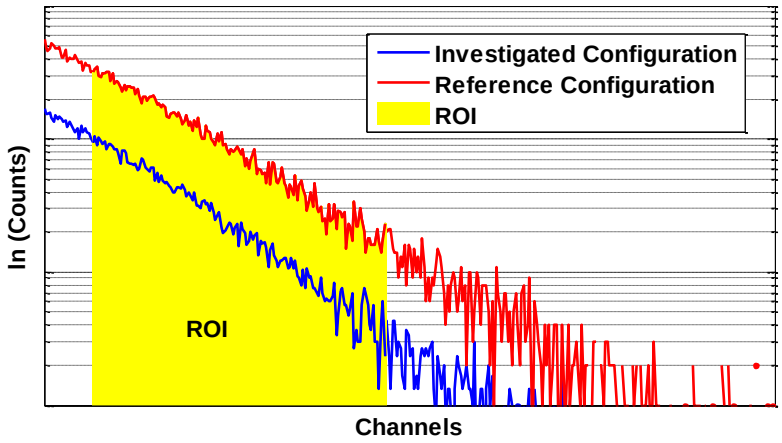

Figure 5.17 – Example of two single photoelectron amplitude spectra, with equal gain, and the defined region of interest.

Figure 5.18 shows the experimental values of gain for $E_{transf1} = 333\ V/cm$, $E_{transf1} = 567\ V/cm$ and $E_{transf1} = 1067\ V/cm$, as function of V_{AC}.

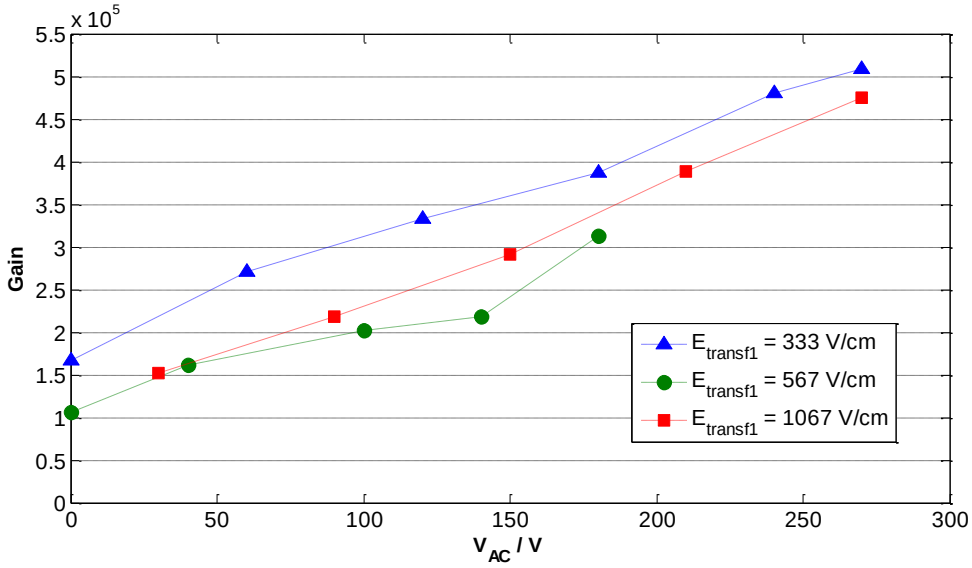

Figure 5.18 – Experimental results of gain as function of V_{AC}, for the THCOBRA configuration illustrated in **Figure 5.15**, in a Ne/CH_4 (95:5) atmosphere, for different $E_{transf1}$s.

Results show that the gain is not dependent on the applied transfer field 1, but it increases with V_{AC}, increasing up to a factor of 5, from roughly 10^5 to 5×10^5, between $V_{AC} = 0\,V$ and $V_{AC} = 300\,V$ respectively. This variation of V_{AC} is achieved by changing the voltage of the cathode, while having the voltage of the anode fixed. This procedure is followed as it is meant to keep the dipole voltage of the THCOBRA fixed, whose variation would expectedly lead to a variation in gain, just as verified for standard THGEMs.

In what regards the interpretation of the IBF results, presented in **Figure 5.19**, it is shown that the transfer field 1 gains an important role to the variation of the IBF. The higher the field is, the higher the ion back flow, being this tendency, for a fixed V_{AC}, consistent with the results verified, for instance, in the aligned configuration. While varying V_{AC}, the tendency is to have an ion back flow reduction with the increase of V_{AC}, having a global maximum between $25\,V$ and $50\,V$. As the best IBF reductions happen for smaller transfer fields and for maximum V_{AC}s, it seems that in order to verify the effectiveness of the THCOBRA structure for ion entrapment, the transfer field 1 cannot be dominant over the field between the THCOBRA upper electrodes.

Therefore, for the presented set of measurements, $E_{transf1} = 333\,V/cm$ is the field that delivers the optimal results, going down to 20% of IBF for $V_{AC} = 300\,V$.

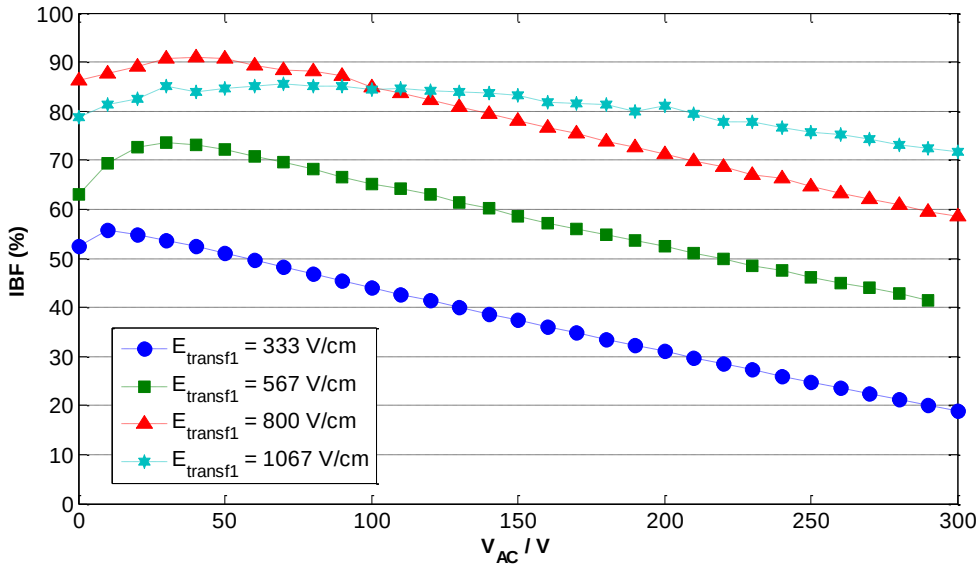

Figure 5.19 – Experimental results of Ion Back Flow as function of V_{AC}, for the THCOBRA configuration illustrated in **Figure 5.15**, in a Ne/CH_4 (95:5) atmosphere, for different $E_{transf1}$s.

In spite of the biggest IBF reduction, $E_{transf1} = 333\,V/cm$ also corresponds, to the best performance for electron collection efficiency, as presented in **Figure 5.20**. This variable, for the referred transfer field, is approximately constant above 95% until $V_{AC} = 200\,V$. Additionally, the dependency of the electron collection efficiency with the transfer field 1 shares the same tendency as the IBF: the higher the magnitude of the transfer field is, the worse the performance. Because

the electron collection efficiency measures the efficiency of the collection of electrons of a given event, a decrease of such efficiency corresponds to a possible loss in the event detection. In this regard, it's important to point out that electrons are transferred from a first stage of amplification with large holes, into the THCOBRA with smaller holes (0.5 and $0.3\,mm$ holes diameter respectively). Larger transfer fields allow a smaller deviation of the electrons due to diffusion, which lead to their possible collection by the upper electrodes of the THCOBRA, leading to a possible decrease in the electron collection efficiency.

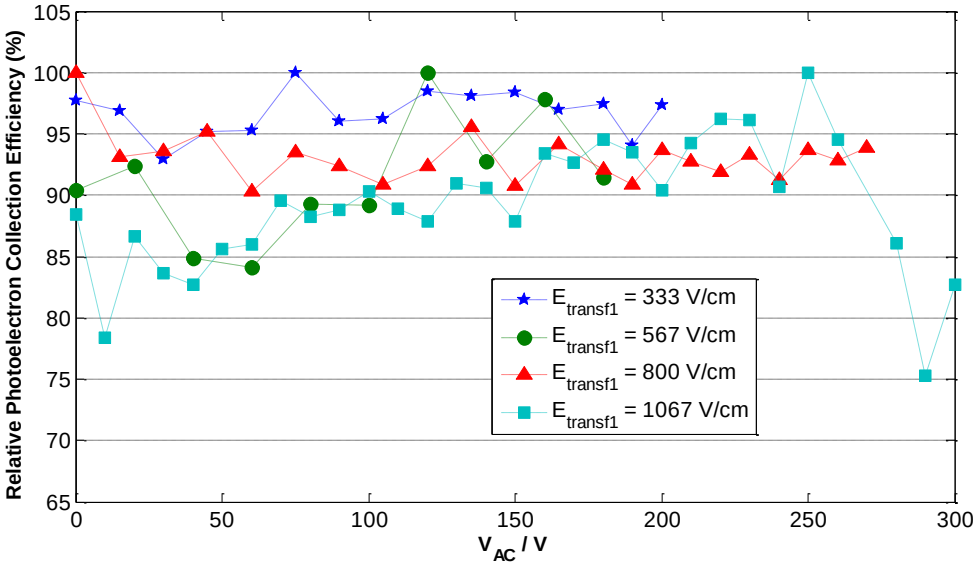

Figure 5.20 – Experimental results of Electron Collection Efficiency as function of V_{AC}, for the THCOBRA configuration illustrated in **Figure 5.15**, in a Ne/CH_4 (95:5) atmosphere, for different $E_{transf1}$s.

Despite the apparent effectiveness of the THCOBRA in the presented configuration, a doubt is introduced of whether a significant variance of V_{AC}, mainly under small transfer field 1, can induce distortions in the dipole fields of THGEM 1, jeopardizing its normal operation principle. In order to answer this question, **Figure 5.21** presents the simulated component of the electric field orthogonal to the THGEM 1 surface, $60\,\mu m$ immediately below its bottom electrode, for the two opposite extreme measured transfer field 1 ($333\,V/cm$ and $1067\,V/cm$), for both $V_{AC} = 0$ and $V_{AC} = 300\,V$). Because the whole set of results is normalized to the same colourbar, a visual and qualitative interpretation is possible.

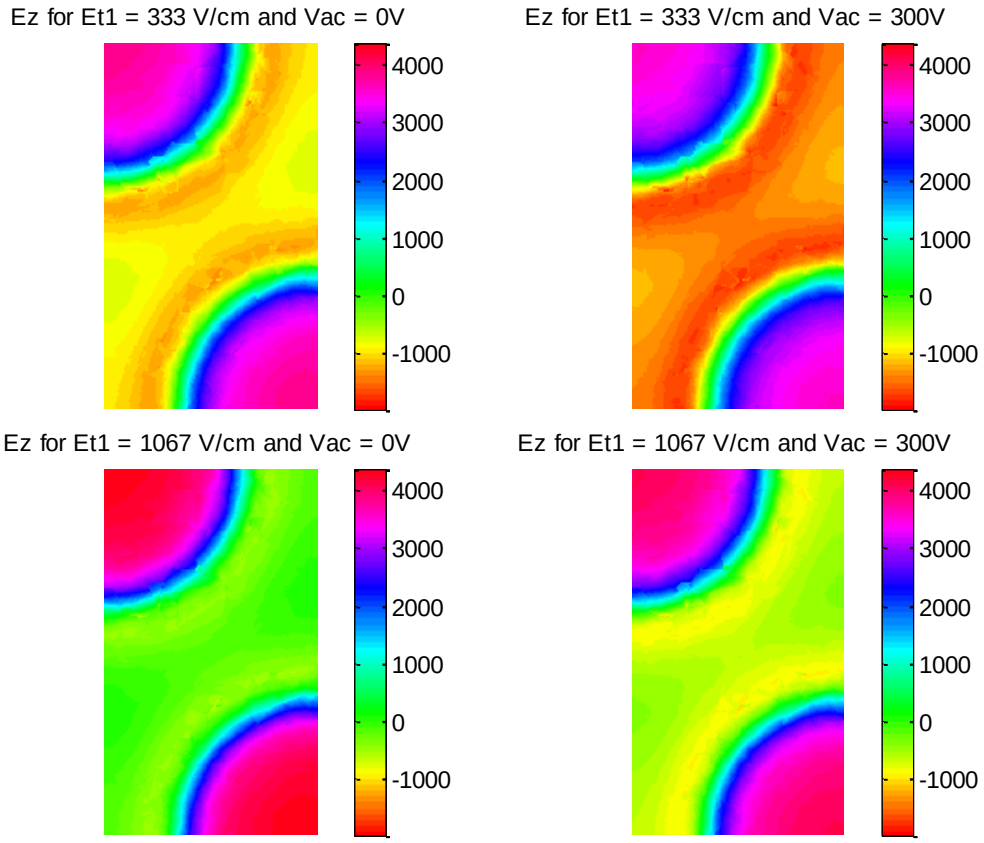

Figure 5.21 – Z component of the calculated electric field, $60\,\mu m$ below the bottom electrode of THGEM 1, in the THCOBRA configuration, for $E_{transf1} = 333\,V/cm$ and $1067\,V/cm$ and $V_{AC} = 0\,V$ and $300\,V$. Calculations were performed for the configuration's unit cell, and the holes are located in the top left and bottom right corners of each image. The electric field results, in V/cm, are normalized to the same colourbar.

The distance at which **Figure 5.21** presents the values of the electric field corresponds, approximately, to the plane after the avalanche region. At such distance, as electrons are mostly concentrated in the hole region (or its surroundings), the dependence of the field on the electrons trajectory is felt essentially on the hole area. Although a variation of the field, in the metallic region, is observed for different $E_{transf1}$s (**Figure 5.20** (top) – $333\,V/cm$; (bottom) – $1067\,V/cm$), and also for different V_{AC}s (**Figure 5.21** (left) – $V_{AC} = 0\,V$; (right) – $V_{AC} = 300\,V$), still, the variation over the hole region, or its surroundings, is negligible, being possible to conclude that the normal functioning of the THGEM is not perturbed in this range of $E_{transf1}$s and V_{AC}s.

For a further understanding of the previous variable studies (gain, electron collection efficiency and IBF), the simulated drift lines for electrons and ions for some $E_{transf1}$ and V_{AC} are presented.

Figure 5.22, **Figure 5.23** and **Figure 5.24** show the calculated electron drift lines (left) and ion drift lines (right) for $E_{transf1} = 333\,V/cm$ with $V_{AC} = 0\,V$ and $V_{AC} = 300\,V$, and $E_{transf1} = 1067\,V/cm$ with $V_{AC} = 300\,V$, respectively.

Starting with the electron drift lines just above THGEM 1, it is possible to observe that higher values of V_{AC} in a lower $E_{transf1}$ (**Figure 5.22**) allow a higher distortion of this field, leading to charge dispersion, which may result in higher electron collection efficiency. Additionally, for the situations where V_{AC} is higher (**Figure 5.22** and **Figure 5.23**), there is a higher focusing of the field lines into the THCOBRA holes, which induce a higher transparency through this structure leading to a higher gain.

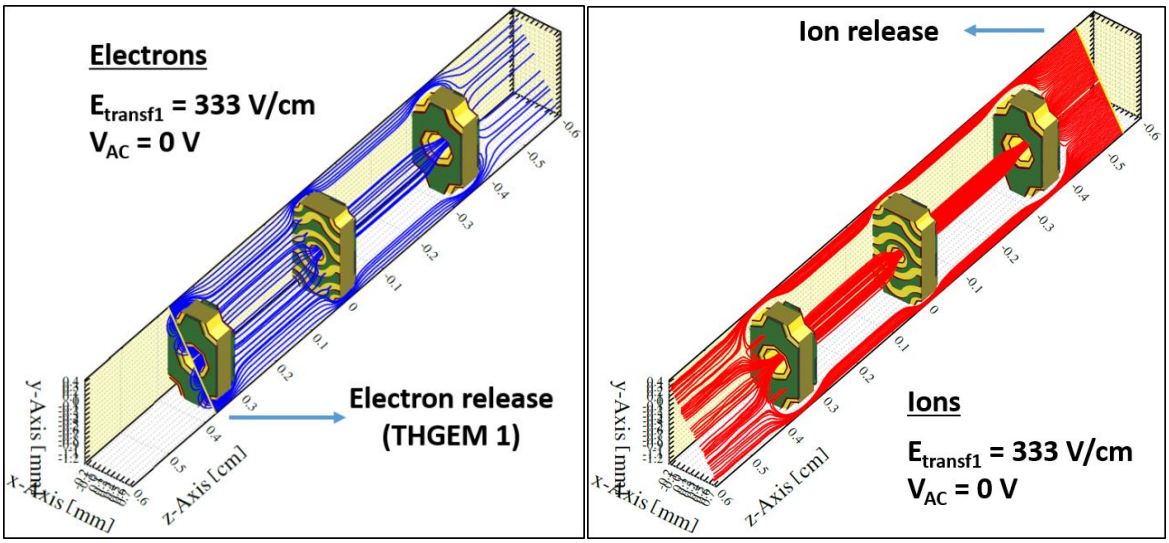

Figure 5.22 – Simulated electron (left) and ion (right) drift lines, for $E_{transf1} = 333\,V/cm$ and $V_{AC} = 0\,V$, for the THCOBRA configuration.

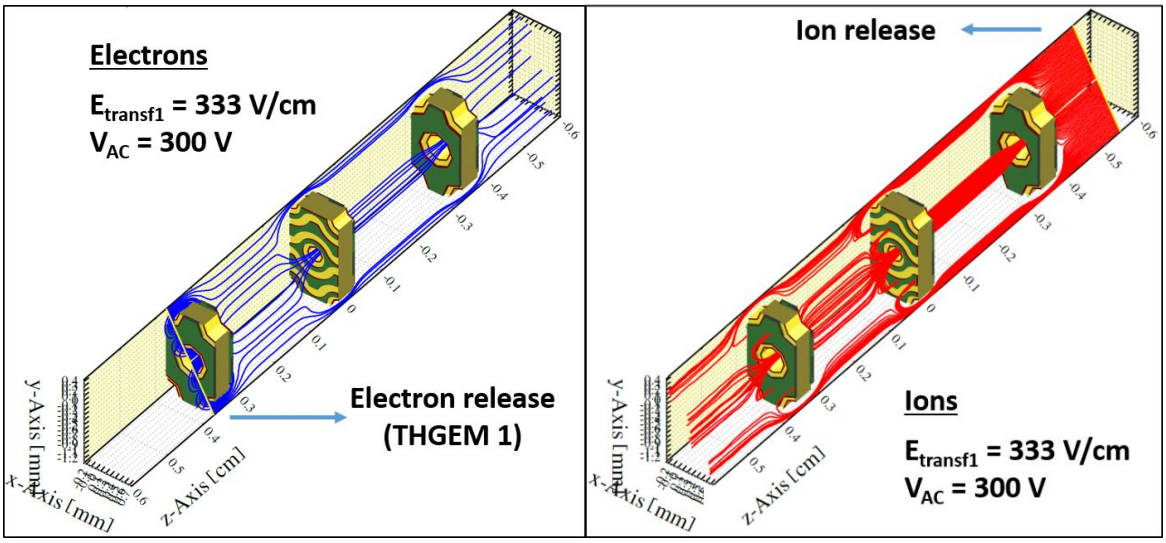

Figure 5.23 – Simulated electron (left) and ion (right) drift lines, for $E_{transf1} = 333\,V/cm$ and $V_{AC} = 300\,V$, for the THCOBRA configuration.

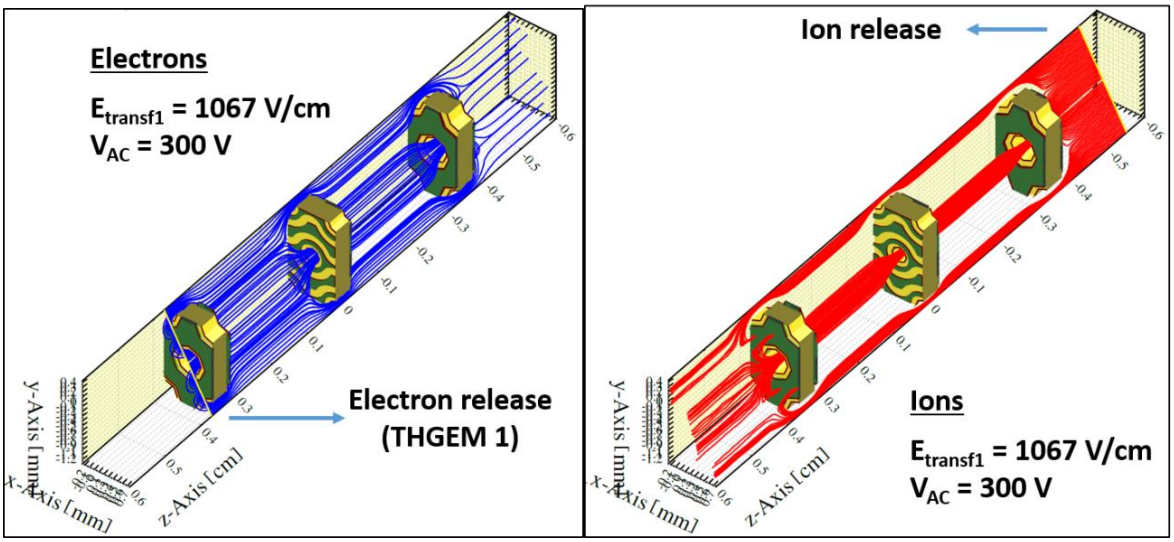

Figure 5.24 – Simulated electron (left) and ion (right) drift lines, for $E_{transf1} = 1067\ V/cm$ and $V_{AC} = 300\ V$, for the THCOBRA configuration.

Regarding the ion back flow behaviour, the drift lines start in the bottom of the detector, below the last THGEM. Thus, **Figure 5.22** shows that for a situation where $V_{AC} = 0\ V$, the THCOBRA doesn't play a different role than a standard THGEM. Nonetheless, keeping a low $E_{transf1}$ and high V_{AC}, as in **Figure 5.23** with $V_{AC} = 300\ V$, ions start being collected by the electrodes of the THCOBRA, decreasing the ion back flow. As shown in **Figure 5.24**, a high $E_{transf1}$ diminishes the effect of V_{AC}, reducing the importance of the THCOBRA as such.

According to these ion drift lines simulations, it's important to point out that, from the ions that reach the drift gap, some fraction is undesirably collected by the upper electrode of THGEM 1, but a large fraction is also lost towards the drift grid. As the IBF experimental measuring method relates the currents in the whole drift gap with the currents in the entire induction gap, it is possible to conclude that the determined IBF is indeed not higher than the real value, as the ions reaching the drift grid are equally considered for the calculation.

Following the presented results for the THCOBRA configuration, low transfer field 1 with high V_{AC} corresponds to the best operation conditions to achieve the highest gain, with the most efficient IBF reduction, with optimal electron collection efficiency. As a way of concluding the effectiveness of the ion collection by the THCOBRA in these conditions, **Figure 5.25** shows the ionization spatial distribution and the ion collection spatial distribution, for the THCOBRA configuration, based on the integration of Monte-Carlo simulations for 50 primary electrons, for $E_{transf1} = 333\ V/cm$ with $V_{AC} = 0\ V$ (left) and $V_{AC} = 300\ V$ (right).

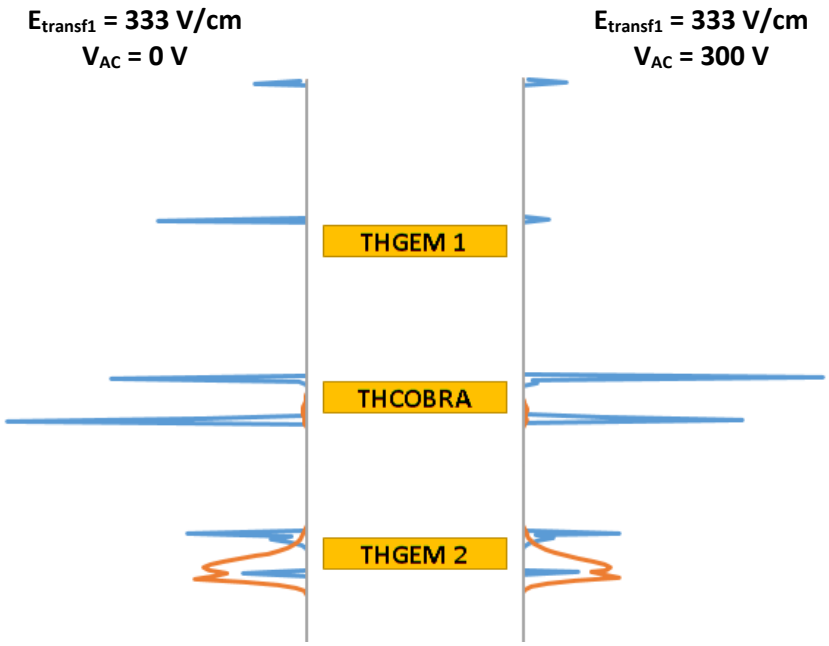

Legend:

- Ionization spatial distribution - Ion collection spatial distribution

Figure 5.25 – Comparison of the simulated ionization spatial distribution, and ion collection distribution, in the THCOBRA configuration, between the situation where $V_{AC} = 0\,V$ (left) and $V_{AC} = 300\,V$ (right), for the same $E_{transf1} = 333\,V/cm$. The results, whose distribution height is not scaled between different configurations, correspond to the integration of 50 primary electrons simulated.

The evaluation of the distribution of ionizations resembles the distribution in the standard triple THGEM detectors, where the majority of the ionizations happens in the last stage of multiplication. Nonetheless, and on the contrary to the former standard configurations, a double peak is observed in the ionization distribution. Such phenomena is a consequence of the THGEM's large rim ($0.1\,mm$), which result in a second stage of multiplication, inside the same structure, near the metallic edges. The V_{AC} of the THCOBRA has no effect on the overall distribution of the ionizations. However, for the ion collection distribution, V_{AC} plays an important role. For $V_{AC} = 0\,V$, large fractions of ions are collected by the bottom and upper electrodes of the THCOBRA, and by the upper electrode of THGEM 1. Tuning V_{AC} to $300\,V$, a redistribution of these fractions is observed. A fraction of ions previously collected by the bottom THCOBRA electrodes and by the top electrode of THGEM 1 are now collected by the THCOBRA anode and cathode, leading to the reduction of the ion back flow. A small fraction of ions, independently from V_{AC}, is collected in the drift grid.

5.3. Conclusions

An ion back flow reduction, imposed by the detector's limitations due to the ion bombardment of the photocathode, was achieved by all the proposed configurations.

In what regards the IBF reduction by staggered hole configurations, results show that both the misaligned and the "flower" configurations are promising approaches. Compared to the aligned configuration, which is the standard triple-THGEM configuration, both allow an IBF reduction up to roughly 1% although the "flower" configuration suffers a non-negligible reduction of gain.

On the other hand, the study of the approach of IBF reduction by dedicated electrodes shows good potential for the application of the THCOBRA concept as ion trap, operating at flipped-reverse mode, in CsI triple-THGEM photon detectors, replacing the middle THGEM. The implementation of this concept allows a reduction of ion back flow down to 20% with a minor effect in the electron collection efficiency. Although these IBF values seem far above the ones achieved by the staggered hole configurations, it's important to point out that a direct comparison is not possible, as different methods for the IBF determination are considered. Because the IBF calculation for this specific configuration considers all ions in the drift gap, it's possible to infer that ions reaching the photocathode, might be just a fraction from the presented value.

Considering all the studied configurations, and since IBF reductions at to at least 5% are aimed, the misaligned configuration appears as the most promising option to be applied in further THGEM photon detectors coupled with CsI photocathodes. The configuration presents IBF of only few percent with possible high gain, and corresponds to the simplest arrangement, with the least geometrical constrains, as long as THGEM with the same pitch are used.

Additionally, through the comparison between simulations and experimental data, it is possible to conclude that, despite the incongruity between the absolute values, simulations share the same trend as the experimental results. Therefore, simulations are a reliable tool that can be used for further detector studies and optimizations.

6. THGEM Based Detectors Performance under Beam Conditions

The THGEM based detectors operation in laboratorial conditions proved to be possible, as described in the previous chapters. Despite the apparent success of such devices under the referred conditions, it's important to emphasise, again, that their development is aimed to RICH detector applications, envisaging, in particular, the upgrade of the RICH-1 detector at the COMPASS experiment.

This tangible application of the detectors under study introduces several new variables, not reproducible in laboratorial environment, which can limit the performance of the THGEM based detectors. These new variables correspond mainly to the operation of the detectors under a radioactive environment and irradiation with Cherenkov photons.

The conditions at which final THGEM-based detectors may possibly operate in the future, can be reproduced at particle accelerator facilities, irradiating the selected detectors with particle beams. The use of particle beams for the testing of detectors is henceforth designated by "test beam".

Several test beams were performed over time, of which two particular campaigns, performed in 2010 and 2012 respectively, are presented, as they are the only two worth presenting. Such experiments aim a deeper understanding of the THGEM-based detectors, comparing their performance with the laboratorial acquired knowledge, while evaluating their stability under more demanding conditions.

6.1. 2010 Test Beam Campaign

The 2010 test beam campaign was performed at the H4 $150\ GeV/c\ \pi^+$ line at CERN. It aimed an initial study of small area THGEM-based photon detectors irradiated with Cherenkov radiation, while exposed to radioactive environment. For this initial study, a comparison between Cherenkov light and UV LED light was performed, along with the study of the time distribution spectra as function of the applied voltage.

6.1.1. Experimental Setup

The setup under study comprised a single chamber containing three sets of THGEM-based photon detectors, and one position sensitive photomultiplier Hamamatsu MAPMT R7600 M16. These four detectors where placed in a quadrilateral way, around the beam axis, but away from the beam acceptance, this is, with no detector directly crossing the beam line. **Figure 6.1** illustrates schematically the detectors' disposition compared to the beam axis, while **Figure 6.2** illustrates the real disposition of the detectors compared to the chamber geometry.

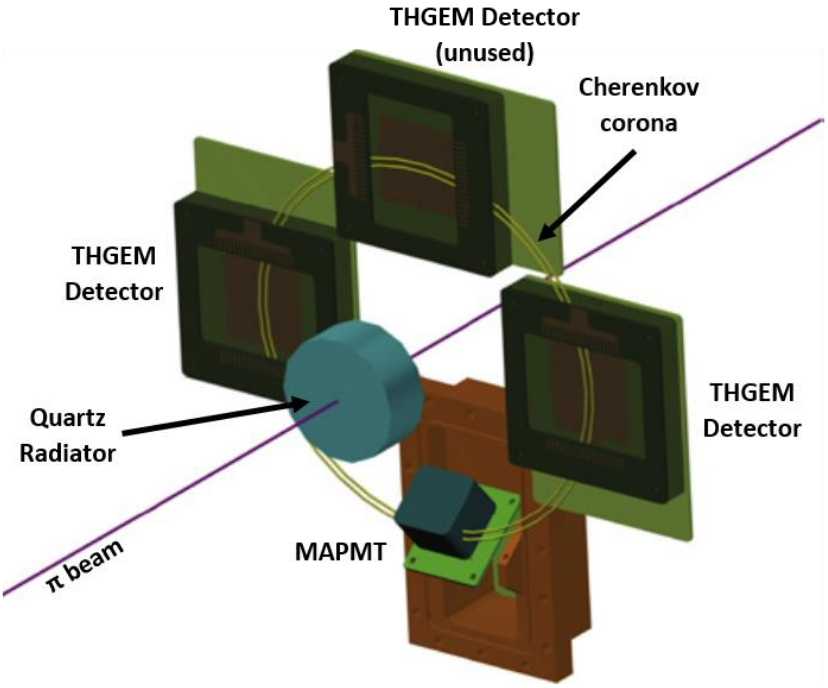

Figure 6.1 – Scheme of the detector operated during the 2010 test beam, where the triple THGEM detectors are visible, as well as the multi-anode photomultiplier, placed around the beam axis. A representation of the Cherenkov corona, created and focused by the hemispheric quartz radiator, is also presented.

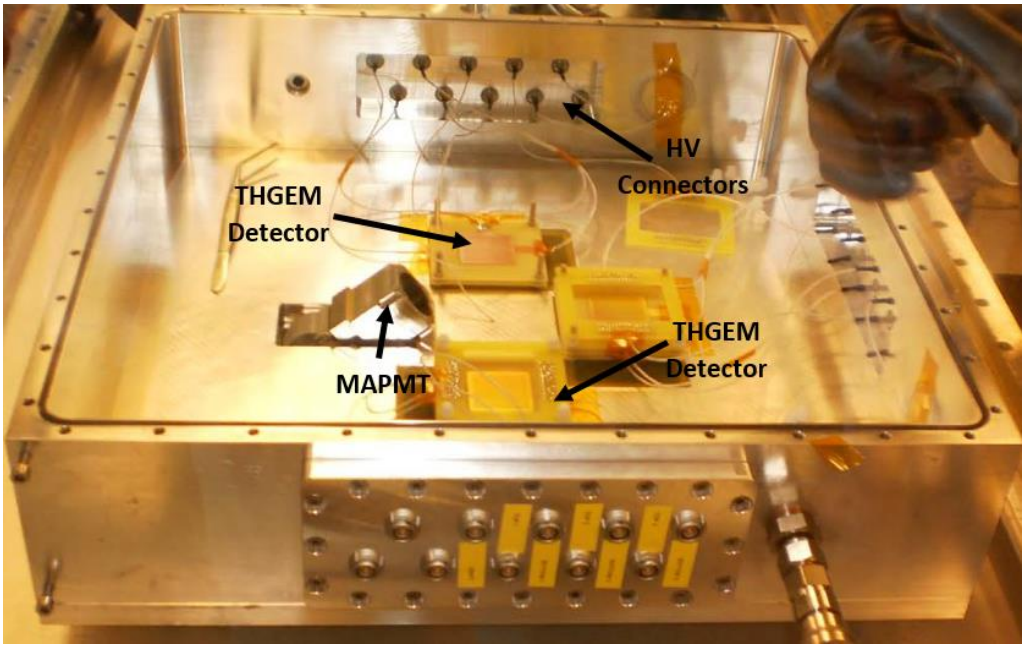

Figure 6.2 – Positioning of the triple THGEM detectors and the MAPMT inside the chamber. The high voltage connectors for the THGEM layers are also visible.

In the upper cover of the chamber containing the detectors, a hemispheric quartz radiator was placed, in order to produce Cherenkov photons and focus them into the photon detectors. Although this radiator provides single photon illumination, the pile-up of events virtually create a corona, from which four arcs are intercepted by the four detectors. This virtual corona, along with the hemispherical radiator, are also illustrated in **Figure 6.1**.

Additionally to the Cherenkov light, a UV LED can be externally mounted in front of each of the lateral THGEM detectors, irradiating the photon detectors through small area quartz windows.

From the three THGEM-based photon detectors, the upper one was not operated, and therefore, from now on it is no longer considered. The two lateral THGEM detectors consisted in triple layer configurations, with all identical $30 \times 30\ mm^2$ THGEMs, with $0.4\ mm$ thickness, $0.4\ mm$ holes diameter, and $0.8\ mm$ pitch, and negligible rim, coupled to a reflective CsI photocathode. The configuration layout, with the respective spacing between layers, is schematically presented in **Figure 6.3**.

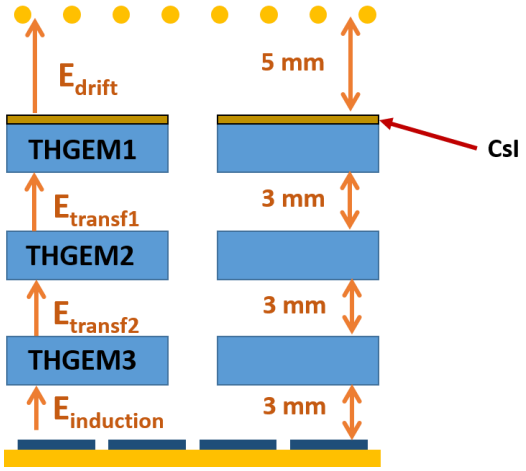

Figure 6.3 – Scheme of the triple layer THGEM configuration used in the 2010 test beam (distances not in scale).

Additionally to the THGEM detectors, the MAPMT was meant to be used as a reference, as it is currently used in RICH-1 detector. This photomultiplier comprises a Bialkali photocathode, a $18 \times 18\ mm^2$ borosilicate glass window, and has 16 (4×4) anode channels. Due to the presence of this window, the MAPMT is oriented in such a way so that the incident Cherenkov photons are perpendicular to the window, avoiding undesirable reflections. Theoretically, the distance from the radiator to the surface of all detectors is the same.

The whole setup was operated under an Ar/CH_4 $(50:50)$ atmosphere, provided through a "once-through" gas circuit type, at atmospheric pressure. All THGEM layers of each detector were powered by CAEN N471A or 1471A (remotely controlled), through a resistive divider, providing voltages and electric fields previously studied and selected. For the set of tested gaseous photon detectors, for the referred gaseous mixture, typical gains are in the order of 10^5.

The charge collection signal from the gaseous photon detectors was achieved by connecting the THGEM-based photon detectors, either to the standard analogue readout chain (Cremat CR-110 charge sensitive preamplifier + Ortex Amplifier + Amptek MCA8000A multichannel analyser), or to a Digital readout. The presented results correspond to measurements performed with this digital readout, which corresponds to the COMPASS RICH-1 MAPMT readout system (chapter 3.4), with the MAD4 preamplifier/discriminator upgraded to a CMAD front end chip.

The operation of the digital readout requires a trigger system in order to start and stop the data acquisition. This trigger system is based in a total of 6 scintillators coupled to photomultipliers, spatially placed accordingly to the scheme presented in **Figure 6.4**.

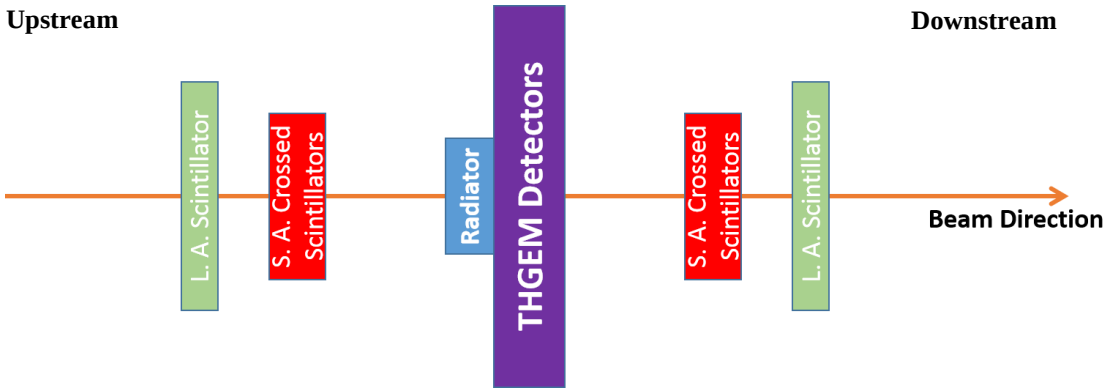

Figure 6.4 – Layout of the trigger components, along the beam axis, compared to the THGEM detectors. Large area scintillators (L. A. Scintillators) are placed in the outer region, while the small area scintillators are placed between the large area ones and the detector (distances not in scale).

Two large area scintillators (L. A. Scintillators) are placed at extreme end points of the experimental setup, one upstream and one downstream. With their active area of $100 \times 100\ mm^2$, they intercept the whole beam, and therefore provide the number of crossing particles, as well as they provide the input signal to start the data acquisition. **Figure 6.5** (left) illustrates the large area scintillator. Additionally, four small area scintillators (S. A. scintillators), with dimensions of $5 \times 3\ mm^2$, are placed, grouped in two, at intermediate distances between each L. A. scintillator and the THGEM-based photon detectors. The two S. A. scintillators of each set are oriented by 90 degrees compared to each other, as exemplified in **Figure 6.5** (right); this disposition allows a xy screening of the beam, allowing the alignment of the radiator with the beam.

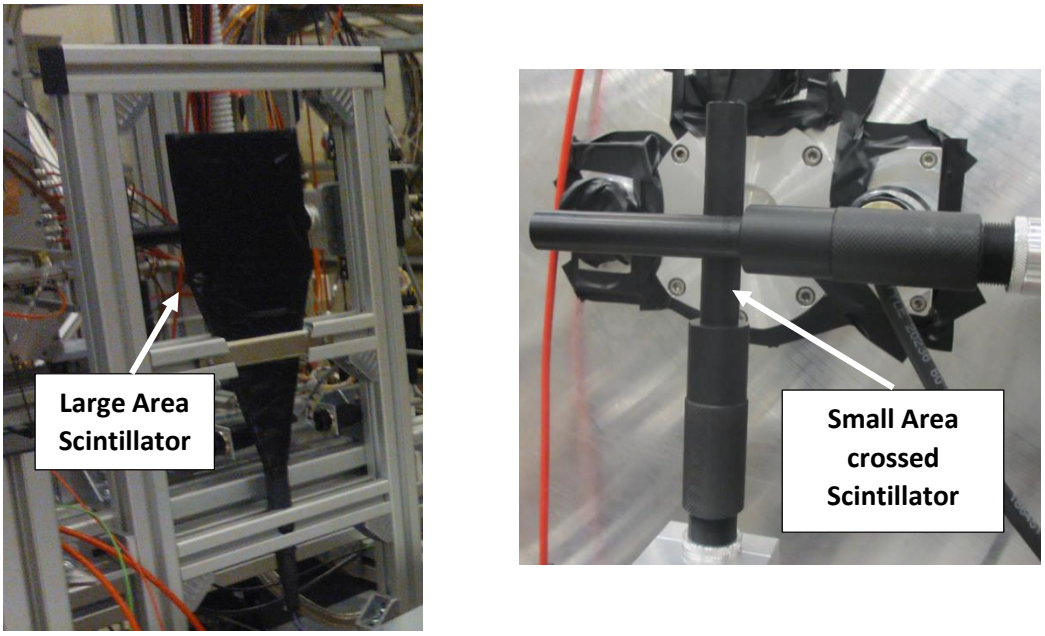

Figure 6.5 – Large area scintillator (left); small area scintillator, with emphasis to perpendicular disposition of 2 scintillators (right).

6.1.2. Cherenkov Light versus LED

Chapters 4 and 5 showed the capability of the THGEM based detectors to operate under VUV light and ionizing radiation. The operation of the mentioned detectors under beam irradiation, although desirable, introduces the unknown uncertainty of the detector's response when compared to previous tested sources. In this regard, a comparison between the operation of the THGEM detectors with beam irradiation and with a $265\ nm$ peaked pulsed LED was performed. The choice of the LED light for this comparison, among the options used in laboratorial tests, was firstly due to simpler hardware implementation, and secondly because of the fact that, due to its nature, it's the one that better compares to Cherenkov light.

An initial test was performed in order to compare the multiplicity of the THGEM detectors operated both with beam and UV LED light. The multiplicity is a measure that correlates, accordingly to equation 6.1, the number of detected photons with the number of triggered events.

$$Multiplicity = \frac{Number\ of\ detected\ photons}{Number\ of\ triggered\ events} \tag{6.1}$$

Figure 6.6 shows the normalized multiplicity distribution, as function of the number of detected photons per event n, for both the presented situations, with the detectors operated with a total applied dipole voltage of $\Delta V_{total} = 4.35\ kV$.

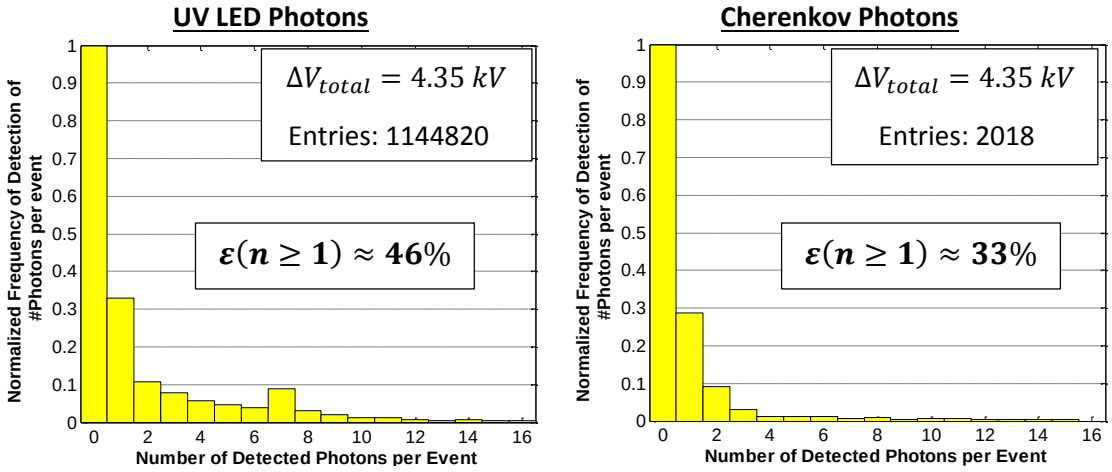

Figure 6.6 – Multiplicity distribution for UV LED photons (left) and Cherenkov photons (right), for $\Delta V_{total} = 4.35\ kV$. The variable $\varepsilon(n \geq 1)$ defines the efficiency of detecting at least one photon per triggered event.

As a first observation, the multiplicity of both sources, follow a rather similar distribution, and suggest an expected Poisson distribution, consequence of operation under a single photon regime.

A more careful observation leads to perceive the existence of minor discrepancies in both distributions, which can be related to the nature of both light sources. In the beam example, a triggered particle crosses the radiator, creating a reduced number of Cherenkov photons. Each of these Cherenkov photons has an approximate probability of 30% of emitting a photoelectron from the CsI photocathode (defined by the QE of the photocathode), each of which, if emitted, can originate a detectable charge in the anode. LED photons, on the other hand, are triggered, irradiating the CsI photocathode with a controlled flux of photons. As the number of UV photons emitted by the LED is significantly higher to the Cherenkov photons, proven by the significantly different number of entries indicated in both distributions, it is reasonable to conclude that it is more likely to detect a higher number of photons per event using a LED. Additionally, although operated in a single photon regime, the LED, due to its high number of emitted photons, has a non-null probability, although small, of overlapping events leading possibly to the slightly higher frequencies of detection of 1 or more photons per event.

Therefore, despite minor differences, the detectors irradiated by UV LED light or Cherenkov light perform in a similar way, with the efficiency ε of detecting at least one photon per event ($n \geq 1$), being function of the number of emitted photon.

A complementary exercise allows the comparison of the time distribution spectra of the collected events. This comparison was performed for $\Delta V_{total} = 4.38\ kV$ and the results are presented in **Figure 6.7**.

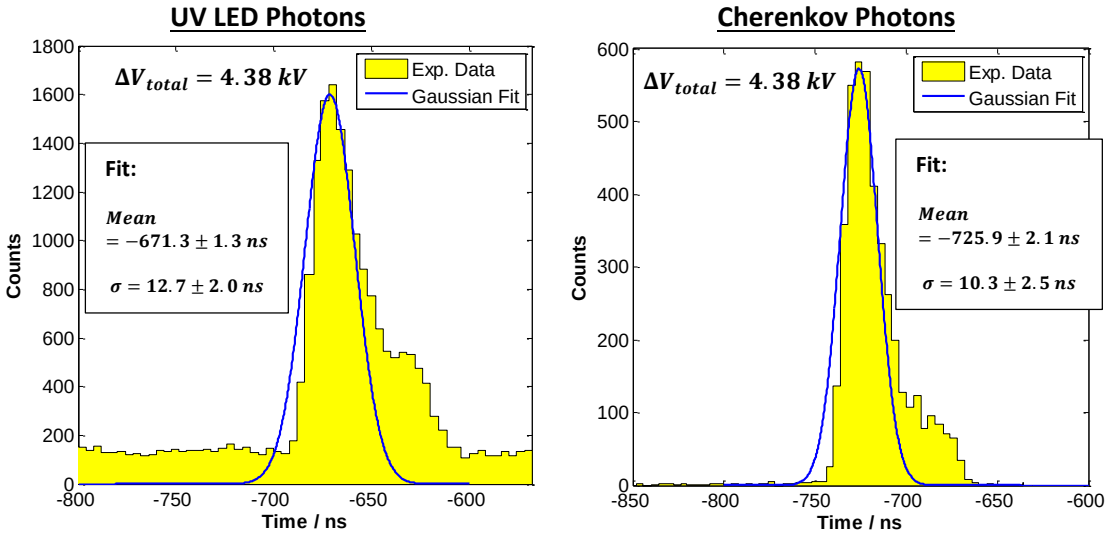

Figure 6.7 – Time distribution spectra for events from UV LED photons (left) and Cherenkov photons (right), for $\Delta V_{total} = 4.38\ kV$.

A primary interpretation of the results show that both the UV LED (left) and the Cherenkov (right) photons result mainly in a Gaussian shaped time distribution of the events. It's important to point out that the Gaussian mean value, independently for each spectrum, does not have a real physical interpretation, as the absolute time scale does not correspond to a defined distance. However, in the cases where the emitted photons have the same origin, a relative evaluation of the mean value is possible. As in this case, the Cherenkov photons and the UV LED photons do not share the same origin, an evaluation of the peak displacement is not allowed.

Additionally, the LED time distribution spectrum shows a baseline not visible in the beam time distribution spectrum. This difference can be once again related to the a significantly higher emission of photons from the LED source when compared to Cherenkov photons, leading to a slightly higher σ, which are respectively 10.3 and $12.7\ ns$. A secondary component, delayed from the primary one is observed too, and consistent for both spectra, and its nature is further explained.

Based on the similarity of the time distribution spectra and the multiplicity distributions, for both sources, it is possible to conclude that both the tested sources induce a very similar response from the detectors, allowing to go further with the beam studies, with assumptions validated from the previous laboratorial exercises.

6.1.3. Signal Time Distributions

As previously mentioned, the absolute mean value of the presented time distribution spectra does not have a physical meaning. Nonetheless, the relative comparison of mean values is possible for equivalent events. In this regard, the MAPMT, assembled in the chamber, is of major interest,

as such technology is very well studied, and its vacuum operation mode guarantees a very fast photon detection. Because the photosensitive surfaces of the MAPMT and the THGEM-based detectors are at the same distance from the radiator, it is possible to measure the delay of the electrons transit time of the THGEM detectors when compared to the MAPMT. **Figure 6.8** shows the time distribution spectra of the MAPMT and of the THGEM-based detector, operated at typical gain, under Cherenkov light irradiation.

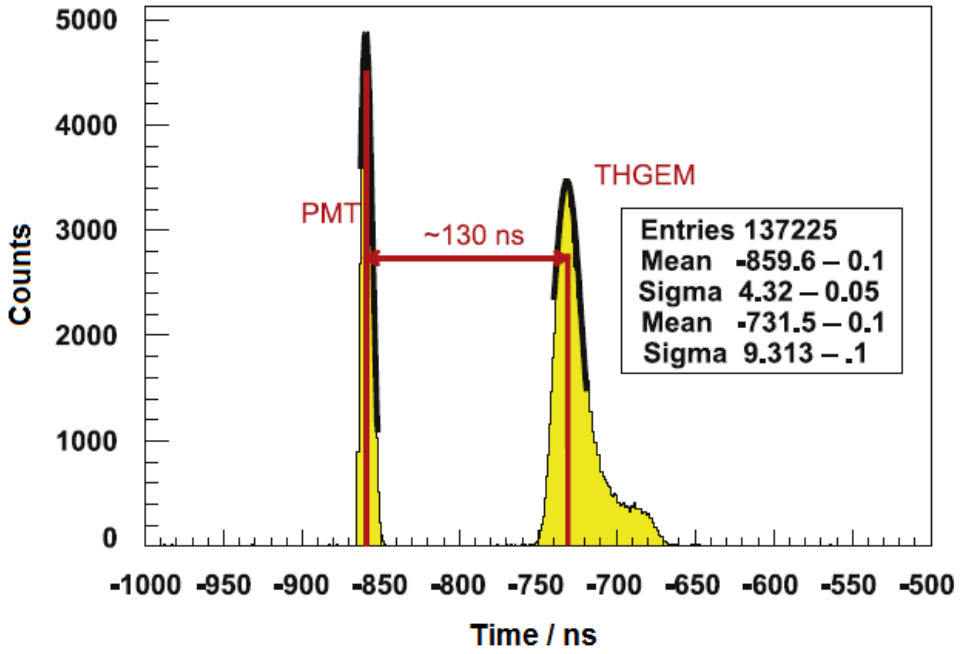

Figure 6.8 – Time distribution spectra from events collected, first from the MAPMT, and secondly from the THGEM-based photon detector, approximately $130\ ns$ later, from Cherenkov photons [107].

As expected, the time distribution spectrum of the photomultiplier is formed earlier in time, with a $\sigma = 4.3\ ns$. By the presented experimental results, the THGEM-based detector response happens approximately $130\ ns$ later, with $\sigma = 9.3\ ns$, denoting the slightly better performance of the time resolution of photomultipliers, as well as their time response. It's important to point that the used Hamamatsu MAPMT R7600 has a transit time, which relates to its time response, of $12\ ns$, leading to an approximate time response of $140\ ns$ for the THGEM detectors.

The experimentally estimated delay in the THGEM response can also be compared with analytical predictions. The electron speed in Ar/CH4 $(50{:}\,50)$, in a considered constant field along the detector of $1.5\ kV/cm$ is approximately $8 \times 10^6\ cm/s$. Considering a transit path of $1\ cm$, consistent with the THGEM detector vertical size, a transit time of approximately $125\ ns$ is expected, being a value consistent with the measured one.

The time distribution spectra can equally be studied, with the THGEM-based detectors using Cherenkov light, as function of the total applied dipole voltages, ΔV_{total}, this is, the sum of ΔV_1, ΔV_2, and ΔV_3, respectively from THGEM 1, 2 and 3. **Figure 6.9** a), b), c) and d) presents the time

distribution spectra for a triple THGEM-based detector, with ΔV_{total} of $4.35\ kV$, $4.38\ kV$, $4.42\ kV$ and $4.53\ kV$, respectively.

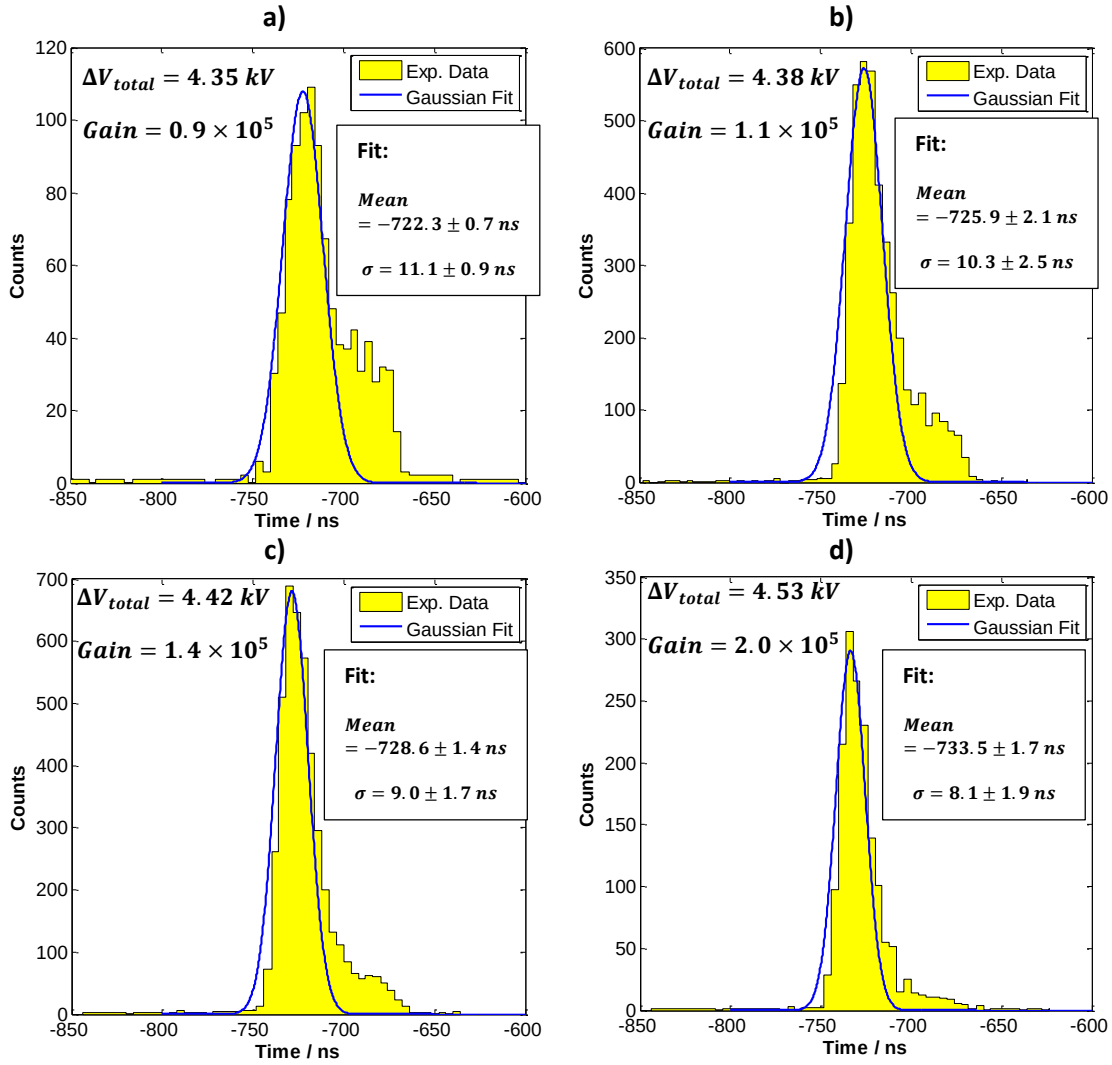

Figure 6.9 - Time distribution spectra from events collected by the THGEM-based photon detector, from Cherenkov photons, for a set of four ΔV_{total}s: a) $4.35\ kV$; b) $4.38\ kV$; c) $4.42\ kV$; d) $4.53\ kV$.

The progressive increase of ΔV_{total}, although not significant, increments the gain by a factor of approximately 2, from 0.9×10^5 for $\Delta V_{total} = 4.35\ kV$, up to 2.0×10^5 for $\Delta V_{total} = 4.53\ kV$. Additionally, following the rise of the total applied voltage, a progressive shrinking of the standard deviation σ of the Gaussian distributed time response peak, proportional to the time resolution of the devices, is observed, from $\sigma = 11.1\ ns$ down to $\sigma = 8.1\ ns$.

Apart from the main component of the time distribution spectra presented in **Figure 6.9**, corresponding to the Gaussian fits, an unexpected secondary component, less populated and delayed by approximately $20\ ns$, is observed. Furthermore, the population of the secondary component, outside the Gaussian distributed peak, greatly reduces down to negligible values, for the maximum applied ΔV_{total}. Considering that while increasing ΔV_{total} from $4.35\ kV$ up to

$4.53\ kV$, ΔV_1 increases from $1.35\ kV$ up to $1.41\ kV$, and considering that the electron drift velocity in a gas is function of the applied electric field, then it is legit to infer that the secondary and undesirable component of the spectra are related to photoelectron extraction efficiency. As mentioned in chapter 4, the electric field at the surface of the photocathode is not uniform, and its magnitude decreases in regions far from the THGEM 1 holes influence. Photoelectrons emitted in regions with lower electric fields can present lower initial drift velocities, resulting in slower responses from the detector. Therefore, high ΔV_{total}, with high ΔV_1 are mandatory, in order to guarantee simultaneously an effective photoelectron extraction and a fast photoelectron collection.

6.1.4. Cherenkov Ring Imaging

The development of the THGEM-based detectors, as repeatedly mentioned along this document, aims their application as RICH detectors. Therefore, the ultimate exercise that is demanded for the referred application, is the test to the THGEM-based photon detector's capability of Cherenkov ring imaging. It's important to recall that each of the triple THGEM detectors comprise a multi-pad anode, with exactly 32, $8 \times 8\ mm^2$ pads, conferring imaging capability. **Figure 6.10** presents superposition of events, for each pad of the two lateral THGEM based photon detectors, operated at a typical gain, under Cherenkov light irradiation.

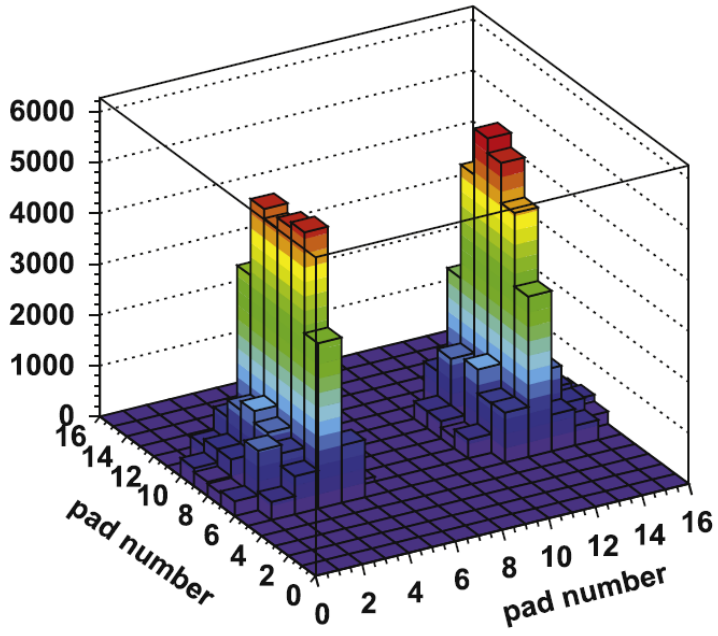

Figure 6.10 – Pile-up events collected by the two lateral THGEM-based photon detectors, where two segments of the Cherenkov corona are clearly visible [107].

Figure 6.10 indicates that the Cherenkov photons are clearly detected by the two lateral THGEM-based detectors, and that the pile-up of events, focused by the hemispheric quartz radiator, result

in two corona segments intercepted by the two detectors. These results, along with all the ones previously introduced, show the capability of $30 \times 30\ mm^2$ THGEM-based detectors operating as RICH detectors.

6.2. 2012 Test-Beam Campaign

The 2010 test beam campaign provided a considerable amount of useful information, necessary to understand THGEM-based detectors in a more detailed way. This test beam campaign, however, did not answer to all the existing questions, and it was limited to the THGEM development achieved so far. After the 2010 test beam, research and development on the subject went on, leading to new definitions of the THGEM parameters to be chosen, to the final assemble of triple-layered THGEM photon detector, while at the same time achieving new milestones, like large area prototypes, important to direct all the efforts towards the aimed final application: RICH-1 detector.

In this regard, in November 2012, a new test beam campaign was performed, divided into two major subjects: first, further studies in $30 \times 30\ mm^2$ THGEM-based photon detector prototypes, complementary to the ones performed in the 2010 test beam campaign, and to laboratorial ones, and second, an initial attempt to operate $300 \times 300\ mm^2$ THGEM-based photon detectors, with Ring Imaging Cherenkov detection capability. These two studies were achieved by assembling the small and big area THGEM detectors in two separate chambers, with the possibility of simultaneous operation, through the disposition of the two chambers, downstream and upstream respectively, in the beam direction, as schematically represented in **Figure 6.11**. A trigger system, equally represented in the mentioned figure, equal to the one used in the previous test beam and described in section 6.1.1, was used for data taking, through the selection of beam particles crossing the detector, based in the scintillators' coincidences.

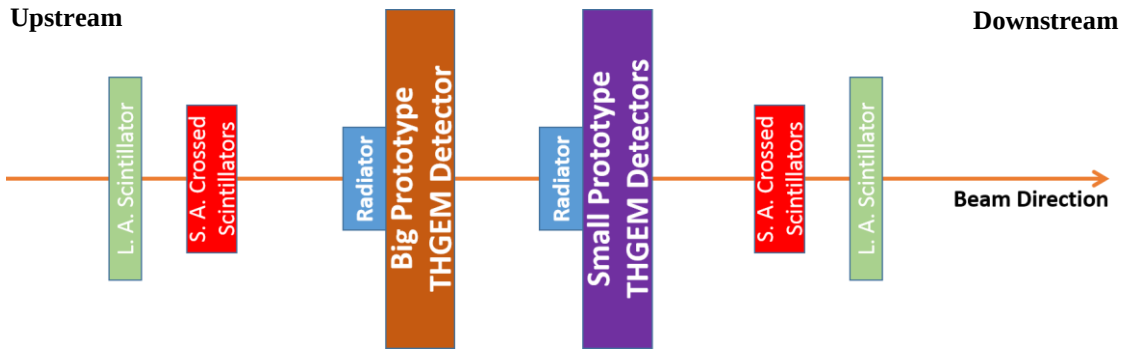

Figure 6.11 – Layout of the disposition of the small area and the big area THGEM detectors, along the beam axis, in between the set of scintillators that constitute the trigger system. Large area scintillators (L. A. Scintillators) are placed in the outer region, while the small area scintillators are placed between the large area ones and the detectors (distances not in scale).

The referred test beam campaign was operated at the CERN Proton Synchrotron (PS), at the T10 facility, under a $6\ GeV/c\ \pi^+$ beam.

6.2.1. Small Area THGEM-based photon detectors

The operation of THGEM-based photon detectors under UV LED photons represents an ideal situation where, theoretically, the incident photons are the only entities responsible for signal creation. Nonetheless, the application of such devices at beam facilities, for RICH purposes, corresponds to a situation where the detector is simultaneously irradiated by Cherenkov light (desirable) and by minimum ionizing particles (undesirable).

The detectors' irradiation by MIPs lead to a faster ageing of the photocathode, while inducing undesirable signals, through both electron emission from the photocathode or ionization of the gas atoms.

Following the application of GEM-based photon detectors, coupled with a CsI photocathode, in the Cherenkov counter, at the Hadron Blind Detector, described in section 2.3.1, where MIPs were suppressed by the application of a mild reverse field, a similar approach was studied for THGEM-based detectors.

Therefore, using small area THGEM detectors prototypes, in order to evaluate a possible MIP suppression, studies were conducted to check the detectors' response to MIPs, to verify the effectiveness of reverse drift fields, and finally, to understand the effect of the reverse drift field on the photoelectron yield.

6.2.1.1. Experimental Setup

The referred studies in $30 \times 30\ mm^2$ THGEM-based photon detectors were performed with the same chamber used in the 2010 test beam, keeping the exact disposition of the detectors as schematically represented in **Figure 6.1**. Again, only two of the three sets of THGEM detectors were used (the lateral ones), which arbitrarily shall be designated of THGEM Detector A and B. Both of these detectors, with identical parameters, kept the configuration illustrated in **Figure 6.3** (including spacing). The configurations used in 2010, where the thicknesses of all THGEMs was $0.4\ mm$, now evolved to the following parameters:

- THGEM 1: $0.4\ mm$ thickness; $0.4\ mm$ holes diameter; $0.8\ mm$ pitch; $10\ \mu m$ rim; coupled with CsI layer.
- THGEM 2 & 3: $0.8\ mm$ thickness; $0.4\ mm$ holes diameter; $0.6\ mm$ pitch; $< 5\ \mu m$ rim.

Note that these sets of thicknesses is the result of previous research, mentioned in section 4.2.3.2, where a thinner first THGEM layer is aimed to allow a better photoelectron extraction efficiency, and two thicker consecutive THGEM layers, in order to allow an higher gain.

The whole setup was operated under an Ar/CH_4 $(60:40)$ atmosphere, provided through a "once-through" gas circuit type, at atmospheric pressure. The high voltage powering remained equal to the 2010 setup, this is, with each electrode being powered through a resistive divider. The drift wires in this case, however, were powered independently through the remotely controlled HV power supply.

Although a zero drift field, this is, drift wires and photocathode at the same potential, is usually desired in the perspective of photon detection, the independent powering of the drift wires allows to perform the study of the possible MIP suppression as function of the drift field. For further reference, the direction of a positive electric drift field points from the photocathode to the drift wires, following the direction indicated in **Figure 6.3**.

At an initial stage, both setups were connected to the analogue readout chain, where gain measurements were conducted with UV LED light irradiation. However, in the final configurations, THGEM Detector A remained connected to the analogue readout system, while THGEM Detector B was connected to the standard digital electronic readout.

For the set of purposed studies, the chamber can either be placed with the quartz radiator centred with the beam, providing therefore Cherenkov radiation, or with the THGEM detectors centred with the beam, evaluating the effect of the ionizing particles in the absence of Cherenkov photons.

6.2.1.2. Response to MIPs

The interaction of charged particles crossing the THGEM-based photon detectors can mainly result in either ionization of the gaseous medium, or in electron emission from the photocathode. While traversing matter, the fluctuations of energy loss of the charged particles produce approximately a Landau distribution [108].

Because pions, from the particle beam, correspond to minimum ionizing particles, then the signal amplitude spectra, from their energy loss due to the interaction with THGEM detectors, should result in a Landau distribution.

In this regard, THGEM detector A was aligned with the beam axis, and potentials were set so that $\Delta V_{total} = 4.93\ kV$ (with $\Delta V_1 = 1.30\ kV$, and $\Delta V_2 = \Delta V_3$). **Figure 6.12** shows a set of three amplitude spectra, acquired for THGEM detector A, with the analogue readout system, for: a) $E_{drift} = -2.0\ kV/cm$; b) $0\ V/cm$; c) $+2\ kV/cm$.

a)

b)

c)

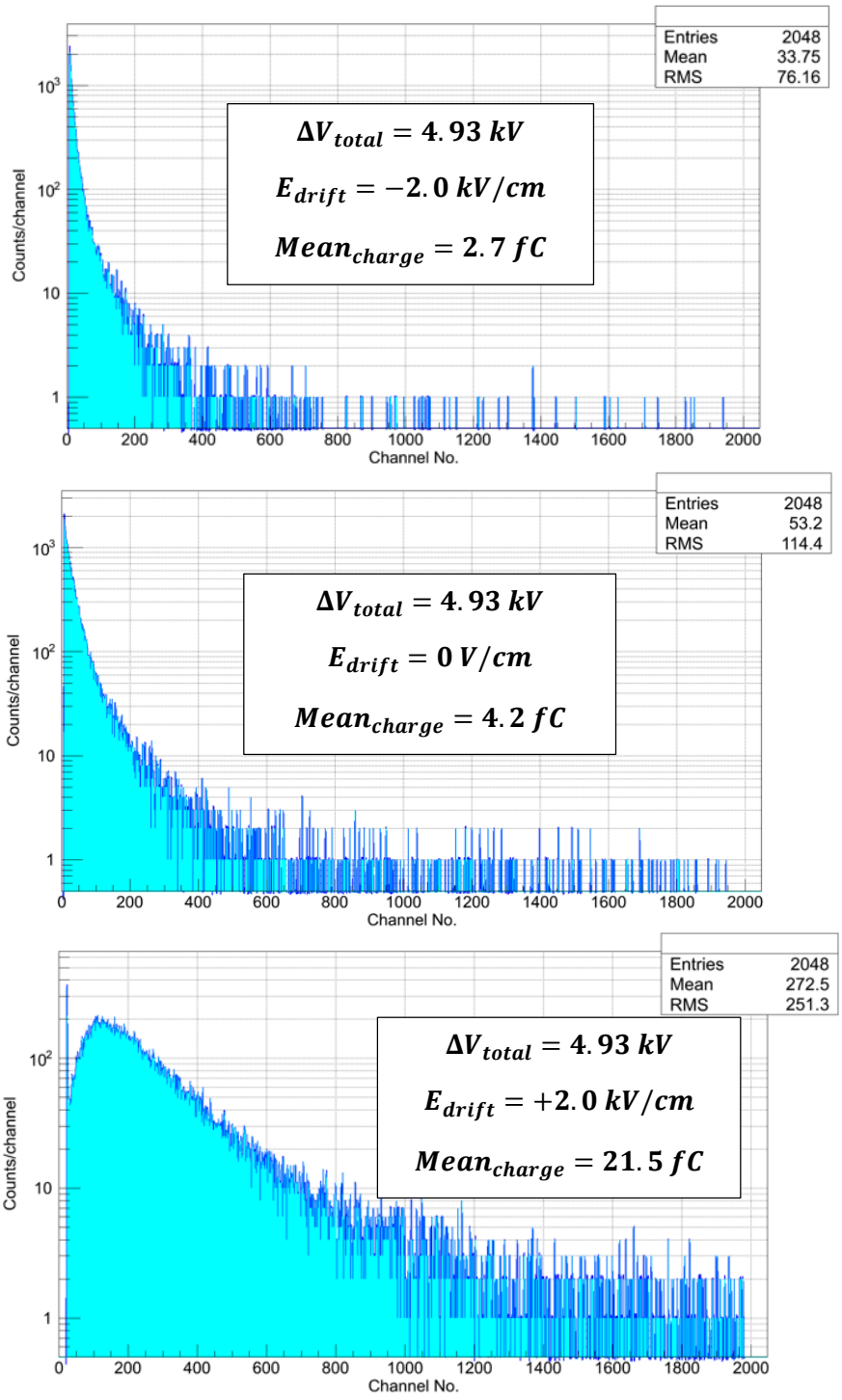

Figure 6.12 – Signal amplitude spectra, acquired with THGEM detector A, with the analogue readout electronics, for the situation where the beam irradiates directly the THGEM detector, and therefore no Cherenkov light is emitted. The results were obtained for $\Delta V_{total} = 4.93\ kV$, for drift fields of: a) $-2.0\ kV/cm$; b) $0\ V/cm$; c) $+2.0\ kV/cm$. The mean values of the charge calibrated distributions are in evidence.

The operation of the detector at $\Delta V_{total} = 4.93\ kV$ corresponds to an approximate gain of 7.3×10^3, when measured with UV LED light, with drift field set to $0\ V/cm$. Although the gain at which the detector is operated is quite low, it's important to point out that, with a high intensity beam crossing directly the detector, it can become rather unstable, due to electrical discharges, and therefore its operation at lower potential is recommended.

The interpretation of the amplitude spectra proves that the MIPs' energy loss is indeed a Landau distribution. For the presented high positive drift field, the spectrum is populated at higher energies, when compared to the two remaining spectra, with particular emphasis to the most probable value (MPV) of the distribution, which is clearly distinguishable for such field. With the decrease of the drift field, the presented spectra tend to be populated in lower energies. For the drift fields of -2 and $0\ kV/cm$, the Landau most probable values are no longer visible.

In the impossibility to compare directly the MPV of the distribution as function of the applied drift fields, the evaluation of the distribution mean values corresponds to a fairly good qualitative method of evaluating the dependence of the drift field in the detectors' response to MIPs. The mean values of the charge calibrated distributions correspond to $2.7\ fC$, $4.2\ fC$ and $21.5\ fC$, for $E_{drift} = -2\ kV/cm$, $E_{drift} = 0\ V/cm$ and $E_{drift} = +2\ kV/cm$, respectively.

Considering that an empty spectra would correspond to the ideal situation where MIPs are suppressed, and therefore, do not interact with the detector, it is possible to conclude, compared to a null field, that negative drift fields are capable of some MIP suppression, while positive drift fields have the opposite effect.

To prove the discussed results, a similar exercise was repeated used THGEM detector B, aligned with the beam axis, and connected to the digital readout system; **Figure 6.13** shows the multiplicity distribution for the number of hits detected as the result of the interact of each MIP. Results presented in the picture, labelled from a) to d), were obtained for the following set of $\Delta V_{total}s$ and E_{drift}s:

a) $\Delta V_{total} = 4.87\ kV$ and $E_{drift} = -0.5\ kV/cm$;
b) $\Delta V_{total} = 4.99\ kV$ and $E_{drift} = -0.5\ kV/cm$;
c) $\Delta V_{total} = 4.87\ kV$ and $E_{drift} = +2.0\ kV/cm$;
d) $\Delta V_{total} = 4.99\ kV$ and $E_{drift} = +2.0\ kV/cm$

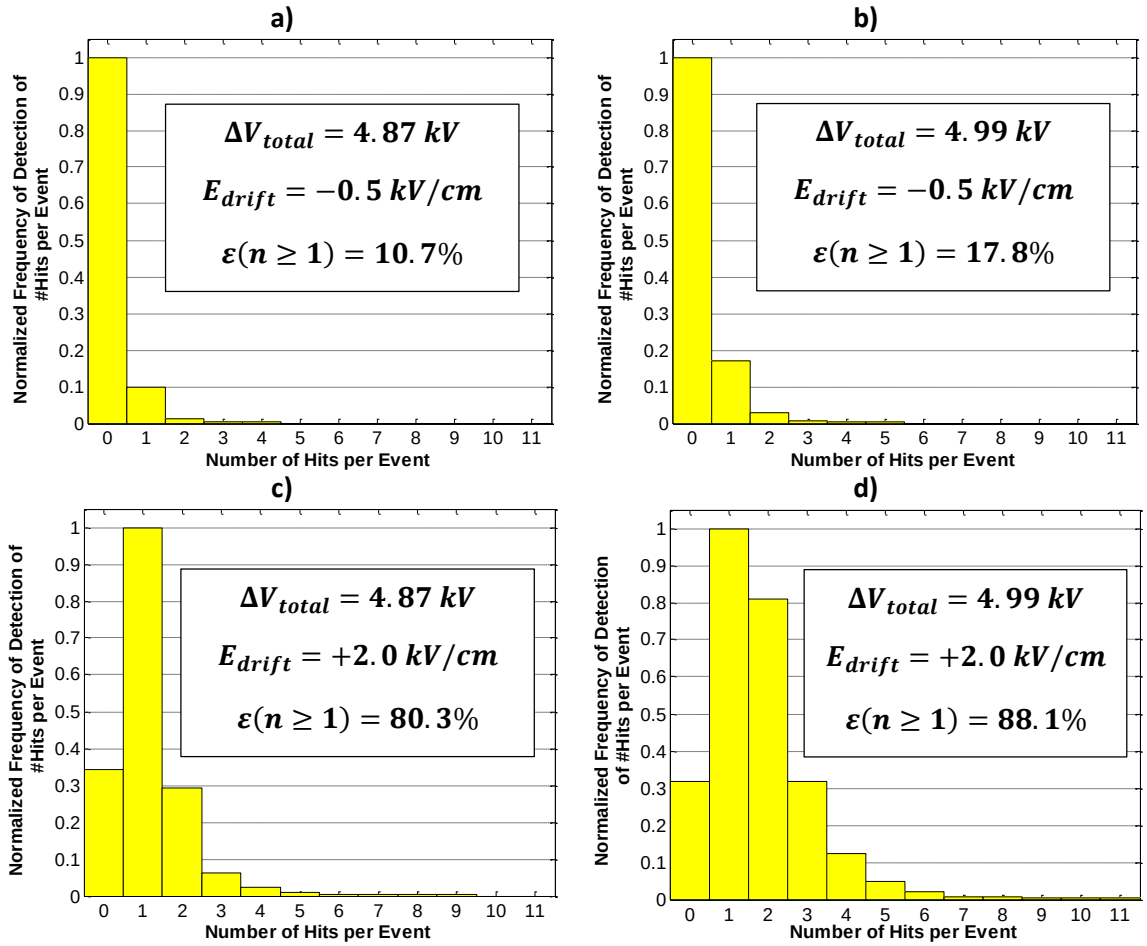

Figure 6.13 – MIPs Multiplicity distribution, as function of the detected events per triggered MIP. Results were achieved with beam irradiating directly in THGEM detector B, with digital readout, for the following set of total applied voltages and drift fields: a) $\Delta V_{total} = 4.87\ kV$ & $E_{drift} = -0.5\ kV/cm$; b) $\Delta V_{total} = 4.99\ kV$ & $E_{drift} = -0.5\ kV/cm$; c) $\Delta V_{total} = 4.87\ kV$ & $E_{drift} = +2.0\ kV/cm$; d) $\Delta V_{total} = 4.99\ kV$ & $E_{drift} = +2.0\ kV/cm$. The variable $\varepsilon(n \geq 1)$ defines the efficiency of detecting at least one event per triggered MIP.

Based on the presented results, it's possible to observe that the probability of a null detection of events due to MIP interaction is higher for both smaller (negative) fields, and for smaller ΔV_{total}. This conclusion is supported by the calculation, based on the presented distributions, of the detection efficiency ε, of at least one event per MIP. For each set of applied voltages, the results are consistent with the results presented in **Figure 6.12**, as $\varepsilon_{a)} < \varepsilon_{c)}$ and $\varepsilon_{b)} < \varepsilon_{d)}$. Additionally, because $\varepsilon_{a)} < \varepsilon_{b)}$ and $\varepsilon_{c)} < \varepsilon_{d)}$, it is possible to conclude that for a fixed drift field, ΔV_{total} has an important role in the response of the detector to minimum ionizing particles. This dependency on ΔV_{total}, can be explained by the fact that, while increasing ΔV_{total} from $4.87\ kV$ to $4.99\ kV$, ΔV_1 is increasing too, from $1.28\ kV$ to $1.32\ kV$ respectively, rising consequently the electron transfer efficiency from the upper THGEM. This increase of the electron transfer efficiency leads to a growing sensibility to charged particles.

These trends can be corroborated by the results shown in **Figure 6.14**, where for the exact same configuration, a multiplicity scan as function of the electric drift field was performed, for the two sets of applied voltages: $\Delta V_{total} = 4.87\ kV$ and $\Delta V_{total} = 4.99\ kV$.

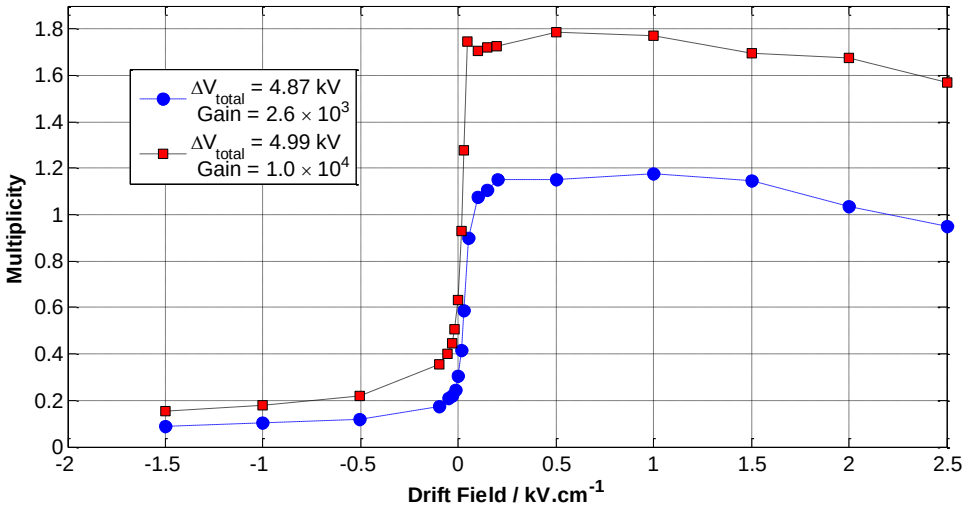

Figure 6.14 – MIP multiplicity as function of the applied drift field, for THGEM detector B, with the beam crossing directly the THGEM detector. Results are presented for $\Delta V_{total} = 4.87\ kV$ and $\Delta V_{total} = 4.99\ kV$. To these set of applied voltages, correspond an effective gain of approximately 2.6×10^3 and 1.0×10^4 respectively, measured at $E_{drift} = 0\ V/cm$ with UV LED light.

The increase from strong negative drift fields up to approximately $-\ 100\ V/cm$ shows a soft increase in the multiplicity. In this range of fields, electrons in the drift gap, product of the interaction of MIPs with the gas, are repelled away from the detector, decreasing the response of the detector to the crossing charged particles. Between approximately $-100\ V/cm$ and $+100\ V/cm$, a steep increase in the multiplicity is observed, corresponding to a range of fields where the electron transfer efficiency increases. Above these drift fields, multiplicities slowly starts to decrease, evidencing that the field in the drift gap starts to be high enough to collect the created electrons in the upper electrode of the first THGEM. Also, as previously described, higher applied voltages lead to consistently higher response from the detector to MIPs.

Therefore, the presented results from the drift scan show the effectiveness of negative drift fields, when compared to the standard $0\ V/cm$ field, to partially supress the detector's response to (the undesirable) MIPs.

6.2.1.3. Photoelectron Yield vs Drift Field

If on one hand, the MIPs multiplicity is desirably small, synonymous of MIP suppression, on the other hand, a large Cherenkov light multiplicity is desirable, in order to provide a maximized photoelectron yield.

In order to evaluate the potential effect of a negative drift field in the Cherenkov photon yield, the radiator was aligned with the beam axis, and the same previously used THGEM detector B was set for Cherenkov photon detection, with $\Delta V_{total} = 4.99\ kV$. At this voltage, with $E_{drift} = 0\ V/cm$, the measured gain was of approximately 1.0×10^4, when irradiated with UV LED light. Although this gain value is considerably small for photon detection, still, the used voltage was important to be kept the same as in the previous exercise. Despite the small multiplicity values due to the low gain, a qualitative analyse is still possible. The photon multiplicity as function of the drift field is then presented in **Figure 6.15**.

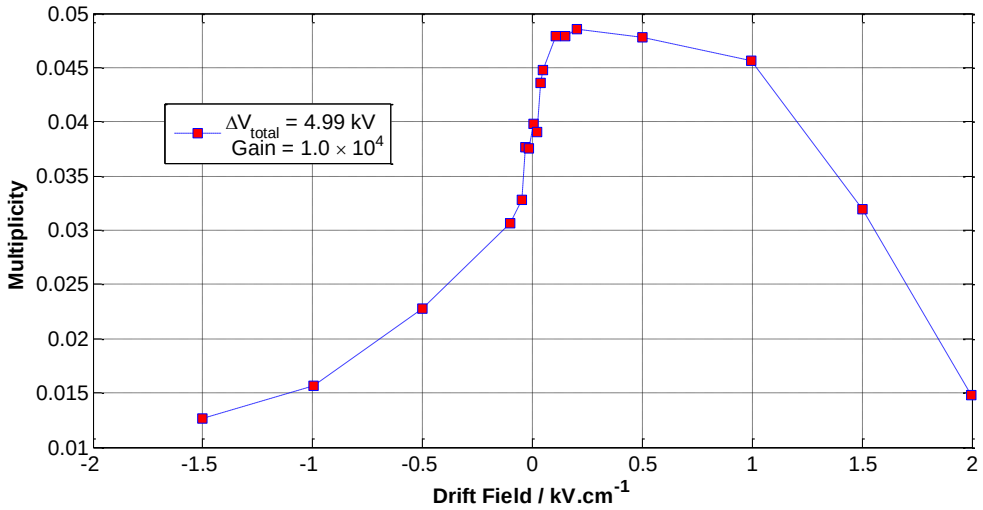

Figure 6.15 – Cherenkov photons multiplicity as function of the applied drift field, for THGEM detector B, with the beam crossing the quartz radiator for Cherenkov light production. Results are presented for $\Delta V_{total} = 4.99\ kV$, to which corresponds an effective gain of approximately 1.0×10^4, measured at $E_{drift} = 0\ V/cm$ with UV LED light.

As the interaction of Cherenkov photons results in the possible emission of photoelectrons from the photocathode, it is not surprising that the photon multiplicity as function of the drift field is significantly similar to the MIPs multiplicity. Despite the similarity, a steeper decrease of the multiplicity is observed for higher positive values of the drift field, consequence of the increasing probability of the photoelectron backscattering.

Based on these results, in what concerns the photoelectron yield, the optimized drift field is slightly positive. In this regard, and merging the two fields of interest, a mild reverse drift field, of only few tens of V/cm, can lead to a non-negligible decrease of the detector's response to MIP's, while not imposing a significant decrease of the response to Cherenkov photons.

6.2.2. Large Area THGEM-based photon detectors

The studies performed progressively all along the period referenced in this document, regarding small area THGEM-based photon detectors, despite all the successes and the knowledge acquired, are only worthy if they allow the construction of larger area prototypes, with equivalent operational properties when compared to the smaller ones.

In this regard, using the $300 \times 300\ mm^2$ THGEM prototypes characterized in section 4.2.4, a large area triple-layer THGEM photon detector was assembled for the very first time. Although such assembly happened during the mentioned test beam campaign, with no prior operation of the device in laboratorial environment, still, it corresponded to a significant milestone, and to the ultimate piece of evidence, so far, that THGEM-based photon detector with large areas are possible.

The studies performed with the $300 \times 300\ mm^2$ THGEM-based detector aimed therefore, to qualitatively evaluate the operability of the device.

6.2.2.1. Experimental Setup

The large area THGEM-based photon detector consisted on a single chamber, comprising three THGEMs with the following parameters, where the numbering of each THGEM follows the standard designation:

- THGEM 1: $0.4\ mm$ thickness; $0.4\ mm$ holes diameter; $0.8\ mm$ pitch; $<\ 5\ \mu m$; coupled with CsI layer.
- THGEM 2 & 3: $0.8\ mm$ thickness; $0.4\ mm$ holes diameter; $0.6\ mm$ pitch; $<\ 5\ \mu m$ rim.

The choice of the mentioned parameters was such, in order to match the parameters used for the small area THGEM based detectors used in the same test beam campaign, which as previously mentioned, are set to maximize the performance of the devices.

The distance between consecutive THGEMs was set to $3\ mm$, while the drift and the induction gaps were set to $5.2\ mm$ and $2.5\ mm$, respectively. The anode was segmented in 576 pads of $12 \times 12\ mm^2$, granting the imaging capabilities to the device. A schematic representation of this configuration is presented in **Figure 6.16**.

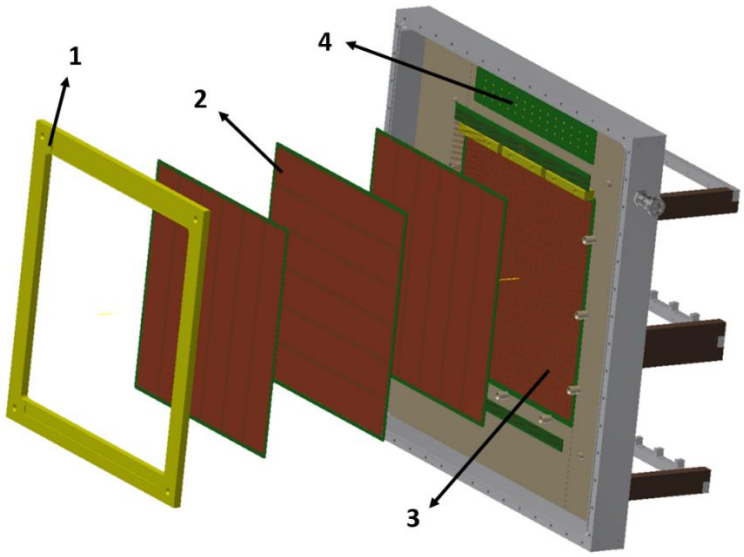

Figure 6.16 – Illustration of the $300 \times 300\, mm^2$ triple THGEM photon detector. The drift gap was to $5.2\, mm$, transfer gaps to $3.0\, mm$, and the induction gap to $2.5\, mm$. 1 – drift wires support; 2 – THGEMs; 3 – Anode; 4 – HV distribution board.

In front of the THGEM detector was placed a truncated cone of fused silica (quartz) radiator, aligned with the beam axis. This radiator was equipped with a cylindrical interceptor, whose movement was remotely controlled by a piezo motor. The variation of the position of the interceptor allowed a variation of the number of emitted Cherenkov photons. In its full retracted position, a fully uncovered radiator allowed the emission of a maximised amount of Cherenkov photons. At this maximum position, the interceptor fully covered the radiator, fully blocking the detector's irradiation with Cherenkov light. **Figure 6.17** (left) illustrates the radiator, coupled to the interceptor, in their physical support. The Cherenkov corona formed by the radiator is equally represented. The radiator was designed so that the Cherenkov corona would be projected at the full extent of the THGEM area. This projection is illustrated in **Figure 6.17** (right).

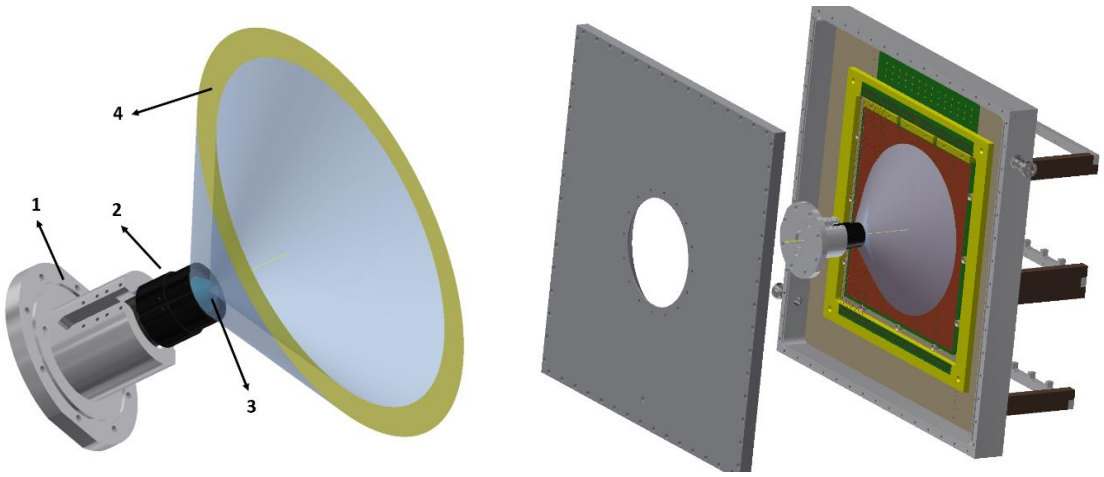

Figure 6.17 – Illustration of the radiator system: 1 – support; 2- interceptor; 3 – quartz radiator;4 – Cherenkov light emission (left); Illustration of the projection of Cherenkov light over the THGEM detector, resulting in a corona shape.

As the radiator is placed at the centre of the large area THGEM detector, in order to project a centred corona, it is important to mention that, on the contrary to the previous chamber, this detector is placed necessarily in the beam acceptance region.

All the set of measurements were performed under an Ar/CH4 $(60:40)$ gas mixture, provided through a "once-through" gas circuit type, at atmospheric pressure. The high voltage powering of each of the 6 sectors of the THGEM-based detector, previously described in section 4.2.4, was provided via individual resistive dividers to each sector (6 channels from the CAEN A1526N board on SY1527 mainframe). Additionally, the detector was coupled to the standard digital readout system, connecting each of the 576 pads, apart from initial tests and gain determination, where the analogue readout connecting sets of grouped pads was used, while irradiating the detector with UV LED light.

6.2.2.2. Detector Performance

Considering that the assembly of the mentioned THGEM detector, for the 2012 test beam campaign, corresponded to the first attempt to operate such device in a triple-layer configuration, it was important, primarily, to evaluate the gain variation as function of ΔV_{total}, and compare it to equivalent measurements achieved with the small area detectors, under equivalent conditions. **Figure 6.18** shows the effective gain of the $300 \times 300\ mm^2$ THGEM detector, measured while irradiating with UV LED light, and compares it to the gain of the small area THGEM detector A and B (introduced in section 6.2.1), operated in equivalent conditions.

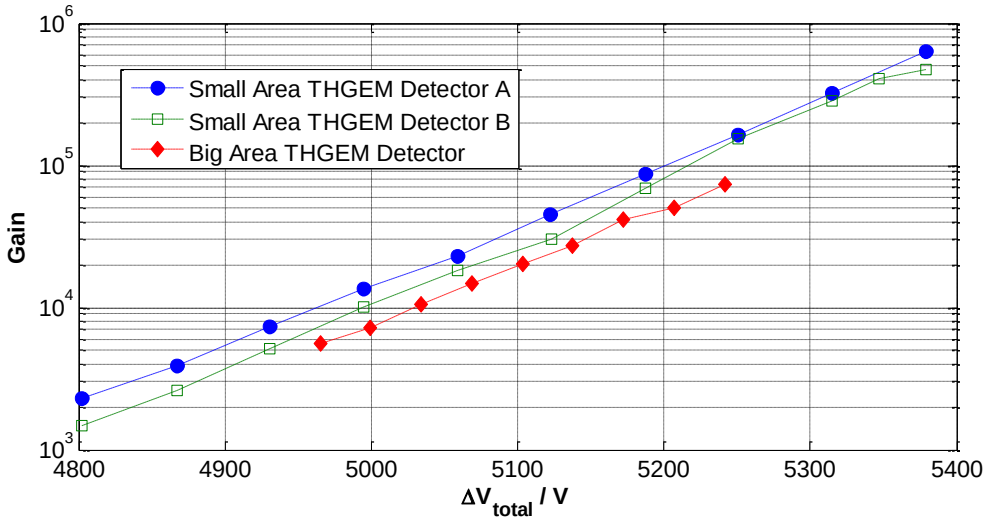

Figure 6.18 – Effective gain variation as function of ΔV_{total}, for the small area THGEM detector A and B, and for the large area prototype THGEM detector. Measurements done while irradiating the detectors with UV LED light.

As a first remark, it's important to point out that the gain determination for the large area detector was performed only for a segment of 1 sector, similarly to what has been done in section 4.2.4.

The evaluation of the gain variation, as function of the total applied voltage, for the two small area photon detectors, indicates that the two detectors, equivalent in parameters and in area, also share an equivalent performance, both in the effective gain, and in the maximum voltage applied, reaching maximum gains of around 5×10^5. The big area THGEM detector, however, presents a lower gain for equivalent voltages which is in line with the behaviour observed in the characterization of single THGEMs, described in section 4.2.4. Additionally, the applied ΔV_{total} at which the gain determination becomes possible, is higher than in the previous detectors, consequence of a slightly higher level of electronic noise. Also, the device stands a maximum ΔV_{total} of around just $5.24\ kV$, leading to maximum gain of approximately 7×10^4, due to electric instabilities, which are possibly consequence of the thicknesses inhomogeneity of each THGEM layer.

The detector's instability, particularly at higher gains, introduced the question of whether the detector is capable of stably operating under beam irradiation. In this regard, the Cherenkov photon multiplicity was measured as function of uninterrupted spills, being therefore, this measurement, simultaneously function of elapsed time. **Figure 6.19** shows the referred multiplicity variation, for the situation where each sector was powered accordingly to the voltages presented in **Table 6.1** (left), and for the situation were all sectors were set to $\Delta V_{total} = 5.03\ kV$ (right).

Table 6.1 - Total applied voltage to each sector of the large area detector

	Sector 1	**Sector 2**	**Sector 3**	**Sector 4**	**Sector 5**	**Sector 6**
ΔV_{total}	5.10 kV	5.07 kV	5.07 kV	5.07 kV	5.07 kV	5.10 kV

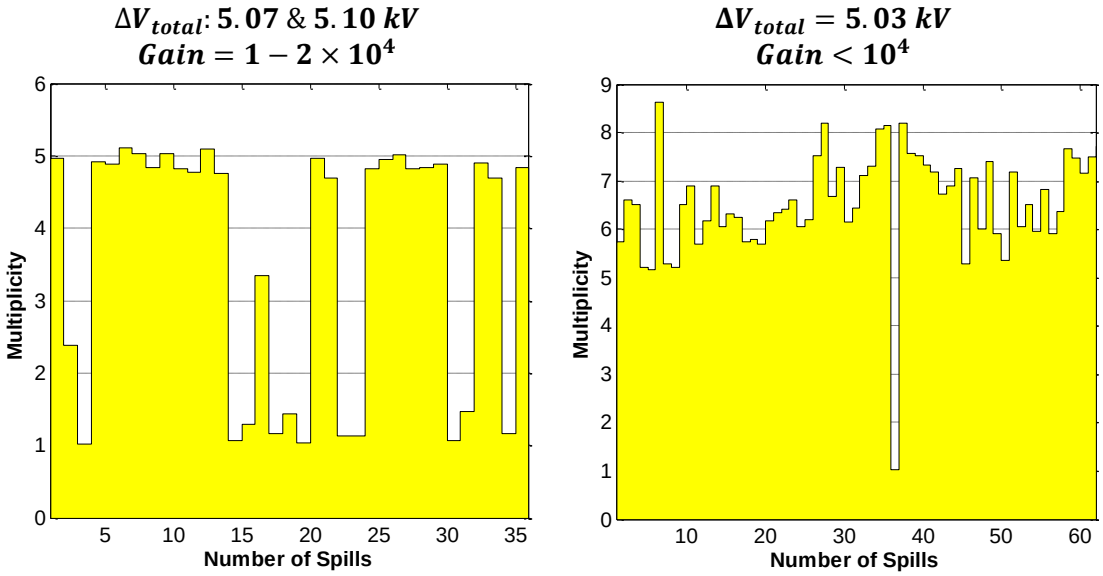

Figure 6.19 – Distribution of the multiplicity as function of the number of uninterrupted spills, for the ΔV_{total} summarised in **Table 6.1** (left) and for $\Delta V_{total} = 5.03\ kV$.

The voltages defined in **Table 6.1** were lower in the central sectors, aiming to have lower gains in the region of major influence of the beam, and higher in the lateral sectors, where the beam is not expected to have a major influence. Despite this attempt to balance the applied voltages, in order to try to guarantee the electric stability of the device, **Figure 6.19** (left) shows that the effort, for the set of presented voltages, was not successful, as the multiplicity over time tends to regularly drop, indicating the loss of performance of the detector. During stable periods, approximately constant multiplicities of 5 are found.

By decreasing the ΔV_{total} applied, despite a loss in gain, an increase of stability is expected. This expectation is verified by **Figure 6.19** (right) where the multiplicity barely drops during a time range of over 60 uninterrupted beam spills. Regardless of this success for $\Delta V_{total} = 5.03\ kV$, the fact that a lower voltage leads to higher multiplicities, compared to the previous situation, together with the visible fluctuations of this variable, lead to conclude that at this voltage the electronic noise level is predominant, indicating that the detector's operation at higher voltages, envisaging Cherenkov photon detection, is mandatory.

6.2.2.3. Operation at Optimized Voltages

Due to the need to stably operate the detector at higher gains, a process of tuning the applied ΔV_{total} of each individual sector was performed, attempting to obtain their optimized performance, while simultaneously guaranteeing the detector's stability under beam irradiation. **Table 6.2** presents these set of voltages.

Table 6.2 – Total applied voltage to each sector of the large area detector.

	Sector 1	**Sector 2**	**Sector 3**	**Sector 4**	**Sector 5**	**Sector 6**
ΔV_{total}:	5.10 kV	5.19 kV	5.14 kV	5.10 kV	5.10 kV	5.07 kV

For these set of voltages, the time distribution spectrum, for each sector, were obtained, and are presented in **Figure 6.20**.

The signals' time distribution, for each individual sector, as desirable and expected, presents similarities with the ones achieved for the small THGEM detectors, back in the 2010 test beam campaign, described in section 6.1.3. Similarly to that specific example, in the absence of a reference, the interpretation of the mean value of the Gaussian time distribution of Cherenkov events has no absolute meaning. However, a qualitative comparison between the performances of each sector is allowed. **Table 6.3** summarises the mean and the standard deviation of the Gaussian time distribution for each sector, as function of their applied ΔV_{total}.

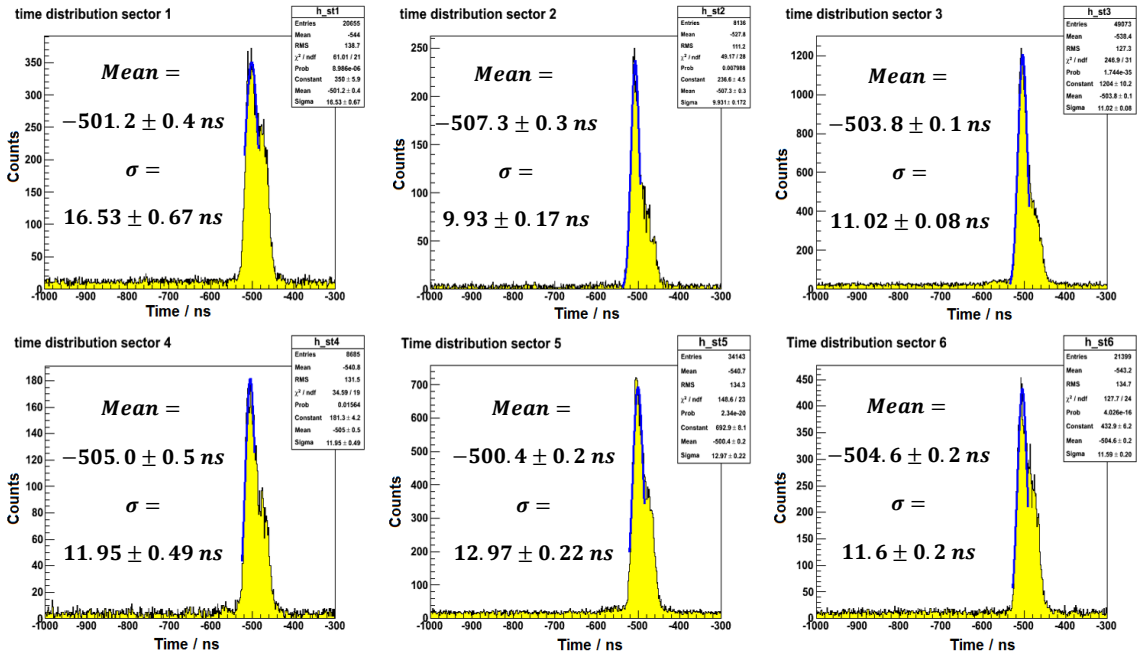

Figure 6.20 – Time distribution spectra from events collected by each sector of the $300 \times 300\ mm^2$ THGEM-based photon detector, from Cherenkov photons, with ΔV_{total} of each sector set at the voltages summarized in **Table 6.2**.

Table 6.3 - Summary of the mean and standard deviation of Gaussian time distributions, for each sector of the large area detector.

	Sector 1	**Sector 2**	**Sector 3**	**Sector 4**	**Sector 5**	**Sector 6**
ΔV_{total} / kV	5.10	5.19	5.14	5.10	5.10	5.07
Mean / ns	501	507	504	505	500	505
σ / ns	16.53	9.93	11.02	11.95	12.97	11.59

The variation of the mean value, despite some statistical fluctuation, remains approximately constant. Indeed, such detail would be expected due to the fact that such variable should depend essentially, for photons emitted at a same distance, on the distance that the photoelectrons are created, and the electric fields that they will be subject, and that will define their drift velocity. As both these variables remain approximately constant despite the applied ΔV_{total}, a constant mean value is therefore foreseen.

The standard deviation of the distribution, however, as previously observed, is dependent on ΔV_{total}. Although not all of the presented values follow the exact same trend, still, sectors with higher applied voltages, namely sector 2 and 3, show clearly a lower standard deviation. Additionally, and as equally reported in section 6.1.3, to higher $\Delta V_{total}s$ correspond distribution with secondary components delayed in time, less populated, due to higher photoelectron

extraction efficiencies that results from higher $\Delta V_1 s$. The time distribution spectrum of the overall detector, results in $\sigma = 11.7\ ns$.

The study of the response of the THGEM-based photon detector to Cherenkov photons is complemented with the study of the photons multiplicity as function of the position of the radiator's interceptor. It's important to recall that a fully retracted interceptor results in a totally unscreened radiator, resulting in a maximum amount of photons. In the other extreme position, the interceptor fully conceals the radiator, blocking all Cherenkov photons. **Figure 6.21** shows the variation of multiplicity as function of the position of the interceptor ($0\ mm$ – fully retracted; $26\ mm$ – fully extended), for the same setup, for both sector 3 and 5.

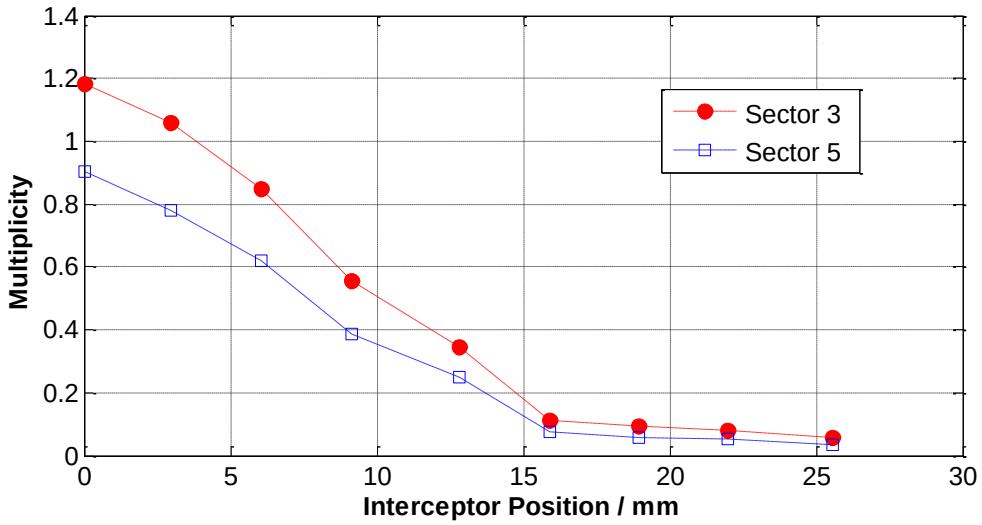

Figure 6.21 – Multiplicity as function of the interceptor position, for sector 3 and 5, with ΔV_{total} of $5.14\ kV$ and $5.10\ kV$, respectively. The interceptor position at $0\ mm$ corresponds to a fully retracted interceptor, while at $26\ mm$, it is fully extanded.

The interpretation of the results allows to conclude that the photon multiplicity is function of the gain, and therefore, function of the total applied voltage. Such deduction is based on the fact that the multiplicity of sector 3, with a higher ΔV_{total}, is consistently superior than its homologous sector 5, with lower ΔV_{total}.

Additionally, the extension of the interceptor up to approximately $16\ mm$ leads to an approximately linear decrease of the measured multiplicity. Above this position, no more Cherenkov photons seem to irradiate the THGEM detector. In the absence of Cherenkov photons, however, an approximately constant multiplicity of 0.1 remains. This value is a consequence of the efficiency in the detection of the (unwanted) signals originated by the beam particles traversing the detector.

6.2.2.4. Cherenkov Ring Imaging

Can $300 \times 300\ mm^2$ THGEM-based photon detectors be operated as RICH detectors? Although the results presented so far were important for the understanding of the large area device, and compare its performance with the one obtained from the small area prototypes, still they did not prove the possible imaging capability of the device. In order to give a definite answer, the imaging capability of the detector was tested, by counting the number of hits detected in each anode pad, which are result of the interaction of the beam's particles with the radiator, or directly with the THGEM detector itself.

As a result of the mentioned test, achieved for the set of applied voltages summarized in **Table 6.2**, the Cherenkov ring imaging capability was successfully proven. **Figure 6.22** illustrates two examples of hits from single events, evidencing a likely ring distribution. **Figure 6.23** shows the pile-up of hits of superimposed events, with emphasis to the corona, due to Cherenkov photons, with full extent over the THGEM area and to the beam detection in the centre of the ring. Finally, **Figure 6.24** illustrates the Cherenkov corona due to the superimposition of events, not considering the beam detection in the centre, in order to enhance the Cherenkov ring.

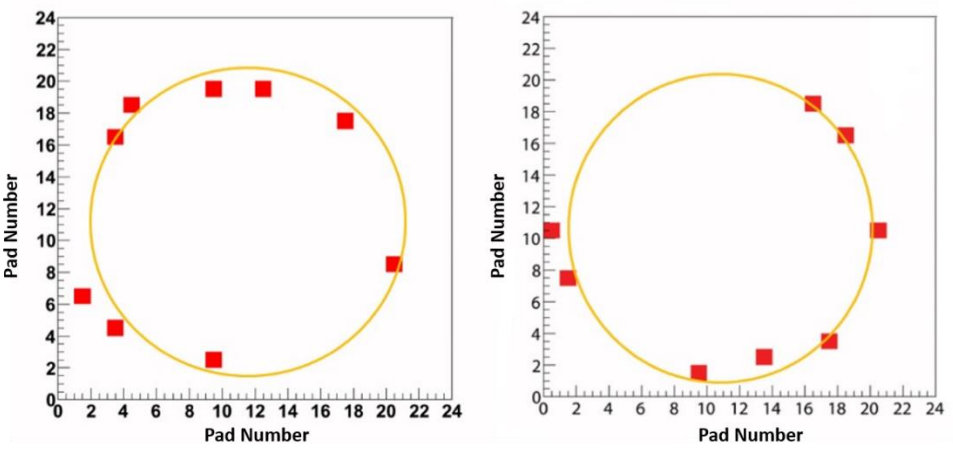

Figure 6.22 – Selected examples of detected hits from single events. A circular fit is drawn, in order to emphasis the likely ring distribution [79].

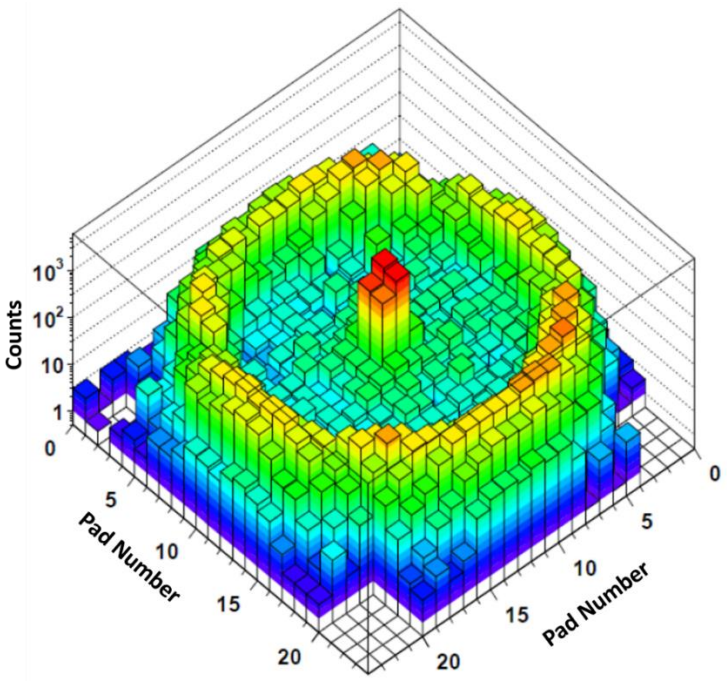

Figure 6.23 – Pile-up of detected hits of superimposed events. A Cherenkov ring is observed in the outer area of the image, while at the centre, a peak, corresponding to the beam interaction with the detector is observed [79].

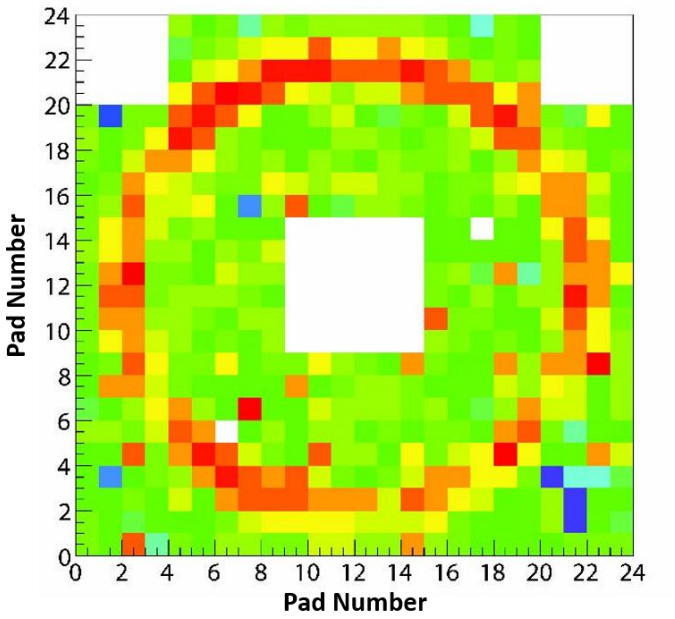

Figure 6.24 – Pile-up of detected hits of superimposed events, with the suppression of the middle pixels, where the beam was observed, in order to enhance the Cherenkov ring [109].

6.3. Conclusions

The studies performed in the test beams campaigns corresponded to an evolution of all the work previously done in laboratorial conditions. The evaluation of the performance of the THGEM-based photon detectors under beam irradiation is, therefore, the ultimate stage in the development of such gaseous photon detectors, as it corresponds to the best approximation to the conditions at which final detectors are meant to operate.

In this regard, the exercises performed along two test beam campaigns had four majors goals, the first three of which achieved with small area prototypes: one, validate that the knowledge acquired in laboratorial conditions with radioactive source and UV light can indeed be extrapolated to beam conditions; two, evaluate the time distribution of signals derived from Cherenkov photon detection; three, to study the THGEM detectors' response to MIP and their possible suppression; and four, the evaluation of the capability of $300 \times 300\ mm^2$ THGEM-based photon detectors to operate under beam conditions, as ring imaging Cherenkov detectors.

The first goal led to the conclusion that Cherenkov light and UV LED photons induce similar responses from the THGEM detectors, sharing identical photon multiplicity distributions, and time distribution spectra, while operating at gains of the order of 10^5. Overall, for small area detectors, responses achieved with UV light, and consequently in laboratorial conditions, could be reproducible with Cherenkov light, validating the first goal.

The study of the time distribution spectra from Cherenkov photons led to conclude about the need to operate the detectors at high gain, where improved time resolutions are achieved, with σ values around $10\ ns$. Additionally, higher gains tend to decrease the population of delayed events, by increasing the photoelectron extraction at the surface of the photocathode. The comparison of the time distribution spectra of events, between the THGEM detector and the MAPMT show that the response from the THGEM detector takes approximately $130\ ns$ longer than the one from the photomultiplier.

Although the THGEM-based photon detectors, coupled with CsI photocathode, were conceived to be sensitive to Cherenkov photons, its evaluation to minimum ionizing particles showed that the mentioned detectors, are also (and undesirably) sensitive to such charged particles. Negative drift fields have proven to be effective in decreasing the sensitivity of the detectors to MIP, although unfortunately, decreasing its responsiveness to Cherenkov photons. However, if just a mild reverse field is chosen, a considerable decrease in the response to MIPs is possible, with only minor effects in photons.

At last, $300 \times 300\ mm^2$ THGEM-based photon detectors, in spite of the challenges related to the inhomogeneity of the thicknesses of the THGEMs, were capable of being operated in beam conditions, but with gain not higher few 10^4. Despite this gain limitation, Cherenkov ring images were successfully acquired, confirming the validity of this technology for RICH applications.

7. Conclusions and Future Work

7.1. General Conclusions

Ring Imaging Cherenkov detectors are devices capable of detecting, with spatial discrimination, Cherenkov photons that were originated by the interaction of high momentum charged particles with a dielectric medium. Because the photon detectors coupled to such devices require, typically, large active areas in the order of several m^2, gaseous photon detectors are considered as they present an appealing relation between cost and performance, when compared, for example, to semiconductor or vacuum photon detectors.

The RICH-1 detector, as part of the COMPASS experiment at CERN, is an example where gaseous photon detectors are used for Cherenkov light detection. 75% of its area is assembled with multiwire proportional chambers, coupled to a solid CsI photocathode. Although the detector is currently operating, it suffers from several limitations. The intrinsic high ion back flow ($\approx 50\%$) leads to a fast ageing and degradation of the photocathode. In order to decrease the number of ions reaching the photocathode, and to avoid electric instabilities, the detector needs to be operated at low gain ($< 10^4$), affecting the single photoelectron detection efficiency, as well as the signal-to-noise ratio. Additionally, and in order to keep the photocathode's ion bombardment low, high irradiation rates are not advised.

To allow the operation of the RICH-1 detector at the same level of performance over the next years, at possible higher rates, an upgrade of the gaseous photon detectors is being planned, as to overcome the limitations from MWPCs coupled to CsI. In this regard, third generation of GPDs, based in THGEM structures, are considered. Their intrinsic properties allow a simple, robust and cheap covering of large areas, as well as they correspond to a closed geometry that strongly reduces the photon feedback. In order to evaluate their applicability as photon detectors for RICH applications, THGEM-based photon detectors were studied and developed.

The development and testing of $30 \times 30\ mm^2$ THGEM prototypes showed that higher applied dipole voltages lead to higher gains, which can be achieved with thicker structures ($0.8\ mm$). However, improved photoelectron extraction efficiencies can be achieved with thinner pieces ($0.4\ mm$). Additionally, a ratio of 1:2 between the holes diameter and the pitch of the THGEM proved to be the optimized ratio for maximizing the active area of the detector and the photoelectron extraction efficiency.

The assembly of THGEM structures into triple THGEM detector configurations allowed the stable operation of the device with gains easily reaching values of the order of 10^5 for Ar/CH_4 gas mixtures, for irradiation with charged particles, UV LED and Cherenkov photons. Also, experience with the aforementioned detectors showed a fast recovery from electrical discharges, in the order of seconds (for THGEMs with negligible rim). Additional studies with Cherenkov photons showed that

higher gains lead to improved time resolutions of the detector, with standard values of $\sigma \approx 10\ ns$, and that the detector's response to photons is of approximately 140 ns. The response of the detector to crossing MIPs was also studied, showing that mild electric drift fields, in the order of few tens of V/cm, is effective to partially suppress MIPs, while not having a major influence in the photoelectron yield.

Although the increase in gain by roughly one order of magnitude of THGEM-based photon detectors, when compared with the MWPCs, and the partial MIP suppression, correspond to desirable successes, still, an increase in gain leads to an increase on the photocathode's ion bombardment in the same proportion. In order to avoid a faster ageing of the photocathode, the IBF needs to be decreased, at least, in the same proportion of the gain's increase, leading to an aimed IBF not higher than 5%. Extensive laboratorial studies regarding this variable showed that an IBF decrease to only few percent was possible using a misaligned configuration, this is, with the vertical misalignment of the holes of the three layers of THGEMs.

Despite the successes with $30 \times 30\ mm^2$ THGEM-based photon detectors, the possible upgrade of the RICH-1 detector requires 12 detectors with $600 \times 600\ mm^2$ each. In this regard, and prior to the development of such large area detectors, prototypes with an intermediate area, $300 \times 300\ mm^2$, were developed and tested. Results evidenced the difficulty of producing large area THGEMs with homogenous thickness, with observed variances over 10%. A previous and meticulous selection of the PCB, prior to the THGEM production, is therefore mandatory.

The operation of the large area triple THGEM detector, under Cherenkov light irradiation, showed the successful response of the detector to light. However, the detector could not be operated at gains higher than approximately 10^4, most likely due to the thicknesses inhomogeneity and to the operation of the detector in the beam acceptance. Despite the gain studies, such large area devices showed the same reproducibility of results achieved with small area detectors, and full Cherenkov rings were acquired for the first time with such devices.

The overall studies with THGEM-based photon detectors showed their capability to replace MWPC photon detectors with improved performances and capable of operating in more demanding conditions. COMPASS RICH-1 will most likely be the first large RICH detector equipped with THGEM-based photon detectors. However, a parallel investigation with a bolder alternative technology has started, pointing to the development of a hybrid detector, based on the coupling of THGEM and Micromegas detectors, combining the high gain and photon detection capability of THGEMs with the high gain and intrinsic ion blocking capability of the Micromegas.

7.2. Future Work

With the defined goal of upgrading the gaseous photon detectors from RICH-1 detector, a set of studies, encompassing the following tasks, should be performed, in order to get to an ultimate detector, capable of fully operating in the desirable conditions:

- As the final detector is aimed to have an active area of $600 \times 600\ mm^2$, the development and characterization of such large area structure, is mandatory. Such task follows the evolution from $30 \times 30\ mm^2$ to $300 \times 300\ mm^2$, and from $300 \times 300\ mm^2$ to $600 \times 600\ mm^2$, with the obvious transfer of knowhow along the evolution chain.
- Extend the IBF studies and conclusions from small area detectors to larger area devices, along with the study of MIP suppression by an applied reverse drift field. Based on these proposals, a large area THGEM-based detector is, therefore, aimed to be operated, at a test beam campaign, with high gain, low IBF and low sensibility to charged particles.
- Exploit the advantages of a large area hybrid detector.

A more remotely achievable proposal is the development of photocathodes for the VUV/ visible range of the electromagnetic spectrum, increasing the Cherenkov photon yield detection.

Globally, the proposed list of work to be performed corresponds, to some extent, to the merging of all the presented studies in this document. The success of such merging will define the success of the application of such technology in the upgrade of RICH-1 gaseous photon detectors.

References

[1] P.A. Cerenkov, Visible Radiation Produced by Electron Moving in a Medium with Velocities Exceeding that of Light, Phys. Rev. 52 (1937) 378.

[2] J. Seguinot, T. Ypsilantis, Photo-ionization and Cherenkov ring imaging, Nucl. Instrum. Methods. 142 (1977) 377–391.

[3] R.A. Holroyd, J.M. Preses, C.L. Woody, R.A. Johnson, Measurement of the absorption length and absolute quantum efficiency of TMAE and TEA from threshold to 120 nm, Nucl. Instrum. Methods Phys. Res. Sect. Accel. Spectrometers Detect. Assoc. Equip. 261 (1987) 440–444.

[4] H.-W. Siebert, W. Beusch, J. Engelfried, F. Faller, S.G. Gerassimov, P. Lennert, et al., The Omega RICH, Nucl. Instrum. Methods Phys. Res. Sect. Accel. Spectrometers Detect. Assoc. Equip. 343 (1994) 60–67.

[5] U. Müller, W. Beusch, M. Boss, J. Engelfried, S.G. Gerassimov, W. Klempt, et al., The recent performance of the Omega RICH detector in experiment WA89 at CERN, Nucl. Instrum. Methods Phys. Res. Sect. Accel. Spectrometers Detect. Assoc. Equip. 371 (1996) 27–32.

[6] E. Albrecht, G. van Apeldoorn, A. Augustinus, P. Baillon, M. Battaglia, D. Bloch, et al., Operation, optimisation, and performance of the DELPHI RICH detectors, Nucl. Instrum. Methods Phys. Res. Sect. Accel. Spectrometers Detect. Assoc. Equip. 433 (1999) 47–58.

[7] A. Breskin, New trends in radiation imaging: CsI-based gaseous detectors, Nucl. Instrum. Methods Phys. Res. Sect. Accel. Spectrometers Detect. Assoc. Equip. 367 (1995) 326–331.

[8] A.F. Buzulutskov, Gaseous photodetectors with solid photocathodes, Phys. Part. Nucl. 39 (2008) 424–453.

[9] J. Almeida, A. Amadon, P. Besson, P. Bourgeois, A. Braem, A. Breskin, et al., Review of the development of cesium iodide photocathodes for application to large RICH detectors, Nucl. Instrum. Methods Phys. Res. Sect. Accel. Spectrometers Detect. Assoc. Equip. 367 (1995) 332–336.

[10] A. Braem, G. De Cataldo, M. Davenport, A. Di Mauro, A. Franco, A. Gallas, et al., Results from the ageing studies of large CsI photocathodes exposed to ionizing radiation in a gaseous RICH detector, Nucl. Instrum. Methods Phys. Res. Sect. Accel. Spectrometers Detect. Assoc. Equip. 553 (2005) 187–195.

[11] F. Gautheron, others, COMPASS-II Proposal, (2010).

[12] F. Sauli, A. Sharma, Micropattern Gaseous Detectors, Annu. Rev. Nucl. Part. Sci. 49 (1999) 341–388.

[13] M. Alexeev, R. Birsa, F. Bradamante, A. Bressan, M. Chiosso, P. Ciliberti, et al., The quest for a third generation of gaseous photon detectors for Cherenkov imaging counters, Nucl. Instrum. Methods Phys. Res. Sect. Accel. Spectrometers Detect. Assoc. Equip. 610 (2009) 174–177.

[14] P. Abbon, E. Albrecht, V.Y. Alexakhin, Y. Alexandrov, G.D. Alexeev, M.G. Alekseev, et al., The COMPASS experiment at CERN, Nucl. Instrum. Methods Phys. Res. Sect. Accel. Spectrometers Detect. Assoc. Equip. 577 (2007) 455–518.

[15] M. Hoch, Trends and new developments in gaseous detectors, Nucl. Instrum. Methods Phys. Res. Sect. Accel. Spectrometers Detect. Assoc. Equip. 535 (2004) 1–15.

[16] M. Titov, New Developments and Future Perspectives of Gaseous Detectors, Nucl. Instrum. Methods Phys. Res. Sect. Accel. Spectrometers Detect. Assoc. Equip. 581 (2007) 25–37.

[17] G.F. Knoll, Radiation detection and measurement, Wiley & Son, Oxford, 2010.

[18] W. Blum, W. Riegler, L. Rolandi, Particle detection with drift chambers, Springer, Berlin; New York, 2008.

[19] A. Peisert, F. Sauli, Drift and Diffusion of Electrons in Gases: A Compilation (With an Introduction to the Use of Computing Programs), (1984).
[20] B.M. Smirnov, DIFFUSION AND MOBILITY OF IONS IN A GAS, Sov. Phys. Uspekhi. 10 (1967) 313–331.
[21] J.M.F. dos Santos, J. a. M. Lopes, J.F.C.A. Veloso, P.C.P.S. Simões, T.H.V.T. Dias, F.P. Santos, et al., Development of portable gas proportional scintillation counters for x-ray spectrometry, X-Ray Spectrom. 30 (2001) 373–381.
[22] C.A.B. Oliveira, H. Schindler, R.J. Veenhof, S. Biagi, C.M.B. Monteiro, J.M.F. dos Santos, et al., A simulation toolkit for electroluminescence assessment in rare event experiments, Phys. Lett. B. 703 (2011) 217–222.
[23] G. Charpak, R. Bouclier, T. Bressani, J. Favier, Č. Zupančič, The use of multiwire proportional counters to select and localize charged particles, Nucl. Instrum. Methods. 62 (1968) 262–268.
[24] Press Release: The 1992 Nobel Prize in Physics, (n.d.).
[25] A. Oed, Position-sensitive detector with microstrip anode for electron multiplication with gases, Nucl. Instrum. Methods Phys. Res. Sect. Accel. Spectrometers Detect. Assoc. Equip. 263 (1988) 351–359.
[26] Physikalisches Institut Heidelberg - CASCADE-Gruppe, (n.d.).
[27] J.F.C.A. Veloso, J.M.F. dos Santos, C. a. N. Conde, R.E. Morgado, Application of a Microstrip Gas Counter in Energy-Dispersive X-Ray Fluorescence Analysis, X-Ray Spectrom. 26 (1997) 237–243.
[28] G. Charpak, F. Sauli, Multiwire proportional chambers and drift chambers, Nucl. Instrum. Methods. 162 (1979) 405–428.
[29] Y. Giomataris, P. Rebourgeard, J.P. Robert, G. Charpak, MICROMEGAS: a high-granularity position-sensitive gaseous detector for high particle-flux environments, Nucl. Instrum. Methods Phys. Res. Sect. Accel. Spectrometers Detect. Assoc. Equip. 376 (1996) 29–35.
[30] G. Charpak, P. Fonte, V. Peskov, F. Sauli, D. Scigocki, D. Stuart, Investigation of operation of a parallel-plate avalanche chamber with a CsI photocathode under high gain conditions, Nucl. Instrum. Methods Phys. Res. Sect. Accel. Spectrometers Detect. Assoc. Equip. 307 (1991) 63–68.
[31] A. Peisert, G. Charpak, F. Sauli, G. Viezzoli, F. Sauli, Development of a Multistep Parallel-Plate Chamber as Time Projection Chamber End-Cap or Vertex Detector, IEEE Trans. Nucl. Sci. 31 (1984) 125–128.
[32] Y. Giomataris, Development and prospects of the new gaseous detector “Micromegas,” Nucl. Instrum. Methods Phys. Res. Sect. Accel. Spectrometers Detect. Assoc. Equip. 419 (1998) 239–250.
[33] I. Giomataris, R. De Oliveira, S. Andriamonje, S. Aune, G. Charpak, P. Colas, et al., Micromegas in a bulk, Nucl. Instrum. Methods Phys. Res. Sect. Accel. Spectrometers Detect. Assoc. Equip. 560 (2006) 405–408.
[34] G. Iakovidis, The Micromegas Project for the ATLAS Upgrade, ArXiv13100734 Hep-Ex Physicsphysics. (2013).
[35] N. Abgrall, B. Andrieu, P. Baron, P. Bene, V. Berardi, J. Beucher, et al., Time projection chambers for the T2K near detectors, Nucl. Instrum. Methods Phys. Res. Sect. Accel. Spectrometers Detect. Assoc. Equip. 637 (2011) 25–46.
[36] F. Sauli, GEM: A new concept for electron amplification in gas detectors, Nucl. Instrum. Methods Phys. Res. Sect. Accel. Spectrometers Detect. Assoc. Equip. 386 (1997) 531–534.
[37] F. Sauli, Imaging with the gas electron multiplier, Nucl. Instrum. Methods Phys. Res. Sect. Accel. Spectrometers Detect. Assoc. Equip. 580 (2007) 971–973.
[38] A. Buzulutskov, A. Breskin, R. Chechik, G. Garty, F. Sauli, L. Shekhtman, The GEM photomultiplier operated with noble gas mixtures, Nucl. Instrum. Methods Phys. Res. A. 443 (2000) 164–180.
[39] F. Sauli, Progress with the gas electron multiplier, Nucl. Instrum. Methods Phys. Res. Sect. Accel. Spectrometers Detect. Assoc. Equip. (2004) 93–98.
[40] B. Ketzer, Q. Weitzel, S. Paul, F. Sauli, L. Ropelewski, Performance of triple GEM tracking detectors in the COMPASS experiment, Nucl. Instrum. Methods Phys. Res. Sect. Accel. Spectrometers Detect. Assoc. Equip. 535 (2004) 314–318.
[41] J.F.C.A. Veloso, J.M.F. Dos Santos, C.A.N. Conde, A proposed new microstructure for gas radiation detectors: The microhole and strip plate, Rev. Sci. Instrum. 71 (2000) 2371–2376.
[42] J.M. Maia, D. Mormann, A. Breskin, R. Chechik, J.F.C.A. Veloso, F.P. Santos, Progress in MHSP electron multiplier operation, in: 2003 IEEE Nucl. Sci. Symp. Conf. Rec., 2003: pp. 525–529 Vol.1.
[43] H. Natal da Luz, J.F.C.A. Veloso, F.D. Amaro, L.F. Requicha Ferreira, J.M.F. dos Santos, A. Breskin, et al., MHSP operation in pure xenon, Nucl. Instrum. Methods Phys. Res. Sect. Accel. Spectrometers Detect. Assoc. Equip. 552 (2005) 259–262.

[44] A. Breskin, R. Alon, M. Cortesi, R. Chechik, J. Miyamoto, V. Dangendorf, et al., A concise review on THGEM detectors, Nucl. Instrum. Methods Phys. Res. Sect. Accel. Spectrometers Detect. Assoc. Equip. 598 (2009) 107–111.
[45] R. Chechik, A. Breskin, C. Shalem, D. Moermann, Thick GEM-like hole multipliers: properties and possible applications, arXiv:physics/0404119. (2004).
[46] F.D. Amaro, C. Santos, J.F.C.A. Veloso, A. Breskin, R. Chechik, J.M.F. dos Santos, The Thick-COBRA: a New Gaseous Electron Multiplier for Radiation Detectors, ArXiv10080830 Phys. (2010).
[47] A.L.M. Silva, C.D.R. Azevedo, L.F.N.D. Carramate, T. Lopes, I.F. Castro, R. de Oliveira, et al., X-ray imaging detector based on a position sensitive THCOBRA with resistive line, J. Instrum. 8 (2013) P05016.
[48] J. Seguinot, T. Ypsilantis, A historical survey of ring imaging Cherenkov counters, Nucl. Instrum. Methods Phys. Res. Sect. Accel. Spectrometers Detect. Assoc. Equip. 343 (1994) 1–29.
[49] E. Nappi, J. Seguinot, Ring imaging Cherenkov detectors: The state of the art and perspectives, RivNuovo Cim. 28 (2005) 1–130.
[50] S. Dalla Torre, Status and perspectives of gaseous photon detectors, Nucl. Instrum. Methods Phys. Res. Sect. Accel. Spectrometers Detect. Assoc. Equip. 639 (2011) 111–116.
[51] J. Va'vra, Long-term operational experience with the barrel CRID at SLD, Nucl. Instrum. Methods Phys. Res. Sect. Accel. Spectrometers Detect. Assoc. Equip. 433 (1999) 59–70.
[52] M. Adams, A. Bastin, G. Coutrakon, H. Glass, D. Jaffe, J. Kirz, et al., π/K/p identification with a large-aperture ring-imaging cherenkov counter, Nucl. Instrum. Methods Phys. Res. 217 (1983) 237–243.
[53] M. Artuso, R. Ayad, F. Azfar, A. Efimov, S. Kopp, R. Mountain, et al., Performance of the CLEO III LiF-TEA ring imaging Cherenkov detector in a high-energy muon beam, Nucl. Instrum. Methods Phys. Res. Sect. Accel. Spectrometers Detect. Assoc. Equip. 441 (2000) 374–392.
[54] F. Piuz, A. Braem, G. Paic, R.S. Ribeiro, T.D. Williams, First observation of Cherenkov rings in a fast RICH detector combining a cesium iodide photoconverter with an atmospheric pressure wire chamber, Nucl. Instrum. Methods Phys. Res. Sect. Accel. Spectrometers Detect. Assoc. Equip. 333 (1993) 404–412.
[55] A. Breskin, CsI UV photocathodes: history and mystery, Nucl. Instrum. Methods Phys. Res. Sect. Accel. Spectrometers Detect. Assoc. Equip. 371 (1996) 116–136.
[56] A. Di Mauro, E. Nappi, F. Posa, A. Breskin, A. Buzulutskov, R. Chechik, et al., Photoelectron backscattering effects in photoemission from CsI into gas media, Nucl. Instrum. Methods Phys. Res. Sect. Accel. Spectrometers Detect. Assoc. Equip. 371 (1996) 137–142.
[57] M. Alexeev, M. Alfonsi, R. Birsa, F. Bradamante, A. Bressan, M. Chiosso, et al., Development of THGEM-based photon detectors for Cherenkov Imaging Counters, J. Instrum. 5 (2010) P03009.
[58] C. Lu, K.T. McDonald, Properties of reflective and semitransparent CsI photocathodes, Nucl. Instrum. Methods Phys. Res. A. 343 (1994) 135–151.
[59] A. Breskin, A. Buzulutskov, R. Chechik, B.K. Singh, A. Bondar, L. Shekhtman, Sealed GEM photomultiplier with a CsI photocathode: ion feedback and ageing, Nucl. Instrum. Methods Phys. Res. Sect. Accel. Spectrometers Detect. Assoc. Equip. 478 (2002) 225–229.
[60] H. Hoedlmoser, A. Braem, G. De Cataldo, M. Davenport, A. Di Mauro, A. Franco, et al., Production technique and quality evaluation of CsI photocathodes for the ALICE/HMPID detector, Nucl. Instrum. Methods Phys. Res. Sect. Accel. Spectrometers Detect. Assoc. Equip. 566 (2006) 338–350.
[61] H. Hoedlmoser, A. Braem, G. De Cataldo, M. Davenport, A. Di Mauro, A. Franco, et al., Long term performance and ageing of CsI photocathodes for the ALICE/HMPID detector, Nucl. Instrum. Methods Phys. Res. Sect. Accel. Spectrometers Detect. Assoc. Equip. 574 (2007) 28–38.
[62] M. Spegel, The impact of the TIC on the physics performance of NA44, Nucl. Instrum. Methods Phys. Res. Sect. Accel. Spectrometers Detect. Assoc. Equip. 433 (1999) 366–371.
[63] R. Gernhäuser, J. Friese, J. Homolka, A. Kastenmüller, P. Kienle, H.-J. Körner, et al., Cesium iodide photon converter performance in a gaseous RICH detector, Nucl. Instrum. Methods Phys. Res. Sect. Accel. Spectrometers Detect. Assoc. Equip. 438 (1999) 104–108.
[64] E. Albrecht, G. Baum, R. Birsa, F. Bradamante, A. Bressan, A. Chapiro, et al., Status and characterisation of COMPASS RICH-1, Nucl. Instrum. Methods Phys. Res. Sect. Accel. Spectrometers Detect. Assoc. Equip. 553 (2005) 215–219.
[65] A. Braem, D. Cozza, M. Davenport, G. De Cataldo, L.D. Olio, D. DiBari, et al., Identification of high p⊥ particles with the STAR-RICH detector, Nucl. Instrum. Methods Phys. Res. Sect. Accel. Spectrometers Detect. Assoc. Equip. 499 (2003) 720–724.

[66] F. Garibaldi, E. Cisbani, S. Colilli, F. Cusanno, S. Frullani, R. Fratoni, et al., A proximity focusing RICH detector for kaon physics at Jefferson lab hall A, Nucl. Instrum. Methods Phys. Res. Sect. Accel. Spectrometers Detect. Assoc. Equip. 502 (2003) 117–122.

[67] R. Chechik, A. Breskin, G.P. Guedes, D. Moermann, J. Maia, V. Dangendorf, et al., Recent Investigations of Cascaded GEM and MHSP detectors, IEEE Trans. Nucl. Sci. 51 (2004) 2097–2103.

[68] A. Breskin, T. Boutboul, A. Buzulutskov, R. Chechik, E.S. Garty G., B.K. Singh, Advances in gas avalanche photomultipliers, Nucl. Instrum. Methods Phys. Res. Sect. Accel. Spectrometers Detect. Assoc. Equip. 442 (2000) 58–67.

[69] D. Mörmann, A. Breskin, R. Chechik, P. Cwetanski, B.K. Singh, A gas avalanche photomultiplier with a CsI-coated GEM, Nucl. Instrum. Methods Phys. Res. Sect. Accel. Spectrometers Detect. Assoc. Equip. 478 (2002) 230–234.

[70] R. Chechik, A. Breskin, Advances in Gaseous Photomultipliers, Nucl. Instrum. Methods Phys. Res. Sect. Accel. Spectrometers Detect. Assoc. Equip. 595 (2008) 116–127.

[71] D. Mörmann, A. Breskin, R. Chechik, C. Shalem, Operation principles and properties of the multi-GEM gaseous photomultiplier with reflective photocathode, Nucl. Instrum. Methods Phys. Res. Sect. Accel. Spectrometers Detect. Assoc. Equip. 530 (2004) 258–274.

[72] Z. Fraenkel, A. Kozlov, M. Naglis, I. Ravinovich, L. Shekhtman, I. Tserruya, et al., A hadron blind detector for the PHENIX experiment at RHIC, Nucl. Instrum. Methods Phys. Res. Sect. Accel. Spectrometers Detect. Assoc. Equip. 546 (2005) 466–480.

[73] R.P. Pisani, T.K. Hemmick, H. Chung, S.C. Johnson, T. Piazza, T. Vongpaseuth, et al., A prototype HBD for PHENIX, Nucl. Instrum. Methods Phys. Res. Sect. Accel. Spectrometers Detect. Assoc. Equip. 433 (1999) 212–216.

[74] A. Milov, W. Anderson, B. Azmoun, C.-Y. Chi, A. Drees, A. Dubey, et al., Construction and expected performance of the hadron blind detector for the PHENIX experiment at RHIC, J. Phys. G Nucl. Part. Phys. 34 (2007) S701.

[75] D. Mörmann, A. Breskin, R. Chechik, D. Bloch, Evaluation and reduction of ion back-flow in multi-GEM detectors, Nucl. Instrum. Methods Phys. Res. Sect. Accel. Spectrometers Detect. Assoc. Equip. 516 (2004) 315–326.

[76] J.F.C.A. Veloso, F.D. Amaro, J.M. Maia, A.V. Lyashenko, A. Breskin, R. Chechik, et al., MHSP in reversed-bias operation mode for ion blocking in gas-avalanche multipliers, Nucl. Instrum. Methods Phys. Res. Sect. Accel. Spectrometers Detect. Assoc. Equip. 548 (2005) 375–382.

[77] A.V. Lyashenko, A. Breskin, R. Chechik, J.F.C.A. Veloso, J.M.F.D. Santos, F.D. Amaro, Advances in ion back-flow reduction in cascaded gaseous electron multipliers incorporating R-MHSP elements, J. Instrum. 1 (2006) P10004.

[78] A.V. Lyashenko, A. Breskin, R. Chechik, J.F.C.A. Veloso, J.M.F.D. Santos, F.D. Amaro, Further progress in ion back-flow reduction with patterned gaseous hole-multipliers, J. Instrum. 2 (2007) P08004.

[79] M. Alexeev, R. Birsa, F. Bradamante, A. Bressan, M. Büchele, M. Chiosso, et al., Status and progress of novel photon detectors based on THGEM and hybrid MPGD architectures, J. Instrum. 8 (2013) C12005–C12005.

[80] A.J. Davies, The finite element method, Clarendon Press, Oxford, 1980.

[81] T.H.V.T. Dias, F.P. Santos, A.D. Stauffer, C.A.N. Conde, Monte Carlo simulation of x-ray absorption and electron drift in gaseous xenon, Phys. Rev. A. 48 (1993) 2887–2902.

[82] R. Veenhof, Garfield - simulation of gaseous detectors, (2014).

[83] T. Francke, M. Suffert, Rich counter using a solid radiator and a low pressure MWPC, Nucl. Instrum. Methods Phys. Res. A. 283 (1989) 608–611.

[84] P. Abbon, M. Alexeev, H. Angerer, G. Baum, R. Birsa, P. Bordalo, et al., The experience of building and operating COMPASS RICH-1, Nucl. Instrum. Methods Phys. Res. Sect. Accel. Spectrometers Detect. Assoc. Equip. 639 (2011) 15–19.

[85] R. Chechik, A. Breskin, C. Shalem, Thick GEM-like multipliers - a simple solution for large area UV-RICH detectors, Nucl. Instrum. Methods Phys. Res. Sect. Accel. Spectrometers Detect. Assoc. Equip. 553 (2005) 35–40.

[86] C.D.R. Azevedo, M. Cortesi, A.V. Lyashenko, A. Breskin, R. Chechik, J. Miyamoto, et al., Towards THGEM UV-photon detectors for RICH: on single-photon detection efficiency in Ne/CH4 and Ne/CF4, J. Instrum. 5 (2010) P01002–P01002.

[87] V. Peskov, M. Cortesi, R. Chechik, A. Breskin, Further evaluation of a THGEM UV-photon detector for RICH - comparison with MWPC, J. Instrum. 5 (2010) P11004–P11004.
[88] D. Cozza, G. De Cataldo, D. Dell'Olio, L. Dell'Olio, D. Di Bari, A. Franco, et al., The CSI-based RICH detector array for the identification of high momentum particles in ALICE, Nucl. Instrum. Methods Phys. Res. Sect. Accel. Spectrometers Detect. Assoc. Equip. 502 (2003) 101–107.
[89] <b>alice Collaboration</B>, F. Carminati, P. Foka, P. Giubellino, A. Morsch, G. Paic, et al., ALICE: Physics Performance Report, Volume I, J. Phys. G Nucl. Part. Phys. 30 (2004) 1517.
[90] B.N. Ratcliff, DIRC dreams redux: Research directions for the next generation of internally reflected imaging counters, ICFA InstrumBull. 22 (2001) 03.
[91] I. Adam, R. Aleksan, L. Amerman, E. Antokhin, D. Aston, P. Bailly, et al., The DIRC particle identification system for the BaBar experiment, Nucl. Instrum. Methods Phys. Res. Sect. Accel. Spectrometers Detect. Assoc. Equip. 538 (2005) 281–357.
[92] P. Abbon, M. Alexeev, H. Angerer, G. Baum, R. Birsa, P. Bordalo, et al., Particle identification with COMPASS RICH-1, Nucl. Instrum. Methods Phys. Res. Sect. Accel. Spectrometers Detect. Assoc. Equip. 631 (2011) 26–39.
[93] E. Albrecht, G. Baum, R. Birsa, M. Bosteels, F. Bradamante, A. Braem, et al., COMPASS RICH-1, Nucl. Instrum. Methods Phys. Res. Sect. Accel. Spectrometers Detect. Assoc. Equip. 478 (2002) 340–343.
[94] E. Albrecht, G. Baum, R. Birsa, F. Bradamante, A. Braem, A. Bressan, et al., COMPASS RICH-1, Nucl. Instrum. Methods Phys. Res. Sect. Accel. Spectrometers Detect. Assoc. Equip. 502 (2003) 112–116.
[95] P. Abbon, M. Alexeev, H. Angerer, R. Birsa, P. Bordalo, F. Bradamante, et al., Design and construction of the fast photon detection system for COMPASS RICH-1, Nucl. Instrum. Methods Phys. Res. Sect. Accel. Spectrometers Detect. Assoc. Equip. 616 (2010) 21–37.
[96] P. Abbon, M. Alekseev, H. Angerer, M. Apollonio, R. Birsa, P. Bordalo, et al., Design and status of COMPASS FAST-RICH, Nucl. Instrum. Methods Phys. Res. Sect. Accel. Spectrometers Detect. Assoc. Equip. 567 (2006) 114–117.
[97] P. Abbon, M. Alexeev, H. Angerer, R. Birsa, P. Bordalo, F. Bradamante, et al., The COMPASS RICH-1 fast photon detection system, Nucl. Instrum. Methods Phys. Res. Sect. Accel. Spectrometers Detect. Assoc. Equip. 595 (2008) 23–26.
[98] P. Abbon, M. Alexeev, H. Angerer, R. Birsa, P. Bordalo, F. Bradamante, et al., Read-out electronics for fast photon detection with COMPASS RICH-1, Nucl. Instrum. Methods Phys. Res. Sect. Accel. Spectrometers Detect. Assoc. Equip. 587 (2008) 371–387.
[99] P. Abbon, E. Delagnes, H. Deschamps, F. Kunne, S. Gerasimov, B. Ketzer, et al., Fast readout of the COMPASS RICH CsI-MWPC photon chambers, Nucl. Instrum. Methods Phys. Res. Sect. Accel. Spectrometers Detect. Assoc. Equip. 567 (2006) 104–106.
[100] J. Va'vra, Photon detectors, Nucl. Instrum. Methods Phys. Res. Sect. Accel. Spectrometers Detect. Assoc. Equip. 371 (1996) 33–56.
[101] M. Alexeev, F. Barbosa, R. Birsa, F. Bradamante, A. Bressan, M. Chiosso, et al., Detection of single photons with ThickGEM-based counters, J. Instrum. 7 (2012) C02014.
[102] F. Paschen, Ueber die zum Funkenübergang in Luft, Wasserstoff und Kohlensäure bei verschiedenen Drucken erforderliche Potentialdifferenz, Ann. Phys. 273 (1889) 69–96.
[103] S. Kane, J. May, J. Miyamoto, I. Shipsey, I. Giomataris, A study of a combination of MICROMEGAS + GEM chamber in Ar-CO2 gas, in: 2001 IEEE Nucl. Sci. Symp. Conf. Rec., 2001: pp. 265–268 vol.1.
[104] S. Kane, J. May, J. Miyamoto, I. Shipsey, S. Andriamonje, A. Delbart, et al., a Study of Micromegas with Preamplification with a Single GEM, in: 2002: pp. 694–703.
[105] M. Alexeev, R. Birsa, F. Bradamante, A. Bressan, M. Chiosso, P. Ciliberti, et al., Ion backflow in thick GEM-based detectors of single photons, J. Instrum. 8 (2013) P01021.
[106] F. Sauli, L. Ropelewski, P. Everaerts, Ion feedback suppression in time projection chambers, Nucl. Instrum. Methods Phys. Res. Sect. Accel. Spectrometers Detect. Assoc. Equip. 560 (2006) 269–277.
[107] M. Alexeev, F. Barbosa, R. Birsa, F. Bradamante, A. Bressan, M. Chiosso, et al., Detection of single photons with THickGEM-based counters, Nucl. Instrum. Methods Phys. Res. Sect. Accel. Spectrometers Detect. Assoc. Equip. 695 (2012) 159–162.
[108] L. Landau, On the energy loss of fast particles by ionization, J.Phys.(USSR). 8 (1944) 201–205.
[109] M. Alexeev, R. Birsa, F. Bradamante, A. Bressan, M. Büchele, M. Chiosso, et al., THGEM-based photon detectors for the upgrade of COMPASS RICH-1, Nucl. Instrum. Methods Phys. Res. Sect. Accel. Spectrometers Detect. Assoc. Equip. 732 (2013) 264–268.